Implications of Aerosol Growth Dynamics and Aerosol-Cloud Interaction to the Sun-Cloud-Climate Hypothesis

Dissertation

Zur Erlangung des Doktorgrades der Naturwissenschaften

im Department für Geowissenschaften

der Universität Hamburg

vorgelegt von

François Benduhn

aus Luxemburg

Hamburg 2008

Als Dissertation angenommen vom Department für Geowissenschaften der Universität Hamburg

Auf Grund der Gutachten von Herrn Prof. Dr. Hartmut Graßl
und Herrn Dr. Frank Müller

Hamburg, den 29. Oktober 2007

Prof. Dr. Kay-Christian Emeis
Leiter des Departments für Geowissenschaften

Implications of Aerosol Growth Dynamics

and Aerosol-Cloud Interaction

to the Sun-Cloud-Climate Hypothesis

François Benduhn

Issue and Objective

Controversial debate and conjectures on the amplitude of solar climate forcing have spread since Svensmark and Friis-Christensen (1997) revealed empirical evidence of an anti-correlation between the solar cycle and the global cloudiness. Several hypotheses about the mechanism of enhanced indirect solar forcing have been evoked. In particular, the theories of Marsh and Svensmark (2000) and Larsen (2005) argue for a solar modulation of the troposphere via secondary aerosol particle formation and cloud microphysics.

The issue of the present study is to develop an appropriate formalism to represent certain aspects of their theories, these are:

1) The sensibility of aerosol growth dynamics to atmospheric ionisation and sulphuric acid formation rate variability.
2) The relative importance of sea salt and secondary aerosol under typically marine conditions.
3) The feedback behaviour of aerosol number and size distribution, and cloud nuclei activation.
4) The relationship between the aerosol and the formation of precipitation.

Based on this formalism computational tools are created that allow investigating specifically the interaction of aerosol and cloud physics. Doing so it is attempted to reduce the uncertainty related to the assumptions of the theories of Marsh and Svensmark (2000) and Larsen (2005), which is the objective of the present study.

Table of Contents

I. Introduction

It is in Theophrastus' short treatise on meteorology *'Concerning weather signs'[1]* that a first indication is found for the solar cycle, that is sunspots, to affect atmospheric cloud properties. It reads: "...if the sun when it rises has a black mark, or if it rises out of clouds, it is a sign of rain." (par. 11) and further: "Also black spots on the sun or moon indicate rain and red spots wind." (par. 27) and conversely: "If the sun rises (..) without any special sign in his orb, it indicates fair weather." (par. 50). From the structure and content of this work the two modern, sometimes in practice antagonistic, forms of scientific investigation are already visible. On the one hand we have empiricism, i.e. scientific knowledge acquisition by observation: "The signs (...) we have described so far as attainable, partly from our own observation, partly from the information of persons of credit." (par. 1) On the other hand there is a will of systematisation that is the basis of investigation through abstract theory. So, the chapters are likely structured in signs related to astronomy, meteorological indicators such as wind direction, and finally the behaviour of animals and plant growth. The same desire of systematisation draws a parallel between the appearance of the sun and of the moon, because "...the moon is as it were a nocturnal sun." (par. 5). It is this desire to create links, of induction, that certainly explains the above statement of the moon potentially having black and red spots, which we today commonly know to be incorrect. This exhibits a common jeopardy to all theoreticians, that in the process of abstract investigation the link with reality is lost due to a lack of consideration of bare facts, be it negligence or absence of observation. Had Theophrastus himself made the related astronomical observations he would have known for the non-existence of moon spots and may have deduced that sun and moon are unequal in their nature.

The present investigation is basically virtual in as much as it tries to reproduce computationally the formation and growth of secondary aerosol particles under marine conditions following a systematised compilation of appropriate pre-known physical laws that describe the subprocesses. The scheme of systematisation underlies a simplification that corresponds to the author's idea of reality, and which he has tried to justify through

---

1   Theophrastus (371-287 B.C.) was Aristotle's main pupil and successor as head of the Athenian Lyceum. Among his remaining oeuvre on natural sciences is *De signis tempestatum*, which apart Aristotle´s *Meteorology* is considered to be a reference on atmospheric physics in the Antiquity (e.g. Hort, A., *Enquiry into Plants and Minor Works on Odours and Weather Signs,* The Loeb Classical Library, Heinemann, London, 1916).

comparison with observations made at his disposal through literature. However, the validation process is also restricted by the same literature in as much as data, be it empirical or not, is still quite limited in time, space and number, and also controversial and unreliable for some processes involved. As an example there are only quite a few attempts to quantify the solar modulation of the atmospheric ionisation rate at the earth's surface, not least because it has been regarded to be irrelevant so far. However, it appeared in the course of this study that the lack of data in this particular case may be of limited relevance only because the modelled process shows little sensitivity to cosmic ray intensity variation. On the other hand satellite observation has made a lot of data available on the variability of the global cloud fraction, but the associated parameters evolve in such a limited way that it is questionable whether their variability may currently be resolved via remote measurements. It is therefore precarious whether the indirect solar climate modulation via the global cloud fraction indicated by certain empirical studies is an existing phenomenon. As a corollary the present investigation can not find proof for the investigated hypotheses, it may merely find support for, restrict the space for manoeuvre of, or within the limits of the model assumptions exclude the validity of these.

II. The solar modulation of global climate

II.1 Empirical evidence

II.1.1 Tropospheric evidence

Conjectures about a solar cycle influence on climate have been a recurrent phenomenon since the original comments of Sir William Herschel at the beginning of the 19th century in the wake of the systematic observation of sunspots. Figure II.1 (Hoyt and Schatten, 1997, p. 5) depicts the publication frequency on the issue, showing that the solar cycle climate link has regularly been in vogue among the scientific community. Interestingly, discussion was not limited
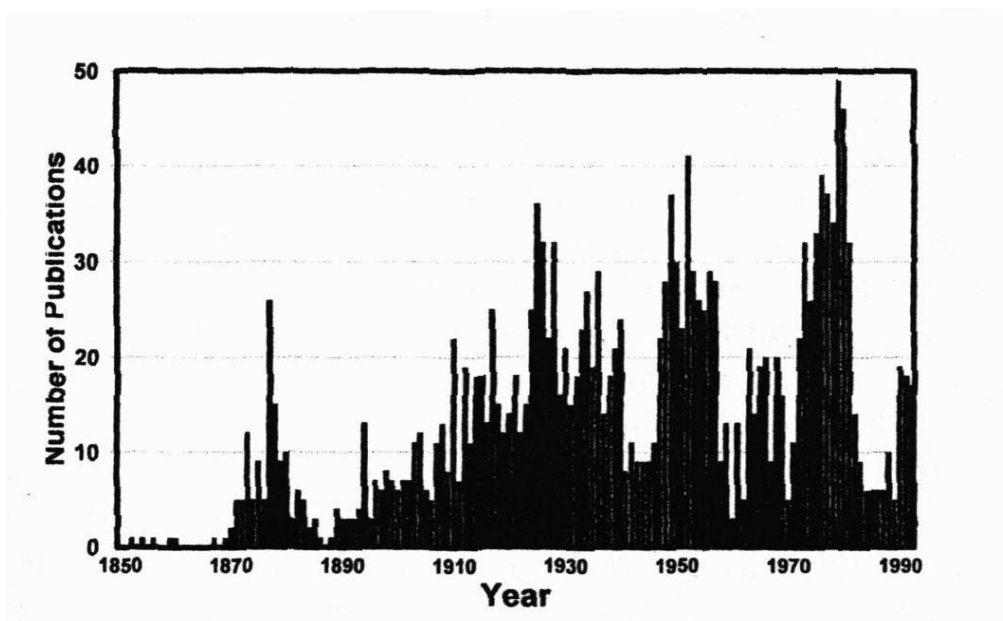
Figure II.1: Number of publications per year on solar modulation of global climate. Adapted from Hoyt and Schatten (1997).

exclusively to the domain of physical science. Thus, around the 1870s climate influence was an issue among economists; and actually a link between the existence of economical cycles of a still sufficiently agrarian society and the sunspot cycle has been suggested by the University of Manchester Professor W.S. Jevons who noted that the mean cycle period was 10.44 and

10.45 years, respectively (Stewart, 1967, p. 30).

After a resting phase during the 1980s, interest in the solar cycle climate link has been increasing again, especially in the context of anthropogenic global warming. A statistical study of Schlesinger and Ramankutty (1992) upholds the pertinence of the ongoing debate. Figure II.2 shows the contribution of greenhouse gases, the solar cycle and sulphate aerosols
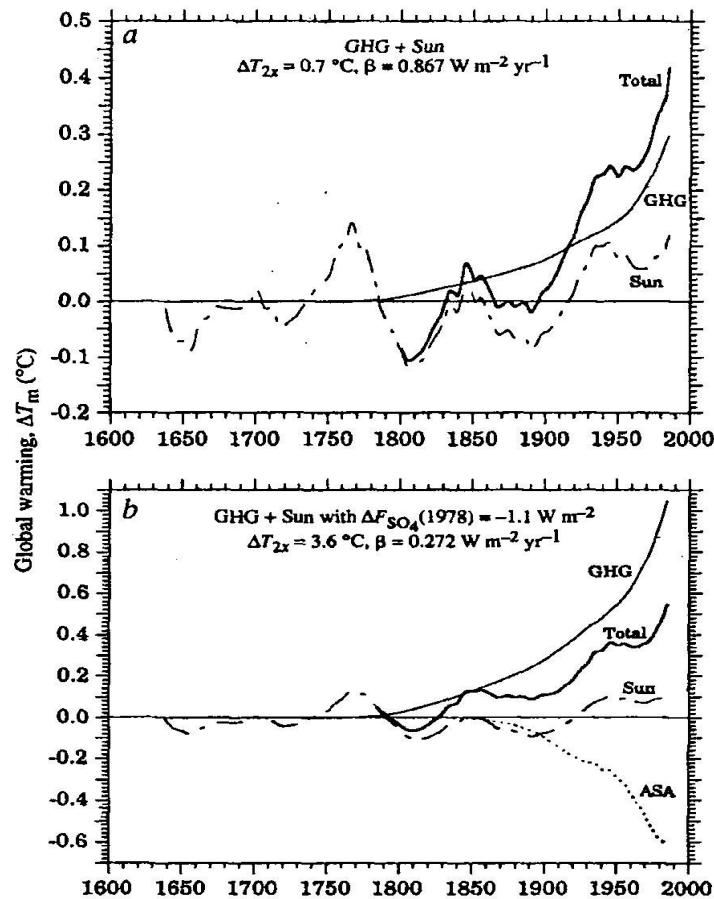
Figure II.2: Part of greenhouse gases (GHG), solar modulation and sulphate aerosols (ASA) in global climate variability according to a statistical study of Schlesinger and Ramankutty (1992). ΔT_{2x} is the climate sensitivity to a doubling of the GHG concentration, β is the energetic solar cycle modulation, according to statistical fitting.

to global mean temperature when fitting their respective radiative variation to the observed climate evolution. ΔT_{2x} stands for the global mean temperature response subsequent to the radiative forcing of a doubled atmospheric concentration of the long-lived greenhouse gases, while β stands for the variation of the solar constant during the solar cycle per year according to the ansatz that $\Delta F_{sun} = \beta \cdot (P - t)$, where P is the mean period of the cycle and t is the mean

15

cycle equivalent point in time. From this relationship we see that β represents the amplitude of solar flux variation, which is assumed to be an unknown determined by the best statistical fit. Comparing the upper with the lower panel it appears that the cooling effect of sulphate aerosols requires the steadily increasing contribution of greenhouse gases while the contribution of the oscillating radiative output of the sun is reduced as it is demonstrated by the reduction of the β-value. Nevertheless, the amplitude of the variability of the solar
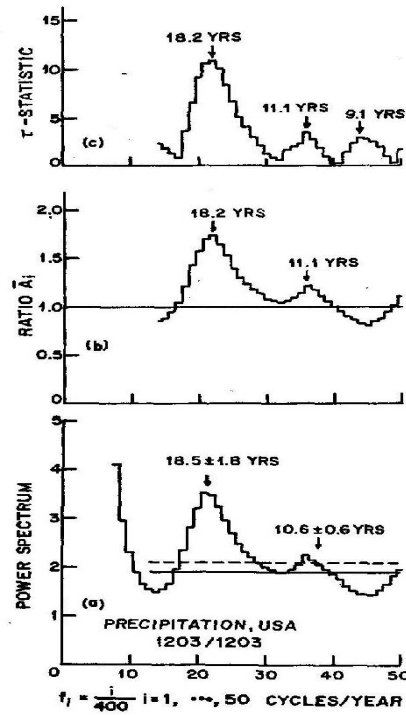
Figure II.3, from bottom to top: a) solar signal in the power spectrum of USA precipitation records, b) its ratio to white noise spectrum indicated by the dotted line in (a), and c) the t-test density distribution value of the afore mentioned ratio. Adapted from Currie (1992).

radiation flux is still approximatively twice its observed value of about 1.36 W/m^2 (Lean, 1991). This statistical result, in the limits of a direct linear response of climate to the variation of its relevant factors on the observed time scale, demonstrates the secondary role of solar variability relative to greenhouse gases. Moreover it is an indication that solar influence on climate may not be well understood in as much as an unknown feedback process or unknown indirect factor acting in parallel may be present. It also stresses that due to the relative weakness of the solar signal, especially on the time scale of the solar cycle, its statistical evaluation should ideally involve more sensitive and therefore expressive tools as direct

16

comparison in terms of correlation coefficients, such as Fourier spectral analysis and statistical testing.

Beneath climatology and economics, the solar signal has been looked for in numerous fields, including in relationship with lake levels and river discharge, seaweed and fish proliferation, as well as storm frequency (see Hoyt and Schatten, 1997). Currie (1992 and 1993) has investigated USA precipitation and temperature records, respectively. He used both the fast Fourier transform spectrum and the maximum entropy spectrum analysis methods, the results
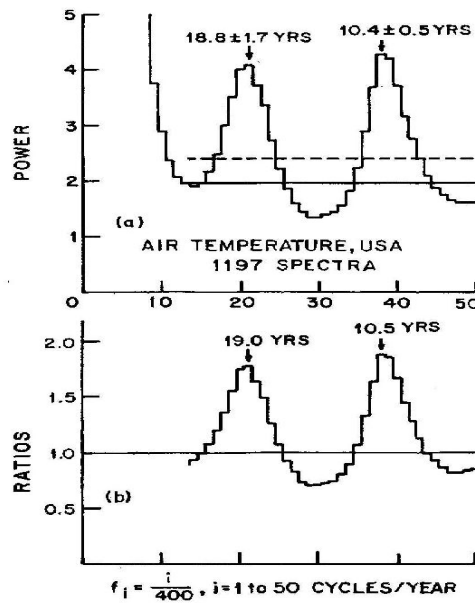
Figure II.4: In analogy to the preceding figure power spectrum and ratio to white noise spectrum of the solar signal in USA surface temperature record, according to Currie (1993).

of which are shown in Figures II.3 and II.4, depicting two prominent power peaks of approximately 11 and 18 years period. The ratios of the temperature and precipitation spectra to the corresponding white noise continuum spectrum (assuming that the generated spectrum is due to random fluctuations) are also shown, as indicated by a dashed line in the upper power spectrum grid. The ratios were tested using Student's t-test and assuming chi-square distribution for random fluctuations of spectral ratios. The result is that both power peaks are significant on the 99.9% level in case of temperature, while the 11.1-year precipitation record peak is significant on the 98% level and the 18 year precipitation signal is also significant on the 99.9% level. Currie identified the 11.1 and the 10.5 year peaks to be the solar cycle signals while the 18.2 and the 18.8 years signals were associated with the 18.6-year luni-solar tidal

17

constituent. The shown spectra are resulting from 1192 single spectra so that the degrees of freedom for the t-tests are virtually infinite making the statistical evidence highly confident.

Marsh and Svensmark (2000) and Kristjansson and Kristiansen (2000) issued contradictory publications on the empirical evidence for a global mean cloud fraction - solar cycle link. While Svensmark and Friis-Christensen's (1998) analysis of data of the International Satellite Cloud Climatology Project and the Defense Meteorological Satellite Program showed a close
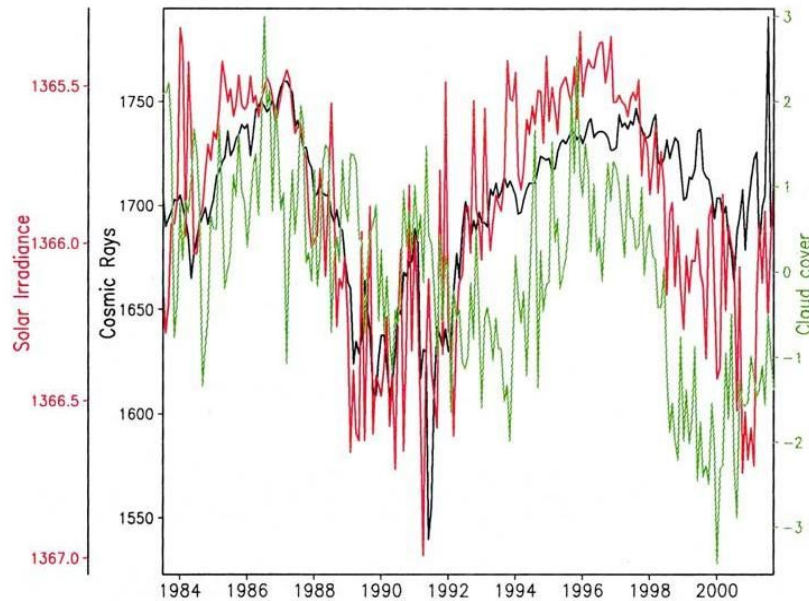
Figure II.5: Solar radiation flux, cosmic rays flux (as evaluated from surface neutron counters) and global low cloud cover variability (see text). Adapted from Kristjansson et al. (2004).

anticorrelation between the cosmic ray flux used as a proxy for solar activity and the low cloud fraction over the midlatitude ocean (depicted in Figure II.5), Kristjansson and Kristiansen (2000) found no significant link using the same datasets as well as synoptic data, but for all types of clouds (not shown).

In a later publication producing a regional analysis of the ISCCP C2 and D2 datasets Kristjansson et al. (2004) found a correlation between the solar cycle and the mean cloud fraction over the central and eastern Pacific (Figure II.6), that is exactly the opposite to Svensmark's evaluation. Kristjansson et al. (2004) attributed the correlation of mean cloudiness and the solar cycle to the influence of the sea surface temperature that presents a similar decadal pattern, stating thus that cloud formation is rather modulated by convective

processes than microphysical parameters. To compare these contradictory results to the robust solar signal proof of Currie, the reader's attention should be drawn to the difference in approach of statistical analysis.

An example of long-time sun atmosphere correlation is given by Neff et al. (2001). They
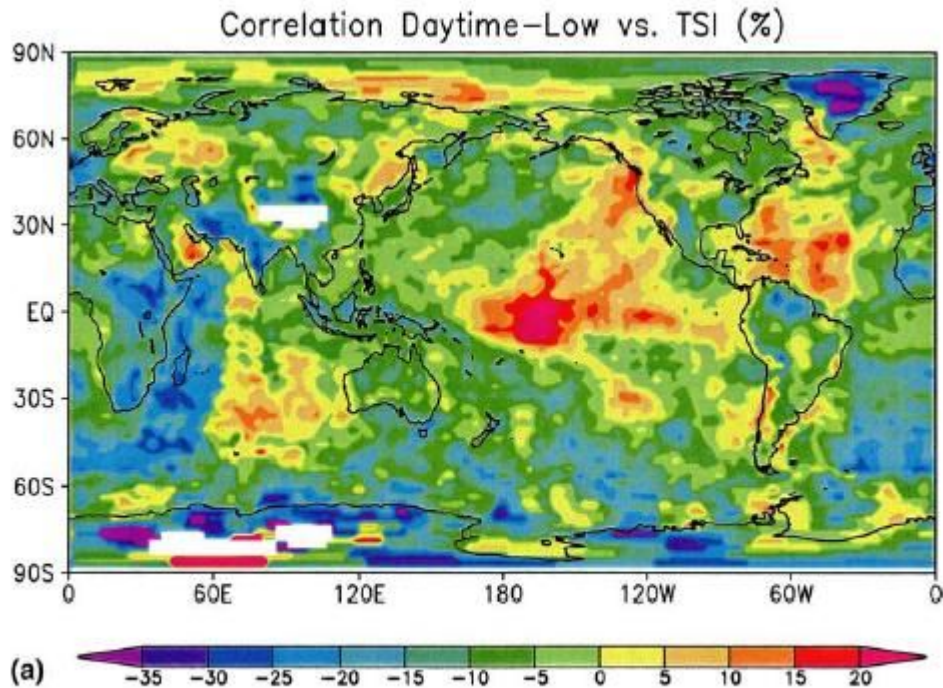
Figure II.6: Surface distribution of the correlation of solar irradiance and low cloud cover showing a tendency for cloud formation to be enhanced over warm surface water. Adapted from Kristjansson et al. (2004).

compared [18]O isotope deviations obtained from a stalagmite in Oman to the evolution of tree ring ^{14}C records. The unstable ^{14}C isotope should be a good proxy of solar activity variability as it forms in the upper part of the atmosphere involving high energy galactic cosmic rays. The stable [18]O isotope undergoes a certain number of processes of fractionation from evaporation at the surface of the water body to condensation and precipitation within the atmosphere, and eventually integration through chemical precipitation in calcite stones. Thus, it serves as a proxy of water origin, the distance between the evaporating water body and the spot of precipitation as hydrometeors, and the temperature under which these processes, especially chemical precipitation, take place. A working hypothesis in this particular publication is that the correlation shown in Figure II.7 between these two proxies shows the

19

link between solar activity and the intensity of the monsoon precipitation in Oman. When solar activity is low the local monsoon intensifies leading to higher precipitation levels and to a lower fractionation tendency of ^{18}O during condensation relative to mean ocean water. The effect should therefore reflect a regional phenomenon following a synoptic process that is summer monsoon. However Marsh and Svensmark (2003) reinterpreted these results as an
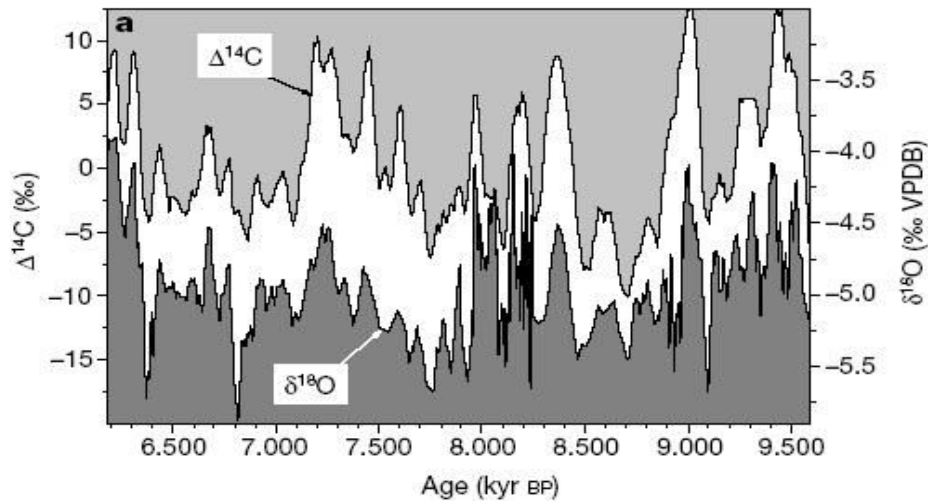
Figure II.7: Correlation between isotopic oxygen anomaly in a stalagmite in Oman supposedly reflecting summer monsoon variability and carbon anomaly from tree rings standing for solar variability, according to Neff et al. (2001).

indication of the microphysical link between the solar cycle and cloud formation, and extended them to the global scale.

II.1.2 Evidence in the upper part of the atmosphere

Labitzke (2003) investigated the link between the stratospheric temperature and the solar cycle, and found that the overall correlation is damped due to the interference with the quasi-biennial oscillation. In the easterly phase the positive correlation is pronounced especially in the subtropical midlatitudes where values above 0.5 are reached throughout, as it is depicted in Figure II.8. The corresponding solar cycle temperature variation reaches 5°C. On the other hand the correlation is low in the westerly phase, for which positive correlations above 0.5 are

20
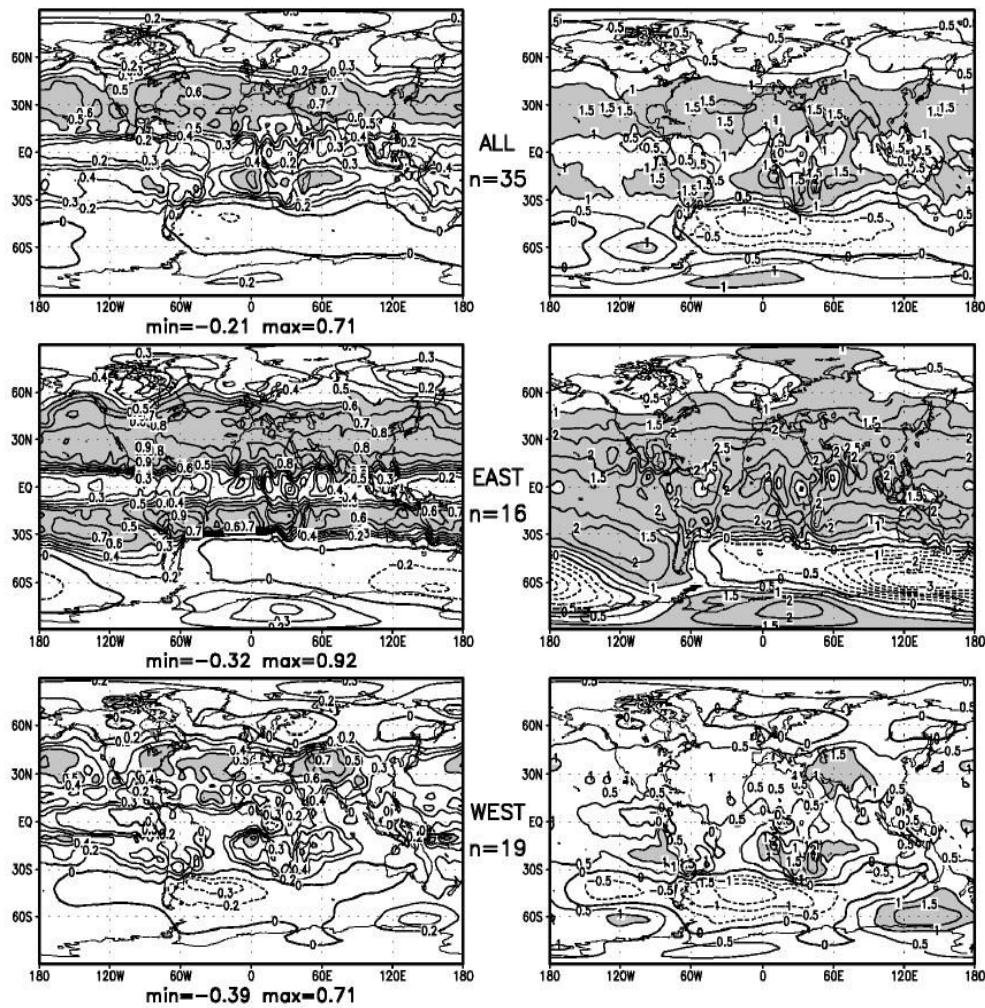
Figure II.8: On the left hand side correlation between the stratospheric temperature, according to the respective phase of the quasi-biennial oscillation (middle and bottom), and the solar cycle. On the right hand side the stratospheric temperature response is shown in degrees Celsius. From Labitzke (2003).

sparse and even negative correlations are attained. In the stratosphere the solar signal appears to be enhanced by ozone absorption of the solar modulated ultraviolet radiation. Solar variability in the UVB and UVC spectrum extends to about 20% of the total variability of the solar constant although that part of the spectrum only stands for approximately 1% of the total energy flux. Since UVC and UVB radiation absorption is considerable in the stratosphere, its modulation may have considerable influence on the thermal properties of that part of the atmosphere. When compared with the troposphere, it thus becomes conceivable that the solar incidence is more readily apparent in the stratosphere.

Hervig and Siskind (2006) produced evidence for the solar signal in mesospheric temperature,

cloud cover and water vapour content. Interestingly the presumed link between the solar cycle and these variables involves once again ultraviolet radiation, which interacts photochemically with water molecules to split these. The photolytic reaction is exothermic, thus inducing a pronounced positive correlation between the solar cycle and mesospheric temperature, as depicted in Figure II.9. Consistently the correlation between water vapour content as well as the cloud amount, and the ultraviolet radiation is negative. The dynamical feature of this process in relationship to the amount of water in the mesospheric reservoir is demonstrated by the time lag between the solar cycle evolution and the maximum absolute correlation index of approximatively one year.
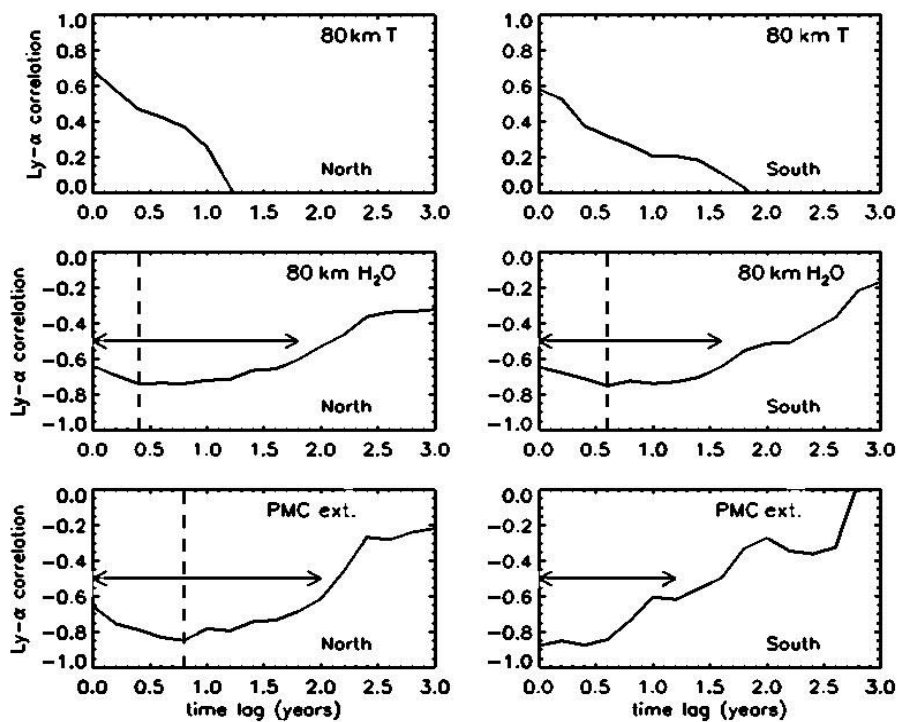
Figure II.9, from top to bottom: Correlation between the solar cycle and mesospheric temperature, moisture content and mean cloudiness, respectively, in the northern (left) and in the southern (right) hemisphere. It is interesting to note that the anticorrelation between solar flux and moisture and cloudiness tends to increase with the correlation time lag, thus showing the dynamical dimension of the process. According to Hervig and Siskind (2006).

II.2 Two hypothesises of indirect solar cycle modulation of the troposphere

II.2.1 Introduction

Within the previous section the presence of a solar signal was shown to be present in the global climate records on the centennial time scale. The results of Schlesinger and Ramankutty (1992) suggest that climate sensitivity to solar radiation is approximately twice as pronounced as the one to greenhouse gases, potentially reflecting the presence of an unknown amplifying process, be it a feedback process or an unknown climate factor. Ultraviolet radiation is a reasonable candidate since its solar modulation is more pronounced when compared to the solar constant and its highly energetic UVC and UVB fraction is almost completely absorbed within the upper part of the atmosphere. Consistently the solar signal is much more apparent in these parts of the atmosphere than in the troposphere, in which it appears to be exclusively detectable with confidence using sensitive statistical methods. For this reason one could argue that the amplified solar signal in the troposphere is a repercussion of the upper atmosphere ultraviolet modulation that is transmitted to the lower part of atmosphere through atmospheric circulation (e.g. Haigh, 1996, Labitzke, 2003).

Nevertheless, based on an indication of empirical evidence for a correlation of the solar cycle and global cloudiness (Svensmark and Friis-Christensen, 1997), conjectures about a direct tropospheric influence have flourished recently. The explanatory theories on the presumed linkage may be divided into two categories involving essentially either small scale processes or both small and large scale processes:

1) The solar cycle not only modulates total solar radiation but also the cosmic rays flux onto the upper atmosphere, mainly the low energy part of their spectrum (e.g. Reiter, 1992). The cosmic rays generate secondary particles upon interaction with the atmospheric gas molecules, most notably elementary atmospheric ions. Atmospheric ionisation through cosmic rays attains a maximum in the lower part of the stratosphere and ulteriorly declines down to the earth's surface (see Figure II.11 and below). Cosmic ray modulation of the atmospheric ionisation may therefore alter the atmosphere's global electric circuit, which in turn may influence the formation of ice particles. Actually, clouds, through the natural ion removal

efficiency discontinuity they constitute, induce a macroscopic atmospheric charge gradient leading to enhanced electroscavenging at their border of small charged particles serving as ice nuclei. Tinsley (2000) stated that the role of ice nuclei as condensation enhancers should alter the thermodynamic evolution of the air to influence storm formation and thus troposphere circulation dynamics. This theory comprising both microscopic and macroscopic elements was qualified by Carslaw et al. (2002) to be the ion-aerosol near cloud mechanism.

2) A second pathway of direct solar modulation of the troposphere involving the ionising potential of cosmic rays was introduced by Marsh and Svensmark (2000). Their theory implies mainly microscale aerosol processes, affects cloud radiative properties and dynamics without involving atmospheric circulation in the first place. Consequently, it was designated by Carslaw et al. (2002) as the ion-aerosol clean air mechanism. An alternative microscale theory, without interference of cosmic rays, but based on the influence of ultraviolet radiation on the diffusion of marine dimethylsulphide to the troposphere was formulated by Larsen (2005).

Consistently with the empirical evidence, the repercussions of the clean air mechanisms should be most pronounced in the low midlatitude marine troposphere (Marsh and Svensmark, 2000), where warm stratocumuli are prominent. It is their similarity through their confinement to the same geographical region and atmospheric level for which controversial empirical evidence has been presented, which predisposes them to become the subject of the present theoretical study on potential direct tropospheric mechanisms of solar cycle climate interaction. The near cloud mechanism theory involves ice nuclei and should therefore concern other climatic regions, for which no specific empirical evidence has been produced so far. It will therefore not be treated here.

II.2.2 The galactic cosmic rays cloud climate hypothesis

2.2.1 Mechanism

The galactic cosmic rays global climate theory described here was introduced by Marsh and Svensmark (2000). Carslaw et al. (2002) provide a concise description of the clean air mechanism that involves the formation of secondary aerosol particles via ion nucleation. These grow to cloud condensation nuclei size, which upon their activation are susceptible to

affect the cloud dynamical and radiative properties, and thus potentially determine the global mean cloud fraction along with the mean cloud survival lapse.

Cosmic Rays ionization rate modulation and new secondary particle formation

The galactic cosmic ray flux is modulated by the solar cycle along with the solar magnetic shield. Cosmic rays, essentially composed of 99% high energy protons and of 1% alpha particles, interact with the atmospheric particles to produce ions as well as a secondary particle flux, mainly electrons and neutrons (concerning the cosmogenic origin of galactic rays we refer to Diehl et al., 2001). It is the latter ones that are measured at the earth's surface and used as a proxy to assess cosmic ray flux variability. Secondary particles constitute the main
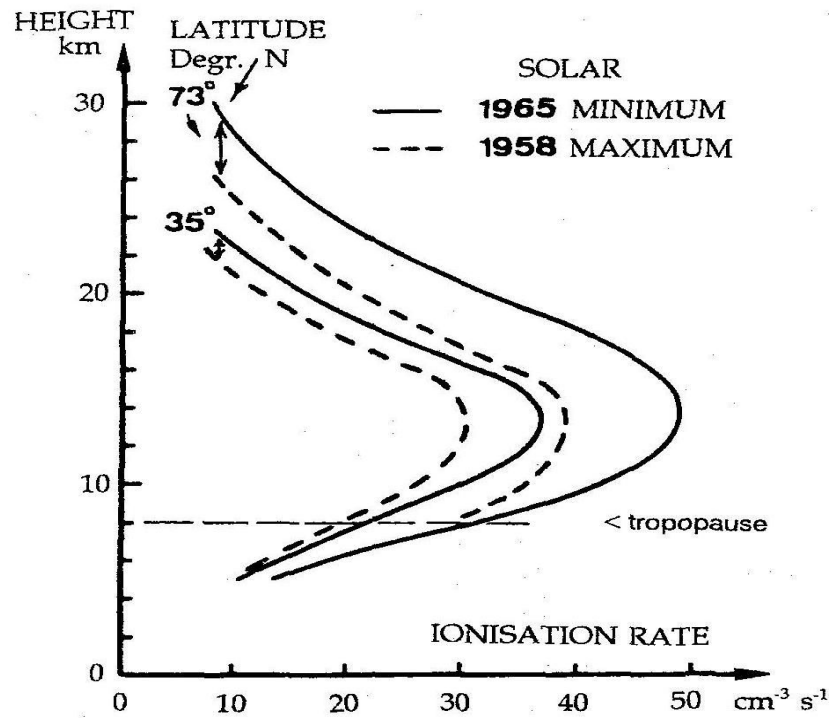
Figure II.10: Solar cycle variability of the ionisation rate as a function of height at two latitudes. The variability is maximal in the stratosphere and rapidly decreases in the troposphere. From Reiter (1992).

factor of ionisation in the lower marine troposphere (where unstable nuclides, mainly radon released at the solid earth's surface, should be negligible). The lower energy part of the cosmic ray spectrum does not penetrate the atmosphere deeply and its ionizing capacity is limited. On the other hand it is more sensitive to solar modulation and should therefore be indirectly

responsible for a solar signal in the ionisation rate of the lower atmosphere (Tanaka, 2005). As already pointed out the ionisation rate is maximum in the lower stratosphere and then continually decreases until the earth's surface (Figure II.10). Due to the earth's magnetic field the ionisation rate also varies with latitude and continually decreases from the magnetic pole to the magnetic equator (Reiter, 1992). The galactic cosmic ray flux is not a constant, even on a day to day basis. It presents abrupt intensity variations, the so-called Forbush decreases associated with solar flares and associated increases of the solar magnetic shield. Forbush decreases are of comparable intensity to solar cycle modulation of the cosmic rays flux.

Elementary ions may combine with uncharged molecules in the atmosphere to form charged particle clusters. Relevant ion clusters in the troposphere mainly consist of water and sulphuric acid mixtures containing a positive or a negative ion. The positive ion is mostly a proton whilst the relevant negative ion is under most circumstances a hydrogenosulphate molecule (Arnold, 2006). Cluster ions show a relatively high survival lapse as their thermal disintegration probability is relatively low while they show an enhanced growth rate through charge attractive forces. In addition they reach more readily a stable size beyond which the disintegration probability is negligible. The theoretical basis to their higher thermodynamic stability was laid by Thomson (1906) who established the Gibbs free formation energy of the charged particle, which is relatively low when compared to a neutral particle, especially for small particles (see next chapter for details). Thus, an enhanced ionisation rate that is correlated with the solar cycle should entail a higher stable ion cluster formation rate, and potentially lead to an increased number of ultrafine secondary particles.

Ultrafine particle growth to cloud condensation nuclei

Ultrafine particles grow through the processes of condensation and coagulation until they eventually reach cloud condensation nuclei size (see Figure II.11). In analogy to cluster ions, ultrafine secondary particles are composed of one or several hygroscopic species, inorganic components such as sulphuric acid and possibly low volatile organics (Kulmala et al., 2007), and water as a solvent. They may bear a certain number of charges, whose the maximum number of charges is dependent on particle size. If the charge number exceeds a certain critical number the particle will disrupt (Pruppacher and Klett, 1997), however the probability of reaching this number is very low because of the repulsion forces engaged. The hygroscopic,

highly solvable substance readily adheres to the particles, that is it condenses, while its evaporation probability is negligible. Water molecules also condensate to a certain limit to the particles bounded by the hygroscopic substance. The driving force of condensation is Brownian motion. Coagulation means the encounter and recombination of two particles. The
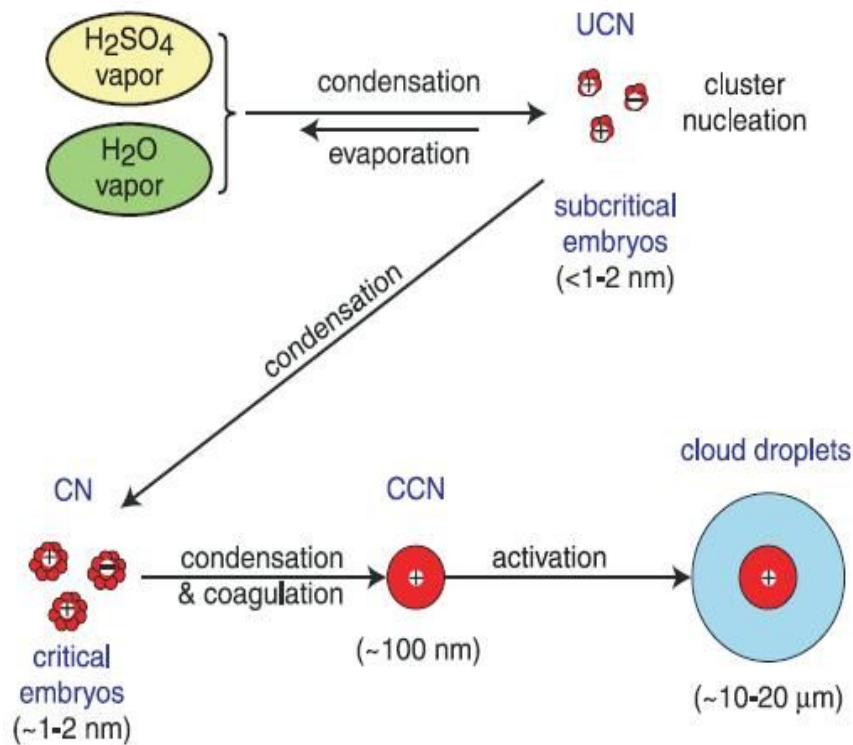
Figure II.11: Ion mediated formation theory of secondary aerosols from gas molecules to cloud droplets, with the respective typical particle size. Adapted from Carslaw et al. (2002).

driving forces of particle encounter are Brownian motion as well as turbulent processes for the larger particles (>1 micrometre). Recombination depends on the encounter trajectory determined by fluid and particle properties as well as surface tension resistance. Particle charge may enhance or impede particle encounter. Coagulation in opposition to condensation is a particle number reducing process and does not require the presence of condensable hygroscopic vapours. Thus an increased secondary particle formation rate should result in an increased number of cloud condensation nuclei concentration, within the limits of negative feedback phenomena. Marsh and Svensmark (2000) assume a simple dependence of the number of cloud condensation nuclei on the secondary particle formation rate.

Cloud condensation nuclei activation

The critical activation size of cloud condensation nuclei depends on the ambient thermodynamic properties of the carrying air, its vertical velocity and mixing properties, as well as the number concentration and size distribution of the aerosol. These variables determine the supersaturation of the gas phase relative to the individual particle in conjunction with its momentary composition. Particles that have reached a specific critical size show a decrease of the saturation pressure with size and thus become activated. The designation of cloud condensation nuclei therefore refers to particles that become activated under given momentary and local ambient conditions, and not to particles exceeding a certain size. Normally, the critical radius of marine aerosol activation is between 0.03 and 0.15 micrometres (note that secondary aerosol size is a function of humidity though, also for unsaturated air). Particles exceeding this size may be designated as potential cloud condensation nuclei. Assuming simple growth dynamics, a higher secondary particle formation rate should lead to a higher quantity of particles that attain this potential size. However, a higher particle number density implies a higher overall condensation rate of water vapour onto these particles, which means a lower supersaturation and a larger critical radius, and eventually a lower number of activated particles. Marsh and Svensmark (2000) assume the system dynamics to be linear and neglect the latter aerosol population negative feedback mechanism. Their assumption also disregards further potential feedback effects linked to cloud microphysical and dynamical properties.

Cloud dynamical and radiative properties

As a first approximation the totally condensed water mass should be indifferent to the cloud droplet number. Condensation is a rapid process when compared to the typical cloud dynamical time-scale so that there should be only negligible interference of the cloud liquid water content and aerosol size distribution and number regarding this process. Condensation alone does not lead to the formation of raindrops, cloud droplet coagulation, that is coalescence, is the triggering process of precipitation formation. When cloud droplets are relatively large upon condensation, accretion is susceptible to take less time, so that the life
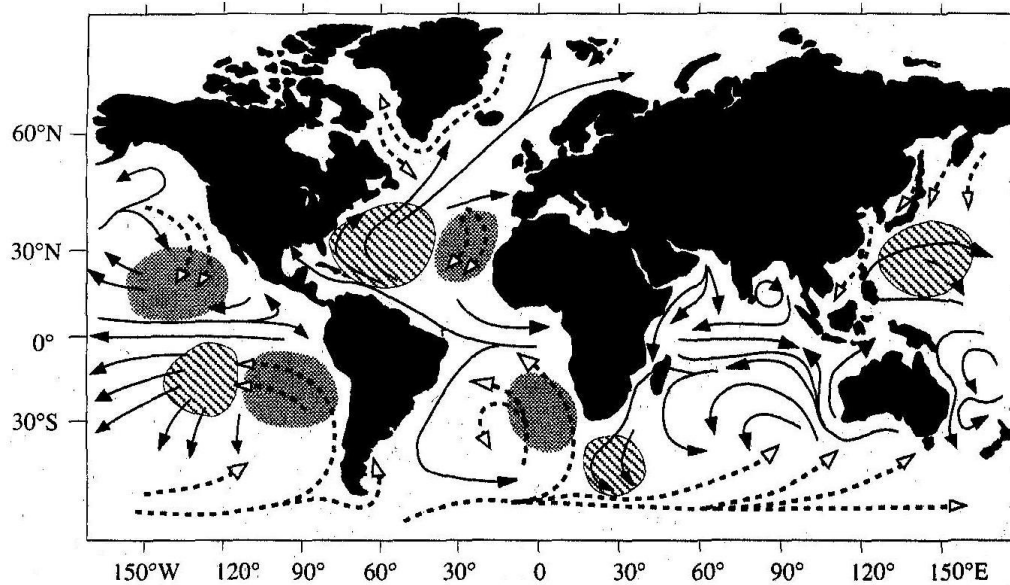
Figure II.12: Areas of prominent oceanic stratocumulus formation, dotted arrows indicating cold water streamlines while full line arrows stand form warm ocean currents. According to Houze (1993).

expectancy of a cloud containing fewer cloud droplets for an equal amount of liquid water should be reduced. Marsh and Svensmark (2000) follow this first hand reflection when they suggest a positive correlation between the condensation nuclei number, the mean cloud lifetime, and the mean cloud fraction. As to their empirical findings (see below) warm midlatitude marine clouds, especially stratocumuli, should be the most sensitive to solar cycle forcing. Marine stratocumuli are prominent in wide areas of the oceans (see Figure II.12). A distinction is made between stratocumuli that form over warm ocean currents and those that form over cold water, mainly in the vicinity of upwelling areas. Warm water stratocumuli formation is attributed to surface released latent and sensible heat that induces boundary layer convection, while cold water stratocumuli formation is driven by longwave radiation cooling at cloud top and consequent downwelling of relative cold air. Both cloud types are capped with a strong inversion. Warm current stratocumuli are preferably of the open cell type, that is subsidence occurs at convection cell centre, while cold current stratocumuli are mostly of the closed type with air ascending at the centre of the cell (Houze, 1993). Closed cell types show a more stratiform morphology, which is consistent with their radiative cooling origin.

A higher fraction of subtropical marine stratocumuli should tend to have an overall cooling effect as the shortwave reflection losses would prevail over the longwave retention effect. Besides this macroscopic effect, the increased droplet number would enhance microphysically

29

the cloud albedo. This is the so-called second Twomey effect of aerosol indirect climate forcing that acts in concert to the first one of cloud fraction variation (Twomey, 1991). The suppression of rain formation through high droplet numbers, and thus the decrease of evaporation cooling of the underlying air mass, should support ongoing convection and through its cloud stabilizing effect further extend cloud life expectancy as a positive feedback effect (Albrecht, 1989). A modification of the local radiation energy balance is susceptible to interact with the activation process and to modify the amount of condensable water, influencing in turn the cloud droplet number and spectrum, precipitation formation, and thus cloud dynamics and mean cloud lifetime. Thus aerosol and cloud droplet dynamics, radiative properties and boundary layer convection form a very complex feedback system whose behaviour is difficult to predict. Marsh and Svensmark (2000) assert that a higher cloud droplet number will cause an increased mean cloud fraction that leads to increased radiative cooling of the atmosphere. They extend their theory to global climate assuming that altered marine stratocumulus cloud properties in relationship with solar cosmic rays modulation should affect in consequence global temperatures leading to a global mean temperature signal in climate records caused by solar forcing.

2.2.2 Evidence

Cosmic rays and the atmospheric ionisation rate

The cosmic ray flux is modulated by the sun´s and the earth´s magnetic field, which is in turn conditioned by the solar wind. As Feynman and Ruzmaikin (1999) point out, the correlation between the solar cycle and the sunspot number, although providing an indication, is low. Sunspots are commonly used as a proxy of historic solar activity and should therefore be used with caution. The direct cosmic ray flux decreases during its transit through the atmosphere, so that it is comparably low in the lower part of the troposphere (see above). Discarding the variability of the earth's magnetic field, the model study of Tanaka (2005) found only negligible solar cycle modulation of the ionisation rate close to the earth's surface. While its ionisation capacity is low, the strongly modulated low-energy part of the cosmic ray spectrum is lost almost entirely in the upper part of the atmosphere. A model study of Shea and Smart (2004) underlines the potential role of the earth magnetic field in amplifying the solar signal

via the rapid drift of the non-dipole components of the field on the centennial time scale. They state that this process should have doubled the solar magnetic field modulation, intensifying the top atmosphere energy flux variation from 20% to 35% during the last 400 years.

In a model study Usoskin et al. (2004) assessed the temporal and regional variation of the ion
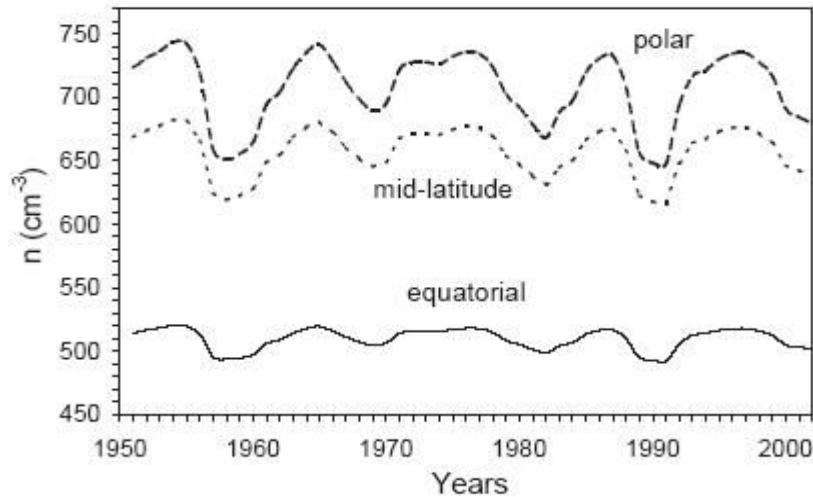
Figure II.13: Assessed variability of the low troposphere (3 km, 711 hPa) ionisation according to model calculations of Usoskin et al. (2004).

concentration in the lower troposphere (Figure II.13). Thus, the typical variability within a typical solar cycle should be approximately 15, 7.5 and 5 % for the polar, mid-latitude and the equatorial latitudes, respectively. Interestingly, if ion recombination is assumed to be the exclusive loss process, and the typical ionisation rate shown in Figure II.14 is compared with the typical ion concentration of Figure II.13, then the ion recombination coefficient has to be one order of magnitude larger than its estimated value based on laboratory measures (e.g. Nolan, 1943, or Smith and Adams, 1982). As a matter of fact Usoskin et al. (2004) have adapted the recombination coefficient to match atmospheric measurements of the ion concentration measures in order to take into account the additional losses through attachment onto aerosols.

The cosmic rays flux is often assessed via secondary neutrons used as a proxy. Their measurement is made by surface based counters and consequently shows the response of the entire, and in particular of the high atmosphere to solar cosmic ray flux modulation. Nevertheless these measures happen to serve as a demonstration of the solar modulation of the cosmic ray flux in the troposphere (e.g. Marsh and Svensmark, 2000). The ionisation rate may

also be directly measured with ionisation chambers, and it is these direct measures that serve as a calibration for the evaluation of neutron counter measures. Consistently, McCracken et al. (2004) show that neutron counter measures taken at Mt. Washington (New Hampshire) correlate well with ion chamber measures at an atmospheric pressure of 50 g/cm^2 in Thule (Greenland). Direct surface measures of the ionisation rate are often corrupted by natural and artificial radioactive contamination of the ionisation chambers, which may cover the solar cycle variability of the near surface ionisation rate. Thus, both indirect and direct measuring methods of low troposphere solar modulation of the ionisation rate may be unsuitable.
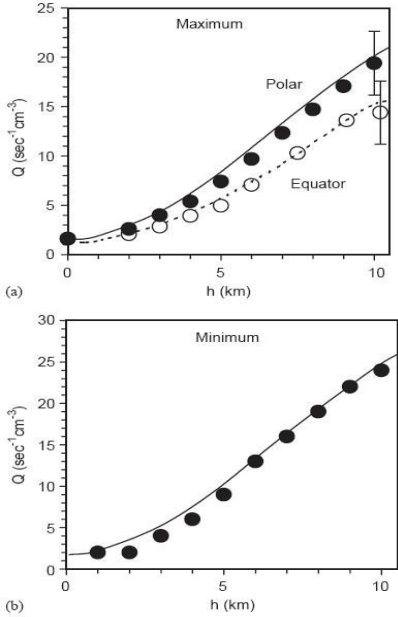
Figure II.14: Measured (dots) ionisation rate as a function of height for solar maximum (top) and minimum (bottom), compared to model calculations (lines). Adapted from Usoskin et al. (2003).

Under continental boreal conditions Tammet et al. (2006) found remarkably stable and realistic low troposphere values of the ionisation rate using inverse calculation, meaning that the ionisation rate is assessed through the solution of the ion number balance equation using observed values of ion and aerosol particle concentrations. The observations of Tammet et al. (2006) do not cover a long enough time interval to infer its near surface temporal variability, even on a daily basis. It should just be noted that this approach might be suitable for future investigations on the solar modulation of the tropospheric ionisation rate.

Atmospheric ions, cluster ions and ion nucleation

Ion nucleation is related to stable cluster ions that form from primary (=elementary) ions. These are mainly the cations N_2^+, O_2^+, N^+, O^+ and the anion O_2^-, which follows free electron attachment to gaseous oxygen (Arnold, 2006). The elementary ions then rapidly grow through molecular attachment to cluster size. Their chemical composition is mainly $HSO_4^-(H_2SO_4)_n$ $(H_2O)_m$, and $H^+A_n(H_2O)_m$, respectively, where A stands for a species of high proton affinity different from water such as CH_3CN or $(CH_3)_2CO$. Nagato et al. (2005) have done ion mobility and mass spectral analyses of the negative ion species present under laboratory
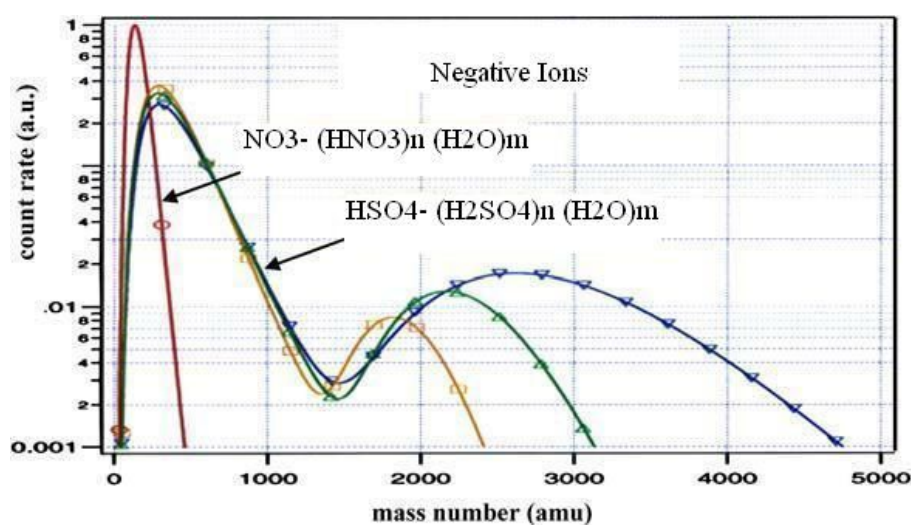
Figure II.15: Two distinct mass modes of stable negative atmospheric ions and their dependence on atmospheric composition conditions. For the lowest sulphuric acid concentration ions do not evolve to greater size and consist of nitrate clusters containing nitric acid. Increasing sulphuric acid produces larger sulphate clusters. Adapted from Arnold (2006).

conditions upon radiative ionisation. They identified peaks of sulphate, hydrogenosulphate as well as small cluster ions, especially $HSO_4^-H_2SO_4$. Interestingly, the spectral distribution evolved from molecular to cluster ions upon increasing the ambient water vapour and sulphur dioxide concentrations. This is reminiscent of nucleation theory that predicts that the process efficiency should be a strong function of the number concentration of the source species (e.g. Yu, 2003). The laboratory investigations presented by Arnold (2006) support the findings of Nagato et al. (2005) and provide even more conclusive information depicted in Figure II.15. Thus, cluster ions appear to show a clear bimodal mass spectral distribution. Such a

distribution is characteristic for a dynamical growth process involving two preferred (as stable) composition ranges separated by an unstable range. Classical ion-induced nucleation theory predicts that particle charge substantially lowers the separating energy barrier, in that elementary ions and nucleated ultrafine particles are separated by stable cluster ions. Arnold (2006) also found a charge sign specificity of the size and composition of cluster ions. Positively charged clusters contain less sulphuric acid as its proton affinity is low compared to the one of methylcyanide and acetone, whilst their water content is not affected. The proton affinity of water is comparable to the one of sulphuric acid, but water is much more prominent in the atmosphere and it thus has a dynamical advantage. Critical cluster ions show comparable sulphuric acid content, so that it might be concluded that the growth mechanism of positively and negatively charged stable clusters to critical size is analogous. However, Arnold (2006) points out that the positive ultrafine particle mode is less pronounced than the corresponding negative mode. He assumes that the tendency of the proton attracting species to detach is higher but does not conclude expressively that the potential of positively charged clusters to induce secondary particles is less important.

Major model studies on ion nucleation are those of Yu and Turco (2001) with a recent update (Yu, 2006b), Laakso et al. (2002) and Lovejoy et al. (2004). Laakso et al. (2002) adopt a purely thermodynamic approach combining classical nucleation theory with the Thomson Equation of the Gibbs free formation energy of charged particles that are assumed to have bulk properties. Yu and Turco (2001), and Lovejoy et al. (2004) adopt a purely mechanical approach with respect to particle growth through particle particle encounters and condensation. Yu and Turco (2001) estimate the evaporation of clusters with macroscopic thermodynamic data, while Lovejoy et al. (2004) evaluate the molecule detaching probability according to new laboratory data. Yu and Turco (2001) qualify the process they assess as *ion-mediated nucleation* in opposition to the classical ion nucleation theory. Doing this they want to stress that ions intervene in the new particle formation process but may not be continuously present as growing particles might undergo neutral stages. It is inherent to the approach of Laakso et al. (2002) that particles bear a charge when they become critical while the unstable size range is not considered explicitly. Classical particle formation may thus be qualified to be *ion-induced*. The classical theory implies that the unstable particle population adapts instantaneously to changing conditions and therefore always is in momentary equilibrium (see Yu, 2003). Interestingly, Laakso et al. (2002) and Yu and Turco (2001) (see also Yu, 2003,

Yu, 2006b) obtain comparable results for the (equivalent) nucleation rate that may lie within one order of magnitude. According to these studies ion enhanced particle formation should be relevant under lower troposphere equivalent temperature and moisture conditions (Yu, 2002). Lovejoy et al. (2004) find considerably lower equivalent nucleation rates under low troposphere conditions (see also Modgil et al., 2005). It is only the considerably lower
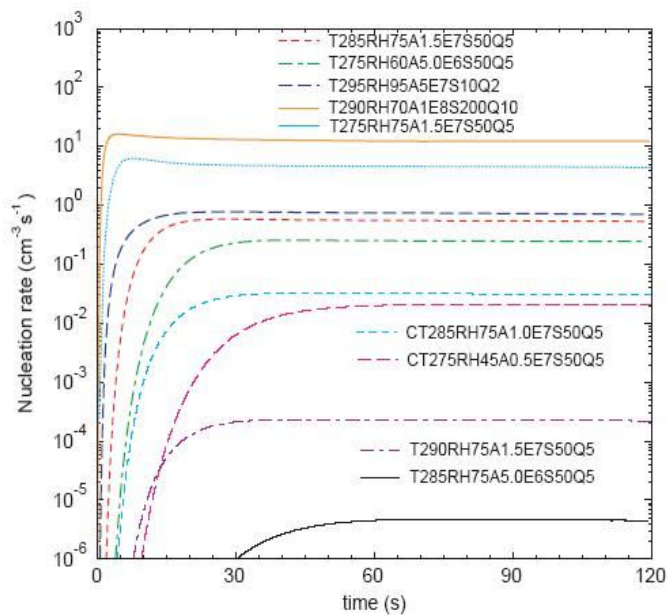
Figure II.16: Stable state ion mediated nucleation rate according to Yu (2006b) along with approximate time intervals to reach this state. The legend comment gives temperature in Kelvin, relative humidity in percent, ambient sulphuric acid concentration in particles per cm³, background aerosol surface area (μm²/cm³) and ionisation rate 10^6 s⁻¹. Adapted from Yu (2006b)
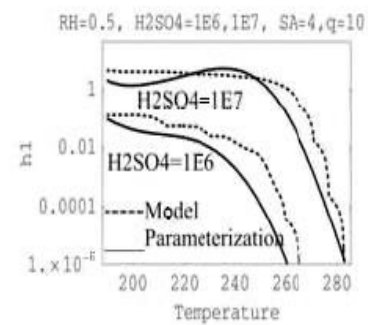
Figure II.17: Temperature dependence (see text) of the nucleation rate according to the model of Lovejoy et al. (2004). From Modgil et al. (2005)

temperature of the upper troposphere that allows ion-mediated nucleation to be effective (Kazyl et al., 2006, undertake a study on the spatial distribution of ion-mediated nucleation according to Lovejoy et al., 2004). Although not named expressively by Lovejoy et al. (2004; in opposition Yu, 2006b, does so) it is the relatively high disintegration probability inferred from laboratory measurements that acts as a limiting factor to new particle formation. Consequently, although assuming most favourable, upper limit conditions, Kazyl et al. (2006) find that cosmic ray induced secondary particle formation does not relevantly enhance the solar cycle forcing of the shortwave radiation balance. Yu (2006) questions the accuracy and pertinence of the laboratory detachment dataset of Lovejoy et al. (2004). Figures II.16 and

II.17 compare typical nucleation rate results of Yu (2006) with those of Lovejoy et al. (2004), respectively.
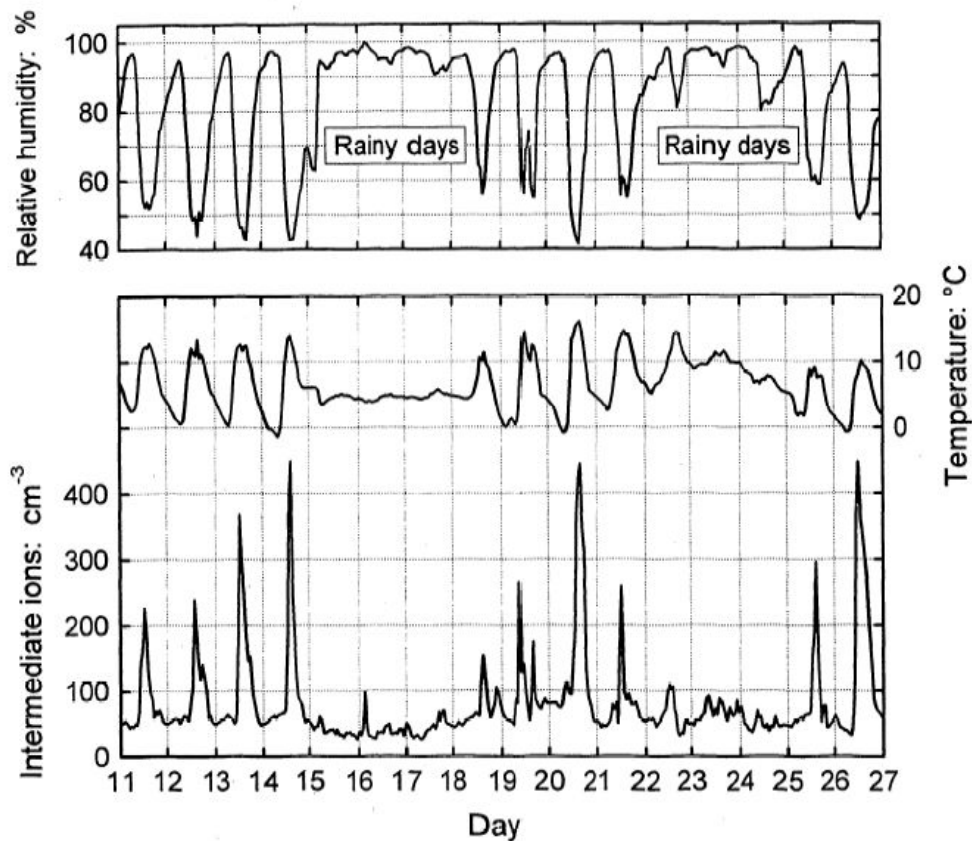
Figure II.18: Intermediate ion (ca. 2-15 nm diameter) concentration under boreal climate conditions (Estonia) as inferred from ion mobility measurements. Also shown are the temperature and humidity conditions. Adapted from Hõrrak et al. (1998).

Eichkorn et al. (2002) found evidence for the presence of supracritical ions in the upper troposphere, which may testify for occasional occurrence of ion-induced nucleation in that part of the atmosphere. Lee et al. (2003) studied aerosol particle distributions in the upper troposphere and lower stratosphere, which they compared to model distributions using the growth model of Lovejoy et al. (2004). They concluded that particle distribution evolution may be well explained by these simulations and that ion-induced nucleation may be the dominating process of particle formation in that part of the atmosphere owing to its relatively low characteristic temperature and background particle concentration. An indication of ion-induced nucleation events in the lower troposphere at a boreal site is reported by Hõrrak et al. (1998). They measured the atmospheric ion concentration as a function of their mobility and

hence inferred their mass and size. As to these observations the quantity of ions of approximately 2-15 nanometre size dramatically increased on certain days around noon and then went back to its original background value while no increase occurred on rainy days (see Figure II.18). Concentration peaks may be interpreted to be nucleation events while their absence during rainy days indicates suppression through the presence of a large quantity of larger particles. This observation is in apparent contradiction with results presented by Radke
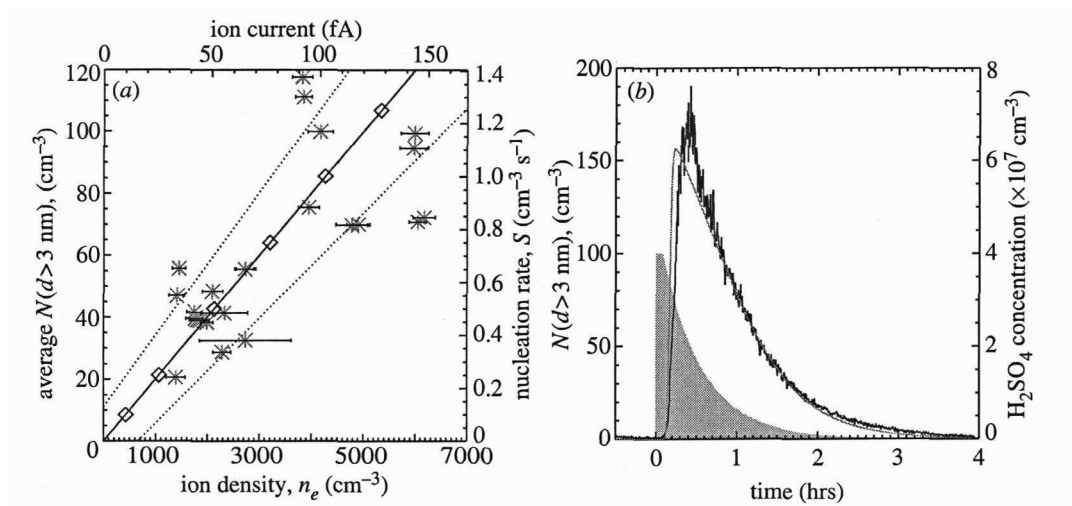
Figure II.19: Four hour average aerosol particle concentration generated through the experiment of Svensmark et al. (2007) as a function of the ion density (left). Also shown is the linear dependence of the nucleation rate derived from model calculations using empirical data as input parameters. Right: temporal evolution of the aerosol number along with assessed sulphuric acid concentration according to an empirical relationship (see text). Adapted from Svensmark (2007).

and Hobbs (1991) who precisely found a by one order of magnitude higher amount of Aitken nuclei around marine cumulus clouds. The occurrence of nucleation bursts during daytime is consistent with nucleation theory since the photolytic process of sulphuric acid synthesis is suppressed at night. The hypothetical bursts also correlated well with ambient humidity variaton. The ion population showed a daily successive increase of small, intermediate (2-15 nm diameter) and large ions (15-23 nm) whilst the number of larger charged particles (23-79 nm) in the Aitken mode decreases. Hõrrak et al. (1998) could not explain the variability of the larger charged Aitken particles while the successive increase of the smaller charged particle number testifies for a dynamical growth process. They argued that nucleation should not induce such a high number of charged particles through ion-attachment unless the process involves ions actively. However it may not be proven that the process actually *is* ion-induced

nucleation.

Svensmark et al. (2007) recently published laboratory evidence that ion-induced nucleation effectively takes place at lower troposphere conditions. Their experiments were conducted with purified air in a reaction chamber to which could be added water vapour, ozone and sulphur dioxide in variable proportions. Sulphuric acid formation was induced photochemically with an ultraviolet radiation source. Beneath natural sources, that is cosmic radiation and radon decay, ionisation could be additionally produced by a gamma radiation source to raise the ion concentration to a higher level, if necessary. The sulphuric acid concentration was estimated using an empirical relationship to the aerosol growth velocity. The nucleation rate was assessed indirectly solving the dynamic growth equation of the aerosols for the nucleation rate as an unknown. Particles above the detection limit of three nanometres in diameter appeared within 10 minutes after the onset of the ultraviolet radiation source. The application of a strong electrical field had little influence on the number of particles reaching detectable size per time increment. This implies that particles are neutralised very quickly, that is within a few seconds, since in the opposite case they would be removed. Also it is a strong indication that particles become critical below the detection size limit unless growth velocity varies several orders of magnitude on the corresponding size range. The assessed nucleation rates (see Figure II.19) were more or less a linear function of the ionisation rate, as predicted by the classical ion-induced nucleation theory. The number of positively and negatively charged particles appeared to be more or less symmetrical. The deduced sulphuric acid concentration was well below the known limit of homogeneous nucleation occurrence but within one order of magnitude of the natural ambient sulphuric acid concentration. The experiments were repeated with synthetic air with no relevant change, thus ensuring that the nucleation process was not due to an impurity in the compressed air. The authors cannot rule out, however, that an impurity could occur along with the introduction of the relevant chemical species. The absence of particle bursts without sulphur dioxide or ozone demonstrates the essential role of these species in the nucleation process.

Thus, the experiments of Svensmark et al. (2007) provide strong direct evidence for the occurrence of ion-induced nucleation under near surface atmospheric conditions with sulphuric acid as condensing source species and independently of the ion charge nature, as well as implicit evidence, as the ambient sulphuric acid concentrations are close to natural values, the indirectly assessed nucleation rate is formally in agreement with the classical

theory of ion-induced nucleation and particles seem to reach stable size well below the detection limit as it is implied by the same theory. However, it is surprising that the experimental bursts were observed at a relatively high temperature of 296 K and a low relative humidity of 35% only. The kinetic model studies of Lovejoy et al. (2004) and Yu and Turco (2001) predict no occurrence of ion-mediated nucleation under these conditions (see Figures II.16 and II.17). Also the classical ion-mediated theory should exclude nucleation under both high temperature and low humidity conditions, since these should considerably enhance the evaporation tendency of subcritical particles. Svensmark et al. (2007) provide no explanation for the unexpectedly high effectiveness of ion nucleation.

Particle growth to cloud condensation nucleus size

The theory of Marsh and Svensmark (2000) of solar modulation of the cloud condensation nuclei number entails that secondary particles are a primary source of these, which means that the sensitivity of the aerosol number to solar activity has to remain relevant from nucleation to cloud condensation nucleus size. This correlation might be lost as the particle number is reduced by coagulation, partly due to particles of different origin, cloud droplet as well as raindrop scavenging.

Quinn et al. (1993) give typical marine aerosol particle size distributions obtained during a field campaign in the north-eastern Pacific off the coast of the state of Washington as well as on a hill at 2 km distance from the Washington coast. The distributions are bimodal in most cases, independently of the air coming from aloft or from the sea (depicted in Figure II.20). The smaller Aitken mode is commonly supposed to be of secondary origin while the larger mode is the so-called accumulation mode, which may be of sea-salt origin (see below). Distributions advected from the ocean show a larger Aitken mode, thus indicating a more important secondary influence relative to examples with air flow from aloft.

It is generally agreed upon that marine when compared to continental aerosols possess a relatively high sensitivity of their number to the atmospheric yield of hygroscopic species such as sulphuric acid (e.g. Hobbs, 1993, Kondratyev, 1999). Fitzgerald (1991) reports in his review on marine aerosols that more than 90% of the Aitken mode particles show a high volatility and should therefore be of secondary, that is non sea salt origin. Measurements by Clarke (1987), however, suggest that wind velocity between 10 and 25 m/s leads to a fraction

of 40% sea salt particles in the Aitken mode size, although the main wind speed variability was observed in the accumulation mode. These observations are confirmed by Clarke et al. (2006) who demonstrate the effectiveness of ocean waves to produce sea salt particles as small as 10 nanometres in diameter. Clarke (1987) as well as Quinn et al. (1993) analysed the particle composition in the accumulation mode and found the particles to contain a major part of sulphate of non sea salt origin. In their survey on marine aerosol chemical composition data
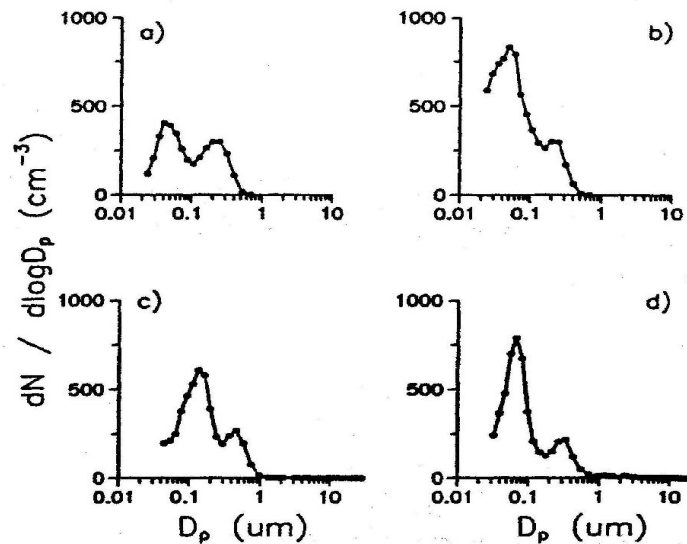
Figure II.20: Typical marine bimodal aerosol size distributions collected during cruises in the north eastern Pacific (a and b) and at a hill site distant 2 km from the shoreline in the state of Washington (USA). For a) and c) the air was coming from the continent and aloft, while c) and d) were taken during westerly wind conditions. For the latter secondary production seemed increased as it is testified by the more pronounced Aitken mode. From Quinn et al. (1993).

obtained during ship cruises in the Pacific over 5 years Quinn et al. (2000) found the non sea salt sulphate aerosol mass content in submicron aerosols approximately twice as high as the total sea salt mass in the subtropical area (see Figure II.21). Other components such as methanesulfonate, outside the polar region, and the residual mass were of secondary importance. The uncertainty related to the measurement technique was also assessed and found to be of the order of a few percent.

This empirical data finds support in model studies, such as the one of Yoon and Brimblecombe (2002), showing that secondary particle formation at the current level of understanding is not able to produce stable realistic levels of potential cloud condensation
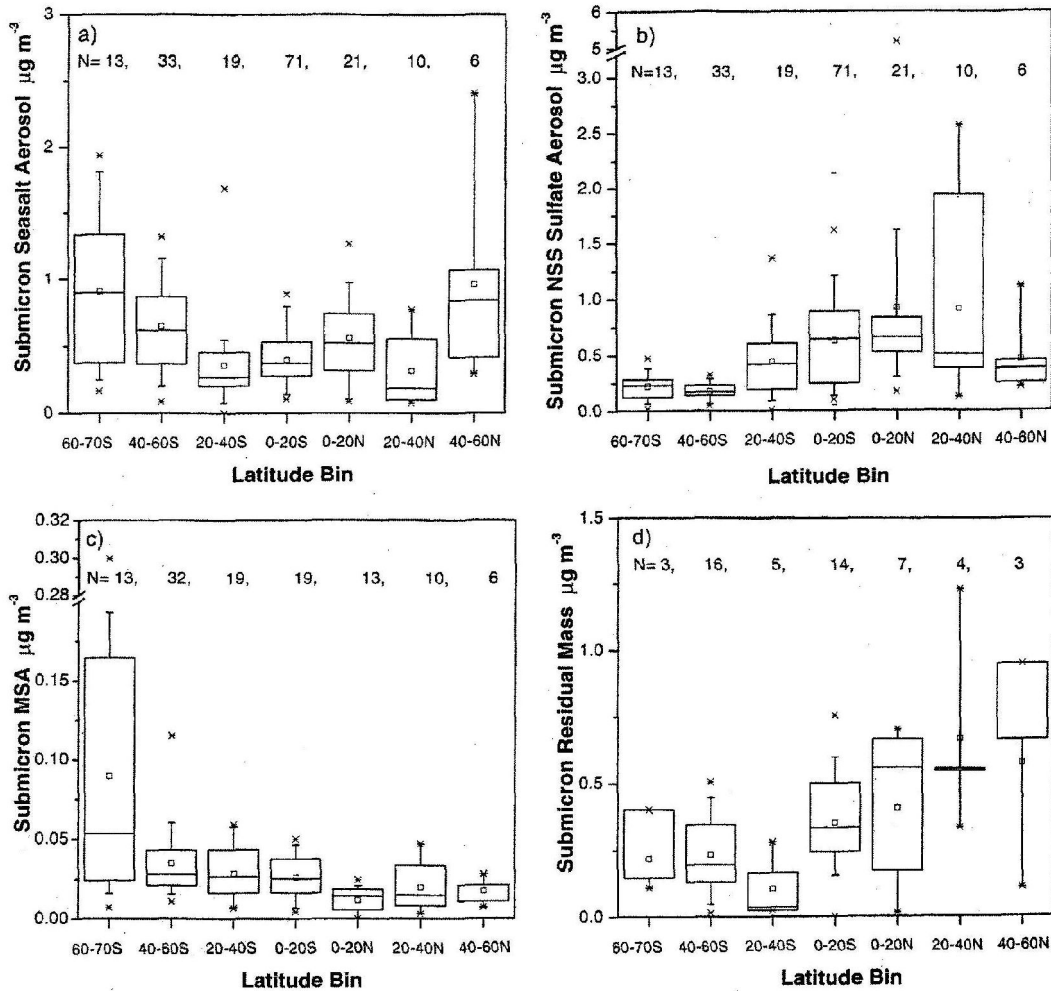
Figure II.21: Empirical marine aerosol mass as a function of geographical latitude from a survey of Quinn et al. (2000). The boxes denote the 25, 50 and 75 percentiles, vertical error bars indicate 5 and 95 percentile values. Extreme values are given by the star symbols. Respective mean values are indicated by open squares. Adapted from Quinn et al. (2000).

nuclei although it is a relevant particle generating process. Depending on the wind velocity, the contribution of sea salt particles should be at least 50% to potential cloud condensation nuclei. Sea salt particles also seem to actively reduce the sensitivity of the cloud nuclei number to secondary particles as they constitute an additional sink of condensable matter and should therefore impede secondary particle growth. According to the work of Yoon and Brimblecombe (2002) entrained particles from the free troposphere should also play a relevant role in marine cloud nuclei formation. As a function of the particle concentration in the free troposphere and based on realistic entrainment velocities the cloud nuclei number in the boundary layer may be halved or doubled due to this process.

Only few process theoretical studies on aerosol growth by coagulation and condensation exist. According to the current state of the art models and state of knowledge, aerosols take up to 2 to 3 days to reach potential activation size as cloud nuclei assuming that the maximum supersaturation leading to activation is limited to about 1% and knowing that the corresponding critical activation radius is 30 nanometres approximately (e.g. Arnold, 2006). Secondary aerosol growth to this size is still largely assumed to be an unsolved question mainly due to the uncertainty linked to the nature of the relevant hygroscopic species and the interference of cloud processing. Aerosols are assumed to undergo several activation/deactivation cycling events and/or become both chemically and mechanically processed as cloud interstitial particles. It has already been pointed out above (Radke and Hobbs, 1991) that clouds may enhance particle nucleation as well as particle growth in their vicinity. Supposed enhancement mechanisms should be increased production rates of hygroscopic species through enhanced photolytic rates of hydroxyl formation as well as facilitated dissolved sulphur dioxide oxidation in the aqueous cloud droplet phase. The influence of clouds on aerosol growth has also been pointed out by Hobbs (1993) and Kondratyev (1999) as one of the main uncertainties related to aerosol growth.

Kerminen et al. (2001) present a model study on the respective influence of the intensity of coagulation and condensation to aerosol growth dynamics. They found that the particle number reducing process of coagulation may decisively reduce the probability of a particle to reach cloud nucleus, or even the detection limit size in the absence of rapid condensational growth. Consequently, the higher the background particle concentration is, the more rapid the condensation process has to be for the particles to survive. Kerminen et al. (2001) concluded that in the absence of one or several supplementary hygroscopic species apart from sulphuric acid the particle growth rate would be insufficient to produce detectable nucleation bursts under most typical atmospheric conditions. Conversely the presence of another condensable species would cause a lot more particle growth events than so far predicted by model studies. In a pure marine situation, however, the action of other species, such as non- or low-volatile organics, should be secondary, as it follows from the analysis of Quinn et al. (2000), so that the growth rate of secondary particles via condensation should dominantly depend on the sulphuric acid formation rate. Also the nucleation mechanisms assumed by Kerminen at al. (2001) were homogeneous binary and ternary nucleation in a H_2SO_4/H_2O (Yu, 2006a) and a $NH_3/H_2SO_4/H_2O$ (Yu, 2006) system, respectively. As the effectiveness of these mechanisms

may be lower than the one of ion nucleation, the limiting capacity of coagulation to produce a realistic amount of cloud nuclei might be weaker.
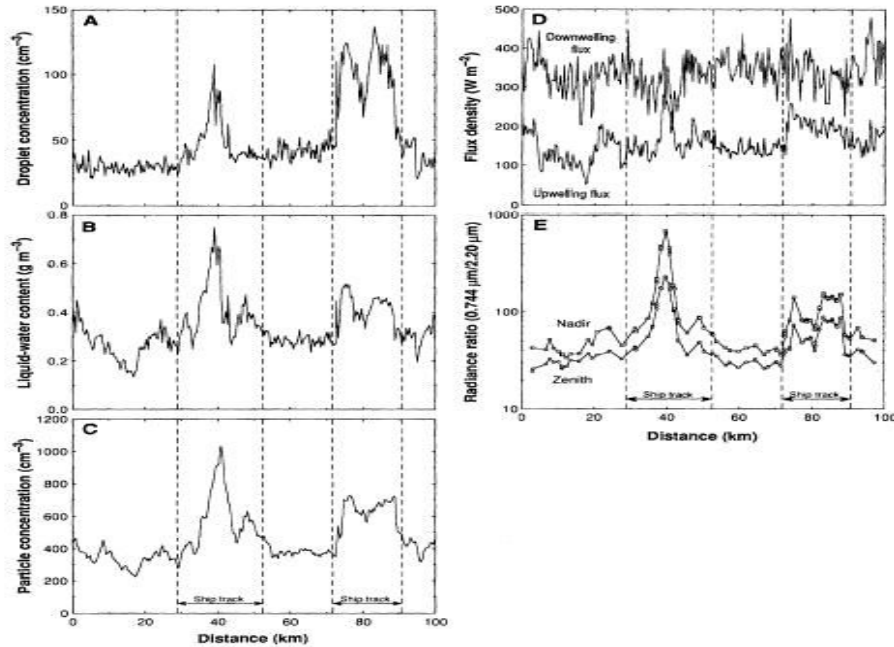
Figure II.22: Modification of cloud properties through ship exhausts. The increased liquid water content indicates precipitation suppression through a higher droplet concentration. Consistent increase of the reflected shortwave flux as indicated on the right hand side. From Radke et al. (1989)

Aerosol cloud processes

The negative feedback of the aerosol number on the cloud droplet number via the maximum ambient water vapour supersaturation is a commonly predicted phenomenon. However, aerosol particle activation itself is a largely unknown and potentially highly complex process involving particle chemical composition and structure. It has been conjectured that ions may have a decisive incidence on particle activation (Kirkby, 2000). This phenomenon may not be understood in the framework of the Thomson equation of the Gibbs free formation energy of a charged particle (Thomson, 1906). The effect predicted by this equation would be insufficient to enhance particle activation in combination with a realistic aerosol particle charge. The role of particle chemical composition and structure has been addressed by Kondratyev (1999) as one of the major unsolved problems regarding aerosol-cloud interaction. He reports in this

43

context that aerosol particles mostly show bimodal behaviour relative to their hygroscopic property resulting in differential activation.

Precipitation suppression in clouds with a higher droplet number (Albrecht, 1989) has been reported in relationship with ship trails in subtropical marine stratocumuli (Radke et al., 1989). Figure II.22 depicts the relationship between aerosol number and precipitation formation under these circumstances. The concentration of aerosols as well as cloud nuclei is substantially augmented in ship tracks due to the particle containing exhausts. The absence of a drizzle mode in the related cloud droplet distribution and the increase in cloud liquid water
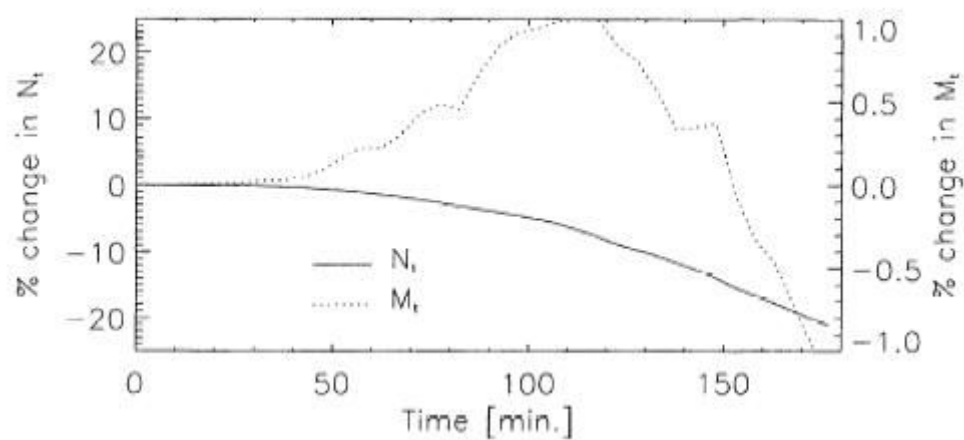
Figure II.23: Decrease of the cloud droplet number through the sole process of coalescence as modelled by Feingold et al. (1996). The control variation of the total droplet mass, inherent to the numerical model, is also shown (dotted line).

content marks the absence of precipitation formation under these conditions. The stability of ship trails as well as their incidence on cloud optical properties is confirmed by satellite imagery. Typically cloud reflectivity increases from around 60 to 68%.

The role of cloud processing has been pointed out in the preceding subsection. Enhanced sulphuric acid within and in the vicinity of clouds following liquid phase oxidation of sulphur dioxide and enhanced photolytic production of hydroxyl radicals may cause the typical bimodal shape of cloud processed aerosols upon deactivation (Hoppel et al., 1986). Higher growth rats would add to the selective activation of aerosol particles as a function of their physico-chemical properties. There is indication that this mechanism is effective in non-precipitating clouds, for which precipitation scavenging is reduced (Hoppel et al., 1994). However there is still controversy on the relative importance of the cloud processing

mechanisms. Koch et al. (2003) analyse statistically data records of cloud cover over Europe and North America as well as air sulphate concentration and find a negative correlation between these. Ulterior tests with a global model indicate that reduced photochemical synthesis well below the clouds and especially precipitation scavenging seem to exceed enhanced liquid phase production in clouds.
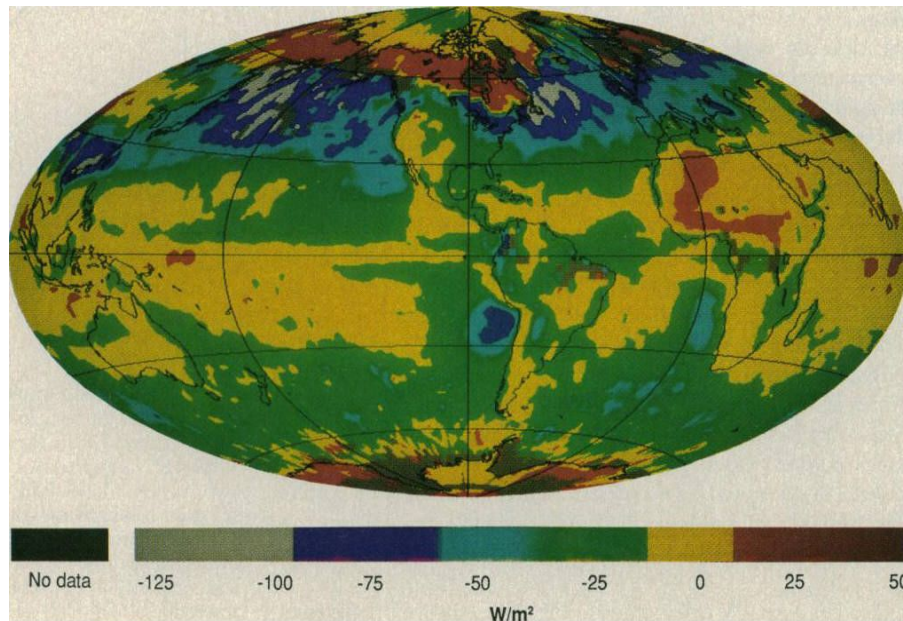
Figure II.24: Net cloud forcing during the month of April 1985 from the Earth Radiation Budget Experiment (adapted from Ramanathan et al., 1989). Comparing with Figure II.12 the strong cooling potential of marine stratocumuli over cold water appears.

Feingold et al. (1996) and Feingold and Kreidenweis (2002) have modelled the incidence of coalescence and wet phase processing on the cloud condensation nuclei spectrum of stratocumuli and the resulting cloud dynamical feedbacks. They found that droplet coalescence has a strong enlarging and number reducing capacity. Droplet number depletion in the absence of liquid phase processing is of the order of 50% within three hours, as it may be inferred from Figure II.23. Feingold et al. (1996) stress the role of turbulent convection and successive cycles of activation and deactivation, as typical in-cloud particle residence time is found to be about 12 minutes per hour only. Considering a total mean residence time of 3.1 hours particle trajectories should cross the cloud boundary to the least 30 times prior to leaving definitively the stratocumulus cloud. The corresponding total time of successive cloud

processing of an aerosol particle would therefore be around 15.5 hours, which is a reasonable value of stratocumulus mean life time according to these authors. The role of wet phase processing is found to be of primary importance when the cloud does not precipitate (Feingold and Kreidenweis, 2002). Coalescence should be of equal importance as soon as this process takes place. This is consistent with the aforementioned observations of Koch et al. (2003) who found aqueous phase processing to be limited by precipitational removal. The work of Feingold and Keidenweis (2002) also indicates a complex feedback of wet phase processing on cloud precipitation properties.

The relationship between the cloud droplet number and the cloud radiative properties has been subject to several simple empirical formulations (Twomey, 1991, Hobbs, 1993). Interestingly
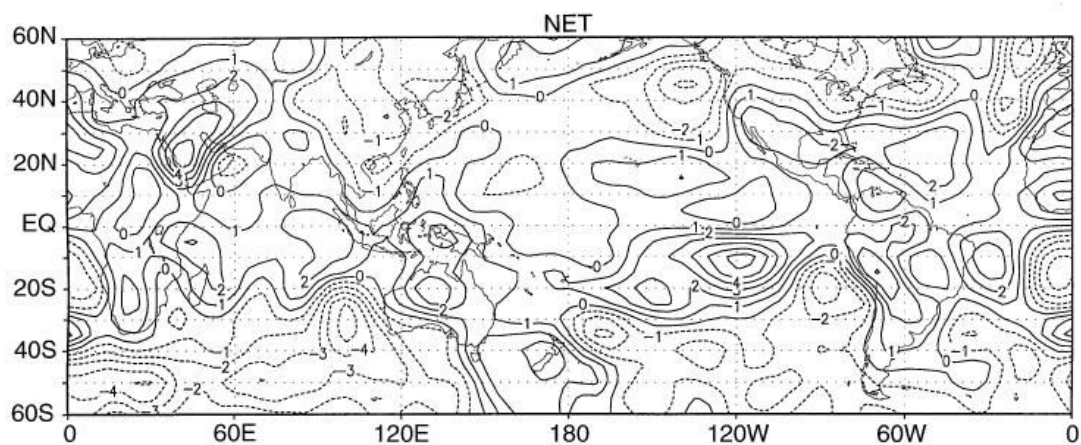
Figure II.25: Net radiation balance sensitivity (W/m²) to a modification of the fractional cloud cover equivalent to 0.1. Comparing with Figure II.12 as well as the preceding shows the particularly strong potential of marine stratocumuli. According to Ringer and Shine (1996).

the sensitivity of cloud optical properties to nuclei number variation is largest when the droplet number is low, that is under marine conditions. The overall effect of clouds on the earth´s surface radiation balance as it is known from the Earth Radiation Budget Experiment (Ramanathan, 1989) shows quite a complex pattern. However, marine regions with prominent stratocumulus clouds clearly have a negative influence on the radiation balance (see Figure II.24). This pattern finds confirmation in a statistical study of Ringer and Shine (1997) on the sensitivity of the earth's radiation balance to fractional cloud cover variation (Figure II.25). Stratocumuli are found to have the highest negative impact on cloud cover variation. Thus, provided that larger particle numbers result in cloud stabilisation through precipitation

suppression as it is suggested by Albrecht (1989) the first Twomey effect should have a negative effect on the radiation balance through increased fractional cloudiness. It is commonly believed that a lower incoming shortwave radiation flux should cause the mean temperature to decrease. Kristjansson and Kristiansen (2000) question this assumption considering that a locally higher longwave radiation flux in relationship with a lower fractional cloudiness, as indicated by measurements, might solely mark the local absence of a cloud that leads to higher local longwave radiation losses, and thus would not necessarily indicate a globally warmer climate. One might also add that in a marine environment short term cloud variability might be effectively damped by the oceanic heat reservoir, meaning that cloud are an ineffective climate factor under these conditions. Clouds have so far not been considered as a time dependent climate factor within studies of theoretical climatology on the millennial time-scale (e.g. Saltzman, 2002), and it is a pertinent question if clouds can take on this role on the decadal or even centennial scale in relationship with a strong dampener such as the oceans.

II.2.3 The ultraviolet radiation cloud climate hypothesis

2.3.1 Mechanism

A more recent theory on the action of the solar cycle on cloud formation emanates from Larsen (2005). It states that the increased number of potential cloud nuclei during low solar activity is not related to the galactic cosmic rays flux but rather to the antiparallel variability of the ultraviolet radiation flux at the earth's surface. Ultraviolet radiation penetrates the ocean water and is thought to have a strong influence on the microorganisms that produce and degrade dimethylsulphide, the marine precursor of sulphuric acid in the atmosphere. A biogenic influence of dimethylsulphide on the atmosphere as implied by Larsen (2005) would be in line with the central theme of biosphere-atmosphere interaction of the Gaia hypothesis (e.g. Charlson et al., 1987).

Although the UVC radiation is almost entirely removed in the upper part of the atmosphere, the less energetic UVB and UVA part of the spectrum is supposed to have a sufficient variability to produce an intense solar signal of plankton growth in the euphotic zone of the ocean. Only a small fraction of dimethylsulphide diffuses into the atmosphere, the major part

is photolysed or removed by bacteria. Photolysis is also positively correlated with the solar cycle and should add further to the supposed mechanism. Bacterial removal is inhibited in the euphotic zone through ultraviolet removal. However, below the euphotic zone, or in the lower part of it, bacterial removal might be enhanced by a positive correlation between the bacterial activity, dissolved organic matter and ultraviolet radiation. Moreover, the euphotic zone might be deeper in case of a high ultraviolet radiation flux following increased transparency as
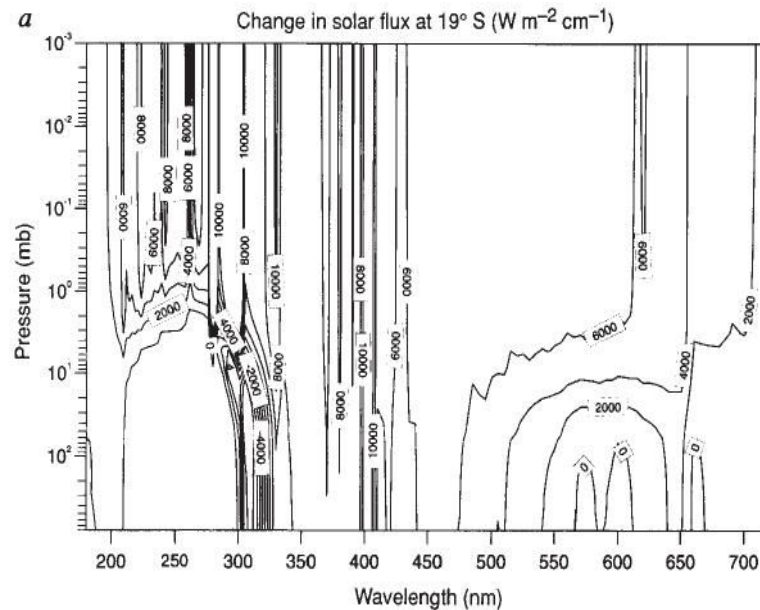
Figure II.26: Spectrally resolved model data on the variability of incoming solar radiation as a function of pressure height. The variability below 300 nm is zero at the earth's surface as it is totally absorbed by stratospheric ozone. The variability is maximal at the surface in the UVA and UVB range. Adapted from Haigh (1994).

photolysis of absorbing material is enhanced, so that eventually the overall bacterial removal may be positively correlated with the solar cycle. The resulting antiparallel correlation between the solar modulation of ultraviolet radiation and the atmospheric sulphuric acid content in relationship with the supposedly primary relevance of secondary particles under marine conditions (see above) should result in lower high solar activity cloud nuclei numbers and thus a reduced mean cloud cover in accordance with the theory of Marsh and Svensmark (2000).

2.3.2 Evidence

The spectrally integrated solar cycle variability of solar radiation is approximately 0.1%, that is 1.36 W/m², while the variability of ultraviolet radiation in the range of 200 to 400 nm, standing for some 8% of the solar constant, is equivalent to 0.41 W/m² or some 30% of its total variability at the top of the atmosphere (Lean, 1997). The 200 to 400 nm range is equivalent to the UVA (320-400 nm), UVB (280-320 nm) and part of the UVC (100-280 nm) radiation ranges. A model study of Haigh (1994) found the solar modulation at the earth's surface to be increasing from the poles to the equator and to be seasonally dependent. In the
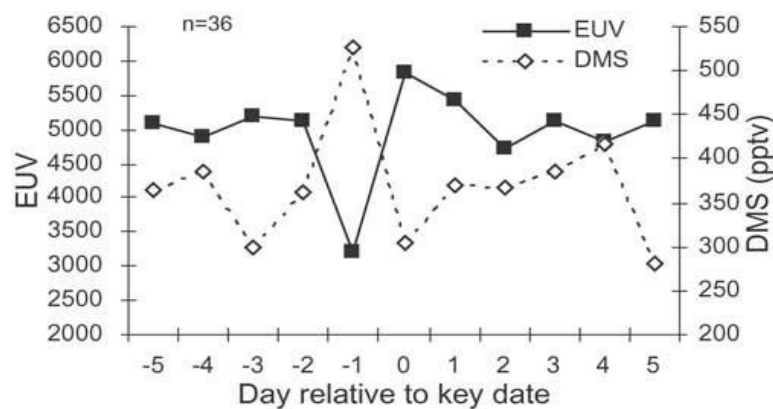
Figure II.27: Averaged anticorrelation of ultraviolet radiation (EUV) and atmospheric dimethylsulphide (DMS) according to 36 solar activity decrease events. Measurements were made at Amsterdam Island in the southern Indian Ocean. Adapted from Kniveton et al. (2003).

austral summer (December 26, 0-40°S) the diurnally averaged variability was about 0.12 W/m² for <730 nm, with most change occurring in the near UVA range of 400 to 410 nm, as depicted in Figure II.26.

Larsen (2005) reports that three out of five studies found ultraviolet radiation to significantly reduce the yield of dimethylsulphide, while the species relevant to dimethylsulphide synthesis in the Southern Ocean seemed to be particularly sensitive. In addition the mixing zone is shallow in the tropical oceans, so that damaged plankton cannot recover outside the euphotic zone making it vulnerable to ultraviolet radiation. This region coincides with the area of extensive occurrence of stratocumuli, and its local radiation balance should be most sensitive to cloud cover and droplet number variation (Ringer and Shine, 1997). An empirical study of Kniveton et al. (2003), spatially limited to the isle of Amsterdam in the southern Indian Ocean

and based on observing selected episodes over five years of the daily variability of ultraviolet flux, found a (at the 5% level) statistically significant anticorrelation between the ultraviolet radiation and the dimethylsulphide atmospheric concentration (see Figure II.27). For the 37 selected events of ultraviolet radiation decrease the average radiation flux reduction was 48% while the dimethylsulphide increase was 39%. The system reaction was remarkably fast with no relevant delay on the time scale of daily measurements.
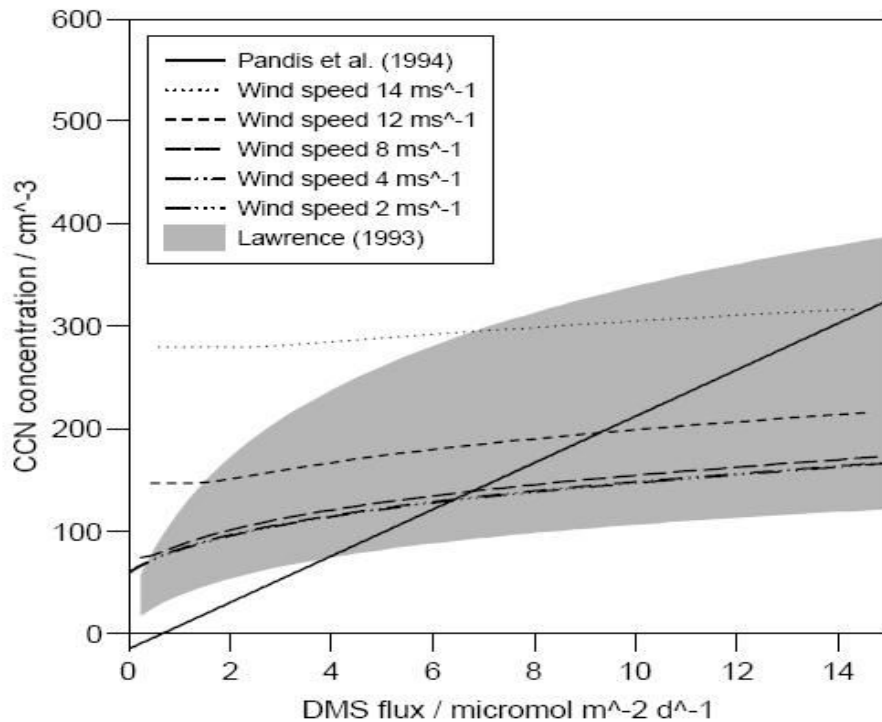
Figure II.28: Modelled cloud condensation nuclei number (diameter>0.1 μm) versus daily dimethylsulphide flux. The cloud nuclei numbers are also a function of wind velocity, as indicated through the positive offset (see text). The solid line shows the sensitivity found by Pandis et al. (1994) without considering sea salt particles. The empirical data range of Lawrence (1993) is indicated by the shaded area. Adapted from Yoon and Brimblecombe (2002).

An empirical study of Bates et al. (1987) points to a linear relationship both between the condensation nuclei concentration and the estimated dimethylsulphide flux from the ocean surface, and between the seasonal variation of solar radiative flux and dimethylsulphide release from the ocean. The cloud condensation nuclei data is from four remote measuring stations in the Southern Ocean while the dimethylsulphide flux estimation data was obtained during ship cruises in the North Atlantic. The simultaneously spatial and temporal ubiquity of

the established linear function should further demonstrate the strong link between these two variables, although the number of independent data points is relatively low. The relative slope of the nuclei number with the dimethylsulphide emission flux is approximately 0.75 (scaling values 1μmol DMS per day and m^2, 100 particles per cm^3). The model study of Pandis et al. (1994) confirms the previous findings pertaining the linear correlation between condensation nuclei number and the marine dimethylsulphide flux in that they find a constant slope of approximately 0.23. However, their study does not include sea salt particle emission and consistently they find a negative offset of the condensation nuclei number for zero dimethylsulphide flux. The study of Yoon and Brimblecombe (2002), which extends the latter to sea salt emission as a function of wind velocity as well as particle entrainment from the free troposphere, reveals a dimethylsulphide cloud nuclei correlation slope of only about 0.07 (see Figure II.28). Consistently they find a significant positive offset that depends on wind speed. A model study of Pirjola and Kulmala (1998) focussing on atmospheric chemistry, dimethylsulphide emission, secondary particle formation in the H_2SO_4/H_2O system and background particles found the cloud condensation nuclei number to be weakly dependent on the dimethylsuphide emission rate although sea salt flux and particle entrainment were not considered. The correlation slope increases from circa 0.01 for a low number of background particles to 0.02 for one hundred times more background particles in the Aitken size range.

II.3 Summary and Outlook

Statistical studies of global climate evolution during the preceding centuries show that the variability of greenhouse gas concentrations alone may not explain the observed variability in climate records. While the solar signal is clearly discernible in the upper atmosphere in relationship with ultraviolet radiation as a high energy chemical reaction enhancer, it may only be found in the troposphere through advanced statistical techniques involving spectral analysis. It may thus be postulated that solar variability influence on global climate, which is obvious in the stratosphere, must be propagating downwards by stratosphere-troposphere interaction. Recent findings of a correlation between global cloud cover and the solar cycle seem to contradict this point of view (Svensmark amd Friis-Christensen, 1997) and may indicate the existence of an intrinsic tropospheric mechanism. The correlation has been observed to be strongest in the marine boundary layer in association with warm subtropical stratocumuli.

The hypothesis put forward by Marsh and Svensmark (2000) postulates a link between cosmic rays, the ionisation rate, secondary aerosol formation via ion nucleation, the potential cloud condensation nuclei number, cloud microphysics, fractional cloudiness, cloud optical properties, the global radiation balance and mean atmospheric temperature. Although cosmic rays are observed to sensibly vary with the solar cycle (1), there is indication that ion critically enhance particle nucleation (2), cloud optical properties are known to be particularly sensitive to the cloud droplet number when their number is low (3) and stratocumuli should have a negative effect on the radiation balance (4), there remains a lot of controversy, also concerning the more substantiated processes. Thus, it is not clear whether the solar cycle notably modulates the ionisation rate in the lower troposphere (I) and there is insufficient knowledge on the dynamical evolution of a growing aerosol population under both cloudy and cloud free conditions (II). Moreover the importance of secondary particles under marine conditions might be lower than commonly expected, so that the sensitivity of the potential cloud nuclei number relative to the nucleation rate may be low (III). There are also a number of question marks regarding the activation process of cloud nuclei (IV) as well as the cloud dynamical and microphysical processes (V), which presumably lead to an overall positive (enhancing) feedback of the nuclei number incidence on cloud radiation properties (VI). The relevance of

the cloud radiative budget for the short term climate evolution under a marine environment may also be contested (VII).

Larsen's (2005) theory that the solar modulation of climate is not enhanced by the galactic cosmic ray flux but rather directly by the biogeochemical relationship between the ultraviolet radiation, the marine dimethylsulphide and the atmospheric sulphate production rate, is consistent with both the supposed stratospheric and mesospheric link and the Gaia hypothesis and its central postulate of biosphere-atmosphere interaction. It implies that the variability of the cloud condensation nuclei number is not triggered by the nucleation rate but rather due to the sensitivity of aerosol growth dynamics to the sulphuric acid formation rate. The dependence of the nuclei number on this value has been indicated by both observation and model studies. For similarity reasons it is bound, however, to the same uncertainties as Marsh and Svensmark's hypothesis as to the degree of relevance of secondary particles to the marine aerosol, as well as to their cloud dynamical and climatic incidence in the marine environment. Besides and most principally, it is uncertain whether solar ultraviolet radiation modulation influences critically the metabolism of the marine organisms that are relevant to the release of dimethylsulphide to the atmosphere.

The aim of a modelling study is to investigate and to corroborate hypotheses on the interconnection of formally known elements. In the present case the triggering mechanisms of solar modulation of cloud formation are still being questioned. For this reason the variability of the low atmosphere ionisation, the solar modulation of ion-enhanced formation of ultrafine secondary aerosol particles as well as the variability of atmospheric sulphur can not be established in this study. The factual establishment of these processes requires further empirical investigations. However, starting from the hypothesis of their existence, their climatic potential in relationship with some of the aforementioned interconnections may be investigated. Precisely, it will be attempted to raise the level of understanding in relationship with the aforementioned controversies II to V. This requires the design of a state of the art model of aerosol growth, and the development of an appropriate formalism of aerosol-cloud droplet interaction, which is to be embedded in a boundary layer model of marine stratocumulus formation. An appropriate nucleation model serves as a source function of a relevant number of ultrafine particles under typical marine boundary layer conditions. The basic theory leading to this model as well as the theory of aerosol growth through condensation and coagulation in turbulent flow is related in the following chapter. A further

chapter exposes the formalism of the aerosol growth module and aerosol-cloud interaction embedded in a one-dimensional model of shallow cloud formation in the marine boundary layer (Chlond et al., 2004). Following a detailed discussion of the results obtained with the ion-induced nucleation scheme, aerosol growth model results are lengthily described and interpreted in two sections, of which the first one is exclusively dedicated to box model results in the absence of aerosol cloud interaction. Zero-dimensional simulation of secondary aerosol formation allows assessing the basic aerosol growth dynamical characteristics. In particular, the sensitivity with respect to the ionisation and sulphuric acid formation rate, and the interaction of primary and secondary particles are investigated. The second section presents in detail the features that were obtained with the scheme of aerosol cloud interaction. One-dimensional model runs of secondary aerosol formation in conjunction with primary particle emission and cloud processing may give a realistic estimate of the sensitivity of the marine aerosol and the cloud droplet number to the ionisation rate and the atmospheric sulphate yield. Finally a conclusion may be drawn as to the potential of the investigated mechanisms of indirect solar modulation of global climate to modify cloud microphysical properties on the local scale.

III. Secondary Aerosol Nucleation and Growth Theory

III.1 Binary nucleation

III.1.1 Preliminary considerations

Secondary aerosols are likely to play an important role in air masses over the oceans, in which primary aerosols are much less prominent. Sulphuric acid is thought to be a primary contributor in the process leading to the formation of secondary particles in the marine environment. It is well known for its hygroscopic property, and is naturally present in marine air as it is chemically generated from dimethylsulphide released from the ocean waters (Charlson et al., 1987). In the atmosphere dimethylsulphide is successively oxidised into sulphur dioxide and, eventually, sulphuric acid involving photolytic reactions (see Seinfeld and Pandis, 1998). Moreover, sulphuric acid should be the dominant species for secondary aerosol particle formation, as other candidates such as nitric acid are scarce under pristine marine conditions (Yu and Turco, 2001). Model results of binary H_2SO_4/H_2O nucleation indicate that the formation rates are several orders of magnitude too low to explain the observed levels of secondary particles in the atmosphere (e.g. Yu, 2006a). At this point the interference of ions could be crucial (Arnold, 2006), as through their attractive forces relative to other molecules they should enhance both the encounter probability and efficiency, and lower the evaporation losses (Yu and Turco, 2001).

Three major approaches to ultrafine secondary particle formation in the H_2SO_4/H_2O system have been outlined above (Yu and Turco, 2001, Laakso et al., 2002, Lovejoy et al., 2004). The classical binary nucleation approach of Laakso et al. (2002) is purely thermodynamical (Stauffer, 1976). The mechanical approach (Yu and Turco, 2001; Lovejoy et al., 2004) implies that the transitional pathway leading to stable particles needs to be considered, knowing that the mechanisms of particle attachment and detachment have not yet been quantified with confidence on the level of ion clusters. The results are very likely to diverge because the formation of new particles is highly sensitive to these mechanisms. Yu and Turco (2001) try introduce sticking coefficients of collision efficiency in relationship with particle attachment, whereas particle detachment is treated with macroscopic thermodynamic data. In his newer

model version Yu (2006b) has used specific data on neutral and negatively charged clusters, however different from the detachment data used by Lovejoy et al (2004). The uncertainty related to particle disintegration is such that the model of Yu and Turco (2001) finds ion nucleation to be of primary importance in the atmospheric boundary layer, while the results of Lovejoy et al. (2004) imply that it is irrelevant and confined to the upper troposphere (Kazil et al., 2006).
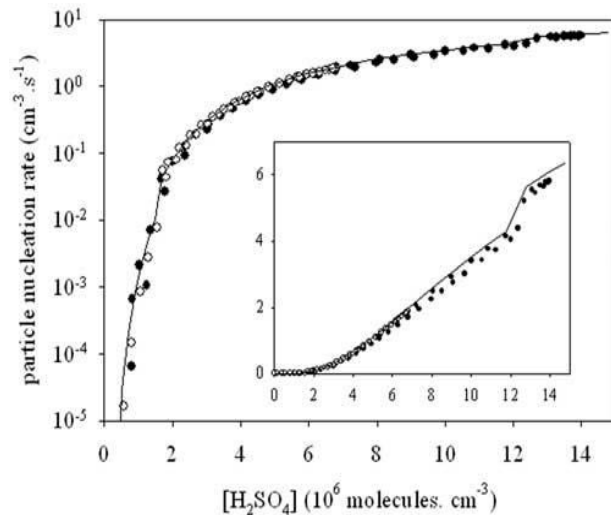
Figure III.1: Dynamical response of the equivalent nucleation rate to a variation of the ambient sulphuric acid concentration compared to the immediate equilibrium values (solid line). Insert shows the same relationship on a linear scale. Adapted from Modgil et al. (2005)
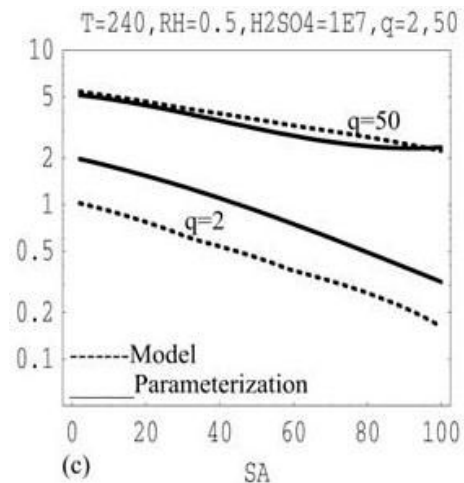
Figure III.2: Dependence of the equivalent nucleation rate (cm^{-3}) on the aerosol surface area ($=SA$, $\mu m^2/cm^3$), q being the ionisation rate (cm^{-3} s^{-1}). According to Modgil et al. (2005)

Interestingly, Laakso et al. (2002) find the relevance of ion-induced secondary particle formation to be comparable to the one implied by Yu and Turco (2001). Their classical thermodynamic approach entails that particle formation is not spatially, that is dynamically, but rather energetically limited. Several deficiencies are inherent to the classical nucleation theory. First, the classical theory implies that unstable particles show momentary equilibrium concentration. This assumption is appropriate only provided that the unstable particle system dynamics are fast enough to react rapidly to variations of the ambient conditions, such as relative humidity, temperature but also the stable particle population. Results obtained with the model of Lovejoy et al. (2004) (see Modgil et al., 2005) seem to indicate that the system's reaction is fast so that the simulated rates are rather close to instantaneous equilibrium values,

as it is depicted in Figure III.1. Second, the nucleation theory does not respect the mass action law, which entails that at equilibrium the net flux of new stable particles should be zero. The requirement is that while the system is close to equilibrium, simultaneously equilibrium and non-equilibrium assumptions can be made. This is a common simplification in physics when treating complex phenomena. Although its frequency might not serve as a justification, the
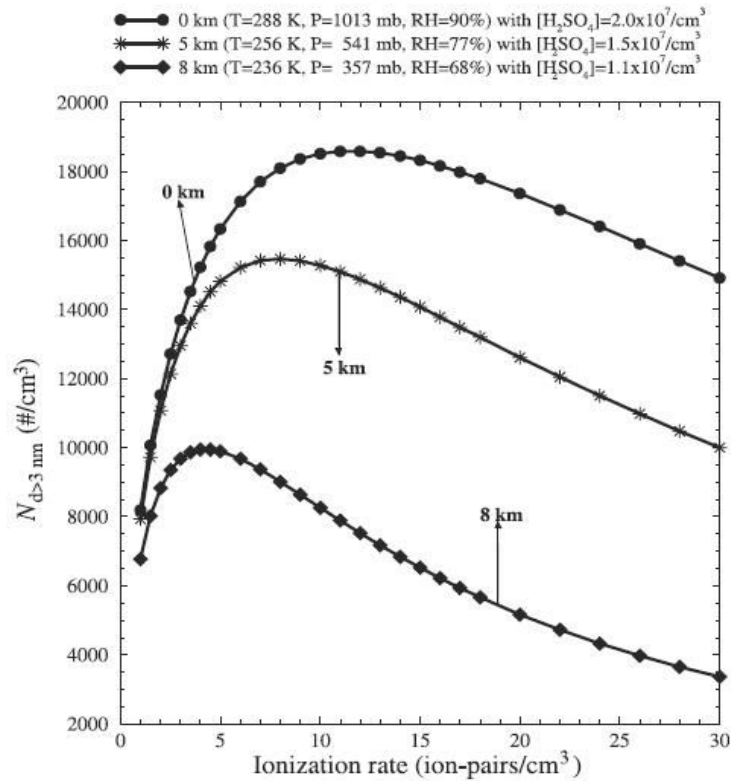
Figure III.3: Ion caused particle numbers may decrease beyond a certain threshold of the atmospheric ionisation rate by the increased neutralisation rate of unstable clusters, an effective limiting factor of stable particle formation. Adapted from Yu (2002).

usage of this approach has shown to give reliable results, for instance when the cloud droplet size spectrum is evaluated assuming the immediate condensation of the integral excess water relative to a flat surface, while the dynamics of vapour condensation onto curved particles are considered in order to estimate the critical activation radius. Third, the thermodynamic approach uses the Thomson equation (Thomson, 1906) to assess the particles's energetic formation barrier. The accuracy of this equation has been formally questioned on cluster level (Yu, 2005). Moreover up to this moment macroscopic thermodynamic data on sulphuric acid

and water vapour pressure over flat solutions has been utilised as input values. On the level of cluster inos the usage of macroscopic evaporation schemes should not be appropriate, as confirmed by measurements of Holland and Castleman (1982) showing that the Thomson equation leads to inaccuracies that cannot be remedied unless it is formally modified. However, the classical theory was shown to perform reasonably well for the hydration of ions. Fourth, the classical nucleation theory regards unstable particles to be disconnected from the stable particle population with respect to coagulation. This is an approximative assumption as stable particles are principally as likely to interact with unstable particles as these are among themselves. Consistently, the incidence of the stable fraction is relevant when the equivalent nucleation rate is assessed (the appearance rate of particles larger than 3 nm) in relationship with mechanical models (Yu, 2003, Modgil et al., 2005). The sensitivity of the equivalent nucleation rate to the aerosol population is depicted in Figure III.2 showing that it may well vary within one order of magnitude although the water vapour and sulphuric acid sources are held constant. Fifth, the interaction of charged particles, stable or not, may lead to non-linearities that can not be treated with the classical theory. Yu (2002) thus found the equivalent nucleation rate to increase with the ion concentration, that is the ionisation rate, to a maximum value until negative feedback processes become relevant that reduce the ultrafine particle formation efficiency. Beyond a certain threshold value ambient ions lead to enhanced particle neutralisation rates that impedes stable particle formation through enhanced particle disintegration (Figure III.3). The classical theory predicts the nucleation rate to be a linear function of ion concentration.

As a conclusion, the thermodynamic approach does include many inconsistencies that lead to a considerable amount of uncertainty related to the accuracy of the deduced nucleation rates. However, more consistent mechanical approaches lead to comparable degrees of uncertainty as the key process of cluster disintegration, and to a lesser degree encounter efficiency, are not yet represented with accuracy. For this reason the method chosen in this study is the classical nucleation method, which presents the additional advantage of being computationally more efficient. Ion-induced nucleation has the potential to produce relevant boundary layer secondary particle formation, which is a prerequisite to enhanced solar modulation of the lower troposphere as required by the hypotheses of Marsh and Svensmark (2000) and Larsen (2005). Although indicated by both observation and laboratory experiments, there is still controversy on the degree of ascertained proof of frequent boundary layer nucleation that is

thereby attained. It is in this context that an affirmative speculative approach with respect to boundary layer nucleation allows exploring the hypothetical implications of aerosol growth and aerosol cloud interaction dynamics to the suggested indirect solar mechanisms.

III.1.2 Binary nucleation in a homogeneous H_2SO_4 / H_2O system

1.2.1 Introduction

In this section an overview is given on the theoretical considerations that lead to the general expression of the ion-induced nucleation in a binary system. The main assumptions and the main steps of the development are indicated along with the most important intermediate results. For more details on secondary nucleation it is referred to Stauffer (1976). In the final part the nucleation rate is combined to the Gibbs free formation energy of a liquid charged particle according to Thomson (1906).

1.2.2 Stauffer's formula of the binary nucleation rate

Below a certain size limit and at a certain composition, cluster ions tend to evaporate immediately, they are thermodynamically unstable. Although these should not exist under average conditions from a thermodynamic point of view, a constant number of gas and liquid particle encounters will generate a constant number of unstable clusters. The ensuing equilibrium distribution of unstable particles reflects the chemical composition of the air and the associated encounter and detachment probabilities. Thermodynamically, the Gibbs free energy variation following the addition of one additional gas molecule is positive whenever the product is unstable. Macroscopically, the particles are unstable as long as the Kelvin effect dominates the free energy variation. With increasing particle size the Gibbs energy reaches a maximum, which depending on the particle composition, presents a local minimum. This is the saddle point of the Gibbs free formation energy distribution function in the sulphuric acid / water phase plane. The underlying assumption of nucleation theory is that the flux of newly formed ultrafine particles effectively passes through the saddle and its vicinity. However, as Reiss (1950) points out, particularities of the Gibbs free energy distribution function could in

principle induce different preferential growth paths.

Reiss (1950) has shown that the equilibrium concentration of unstable clusters is:

$$N_{eq}(a,b) = N e^{\left(\frac{-\Delta G_f(a,b)}{kT}\right)}$$

f III.1

where N_{eq} is the equilibrium number concentration of the cluster as a function of its components a and b, T is absolute temperature, k is the Boltzmann constant and ΔG_f is the Gibbs free formation energy of the liquid particle from its gaseous components. N is defined by:

$$N = N_a + N_b + \sum N(a,b)$$

f III.2

where N_a and N_b are the number concentrations of molecules a and b in the gas phase, respectively, and $N(a,b)$ is the concentration of clusters containing a molecules of species a, and b molecules of species b. To a very good approximation this equation reduces to the first and second term.

Equation III.1 is obtained considering the partial derivative of the Gibbs free energy of the colloid to an infinitesimal variation of its gas and liquid phase constituents in conjunction with the mass conservation equations of species a and b.

The attachment and detachment of clusters may be assumed to be negligible, so that the two-component particle nulceation J_{ab} relative to a particle $N(a,b)$ is:

$$\begin{aligned}
J_{ab} &= J(a+1,b) + J(a,b+1) \\
&= R_a(a,b)N(a,b) - E_a(a+1,b)N(a+1,b) \\
&\quad + R_b(a,b)N(a,b) - E_b(a,b+1)N(a,b+1)
\end{aligned}$$

f III.3

where $J(a+1,b)$ and $J(a,b+1)$ are the nucleation fluxes directed towards particles $N(a+1,b)$ and $N(a,b+1)$, respectively, and R and E are the respective condensation and evaporation rates.

The evaporation rate may be determined at equilibrium condition $J(i+1,j)=0$:

$$E_i = R_i \frac{N_{eq}(i,j)}{N_{eq}(i+1,j)} \quad .$$

<div align="center">**f III.4**</div>

Thus the variation in time is given by:

$$\frac{dN(a,b)}{dt} = J(a-1,b) - J(a+1,b) + J(a,b-1) - J(a,b+1)$$

$$\simeq -div(\mathbf{J}_{ab})$$

$$\simeq div\left(N_{eq}(a,b)\,\mathbf{R}\cdot grad\left(\frac{N(a,b)}{N_{eq}(a,b)}\right)\right) \;,\;\; \mathbf{R} = \begin{pmatrix} R_a(a,b) & 0 \\ 0 & R_b(a,b) \end{pmatrix} \quad .$$

<div align="center">**f III.5**</div>

Since *curl(grad(x))=0*, the preceding equation rereads under equilibrium conditions:

$$curl\left(N_{eq}^{-1}(a,b)\,\mathbf{R}^{-1}\cdot\mathbf{J}(a,b)\right) = 0 \quad .$$

<div align="center">**f III.6**</div>

The preceding equation combined to the relationship *curl(a v)=a curl(v) − v ⊗ grad(a)* and Equation III.1 leads to (Stauffer, 1976):

$$curl(\mathbf{R}^{-1}\cdot\mathbf{J}) = (\mathbf{R}^{-1}\cdot\mathbf{J})\otimes grad\left(\frac{\Delta G_f^*}{kT}\right) \quad ,$$

<div align="center">**f III.7**</div>

where $\Delta G_f^* = \dfrac{\Delta G_f}{kT}$ is the normalised Gibbs free formation energy of the liquid particle.

Stauffer (1976) analysed the repercussions of this relationship on the direction of the nucleation flux at the saddle point. He made the assumption that in a Taylor expansion of the Gibbs free formation energy the first spatial derivative, when compared to the second, is negligible in the vicinity of the saddle point. Furthermore, to simplify calculations, a two-step coordinate system transformation of the composition phase plane is introduced. The first one is a simple translation of the origin to the saddle point. Note that the expression III.5 is conserved during this operation. The second one is a rotation of the coordinate system to the direction of cluster growth at the saddle point, which is assumed to be constant for the whole saddle point region. Thus the nucleation flux is null in the new y-direction, while it is parallel to the new x-direction.

The above equation becomes:

$$\sin\phi\,\frac{\partial\left(R_b^{-1}J_x\right)}{\partial a_{sp}}-\cos\phi\,\frac{\partial\left(R_a^{-1}J_x\right)}{\partial b_{sp}}=R_a^{-1}\cos\phi\,J_x\,\frac{\partial\Delta G_f^*}{\partial b_{sp}}-R_a^{-1}\sin\phi\,J_x\,\frac{\partial\Delta G_f^*}{\partial a_{sp}}\quad,$$

$$\boldsymbol{R}^{-1}\cdot\boldsymbol{J}=\begin{pmatrix}R_a^{-1} & 0\\ 0 & R_b^{-1}\end{pmatrix}\cdot\begin{pmatrix}\cos\phi\,J_x\\ \sin\phi\,J_x\end{pmatrix}\quad,$$

f III.8

where the subscript *sp* indicates translated coordinates at the saddle point, and φ is the growth flux direction at the saddle point, i.e. the angle between the axes *x* and *a*.

Together with:

$$\delta\left(\Delta G_f\right)_{sp}=D_{aa}\,a_{sp}^2+2\,D_{ab}\,a_{sp}\,b_{sp}+D_{bb}\,b_{sp}$$

f III.9

and the ansatz:

$$J_x=\left(J_x\right)_{sp}e^{-Wy^2}$$

f III.10

Equation III.8 leads to a condition of the form $F_a\,a_{sp}+F_b\,b_{sp}=0$, the solution of which yields:

$$\tan\phi=0.5\left(\frac{R_b}{R_a}\frac{D_{bb}}{D_{ab}}-\frac{D_{aa}}{D_{ab}}\right)+\sqrt{0.25\left(\frac{R_b}{R_a}\frac{D_{bb}}{D_{ab}}-\frac{D_{aa}}{D_{ab}}\right)+\frac{R_b}{R_a}}\quad,$$

f III.11

where D_{ij} is half the second partial derivative of the normalised Gibbs free formation energy to the species *i* and *j*. Note that the ansatz of Equation III.10 is related to the assumption that the nucleation flux goes through the saddle point.

The above equation can be further simplified as the condensation rate of sulphuric acid is much lower than the one of water vapour. It is:

$$\tan\phi\simeq-\frac{D_{aa}}{D_{ab}}+\frac{R_b}{R_a}\frac{D_{bb}}{D_{ab}}-\frac{R_b}{R_a}\frac{D_{ab}}{D_{aa}}\quad.$$

f III.12

The total nucleation flux of newly formed stable ultrafine condensation nuclei, i.e. the nucleation rate, is given by the following integral:

$$J_{tot} = \int\limits_{-\infty}^{+\infty} J_x(y)\,dy$$

<div align="center">**f III.13**</div>

Using Equation III.5 Stauffer (1976) finds the following relationship:

$$\frac{J_x}{R_{av}} \int\limits_{-\infty}^{+\infty} N_{eq}^{-1}(x,y)\,dx \equiv (\boldsymbol{R}^{-1}\cdot\boldsymbol{J})_x \int\limits_{-\infty}^{+\infty} N_{eq}^{-1}(x,y)\,dx = -\int\limits_{-\infty}^{+\infty} grad\left(\frac{N(x,y)}{N_{eq}(x,y)}\right)dx$$

$$= -\left(\left(\frac{N(+\infty,y)}{N_{eq}(+\infty,y)}\right) - \left(\frac{N(-\infty,y)}{N_{eq}(-\infty,y)}\right)\right) = -(0-1) = 1 \qquad ,$$

<div align="center">**f III.14**</div>

where:

$$R_{av} \equiv \frac{J_x}{(R^{-1}\cdot J)_x} = \frac{R_a R_b}{R_a \sin^2\phi + R_b \cos^2\phi}$$

<div align="center">**f III.15**</div>

Here two assumptions have been made. First, it is assumed that the net growth flux as well as the condensation rate tensors are constant in the vicinity of the saddle point. This means that the fraction of the particle spectrum that is relevant to the nucleation flux according to the previous equation, that is the vicinity of saddle point for which particle number concentrations are low (c.f. Equation III.1), is at quasi-equilibrium. Second, it is implied via Equation III.5 that the evaporation rate remains fairly constant within this part of the composition phase plane, and may be expressed by its equilibrium value.

When the preceding Equation III.14 is integrated into Equation III.13 one obtains:

$$J_{tot} = R_{av}(N_{eq})_{sp}Z$$

<div align="center">**f III.16**</div> ,

where Z is the so-called Zeldovitch non-equilibrium factor given by:

$$Z \equiv \int\limits_{-\infty}^{+\infty}\left(\int\limits_{-\infty}^{+\infty}\frac{(N_{eq})_{sp}}{N_{eq}}\,dx\right)^{-1}dy$$

<div align="center">**f III.17**</div>

It may be shown that the previous expression is equivalent to:

$$Z = -\frac{D_{aa}\cos^2\phi + D_{bb}\sin^2\phi + 2D_{ab}\cos\phi\sin\phi}{\sqrt{-(D_{aa}D_{bb} - D_{ab}^2)}}$$

.

f III.18

Hence Stauffer (1976) has expressed the binary homogeneous nucleation rate to be a function of the saddle point average condensation flux at equilibrium conditions multiplied by the Zeldovitch factor, which is a function of the growth angle and the second composition phase derivatives of the Gibbs free formation energy of the critical particles. The newly defined Zeldovitch factor expresses the two-dimensional property of the composition phase related to binary nucleation.

III.1.3 Ion-induced nucleation rate in a H₂SO₄ / H₂O system

1.3.1 Preliminary Considerations

There is experimental evidence (Arnold, 2006) that ion nucleation is related to a certain degree to the chemical nature of the ion. Nucleation involving positively charged ions might thus be less effective as these fail to bind sulphuric acid effectively (see above). Ideally ion nucleation should be related to a mechanical formalism that takes into consideration the respective thermodynamic properties of the species involved. Ion nucleation in the *H₂SO₄/H₂O* system might therefore be regarded as a ternary mechanism involving elementary ions of respective chemical nature, sulphuric acid and water vapour. Classical theory, however, requires the number of chemical species to be restricted, namely to one or two species. Besides ions do not constitute a conservative quantity such as mass, in as much as their number is reduced by mutual neutralisation. For relatively small particles, such as clusters and ultrafine particles, the number of charges per particle is limited to the equivalent of a single elementary ion unless the particle will disrupt (e.g. Pruppacher and Klett, 1997), so that their representation as an independent species undergoing condensation and evaporation in the component phase space does not make sense. For these reasons the chemical nature of ions is not considered within the present ion-induced formalism. Consistently a distinction between anions and cations as to their potential to enhance secondary particle nucleation is not made.

1.3.2 Adaptation of Stauffer's nucleation rate formula

The nucleation rate of secondary particles within the H_2SO_4 / H_2O system is:

$$J_{tot} = Z R_{av} N e^{-\frac{\Delta G_f}{kT}}.$$

f III.19

As the coagulation of subcritical clusters is excluded (see above), N reduces to the first and the second term of Equation III.2.

The previous equation involves the saddle point equilibrium concentration of secondary particles in a binary system containing neutral particles exclusively (see Equation III.1). This problem was solved by Reiss (1950). Following Reiss it is to be formulated as follows for a system containing cluster ions:

$$f\{x_{ij}\} = d_f G = \mu_{ag} dN_a + \mu_{bg} dN_b + \sum_{i=1}^{\infty} \sum_{i=1}^{\infty} \mu_g \{N_{ij}\} \ dN_{ij} + \mu_g \{N_{\pm}\} \ dN_{\pm} = 0 \qquad (1)$$

$$g_1\{x_{ij}\} = dN_a + \sum_{i=1}^{\infty} i \sum_{j=1}^{\infty} dN_{ij} + a_{\pm} dN_{\pm} = 0 \qquad (2)$$

$$g_2\{x_{ij}\} = dN_b + \sum_{j=1}^{\infty} j \sum_{i=1}^{\infty} dN_{ij} + b_{\pm} dN_{\pm} = 0 \qquad (3)$$

$$g_3\{x_{ij}\} = dN_{\pm} + \sum_{i=1}^{\infty} \sum_{j=1}^{\infty} dN_{ij} = 0 \qquad (4)$$

f III.20

where $a_{\pm}$ and $b_{\pm}$ is the number of molecules of species a and b in the cluster ion $N_{\pm}$, respectively, μ_{ig} is the chemical potential of the gaseous species i and $\mu_g\{N_{ij}\}$ is the chemical potential of the subrital cluster ion N_{ij} in the gaseous colloid. Note that the inital ion $N_{\pm}$ is not an elementary ion but rather a stable cluster ion containing in general several molecules i and j (Raes and Janssens, 1985, Albrecht, 2006).

Equation (1) represents the Gibbs free energy variation upon recombination in the mother phase, comprising the totality of the gaseous and liquid particles containing species a and/or b in the atmosphere. Equations (2) and (3) stand for the mass conservation of species a and b, respectively. Equation (4) testifies for the conservation of the particle total charge assuming that particle charge is restricted to one elementary charge and that ion recombination is negligible. Equations (2) through (4) state that the atmosphere is in a chemical equilibrium

with respect to the gaseous species *a* and *b* as well as to small ions. Chemical equilibrium implies that each species' partial derivative of Equation (1) also has to be equal to zero. This situation is equivalent to the calculation of an extreme with side conditions (see Reiss, 1950). The characteristic equation of this problem is:

$$F\{x_{ij}\}=f\{x_{ij}\}+L_1\ g_1\{x_{ij}\}+L_2\ g_2\{x_{ij}\}+L_3\ g_3\{x_{ij}\}$$

f III.21 ,

L_i being the Lagrange multipliers.

The subsequent system to be solved is:

(1) $\quad \dfrac{dF}{ddN_a}=\mu_{ag}+L_1=0$

(2) $\quad \dfrac{dF}{ddN_b}=\mu_{bg}+L_2=0$

(3) $\quad \dfrac{dF}{ddN_{ij}}=\mu_g\{N_{ij}\}+i\,L_1+j\,L_2+L_3=0$.

(4) $\quad \dfrac{dF}{ddN_\pm}=\mu_g\{N_\pm\}+a_\pm L_1+b_\pm L_2+L_3=0$

f III.22

After the elimination of the Lagrange multipliers one obtains for each cluster ij:

$$\left(\mu_g\{N_{ij}\}-i\,\mu_{ag}-j\,\mu_{bg}\right)-\left(\mu_g\{N_\pm\}-a_\pm\mu_{ag}-b_\pm\mu_{bg}\right)=0$$

f III.23 ,

with:

$$\mu_g\{N_{ij}\}=i\,\mu_{al}\{N_{ij}\}+j\,\mu_{bl}\{N_{ij}\}+\Delta\mu\{surf.\,ten.,N_{ij}\}+\Delta\mu\{electr.\,f.,N_{ij}\}+kT\ln\frac{N_{ij}}{N}$$

,

f III.24

where μ_{il} is the liquid phase chemical potential of species *i*,

and:

$$\mu_g\{N_\pm\}=a_\pm\mu_{al}\{N_\pm\}+b_\pm\mu_{bl}\{N_\pm\}+\Delta\mu\{surf.\,ten.,N_\pm\}+\Delta\mu\{electr.\,f.,N_\pm\}+kT\ln\frac{N_\pm}{N}$$

.

f III.25

The first two terms stand for the partial free energy of the species in solution, the third and the fourth term stand for the contribution of the surface tension and the electrostatic force, respectively, and the last term stands for the dilution of the particles in the atmospheric colloid, for which fugacity effects ar neglected. Note that the chemically specific contribution of the charged molecule to the particle free energy is not taken into consideration.

The chemical potentials of species a and b in solution are (c.f. Appendix 1):

$$\mu_{al}\{N_{ij}\}=\mu_{al}^{o}+kT\ln\alpha_{al}=\mu_{ag}^{o}+kT\ln p_{a}^{o}+kT\ln\frac{p_{al}}{p_{a}^{o}}$$

$$\mu_{ag}=\mu_{ag}^{o}+kT\ln p_{ag}$$

,

f III.26

where μ^{o} is the respective pure substance standard chemical potential, α is the fractional activity, p_{a}^{o} is the partial pressure over the flat pure liquid a, p_{ag} is the actual gas phase partial pressure of a, p_{al} is the partial pressure of species a over the mixture ij. Note that in equilibrium for pure gas and liquid phases a we have: $\mu_{ag}\equiv\mu_{al}.$.

Combining Equations III.23, III.24, III.25 and III.26 leads to:

$$\Delta_{f}G\{N_{ij}\}-\Delta_{f}G\{N_{\pm}\}+kT\ln\frac{N_{ij}}{N_{\pm}}=0$$

,

f III.27

with:

$$\Delta_{f}G\{N_{xy}\}=\left(x\,kt\,\ln\frac{p_{xy,al}}{p_{ag}}+y\,kt\,\ln\frac{p_{xy,bl}}{p_{bg}}+\Delta\mu\{surf.\,ten.\,,xy\}+\Delta\mu\{electr.f.\,,xy\}\right)$$

,

f III.28

where the lower index xy stands for either ij or $\pm$.

For the equilibrium concentration at the saddle point it follows from Equation III.27:

$$\left(N_{eq}\right)_{sp}=N_{\pm}e^{-\frac{\Delta\Delta_{f}G}{kT}}$$

.

f III.29

Using Equation III.16 the ion-induced nucleation rate thus becomes (e.g. Laakso et al., 2002):

$$\left(J_{tot}\right)_{\pm}=ZR_{av}N_{\pm}e^{-\frac{\Delta\Delta_{f}G}{kT}}$$

.

f III.30

1.3.3 Gibbs free formation energy of the ionized nucleus and the critical radius

Thomson (1906) quantified the contributions of the surface tension and the electric field term of Equation III.28:

67

$$\Delta_r G(a,b) = -a\,k\,T \ln\left(\frac{\alpha_{ag}}{\alpha_{al}}\right) - b\,k\,T \ln\left(\frac{\alpha_{bg}}{\alpha_{bl}}\right)$$
$$+ 4\pi r^2 \sigma + \frac{q^2}{8\pi\epsilon_0}\left(1 - \frac{1}{\epsilon_r}\right)\left(\frac{1}{r} - \frac{1}{r_{\pm}}\right) \quad ,$$

f III.31

where σ is the surface tension, ε_0 is the vacuum permittivity, ε_r is the dielectric constant or the so-called relative permittivity of the solution, r is the particle radius of the cluster ions at saddle point, r_0 is the radius of the initial cluster ion, and q is the electric charge of the cluster. The surface tension of the nucleus is a function of both the temperature and the radius. Note that $\Delta_r G$ corresponds to $\Delta\Delta_f G$ in Equation III.29.

According to Pruppacher and Klett (1997, p. 844) the dielectric constant of pure water may be computed using:

$$\epsilon_w = 87.740 - 0.4008(T - 273.15) + 9.398\text{e-}4(T - 273.15)^{-2} - 1.410\text{e-}6(T - 273.15)^{-3}$$

f III.32 .

When the ion is imagined to be a sphere at the centre of the nucleus, then the total mass of species a and b is equal to:

$$\frac{a\,m_a + b\,m_b}{n_{AV}} = \frac{4}{3}\pi(r^3 - r_0^3)\rho \quad .$$

f III.33

Now it may be proceeded to the estimation of the critical radius, i.e. the radius of the cluster ion at the saddle point. At this point the first derivative of the Gibbs free energy is zero for both species. When the radius dependence of the activity and of the surface tension is neglected, one finds:

$$\frac{\partial \Delta_r G}{\partial i} = -kT \ln\frac{\alpha_{ig}}{\alpha_{il}} + 8\pi r\sigma\left(1 - \frac{q^2}{64\pi^2\epsilon_0\sigma}\left(1 - \frac{1}{\epsilon_r}\right)\frac{1}{r^3}\right)\frac{\partial r}{\partial i} \quad .$$

f III.34

Using Equation III.33 the partial derivative of the cluster radius becomes:

$$\frac{\partial r}{\partial a}=\frac{m_a}{4\pi\rho r^2 n_{AV}}\left(1+\frac{X_b}{\rho}\frac{\partial\rho}{\partial X_b}\right)$$

$$\frac{\partial r}{\partial b}=\frac{m_b}{4\pi\rho r^2 n_{AV}}\left(1-\frac{1-X_b}{\rho}\frac{\partial\rho}{\partial X_b}\right)\ ,$$

<div align="center">**f III.35**</div>

with X_b [-], the mass fraction of species b:

$$X_b=\frac{b\,m_b}{a\,m_a+b\,m_b}\ .$$

<div align="center">**f III.36**</div>

Thus the derivative of the Thomson equation may be expressed independently of the radius of the initial ion r_0, which is unknown at this point. The derivative of the density of the solution to the mass fraction of species *b* may be approximated using empirical macroscopic data (see Appendix 2). Dividing both equations of System III.34 at the saddle point conditions, one finds:

$$\frac{\ln\frac{\alpha_{ag}}{\alpha_{al}}}{\ln\frac{\alpha_{bg}}{\alpha_{bl}}}-\frac{\frac{\partial r}{\partial a}}{\frac{\partial r}{\partial b}}=0\ .$$

<div align="center">**f III.37**</div>

This equation may be solved iteratively, provided that an appropriate formalism of activity assessment is at hand (see Appendix 1 and 2). Note that this equation is not an explicit function of the particle radius but solely of solute composition.

Knowing the critical composition and the species' activities, and thus all coefficients of Equations III.34, it may now be proceeded to the solution of these equations, which are of the fourth degree:

$$r^4+Ar^3+D=0,$$

$$A=-8\pi\sigma F,\quad D=HF,\quad F=\frac{r^2\frac{\partial r}{\partial a}}{kT\ln\frac{\alpha_{ag}}{\alpha_{al}}},\quad H=\frac{q^2\left(1-\frac{1}{\epsilon_r}\right)}{8\pi\epsilon_0}\ .$$

<div align="center">**f III.38**</div>

There may be two real positive solutions:

$$r = -0.25\,A + 0.5\,\Delta \pm 0.5\,E$$

,

with:

$$E = \sqrt{0.75\,A^2 - \Delta^2 - 0.25\frac{A^3}{\Delta}}$$

$$\Delta = \sqrt{0.25\,A^2 + Y} ,$$

$$Y = \sqrt[3]{A^2\frac{D}{2^4} + \sqrt{A^4\frac{D^2}{2^8} - \frac{D^3}{3^3}}} + \sqrt[3]{A^2\frac{D}{2^4} - \sqrt{A^4\frac{D^2}{2^8} - \frac{D^3}{3^3}}} .$$

The second derivative of the Thomson equation may be approximated by:

$$\frac{\partial^2 \Delta_r G}{\partial i\,\partial j} \simeq \frac{\delta\left(\dfrac{\partial \Delta_r G}{\partial i}\right)}{\delta j} .$$

These are needed for the computation of the growth direction of the clusters in the vicinity of the saddle point and of the Zeldovitch factor (Equation III.18).

1.3.4 Condensation rate

According to the Maxwell-Boltzmann distribution of Brownian motion the mean particle velocity is (e. g. Chapman and Cowling, 1990):

$$\overline{v_i} = \sqrt{\frac{8\,k\,T\,n_{AV}}{\pi\,m_i}} .$$

The mean relative velocity of two particles is:

$$\overline{v_{rel}} = \overline{\left(\sqrt{(\boldsymbol{v_i} - \boldsymbol{v_j})^2}\right)} = \overline{\left(\sqrt{v_i^2 + v_j^2 - v_i\,v_j\cos(\boldsymbol{v_i},\boldsymbol{v_j})}\right)} = \sqrt{\left(\overline{v_i}\right)^2 + \left(\overline{v_j}\right)^2} ,$$

implying that the mean relative movement of two particles is perpendicular. The mean value results of a triple integration over the respective Brownian motion velocity spectrum and over the angle between the two related velocity vectors. The mean condensation rate, as given by

the rate of particles i colliding with a particle j on the molecular scale, thus becomes:

$$R_i = N_i \pi (r_i + r_j)^2 \overline{v_{rel}} = N_i \pi (r_i + r_j)^2 \sqrt{\frac{8 \, kTn_{av}}{\pi} \left(\frac{1}{m_i} + \frac{1}{m_j} \right)} \; .$$

f III.44

When the colliding particles i are relatively small one may use the following approximation:

$$R_i = N_i r_j^2 \sqrt{\frac{8 \pi \, kT \, n_{AV}}{m_j}} \; .$$

f III.45

It is inherent to this formula that the velocity of the particles relative to the macroscopic flow field is negligible. In the following sections when quantities related to the Brownian velocity of a particle are addressed it is implied that these are statistical mean values.

III.2 Brownian condensation

III.2.1 Formalism

For Brownian motion induced condensation onto charged particles in the H_2SO_4 / H_2O system the following formalism is adopted:

-The condensation of water molecules onto the particles is assumed to be instantaneous. The atmospheric water molecules concentration is several orders of magnitude higher than the one of sulphuric acid. For this reason particles are assumed to always reach thermodynamic equilibrium with respect to the atmospheric moisture prior to the absorption of a new sulphuric acid molecule (Hamill, 1975). Consistently the particle growth rate is considered to be exclusively limited by the ambient sulphuric acid concentration. The binary nucleation flux simplifies to a unary H_2SO_4 particle growth formalism with instantaneous equilibration to the moisture content of the medium.

-Particle growth through condensation of sulphuric acid is assumed to be a one-way phenomenon. Due to the hygroscopic property of sulphuric acid, evaporation of water molecules is highly unlikely. This is a common assumption in relationship with particle growth in the H_2SO_4 / H_2O system (e.g. Raes et al., 1986; Laakso et al., 2002; Lovejoy et al., 2004).

-On the molecular scale condensation may be associated with a collision process involving spheres moving in a vacuum and independently of their environment. When the aerosol particle is large, its velocity becomes negligible relative to the velocity of the condensing species, so that the condensation rate becomes a function of the sole velocity of the impinging gaseous species. Moreover, the large size in conjunction with the high removing efficiency of the aerosol particle creates a concentration gradient in its vicinity. The gaseous particle flux thus becomes radially directed onto the aerosol particle's surface and may be assessed by the probability of a particle to move in that direction. Collision processes taking place under the

former microscale conditions are referred to in literature as taking place in the molecular regime, while the latter macroscale situation is referred to as the diffusion regime (e.g. Pruppacher and Klett, 1997). Condensation in the molecular regime is related to the total collision cross-section of the particles while diffusion is a function of the aerosol particle's surface area. Through their nature both regimes stand for idealised extreme situations, which are separated by a large intermediate range. Condensation within this size range is addressed to as taking place in the transition regime. The related formalism is obtained following extensive analytical treatment (e.g. Smirnov, 1971, Sahni, 1966; Fuchs, 1964) that will not be presented in detail here.

III.2.2 Condensation kernels in the free molecular and the diffusion regime

The general formula of the Brownian condensation rate in the free molecular regime onto an aerosol particle per number concentration of the impimg gas, the so-called condensation kernel is (e.g. Nadykto and Yu, 2003):

$$K_B^n = P_{st} \ E_B \ \pi \, r_{tot}^2 \sqrt{v_p^2 + v_m^2} \quad ,$$

f III.46

where K_B^n is the Brownian condensation kernel of particles containing n previously impinged gas molecules, P_{st} is the sticking coefficient, E_B is the Brownian condensation enhancement factor, r_{tot} is the sum of the radii of the aerosol particle and the impiging gas molecule, and v_p and v_m are the particle and gas molecule Brownian velocity, respectively.

The condensation kernel stands for the frequency of collision of gas molecules onto a certain particle per number concentration of the impinging gas. In order to obtain the number of collisions per unit volume during a certain time interval, the kernel has to be integrated over the concentration of the impinging gas, the aerosol size spectrum, and the considered time interval. For a monodisperse aerosol of n impinged molecules and a small enough time interval, this value is equivalent to the formation number of particles containing $n+1$ impinged gas molecules.

The sticking coefficient relates the probability that a collision efficiently leads to condensation. It is a strong function of the kinetic energy involved and therefore needs to be

averaged over the Maxwell-Boltzmann velocity distribution. The sticking probability is also strongly dependent on the chemical nature of the species involved. Besides, particle charge may have an enhancing effect on the sticking efficiency depending on the polarizability of the condensing species (Yu and Turco, 2001; Nadykto and Yu, 2003). In the sulphuric acid/water vapour system, it is assumed here that the condensation sticking coefficient is equal to unity owing to the hygroscopic property of the strong acid (e.g. Laakso et al., 2002). The enhancement factor describes the density increase of the flux of gas molecules onto the particle due to electrostatic interaction between the charged aerosol particle and the polar condensing species. It will be established in detail below.

In the diffusion regime the condensation flux onto an aerosol particle is proportional to the radially directed concentration gradient of the condensing species (e.g. Kulmala, 1990):

$$\phi_D^n = P_{st} \; E_D \; 4\pi (r_p + r_m)^2 \; D \; \frac{d\,N_a}{d\,r} \simeq P_{st} \; E_D \; 4\pi r_p \; D \; N_a \quad ,$$

f III.47

where φ_D^n is the diffusion flux per aerosol particle, E_D is the diffusion enhancement factor, and D is the diffusion coefficient (see below for details).

In analogy to the molecular regime a diffusion condensation kernel may be defined:

$$K_D^n \equiv P_{st} \; E_D \; 4\pi r_p \; D \quad .$$

f III.48

It should be noted that the derivative in Equation III.47 is not to the radius of the particle but to the radial component of the spherical coordinate system originating in the centre of the aerosol particle. The concentration gradient may be approximated from constant flow assumption at steady state (Pruppacher and Klett, 1997):

$$\frac{\partial N_a}{\partial t} = \frac{D}{r} \frac{\partial^2 r\,N_a}{\partial r^2} \simeq 0 \quad .$$

f III.49

Rewriting and considering the boundary conditions:

$$\frac{\partial^2 N_a}{\partial r^2} + \frac{2}{r}\frac{\partial N_a}{\partial r} \simeq 0, \quad N_a\{r=r_p\}=0, \quad N_a\{r=r_\infty\} \equiv N_a \quad ,$$

f III.50

the solution is:

$$N_a\{r\} \simeq N_a \left(1 - \frac{r_p}{r}\right) \quad .$$

f III.51

The derivation at $r=r_p$ yields:

$$\left(\frac{\partial N_a}{\partial r}\right)_{r_p} \simeq \frac{N_a}{r_p} \quad .$$

f III.52

III.2.3 Relationship between the diffusion coefficient and the mean free path of a gas molecule

Diffusional growth takes place when the impinging molecule is much smaller than the liquid particle. It may thus be regarded as a sphere of infinite radius whose surface is constantly hit by gas particles. Although this flow is statistically radially directed, on the molecular scale the trajectory of the single gas molecule follows from its previous encounter of another particle. The mean distance between two successive encounters is denoted by the mean free path. Making the assumption that the gas medium is isotropic with respect to this quantity, the flux per unit surface of impinging particles at velocity v and incident angle ψ becomes (von Schilling, 1972):

$$d\frac{d\phi_m}{dS} = \frac{2\pi}{4\pi} N\{r\} f\{v\} v \sin\psi \cos\psi \, dv \, d\psi \quad ,$$

f III.53

where $N\{r\}$ is the number concentration of the gas molecules as a function of the distance between these and the particle at the preceding collision, and $f\{v\}$ indicates the velocity distribution function of the molecules. Note that the flux is assumed to be rotation symmetrical.

The distance r of the incident flux at angle ψ is given for the isotropic case by:

$$r = -\lambda \sin\psi \quad ,$$

f III.54

where λ is the mean free path of the molecules.

A Taylor expansion of the right hand side of Equation III.53 leads upon integration to the disappearance of the first term. Assuming a linear function at particle surface of the

75

condensing species concentration with distance r, the second term of the expansion combined with the preceding equation leads to:

$$\frac{d\,\phi_m}{d\,S}=-0.5\int_0^\infty\int_{-\frac{\pi}{2}}^{\frac{\pi}{2}}\lambda\sin\psi\,\frac{d\,N}{d\,r}\Big|_{r_0}f(v)\,v\cos\psi\sin\psi\,d\,v\,d\,\psi$$

<div align="right">

f III.55
</div>

Upon integration one finds:

$$\frac{d\,\phi_m}{d\,S}=-\frac{\lambda\,\bar{v}}{3}\frac{\partial\,N}{\partial\,r}$$

<div align="center">

f III.56
</div>

If this equation is compared to the diffusion law:

$$\frac{d\,\phi_m}{dS}=-D\frac{\partial\,N}{\partial\,r},$$

<div align="center">

f III.57
</div>

one finds that:

$$D=\frac{\lambda\,\bar{v}}{3}.$$

<div align="center">

f III.58
</div>

It should be stressed that this formula is obtained with a certain number of simplifications, the most important among which are the isotropy of the medium concerning the mean free path and the linear approximation to the impinging species' concentration gradient. In the above formula both the diffusion coefficient and the mean free path are unknowns at first hand.

In this context the Knudsen number may be defined, which stands for the ratio of the mean free path to the particle radius. It is:

$$Kn=\frac{\lambda}{r}.$$

<div align="center">

f III.59
</div>

Consistently to the above considerations a particle whose radius is large relative to the mean free path of the condensing species may be regarded to grow through condensation in the diffusion regime, while in the opposite case condensation takes place in the molecular regime.

III.2.4 The diffusion coefficient

Chapman and Cowling (1939) give the following expression for the binary diffusion coefficient in a gas phase:

$$D_{ab} = \frac{30}{3.2\, N\, \sigma_{ab}^2} \left(\frac{8\, R\, T}{\pi} \left(m_a^{-1} + m_b^{-1} \right) \right)^{0.5} ,$$

f III.60

where σ_{ab} is the mean effective collision diameter of the gas molecules of the diffusive medium a (air in this study) and the diffusing species b (sulphuric acid), which is defined by:

$$\sigma_{ab}^2 = 0.5 \left(\sigma_a^2 + \sigma_b^2 \right) ,$$

f III.61

and N is the concentration of both species which is assumed to be linked to the total pressure by the ideal gas law.

Chapman and Cowling's formula relies on the so-called hard shell model of particle encounter. Collisions limit the diffusivity of the medium, and the collision rate in the medium increases with the collision cross-section, which is classically not regarded to be a temperature function. In practice, however, particles are said to become softer with increasing temperature so that their effective diameter diminishes. It is this stronger temperature dependence of the diffusion constant that Fuller et al. (1966) have allowed for when they suggested the following ansatz to the binary diffusion constant:

$$D_{ab} = \frac{C\, T^b \left(m_a^{-1} + m_b^{-1} \right)^{0.5}}{p \left(\left(\sum_A \upsilon_i \right)^{a1} + \left(\sum_B \upsilon_i \right)^{a2} \right)^{a3}} ,$$

f III.62

where υ_i are the so-called special atomic diffusion volumes, that is the virtual volumes characterising the species' diffusional behaviour.

Numerical regression converges well when the values ensuing from Equation III.60 are assumed for the coefficients $a1$ to $a3$, that is $a1=1/3$, $a2=1/3$ and $a3=2$. In this case the regression results are the following for the remaining parameters:

$$C = 10^{-7.5}$$
$$b = 1.75 \quad ,$$

f III.63

with the special atomic diffusion volumes for sulphuric acid, water vapour as well as for dry air:

$$\upsilon_{air} = 20.1 \cdot 10^{-6}$$
$$\upsilon_{H_2SO_4} \simeq 56.02 \cdot 10^{-6}$$
$$\upsilon_{H_2O} \simeq 12.7 \cdot 10^{-6}$$

f III.64

It is useful to point out that the special atomic diffusion volume is specific to this formula. It is not an evaluation of the actual molal volume of these molecules. Here, the atomic diffusion volume of sulphuric acid is approximated roughly by the sum of the volume of sulfur dioxide and twice the volume increments of atomic hydrogen and oxygen, respectively (Fuller et al., 1966).
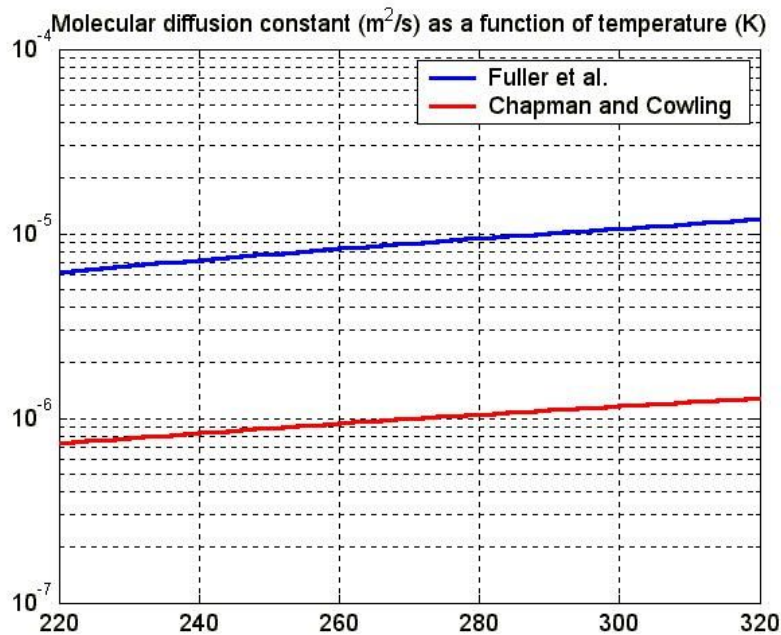
Figure III.4: Temperature dependence of the binary diffusion coefficients of Chapman and Cowling (1990) and of Fuller et al. (1966).

Figure III.4 depicts the temperature dependence of the molecular binary diffusion coefficient according to the hard-shell assumtpion of Chapman and Cowling (1990) and the soft shell ansatz of Fuller et al. (1966). The semi-empirical formalism of the latter makes the diffusion coefficient approximately one order of magnitude larger under typical atmospheric conditions.

III.2.5 The enhancement factor and its potential incidence on nucleation

There have been two major approaches to quantify the Brownian condensation enhancement factor. Consistently with the free molecular regime both methods rely on the consideration of the encounter trajectory of two particles moving freely in a vacuum. Velocity is defined relative to the centre of one particle, which remains fixed relative to the observer. The impact parameter is thus defined according to Figure III.5 as the distance between the moving particle's trajectory line at infinite and a parallel going through the fixed particle's centre. The critical impact parameter stands for the limiting value beyond which the encounter does not imply collision any longer.
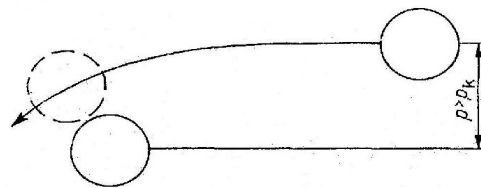
Figure III.5: Definition of the critical impact parameter p_k as the limiting trajectory leading to tangential particle encounter. Adapted from von Schilling (1972).

Hoppel and Frick (1986) determined the critical impact parameter according to the Maxwell-Boltzmann distribution of the particle velocity, and thus introduce the concept of the mean critical impact parameter, which due to non-linearities is different from the critical impact parameter at mean velocity. Their simple consideration of particle charge may be applied to both ions and dipoles but does not consider the polarizability of the condensing species. Nadykto and Yu (2003) suggested a new formalism taking into account this specific feature of dipoles such as water and sulphuric acid. On the other hand, their method does not account for

velocity distribution caused non-linearities.

Von Schilling (1972) demonstrates how the impact parameter is modified as a function of an attraction force, through the action of which the moving particle rotates around the fixed particle. According to Kepler's second law the following relationship has to hold:

$$0.5 \, r \otimes \frac{d \, r}{d \, t} = const$$

f III.65

Note that the above equation involves a vectorial product and that the origin of the coordinate system is at the centre of the fixed particle thus defining the position vector **r**.

Von Schilling shows that if one compares the value of the latter equation at an infinite and at a general position, one finds the following relationship:

$$r^2 \, \frac{d \phi}{dt} = pv$$

f III.66

where $d\varphi/dt$ is the angular velocity of the particle, and r is the length of the vector of position (in this particular case).

In addition according to Newton's energy conservation law the following relationship is valid:

$$0.5 \mu \left(\left(\frac{dr}{dt} \right)^2 + r^2 \left(\frac{d \phi}{dt} \right)^2 \right) + E_{pot}\{r\} = 0.5 \mu v^2$$

f III.67

where μ is the reduced mass of the two particles, and E_{pot} is the potential energy according to the considered force of attraction.

The reduced mass is given by:

$$\mu = \left(M_p^{-1} + M_m^{-1} \right)^{-1}$$

f III.68

where M_p is the mass of the fixed particle and M_m is the mass of the moving gas molecule.

When the angular velocity is replaced by the relationship given in Equation III.66 and the above equation s solved for critical p under the condition that $dr/dt=0$ for $r \equiv r_p + r_m$, one finds:

$$p_k = (r_p + r_m) \sqrt{1 - 2 \, \frac{E_{pot}\{r_p + r_m\}}{\mu v^2}} \quad .$$

With the following transformation, considering the mean square velocity as well as Equations III.42 and III.68:

$$\mu \overline{v^2} = \mu (\overline{v_p^2} + \overline{v_m^2}) = \frac{M_p M_m}{M_p + M_m} \frac{3}{2} kT \left(\frac{2}{M_p} + \frac{2}{M_m} \right) = 3 \, kT \quad ,$$

finally:

$$p_k = (r_p + r_m) \sqrt{1 - \frac{2}{3} \, \frac{E_{pot}\{r_p + r_m\}}{kT}} \quad ,$$

where p_k is the critical impact parameter.

It should be noted that the inner square root ratio is equal to the ratio of the potential energy at minimum distance to the kinetic energy at infinite distance.

Through inspection one finds that $p_k^2 = E_B (r_p + r_m)^2$, and thus:

$$E_B = 1 - \frac{2}{3} \, \frac{E_{pot}\{r_p + r_m\}}{kT} \quad .$$

The formalism that has led to the preceding equation is specific to the molecular regime. The aerosol particle's radius has to be much smaller than the condensing molecule's mean free path, so that it may be considered to originate from infinite distance. The determination of the enhancement factor in the diffusion regime is more complex. An inherent property of the diffusion flux is that if considered at the molecular scale it has to be expressed differentially at a certain angle of incidence relative to the particle's surface (see above). Relative to this angle the modification of the flux through the attraction force has to be formulated. However, considering Equation III.72 it may be inferred that the enhancement factor due to ion dipole interaction may rapidly become negligible with increasing particle radius (see Figure III.6 for confirmation) so that it may be assumed that:

$$E_D \simeq 1$$

f III.73

The potential energy of a dipole in an electrical field is (Nadykto and Yu, 2003; Loeb, 1955):

$$E_{pot} = -L E \left(\frac{e^z + e^{-z}}{e^z - e^{-z}} - z^{-1} \right) - 0.5 \alpha \epsilon_0 E^2$$,

f III.74

where:

$$E = \left(1 - \frac{1}{\epsilon_r} \right) \frac{q}{4 \pi \epsilon_0 r^2}$$,

f III.75

and:

$$z = \frac{L E}{kT}$$,

f III.76

with L being the dipole moment of the impinging gas molecule, E the electric field generated by the charged particle, and α the polarizability of the dipole.

In Equation III.74 the first term basically stands for the electric force of attraction due to the charge of the ion and the partial charge of the dipole, while the second term stands for the induced electric force due to the dipole's tendency to increase its partial charge under the influence of an electric field. The polarizability of a dipole is specific to its chemical nature. The third factor of the first term is the Langevin function which expresses the dipole's mean orientation in the electrical field.

Nadykto and Yu (2003) provide the following data:

$$L_{H_2SO4} = 2.84 \ D$$
$$L_{H_2O} = 1.85 \ D$$
$$\alpha_{H_2SO_4} = 6.2 \cdot 10^{-30} m^3$$,
$$\alpha_{H_2O} = 1.19 \cdot 10^{-30} m^3$$

f III.77

where the dipole moment is expressed in debye (1 D≡3.336·10⁻³⁰C m).

It follows that the interaction force between the charged particle and a sulphuric acid molecule is stronger than the corresponding force between the particle and a water molecule because of

both the dipole moment at infinite distance and the electric field induced polarisation.

Figure III.6 shows that when small particles, especially of subcritical size, are considered, the enhancement factor should not be negligible. The repercussions of the enhancement factor on the ion-induced nucleation rate therefore need to be explored. According to Equation III.30, the nucleation rate is a function of a characteristic impinging rate, that is the so-called mean condensation rate at the saddle point. The mean condensation rate is according to Equation III.15 a function of the condensation rate of sulphuric acid and of water combined with the mean growth direction. The nucleation rate is thus a special case of the Brownian molecular regime condensation flux. The exclusive dependence of the nucleation rate on the gas molecule impinging rate at the saddle point stems from the consideration that the equilibrium concentration of clusters is relatively low in the vicinity of the saddle point when compared to subcritical regions distant from this latter point (see Equation III.14). It is therefore suggested that the enhancement factor should be incorporated into Equation III.30 as part of the saddle point condensation flux, resulting in:

$$\left(J_{tot}\right)_{\pm, E} = E_B\{(r_p)_{sp}, r_i\}\left(J_{tot}\right)_{\pm}$$

f III.78

where the subscript E stands for the enhanced nucleation rate.
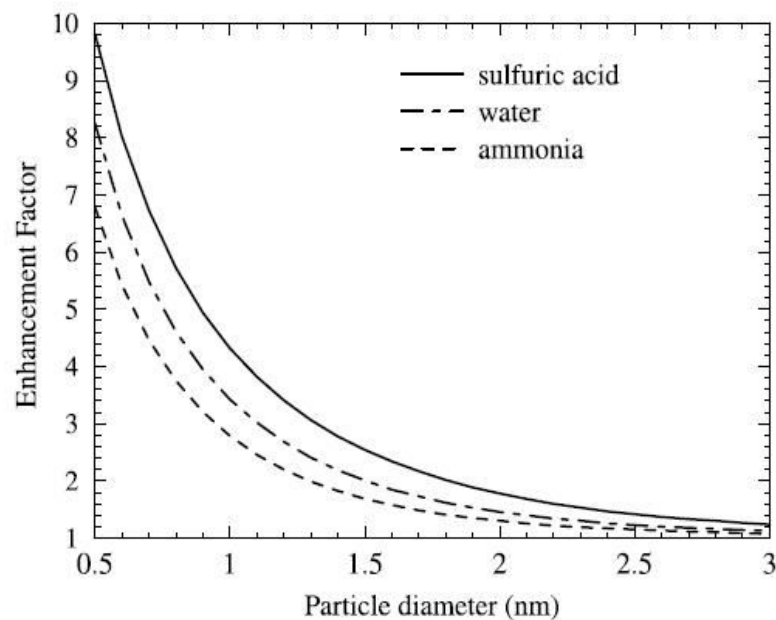
Figure III.6: Dependence of the ion-dipole enhancement factor according to Equations III.72 and III.74 as a function of the charged particle radius for three different condensing species. Adopted from Nadykto and Yu (2003).

III.2.6 Condensation in the transition regime

It appears reasonable to assume that a relevant fraction of condensation in relationship with submicron aerosol particles takes place in the transition regime, that is in between the idealisations of the free molecular and the diffusion regimes. The issue of intermediate regime condensation is in analogy to the neutron flux problem in nuclear physics, which is key for the calculation of the critical mass of a radioactive substance, or for the assessment of the disintegration rate in a nuclear reactor. Referring to the works of Davison (1951) and Sahni (1966), Smirnov (1971) has summed up the findings to this issue and has generalised these with respect to the sticking probability of condensing molecules onto aerosol particles.
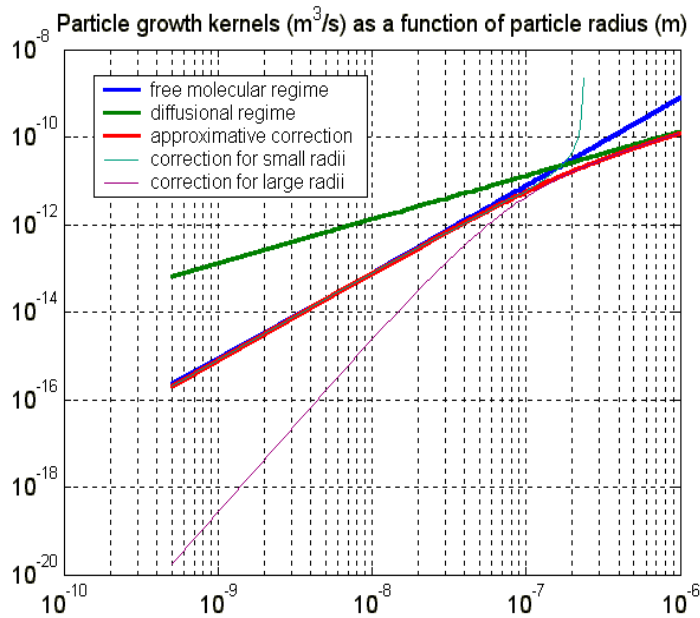
Figure III.7: Condensation kernel in the diffusional and the free molecular regime, as well as in the transition regime using the approximation formulas III.79, III.80 and III.81. Condensation enhancement as well as sticking probability are left out. Temperature is 300 K, the atmospheric pressure is 1 atm.

According to Smirnov (1971) the transition factor τ_m in relationship with aerosol particles acting as perfect absorbers ($P_{st}=1$), tends for very small particles, i.e. $Kn>>1$, to the following expression:

$$\tau_m = 4/3 - 5/9\,Kn^{-1} + 0.97827\,Kn^{-2}\ln(Kn) + \epsilon$$

f III.79

84

The corresponding value for large particles, i.e. *Kn<<1*, tends to:

$$\tau_m = 0.7104 + 0.5047\, Kn + 0.2336\, Kn + \epsilon$$

f III.80

An approximation to the transition factor appropriate for a larger Knudsen number range is (Fuchs and Sutugin, 1971):

$$\tau_m = \frac{1 + Kn}{4/3\, P_{st}^{-1}\, Kn^2 + 4/3\, P_{st}^{-1}\, Kn + 0.377\, Kn + 1}$$

f III.81

The above transition factors apply exclusively to the diffusion regime condensation kernel and not to the free molecular kernel. A common assumption to these expressions is that the impinging molecule has to be of negligible size relative to the aerosol particle. It should be stressed that these numerical expressions of the transition factor render approximate results and have to be used with caution as it is demonstrated by Figures III.7 and III.8.
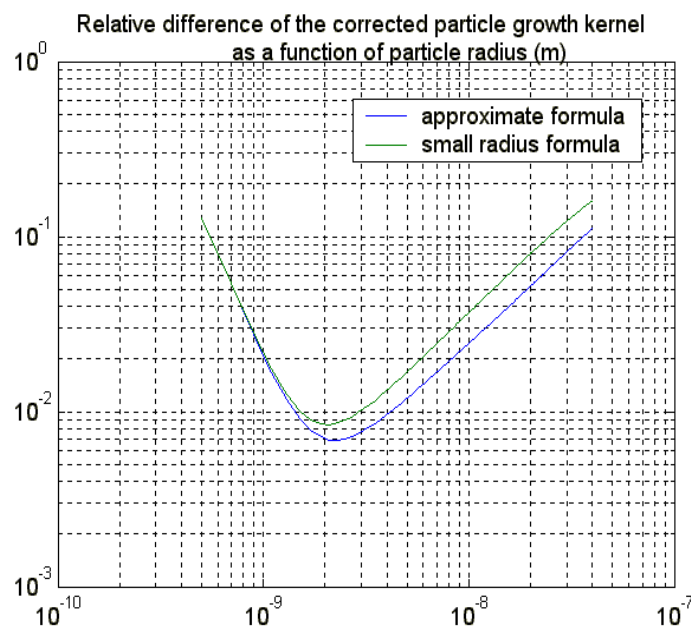
Figure III.8: Relative error of the free molecular regime condensation kernel to the values obtained using Equations III.79 and III.81, respectively. It is shown that the error value diminishes until a certain threshold radius close to 2 nm, below which it inconsistently increases again thus demonstrating the lower confidence limit of the transition factor formulas.

Figure III.7 shows assessed values of the molecular as well as the diffusion regime condensation kernel assuming unit enhancement and sticking coefficients. Results obtained

with the above approximations to the transition factor are also displayed. It clearly appears that Equations III.79 and III.80 may not be applied beyond a certain threshold value of particle size while both the approximation formulas III.81 and III.79 appear to perform quite well for nanometre particles. However, it is depicted in Figure III.8 that their performance actually hits a maximum at around two nanometres while it deteriorates again at smaller size. These findings are consistent with and should be inherent to the assumption of negligible size of the condensing species. Considering these results along with the size limit of relevant molecular regime condensation enhancement as depicted in Figure III.6, the molecular regime is therefore arbitrarily limited to particles smaller than 10 nanometres in this study, while larger particles are assumed to be in the transition regime. According to the above findings the condensation kernel in the transition regime reads in analogy to Equation III.48:

$$K_T^n\{r > 10\,nm\} = \tau_m\, 4\,\pi\, r\, D_{AB}$$

f III.82

III.3 Brownian coagulation

III.3.1 Preliminary considerations

Coagulation mechanistically differs from condensation as the impinging particles are typically several orders of magnitude larger than the condensing gas phase species, and the coagulating particles' size may be of equal order of magnitude. On the one hand particle velocity may be sensibly lowered by frequent encounters with the surrounding gas molecules, resulting in a non-negligible friction term in the motion equation, whilst on the other hand the size and velocity of each of the particles involved has to be considered when the coagulation kernel is assessed. For these reasons, both the diffusion coefficient and the transition factor have to be given a formulation specific to Brownian coagulation.

In the previous section the formulation of the condensation enhancement factor through a centripetal force relied on charge dipole interaction considerations in the free molecular regime. In the context of particle coagulation the interaction of particles bearing one or more elementary charges of equal or opposed sign may induce either intensive repulsion and attraction, so that electric interaction may not be negligible any more in the diffusion regime, and a specific formalism to the coagulation enhancement factor is requested.

III.3.2 Brownian coagulation kernel in the diffusion regime

According to Pruppacher and Klett (1996, p. 447) the motion equation of an aerosol particle subject to friction exerted by the gaseous medium is:

$$M_p \frac{d v_p}{d t} = F_f + F_B\{t\}$$

f III.83

where F_f is the frictional drag force and F_B is the Brownian motion force exerted on the particle.

Further, if it is assumed that the drag exerted on the particle is important enough for the Reynolds Number to be small, then Stokes' law may be applied (e.g. Landau and Lifshitz, 1976):

$$\boldsymbol{F}_f = -6\pi r_p \eta_a \boldsymbol{v}_p \equiv -\beta M_p \boldsymbol{v}_p ,$$

f III.84

where η_a is the dynamic viscosity of the air defined by:

$$dF_{f,\perp} = \rho_a \nu_a \, grad \, \boldsymbol{v_a} \cdot \boldsymbol{dS} \quad , \eta_a = \rho_a \nu_a ,$$

f III.85

relating that the friction force exerted perpendicularly onto a particle surface element in a fluid flow is proportional to its dynamic viscosity; ν_a being the cinematic viscosity.

The scalar product of III.83 and the position vectors combined to III.84 yields:

$$\boldsymbol{r} \cdot \frac{d \boldsymbol{v}_p}{dt} = \frac{d}{dt} \overline{\boldsymbol{r} \cdot \boldsymbol{v}_p} - \overline{\boldsymbol{v}_p^2} = -\frac{6\pi r_p \eta_a}{M} \overline{\boldsymbol{r} \cdot \boldsymbol{v}_p} + \frac{\overline{\boldsymbol{r} \cdot \boldsymbol{F}_B}}{M} .$$

f III.86

The last term on the right hand side as well as the first term within the middle expression are equal to zero as Brownian motion is isotropic, in addition, considering:

$$1/2 \, M \, \overline{\boldsymbol{v}^2} = 3/2 \, kT$$

f III.87

the above differential equation becomes:

$$1/2 \frac{d \overline{r^2}}{dt} = \overline{\boldsymbol{r} \cdot \boldsymbol{v}_p} = \frac{kT}{2\pi r_p \eta_a} .$$

f III.88

Integration leads to:

$$\overline{z^2} = \frac{\overline{r^2}}{3} = \frac{kT}{3\pi r_p \eta_a} \, t .$$

f III.89

This equation relates the mean square distance covered by a particle under the influence of Brownian motion and frictional force according to Stokes' law during the time interval t.

Now, a link between the diffusion constant and the mean square distance z is to be established. Rewriting Equation III.49 1-dimensionally and integrating over z yields:

88

$$\int_{-\infty}^{+\infty} z^2 \frac{\partial N_a}{\partial t} d z = D_p \int z^2 \frac{\partial^2 N_a}{\partial z^2} dz \quad .$$

f III.90

The first integral is solved by:

$$\int_{-\infty}^{+\infty} z^2 \frac{\partial N_a}{\partial t} d z = \frac{\partial}{\partial t} \int_{-\infty}^{+\infty} z^2 N_a d z = \frac{\partial}{\partial t} \overline{z^2} N_a^{tot} = N_a^{tot} \frac{\partial \overline{z^2}}{\partial t} \quad ,$$

f III.91

where N_a^{tot} is the total number of particles a in a z-column.

The second integral is solved through partial integration:

$$\int_{-\infty}^{+\infty} z^2 \frac{\partial^2 N_a}{\partial z^2} dz = -2 \int_{-\infty}^{+\infty} z \frac{\partial N_a}{\partial z} d z = 2 \int_{-\infty}^{+\infty} N_a dz = 2 N_a^{tot} \quad .$$

f III.92

The previous relationship was obtained assuming that the spatial particle number concentration is radially symmetrically distributed, meaning $N_a\{z\}=N_a\{-z\}$. After integration over time the following relationship is found:

$$\overline{z^2} = 2 D_p t \quad .$$

f III.93

Comparison with Equation III.89 yields for the diffusion constant:

$$D_p = \frac{kT}{6 \pi r_p \eta_a} \quad .$$

f III.94

In analogy to the previous section the coagulation kernel is:

$$K_P = 4 \pi (r_{p1} + r_{p2}) D_{p1,2} \quad .$$

f III.95

The flux of particles $p2$ onto a particle $p1$ is obtained by multiplying the coagulation kernel by the concentration of particles $p2$. The flux of particles $p1$ on a particle $p2$ is obtained by the inverse operation using the same coagulation kernel. This indicates the relative character of the Brownian coagulation kernel diffusion constant, as indicated by the subscript $p1,2$ in the previous equation. The relationship between the individual diffusion constants and the relative constant is revealed through the link between the mean displacements of the particles at time t:

$$\overline{|r_{p1} - r_{p2}|^2} = \overline{r_{p1}^2} + \overline{r_{p2}^2} - 2 \overline{r_{p1} \cdot r_{p2}} \quad .$$

f III.96

Due to the unorientated pattern of Brownian motion, the third term of the right hand side vanishes in the previous equation. Considering Equations III.89 and III.93, the left hand side is equal to $6\,D_{p1,2}$ whilst the remaining terms on the right hand side are equal to $6\,D_{p1}$ and $6\,D_{p2}$ respectively. Thus it is demonstrated that (e.g. Pruppacher and Klett, 1997):

$$D_{p1,2} = D_{p1} + D_{p2}$$
$$\textbf{f III.97}$$

Stokes' law (Equation III.84) applies to macroscopic spheres in a laminar flow. Aerosol coagulation, however, tends to take place on the sub-micrometre scale, for which the drag is a function of particle size. For this reason the macroscale particle diffusion coefficient is corrected for the decreasing drag with decreasing size with the so-called Cunningham slip flow correction factor. The following semi-empirical formula is assumed to relate the shape of the Cunningham factor (Pruppacher and Klett, 1997):

$$C = (1 + A\,Kn), \quad A = a + b\,e^{-\frac{c}{Kn}}$$
$$\textbf{f III.98}$$

Pruppacher and Klett indicate the following values of the empirical parameters to be appropriate:

$$a = 1.257 \; ; \; b = 0.400 \; ; \; c = 1.10$$
$$\textbf{f III.99}$$

The Knudsen number in Equation III.80 stands for the ratio of the typical mean free path of the gaseous constiturents of the air to the radius of the considered aerosol particle. The characteristic atmospheric mean free path may be evaluated considering a pure gas of virtual mean air molecules with specific viscosity. An approximation of this value is given in Jacobson (1999):

$$\lambda_m = \frac{2\,\eta_a}{\rho_a v_m},$$
$$\textbf{f III.100}$$

where λ_m and v_m are the mean free path and Brownian motion velocity of a virtual air molecule, respectively. The mean velocity of a gaseous molecule is given by Equation III.42. The dynamic viscosity of air is according to Jacobson (1999, p.92):

$$\eta_a = 1.8325\text{e-5}\left(\frac{416.16}{T+120}\right)\left(\frac{T}{296.16}\right)^{1.5}$$
$$\textbf{f III.101}$$

III.3.3 Brownian coagulation transition factor

Davison (1951) has formulated analytical solutions to the transitory problem between the free molecular regime and the diffusional regime at the extrema of negligibly small particles impinging onto large particles and the interaction of particles of equal size. Coagulation of aerosol particles in the atmosphere, however, may not be associated to a monodisperse situation, as aerosols typically show a broad multimodal size spectrum. It is N.A. Fuchs who in his comprehensive work *'The Mechanics of Aerosols'* (1964) has established a conceptual expression to the monodisperse situation that may easily be extended to aerosols of unequal size.

In analogy to the determination of a simple link between the mean free path and the diffusion constant Fuchs looks at the collision process as one impinging particle $p1$ moving towards a fixed particle $p2$ of radius $r_{p1}+r_{p2}$. The main implicit idea of Fuchs' consideration of coagulation in the transition regime is that the flux of impinging particles may be subdivided into an area of statistically radial diffusion flux and an area of free molecular flux. The separation surface between these two areas constitutes a virtual sphere of radius equal to the fixed particle radius plus a geometric weighing function of the impinging particle mean free path $f\{\lambda_{p1,2}\}$, which reflects that the moving particles collide at a certain angle. Adapting Equation III.51 to the limiting condition that at the surface of the virtual sphere $N_{p2}\{r_{p1}+r_{p2}+f\{\lambda_{p1,2}\}\}=N'_{p2}$, the diffusion particle flux of $p2$ particles onto this surface is:

$$\phi_{D,p2\rightarrow S}=4\pi(r_{p1}+r_{p2}+f\{\lambda_{p1,2}\})D_{p1,2}\ (N_{p2}-N'_{p2})$$

.

f III.102

In the free molecular regime the number of particles $p1$ impinging on particles $p2$ would be:

$$\phi_{B,p2\rightarrow p1}^{S}\simeq\pi(r_{p1}+r_{p2})^2 v_{p1,2} N'_{p2}$$

,

f III.103

where $v_{p1,2}$ is assessed according to Equations III.42 and III.43.

Note that the molecular flux is not proportional to N_{p2} due to the influence of the fixed particle on the particle number concentration field. Fuchs (1964) stated that in thermodynamic equilibrium this quantity would be equal to the quantity of 'evaporating' $p2$ particles. Therefore the fluxes in the previous two equations may be assumed to be equal. It may also be observed that the virtual sphere resulting from the sum of $r_{p1,2}$ and $f\{\lambda_{p1,2}\}$ separates the area in which the particle flux onto the fixed particle takes place in the transition regime from the

area in the molecular regime (e.g. Hoppel and Frick, 1986). This view does not presuppose equilibrium between detachment and attachment but still relies on the supposition about the existence of a constant diffusion flux onto the surface of the virtual sphere around a particle in the transition regime.

To solve Equations III.102 and III.103 a link among the diffusion constant, the mean relative velocity and the relative mean free path of an aerosol particle subject to friction force needs to established. According to the Einstein relation (Pruppacher and Klett, 1997, p. 451):

$$D_p = \frac{kT}{M_p} \, t_{\lambda p} \quad .$$

f III.104

As the previous equation and Equation III.94 have to be equivalent, the following relationship has to hold, using the definition of Equation III.84:

$$\beta = 1/t_{\lambda p}$$

f III.105 ,

where $t_{\lambda p}$ is the time needed for a particle to cover a distance equivalent to its mean free path. With Equation III.42 one finds:

$$\lambda_p v_p = t_{\lambda_p} v_p^2 = \frac{8}{\pi} D_p \quad .$$

f III.106

This formula allows evaluating the individual as well as the relative mean free path of the concerned aerosol particles. It slightly differs from the expression of Equation III.58, which is based on the consideration of infinitely small impinging particles moving without frictional force.

Replacing the mean relative velocity through this previous equation and isolating N'_{p2} assuming equality of Equations III.102 and III.103 leads to:

$$N'_{p2} = \frac{4\pi(r_{p1}+r_{p2}+f\{\lambda_{p1,2}\})}{\dfrac{8(r_{p1}+r_{p2})^2}{\lambda_{p1,2}}+4\pi(r_{p1}+r_{p2}+f\{\lambda_{p1,2}\})} \, N_{p2} \quad .$$

f III.107

Inserting this result into Equation III.103 finally yields:

$$\phi_{p2 \to p1} = \frac{4\pi(r_{p1}+r_{p2})(D_{p1}+D_{p2})}{\dfrac{(r_{p1}+r_{p2})}{(r_{p1}+r_{p2})+f\{\lambda_{p1,2}\}}+\dfrac{4(D_{p1}+D_{p2})}{(r_{p1}+r_{p2})\sqrt{v_{p1}^2+v_{p2}^2}}} N_{p2} \qquad .$$

<div align="right">**f III.108**</div>

It is important to note that this formula consistently reduces to the diffusion case when one particle is large while the other one is fast so that the relative mean free path is small, or alternatively when both particles are very large. It may also reduce to the free molecular case when the mean free path is large relative to the particle radii. Beyond its values at the extrema of particle size, it may however lack from its basic assumptions and therefore give approximate values only.

Fuchs (1964, p. 291) gives the solution of the function $f\{\lambda_{pi}\}$ for a particle impinging onto a fixed particle:

$$f\{\lambda_{pi}\} = \frac{(r_{p1,2}+\lambda_{pi})^3 - (r_{p1,2}^2+\lambda_{pi})^{1.5}}{3 r_{p1,2}\lambda_{pi}} - r_{p1,2} \quad ,$$

<div align="center">**f III.109**</div>

where i designates the impinging particle.

As a first approximation to the mean *relative* distance covered Fuchs assumes the following formula to be appropriate

$$f\{\lambda_{p1,2}\} \simeq \sqrt{(f\{\lambda_{p1}\})^2 + (f\{\lambda_{p2}\})^2} \qquad .$$

<div align="center">**f III.110**</div>

III.3.4 Brownian coagulation enhancement factor

3.4.1 Introduction

Charge enhanced coagulation of aerosol particles is equally subject to the transition from the free molecular to the diffusion regime as a function of particle size. As a prerequisite, the electrostatic interaction needs to be accurately formulated. While the interaction of a charged and a polarized particle is relatively easy to represent due to the weak electric forces engaged, the interaction of fully charged particle is much stronger and more complicate due to the presence of relevant image forces: Attraction is dynamically enhanced, repulsion is weakened, and the resulting trajectory of particle encounter in the presence of strong electric force shows

a more complex pattern.

Thus the critical trajectory, separating encounter from non-encounter trajectories, is not related any more to the sum of the particle radii, but may show a larger critical apsidal distance (see Figure III.9). Closer trajectories, although having no apse, result in a spiralling collision movement, so that the effective collision cross-section is effectively enlarged. In case of charge dipole interaction the attraction force is so weak that the theoretical spiralling solutions lie within the charged particle.
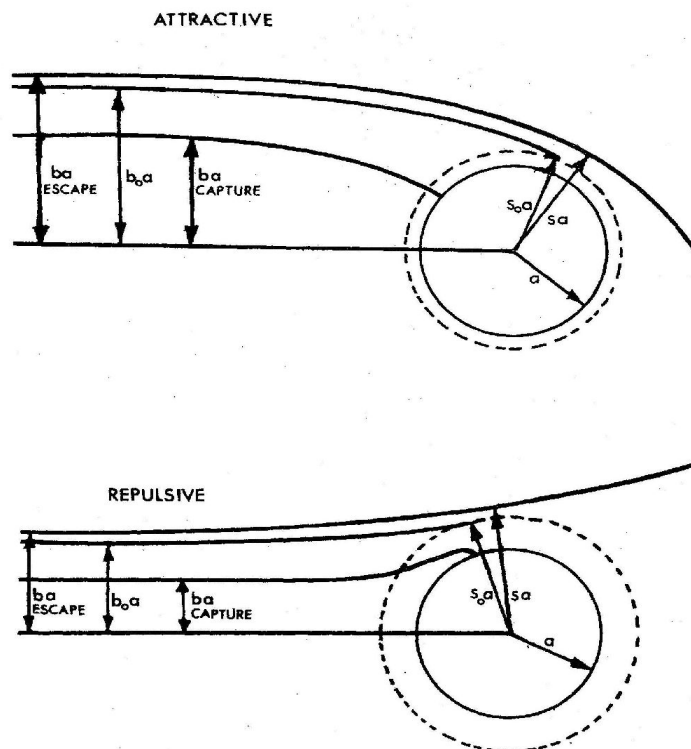
Figure III.9: Charged particle trajectories and the critical apsidal distance in the presence of image forces. Note that in case of attraction the critical apsidal distance is shorter due to image charges. In the repulsive case the image charge may induce spiralling collision as indicated through the trajectory ba. *Adopted from Hoppel and Frick (1986).*

Hoppel (1977), and Hoppel and Frick (1986) give a theoretical development and numerical assessment of this phenomenon for the case of ion uptake through aerosols. The collision enhancement factor is a function of the relative velocity of the particles, so that when considering particle interaction at mean relative velocity, the enhancement factor should be weighed over the velocity spectrum. If the coagulating particles are of molecular size, the influence of the surrounding charged particles is relevant to the effective collision cross-

section. This issue is addressed in the three body-trapping theory (see Hoppel, 1977), which describes ion-ion recombination as well as ion attachment onto an aerosol particle. The state of the art assessment of the enhancement factor is a rather complex task, the tackling of which would merit a whole study on its own. In order to keep the model of aerosol growth and aerosol cloud interaction within reasonable limits of computational expense consistent simplifications have to be found.

3.4.2 Free molecular regime enhancement factor

The charge enhanced Brownian coagulation kernel of aerosols in the molecular regime is:

$$K_{PB} = E_{PB} \pi r_{a,k}^2 v_{pl,2} \quad,$$

f III.111

where E_{PB} is the enhancement factor defined by (Hoppel and Frick, 1986):

$$E_{PB} = r_{a,k}^{-2} v_{pl,2}^{-1} \int_0^\infty v_{pl,2} \left(p_k \{ r_{a,k} \} \right)^2 F_B \{ v_{pl,2} \} dv_{pl,2} \quad,$$

f III.112

and p_k is the critical impact parameter defined by Equation III.69, while $r_{a,k}$ is the critical apsidal distance. F_B is the Maxwell-Boltzmann velocity density function of Brownian movement.

The potential between two particles due to electrodynamic interaction involving image charges is at the apsidal distance r_a (Hoppel and Frick, 1986):

$$\psi \{ r_a \} = (4 \pi \epsilon_0)^{-1} \left(\frac{q_1 q_2}{r_a} - \frac{e^2 (r_1 + r_2)^3}{2 r_a^2 (r_a^2 - (r_1 + r_2)^2)} \right) \quad.$$

f III.113

The first term on the right hand side of the previous equation stands for the direct electrostatic field while the second term represents the image force.

The impact parameter may be normalised by the sum of the particle radii. Replacing in III.69 the potential energy function through the previous expression and defining:

$$s \equiv \frac{r_a}{(r_1 + r_2)} \quad,$$

f III.114

leads to:

$$P=\sqrt{s^2-(4\pi\epsilon_0)^{-1}\frac{2q_1q_2}{(r_1+r_2)\mu v_{pl,2}^2}s+(4\pi\epsilon_0)^{-1}\frac{e^2}{(r_1+r_2)\mu v_{pl,2}^2}(s^2-1)^{-1}} \quad ,$$

<div align="right">**f III.115**</div>

where P is the normalised impact parameter.

The derivation $dP/ds=0$ of the previous expression yields an equation of the fifth degree, the solution of which permits to determine the critical apsidal distance.

A special case arises when the image charge is neglected. Under this circumstance the solution of the equation $dP/ds=0$ does not yield a physical solution any longer and the critical apsidal distance may be assimilated with the sum of the particle radii, so that the critical impact parameter is exclusively a velocity function via the kinetic energy of the particles. Thus, the spectrally weighed critical impact parameter without image charge contribution reads (Hoppel, 1977):

$$E_{PB}=1-(4\pi\epsilon_0)^{-1}\frac{q_1q_2}{(r_1+r_2)kT} \quad .$$

<div align="right">**f III.116**</div>

This expression suggests that the enhancement factor has to be inferior to unity in case of particles charged equally in sign. A negative enhancement factor stands for the impossibility of collision because of mutual repulsion. Numerical evaluation of the enhancement factor taking into account the image force (Hoppel, 1977) indicates however that the enhancement factor of particles charged equally in sign might be superior to unity when the image force becomes dominant, that is in case of ion-ultrafine aerosol coagulation. More precise estimations of Hoppel and Frick (1986), however, including three-body trapping, lead to values well below unity.

Nevertheless, the image force has a relevant influence on the critical impact parameter, the assessment of which is complicated further by integration over the Maxwell-Boltzmann velocity spectrum. A simple solution to avoid iterative evaluation is to assimilate the critical apsidal distance with the sum of the aerosol radii and to rely on a semi-empirical formula of the potential energy between two particles in an electric field given by Fuchs (1964, p. 307):

$$\psi\{\infty,r_{1,2}\}=(4\pi\epsilon_0)^{-1}\left(\frac{q_1q_2}{(r_1+r_2)}(1+\frac{15}{448}+\epsilon)-\frac{q_1^2+q_2^2}{r_1+r_2}(\frac{1}{16}+\frac{1}{64}+\frac{1}{256}+\epsilon)\right) \quad .$$

<div align="right">**f III.117**</div>

This formula and Equation III.113 are partially in formal analogy.

When the expression of Equation III.116 is compared to Equation III.72 of the enhancement

factor through dipole-ion attraction in the free molecular regime, for which no integration over the velocity distribution has been effected, one finds that this integration is equivalent to replacing the mean kinetic energy 2/3 kT through kT, meaning that the faster velocities of the distribution have more weight to the enhancement factor. Still assimilating the critical apsidal distance to the particle radii sum, the following formula for the ion-induced aerosol-aerosol enhancement factor in the free molecular regime may thus be retained:

$$E_{PB}\{\infty, r_{1,2}\} = 1 - \frac{1.00335\, q_1 q_2 - 0.08203125\,(q_1^2 + q_2^2)}{4\pi\,\epsilon_0 (r_1 + r_2)\, kT} .$$

f III.118

Although the repulsion force effect is lowered to a certain degree thus testifying for the image charge as discussed previously, the above formula may produce negative values. In principle, this result is consistent, showing that particles moving at mean Brownian relative velocity of given respective charge may not be able to collide. Statistically, however, this result is not appropriate since collisions due to particles moving much faster than mean velocity are thus not taken into account. In order to allow for this effect Laakso et al. (2001) used the following conceptual formula in case of repulsion that is supposed to reflect the probability of high velocity encounters:

$$E_{PB}\{\infty, r_{1,2}\} = e^{-\frac{\psi\{\infty, r_{1,2}\}}{kT}} .$$

f III.119

3.4.3 Diffusion regime enhancement factor

Fuchs (1964, p. 305 ff.) derived a formula for the assessment of the coagulation enhancement factor in the diffusion regime in the presence of a centripetal attraction force under certain simplifying assumptions. The main steps leading to his formula are reproduced here. The Fokker-Planck equation describes conjoint diffusion and action of an ordered centripedal force:

$$\frac{\partial N_p}{\partial t} = -div(N_p V_p) + D_{p1,2}\, div(grad(N_p)) ,$$

f III.120

where V_p is the ordered part of the velocity of the particles.
The acceleration of the particles is:

$$\frac{dV_p}{dt} = -\beta V_p + \frac{F}{M_p} \quad ,$$

f III.121

where F is the centripetal force and β is defined in Equation III.84.

If both the concentration and the ordered part of the velocity of the particles are assumed to be constant, the following relation has to hold:

$$D_{p1,2} \, div(grad(N_p)) = \frac{div(F N_p)}{\beta M_p} \quad ,$$

f III.122

or in spherical polar coordinates after integration over the radial component r:

$$4\pi \left(D_{p1,2} r^2 \frac{\partial N_p}{\partial r} - r^2 \frac{F N_p}{\beta M} \right) = const = \phi_p \quad .$$

f III.123

In literature this equation is known as the steady state diffusion-mobility equation (e.g. Hoppel and Frick, 1986).

Replacing $D_p \beta m = kT$ (Eq. III.104), the special solution of the previous heterogeneous first order second degree linear differential equation with boundary conditions $N_p\{r_{p1,2}\}=0$ and $N_p\{r \rightarrow \infty\}=N_p$ reads:

$$N_p = \frac{\phi_p}{4\pi D_{p1,2}} \int_\infty^{r_{p1,2}} -r^{-2} \exp\left(-\frac{1}{kT} \int_\infty^r F\{r\} dr \right) dr \quad .$$

f III.124

Defining the inner integral $\psi\{r\}$, one gets after integration variable transformation $x \equiv r_{p1,2}/r$ and isolation of the particle flux:

$$\Phi_p = \frac{4\pi D_{p1,2} r_{p1,2} N_p}{\int_0^1 \exp\left(\frac{\psi\{r_{p1,2}, x\}}{kT} \right) dx} \equiv E_{PD} 4\pi D_{p1,2} r_{p1,2} N_p \quad .$$

f III.125

Still according to Fuchs (1963):

$$\psi\{r_{p1,2}, x\} = (4\pi\epsilon_0)^{-1} \left(\frac{q_1 q_2}{(r_1+r_2)}\left(x + \frac{15}{448}x^7 + \epsilon\right) - \frac{q_1^2 + q_2^2}{(r_1+r_2)}\left(\frac{1}{16}x^4 + \frac{1}{64}x^6 + \frac{1}{256}x^8 + \epsilon\right) \right) \quad .$$

f III.126

When charge interaction is neglected with respect to the preceding formula, Equation III.109 may be solved analytically.

The solution is for *abs(q₁q₂)=q₁q₂*:

$$E_{PD} = \frac{\dfrac{q_1 q_2}{4\pi\epsilon_0 r_{p1,2} kT}}{\exp\left(\dfrac{q_1 q_2}{4\pi\epsilon_0 r_{p1,2} kT}\right) - 1} \quad .$$

<div align="right">**f III.127**</div>

For *abs(q₁q₂)=-q₁q₂* one finds:

$$E_{PD} = \frac{\dfrac{|q_1 q_2|}{4\pi\epsilon_0 r_{p1,2} kT}}{1 - \exp\left(\dfrac{-|q_1 q_2|}{4\pi\epsilon_0 r_{p1,2} kT}\right)} \quad .$$

<div align="right">**f III.128**</div>

Still according to Fuchs (1964) the error committed using these approximate equations in the diffusion regime is of the order of magnitude of 1% if both the impinged and the impinging particles are elementarily charged. If one particle bears twice the elementary charge the error is still of the order of 5 %. The steady state assumption, that has lead to the present estimation formula of the diffusion enhancement coefficient, is consistent with the assumptions made in the previous subsections for the coagulation kernels in the diffusion and the transition regimes. In the diffusion regime particles show a mean radial movement, which is strengthened through the presence of electrostatic interaction, thus showing the formal compatibility of these processes.

3.4.4 Enhanced coagulation kernel in the transition regime

In analogy to the coagulation kernel in the transition regime (see above), the enhanced version is derived via the concept that particles show purely diffusive behaviour until they reach a distance related to their mean free path. From this point on their behaviour is evaluated according to the free molecular formalism, so that in the charge enhanced case the considerations set forth in section 3.4.2 apply. This leads to the following relationship (c.f. Equations III.102 and III.103):

$$E_{PD}\{\Delta\} 4\pi D_{12}\Delta\left(N_{p2}\{\infty\} - N_{p2}\{\Delta\}\right) = 4\pi\Delta^2 \frac{v_{p1,2}}{4} \frac{r_{a,k}^2 E_{PB}\{\Delta, r_{a,k}\}}{\Delta^2} N_{p2}\{\Delta\} \quad ,$$

<div align="right">**f III.129**</div>

where the distance Δ is defined by:

$$\Delta = r_{a,k} + f\{\lambda_{p1,2}, r_{a,k}\}$$

f III.130

The factor 1/4 in the relationship III.129 stands for the probability for the impinging particle to cross the surface defined by the virtual Δ-sphere, while the ratio r_a^2/Δ^2 stands for the fraction of particles penetrating the Δ sphere that actually reaches the p1 particle. Since the critical apsidal distance has been chosen to corespond to the radius $r_{p1,2}$, the transition regime enhancement factor has to be expressed in consequence.

Assuming that the limiting sphere radius may be considered to be large relative to $r_{p1,2}$, the molecular regime enhancement factor relative to the virtual sphere surface is:

$$E_{PB}\{r_{p1,2}, \Delta\} = 1 - \frac{\psi\{r_{p1,2}\} - \psi\{\Delta\}}{kT},$$

f III.131

where $\psi\{\Delta\}$ is given by III.126.

Proceeding in analogy to the calculations leading to Equation III.108, one finds the following expression:

$$\Phi_{p2 \to p1} = \frac{4\pi(r_{p1} + r_{p2})(D_{p1} + D_{p2})}{\dfrac{1}{E_{PD}\{\Delta'\}} \dfrac{(r_{p1} + r_{p2})}{\Delta'} + \dfrac{1}{E_{PB}\{r_{p1,2}, \Delta'\}} \dfrac{4(D_{p1} + D_{p2})}{(r_{p1} + r_{p2})\sqrt{v_{p1}^2 + v_{p2}^2}}} N_{p2}.$$

f III.132

The limiting sphere radius Δ' under the approximation that $r_{a,k} = r_1 + r_2$ is:

$$\Delta' = r_{p1,2} + f\{\lambda_{p1,2}, r_{p1,2}\}$$

f III.133

3.4.5 Special case of ion attachment

In principle Equation III.132 is also valid for the assessment of the flux of ions onto an aerosol particle. However, the characteristic equation of ion displacement in the atmosphere is not determined by Brownian movement and friction force but tends to be dominated by electrostatic interaction with the surrounding ions. Thus, one finds in analogy to Equation III.86:

$$-\langle \boldsymbol{v}_{ion}^2 \rangle = -\frac{\beta + \dfrac{q}{\mu_{ion}}}{M_{ion}} \langle \boldsymbol{r} \cdot \boldsymbol{v}_{ion} \rangle + \frac{\langle (\boldsymbol{F}_e + \boldsymbol{F}_B) \cdot \boldsymbol{r} \rangle}{M} \cong -\frac{q}{\mu_{ion} M_{ion}} \langle \boldsymbol{r} \cdot \boldsymbol{v}_{ion} \rangle \quad ,$$

f III.134

where F_e is the electrostatic force and μ_{ion} is the ion mobility, which in the absence of friction force is defined by (Feynman, 1963, p. 43-6):

$$M_{ion} \frac{d\,v_{ion}}{dt} = -\frac{q_{ion}}{\mu_{ion}} v_{ion} + F = 0 \quad ,$$

f III.135

where v_{ion} is the so-called drift velocity of the ion. According to Mohnen (1977) the characteristic mobilities of atmospheric anions and cations are 1.24 and $1.14 \cdot 10^{-4}$ $m^2 V^{-1} s^{-1}$, respectively.

It is noteworthy that the ion mobility term in Equations III.134 and III.135 stands for the decelerating interaction of the ion with the surrounding charged particles, which is formally equivalent to a friction force. It is clear that this term is also proportional to the ion velocity since the number of charged particles the ion interacts with per time increment increases with its velocity. The accelerating terms of Brownian motion and electrostatic forces stand for the dominating local interaction process with a single distinct particle. Due to their fortuitous character the driving forces are not correlated with the position vector.

Together with Equation III.87 and Equation III.93 one finds in analogy:

$$D_{ion} = \frac{\mu_{ion}}{q} kT \quad .$$

f III.136

Through comparison of Equations III.136 with Equation III.94, it is easily seen that the diffusion coefficient of an ion tends to be much larger than the diffusion coefficient of an aerosol particle. Thus:

$$D_{ion,p} = D_p + D_{ion} \cong D_{ion} \quad .$$

f III.137

As the radius of the ion is negligible relative to the particle radius, the flux of ions onto an aerosol particle becomes in analogy to Equation III.132:

$$\Phi_{ion \to p} = \cfrac{4\pi r_p D_{ion}}{\cfrac{1}{E_{PD}\{\Delta'_{ion}\}}\cfrac{r_p}{\Delta'_{ion}} + \cfrac{1}{E_{PB}\{r_p, \Delta'_{ion}\}}\cfrac{4 D_{ion}}{r_p v_{ion}}} N_{ion} \quad ,$$

f III.138

where:

$$\Delta'_{ion} = r_p + f\{\lambda_{ion,p}, r_p\}$$

f III.139

The relationship between the mean free path, the ion mobility and the mean velocity of an ion is (Hoppel and Frick, 1986):

$$\lambda_{ion} = \frac{4}{3}\frac{M_{air}}{q\,\mu_{ion}}\left(1 + \frac{M_{air}}{M_{ion}}\right)^{-1/2} v_g v_{ion} \quad .$$

f III.140

According to Hoppel and Frick (1986) the characteristic atmospheric ion mean free path is approximately $2.21 \cdot 10^{-8}$ m.

III.4 Turbulent Coagulation

III.4.1 Introduction

The indirect solar climate theories investigated here are closely related to the atmospheric boundary layer, which is characterised by turbulent motion. Whereas submicron particles tend to move with the flow field, larger particles tend to have a relevant relative motion due to their larger inertia. Moreover, larger particles are also subject to gravitational settling. As gravitation and turbulence forces simultaneously lead to macroscale aerosol coagulation processes in the turbulent flow field, they are frequently treated together (e.g. Saffman and Turner, 1956; Pruppacher and Klett, 1997; Pinsky et al., 1999).

Changing the scale from Brownian to turbulent motion has implications to the formalism of aerosol-aerosol interaction. Let a small submicron particle move onto a large particle. The small particle will tend to move with the flow field while the larger particle´s inertia leads to a relative displacement. Consequently, the trajectory of the small particle will be deviated by the influence of the large particle on the turbulent flow field in its vicinity. Thus, whereas aerosol collision in the free molecular regime considers two particles particles moving in a vacuum, and diffusion regime collision is a statistical extension of the previous, aerosol encounter on the turbulent scale involves the effect of turbulent friction that has to be treated specifically to the particles involved. In analogy to coagulation in the free molecular regime, the characteristic surface of turbulent coagulation is given by the collision cross-section. The effective cross-section of particle encounter is linked to the sum of the particle radii by the *relative effective collision cross-section*, similarly to the Brownian enhancement factors of condensation and coagulation. Through hydrodynamic suction effects, involving large particles of similar size in turbulent flow, the value of the relative cross-section may be above unity.

Turbulent coagulation may also be enhanced by electrostatic forces between charged particles. This process adds considerable complexity to particle encounter in the turbulent flow field, especially in relationship with the effective collision cross-section. Focus will not be put onto this process and simple scheme based on the free molecular formalism will be adopted. For a

more thorough treatment of charged particle interaction in the turbulent flow it is referred to Tinsley et al. (2000).

It is noteworthy that Brownian diffusion processes and turbulent coagulation take place simultaneously. As their driving force is different, it may be possible to separate these processes formally. The interaction of turbulent and Brownian motion coagulation will be investigated below.

III.4.2 Processes of turbulent and gravitational coagulation

4.2.1 Turbulent shear coagulation

Turbulent shear coagulation is caused by the anisotropy of the turbulent flow field on the length scale of particle encounter. Turbulent flow is characterised by eddies of different size. If the particles are much smaller than the smallest eddy, the flow field anisotropy may be represented by a constant radial velocity gradient orthogonal to the flow. If the flow is parallel to the z-direction, then the turbulent velocity gradient flux of particles n_2 onto a particle n_1, whose centre coincides with the origin, is (Pruppacher and Klett, 1997):

$$\phi_{\Gamma, n_2 \to n_1} = 2\Gamma n_2 \int_0^{r_e} \int_{-\frac{\pi}{2}}^{\frac{\pi}{2}} r\cos\phi \ r\,d\phi\,dr = \frac{4}{3}\Gamma r_e^3 n_2 \quad,$$

f III.141

where Γ is the turbulent relative velocity gradient and r_e is the effective collection cross-section radius (see Equation III.155 below). The factor $cos\varphi$ accounts for the fact that the velocity is constant in the y-direction while the relative velocity is equal to Γx; x is the separating distance between the particle centres in the x-direction.

The Reynolds number of an eddy in the turbulent flow field is given by:

$$Re_{\lambda_e} = \frac{v_e \lambda_e}{v_g} \quad,$$

f III.142

where v_e is the characteristic velocity of the eddy and λ_e is the characteristic length scale, that is the size of the eddy.

The length scale of turbulent particle encounter is considerably smaller than the largest eddies of the boundary layer. However, for the above constant gradient assumption to be consistent it is to be shown that the colliding particles are much smaller than the smallest eddies. The characteristic velocity of these eddies is understood to be independent of the size of the largest eddies and their associated large scale velocity variability (see Pruppacher and Klett, 1997). Moreover, this value should be independent of the kinematic viscosity of the air, since eddies cannot develop on a scale on which viscosity is relevant. However, since all eddies are part of a break-up chain of larger eddies into smaller ones eventually leading to the dissipation of kinetic energy through viscosity, the characteristic velocity of the eddies should be a function of the rate of energy dissipation per unit mass. Through a dimensional consideration it is:

$$v_e \simeq \epsilon^{1/3} \lambda_e^{1/3}$$

f III.143 ,

where ϵ is the kinetic energy dissipation rate per unit mass.

For the smallest eddies the Reynolds number should be more or less equal to unity. Thus Equation III.142 combined with the preceding yields the characteristic length scale of the smallest eddies, that is the so-called Kolmogorov microscale length:

$$\lambda_{e,K} = \left(\frac{v_g^3}{\epsilon} \right)^{1/4} .$$

f III.144

A similar dimensional consideration yields the corresponding characteristic time of the Kolmogorov microscale eddy:

$$\tau_{e,K} = \frac{\lambda_{e,K}^2}{v_g} = \left(\frac{v_g}{\epsilon} \right)^{1/2} .$$

f III.145

The velocity gradient on the aerosol particle scale may thus be approximated by the gradient on the Kolmogorov microscale, which is approximately:

$$\Gamma \simeq \frac{v_{e,K}}{\lambda_{e,K}} = \tau_{e,K}^{-1} \simeq \frac{\epsilon^{0.5}}{v_g^{0.5}} .$$

f III.146

The mean dissipation rate of kinetic energy is quite variable in the atmospheric boundary layer. Dimensional considerations along with the consideration that according to Equation

III.143 ε should not depend on the air viscosity, lead to the following approximation (Pruppacher and Klett, 1997):

$$\epsilon \simeq \frac{\Delta u^3}{l} \quad ,$$

f III.147

where Δu is the velocity variation on the largest eddy circulation scale, and l is the characteristic length of this scale.

Measurements of these Figures indicate that ε varies from $3 \cdot 10^{-4}$ to $114 \cdot 10^{-4}$ m²/s³ under cloud free conditions (Pruppacher and Klett, 1997, p. 467). Under well developed conditions of cumulus circulation ε rises to typically $200 \cdot 10^{-4}$ m²/s³, while strong cumulonimbi induce kinetic energy dissipation rates of as much as $2000 \cdot 10^{-4}$ m²/s³. These figures imply the Kolmogorov microscale length to be of the order of 10^{-2} to 10^{-1} m, which is much smaller than the aerosols formed through gas to particle conversion. The approximation of the velocity gradient through the linear velocity variation on the scale of the smallest eddies thus seems appropriate.

4.2.2 Inertial coagulation

For the preceding turbulent shear coagulation to be relevant at least one of the encountering aerosol particles needs to be large enough for the velocity difference to be important. Inertial coagulation takes place under the additional condition that the considered aerosol particles have distinct mass. Particles thus have different inertial properties upon turbulent flow field acceleration, and thus have a differential proper velocity relative to the gaseous medium.

The turbulent inertial coagulation flux of smaller particles n_2 onto a larger particle n_1 may be formally represented by (Pruppacher and Klett, 1997):

$$\phi_{I, n_2 \to n_1} = \pi r_e^2 (v_{I,1} - v_{I,2}) N_2 \quad .$$

f III.148

On the Kolmogorov microscale the frictional force may be assumed in equilibrium with turbulent acceleration. In the Stokes regime of turbulent flow Equation III.84 applies (Puppacher and Klett, 1997):

$$\left(1-\frac{\rho_g}{\rho_i}\right)a_{e,K}=\beta\,C_i^{-1}\,v_{I,i}=C_i^{-1}\frac{6\pi\,\eta_g\,r_i\,v_{I,i}}{M_i} \quad,$$

f III.149

where $a_{e,K}$ is the typical turbulent acceleration on the Kolmogorov microscale, β is the Stokes friction constant for spheres in a laminar flow, C is the Cunningham slip-flow correction according to Equation III.98 and v_I is the velocity of the particle relative to the air due to turbulent acceleration at the microscale.

According to the above equation the characteristic velocity of the smaller particles n_2 relative to the turbulent flow field is lower because of their relatively high frictional deceleration, so that the velocity difference in Equation III.148 is strictly positive for unequal particles. The friction force may be assumed to be in the laminar flow regime, since the related Reynolds number is assumed to be of the order of unity.

The microscale acceleration is given by:

$$a_{e,K}=\frac{v_{e,K}^2}{\lambda_{e,K}}=\frac{\lambda_{e,K}}{\tau_{e,K}^2}\simeq\frac{\epsilon^{3/4}}{v_g^{1/4}} \quad,$$

f III.150

leading to the following expression for the turbulent inertial coagulation kernel:

$$K_I=\pi\,r_e^2\frac{\left(1-\dfrac{\rho_g}{\rho_l}\right)\epsilon^{0.75}}{6\pi\,\rho_g\,v_g^{1.25}}\left(\frac{C_1M_1}{r_1}-\frac{C_2M_2}{r_2}\right) \quad.$$

f III.151

The formula given by Pruppacher and Klett (1997) does not include the Cunningham slip flow correction. For the formula to be as general as possible it is included here, although turbulent coagulation may not be relevant for particles for which the slip flow correction is. Also the typical velocity relative to the flow field included in this formula comprises a relative density factor in analogy to the formula given by Saffman and Turner (1956). Hypothetical particles that have the same density than air should not be accelerated differentially, and should therefore move with the air, excluding inertial coagulation.

4.2.3 Gravitational coagulation

Following the assumption of isotropy of the flow field on the Kolmogorov microscale,

gravitational coagulation may be associated with the movement of small spheres evolving in a laminar flow and settling differentially according to their respective mass. The flux of smaller particles n_2 onto a larger particle n_1 due to gravitational settling (Pruppacher and Klett, 1997) is:

$$\Phi_{G,n_2 \to n_1} = \pi r_e^2 (v_{G,1} - v_{G,2}) N_2$$

f III.152

This formula is analogous to Equation III.148. The relative velocity of the particles due to gravitational acceleration is given by the following expression:

$$\left(1 - \frac{\rho_g}{\rho_i}\right) g = C_i^{-1} \beta v_{G,i}$$

f III.153

Here again equilibrium has been assumed between the driving force and the dissipative term, so that particles settle at terminal velocity.. The Stokes friction constant β is equal to the inverse of the relaxation time (see Equations III.98 and III.105). Thus the gravitational coagulation kernel is (Saffman and Turner, 1956):

$$K_G = \pi r_e^2 \frac{\left(1 - \frac{\rho_g}{\rho_l}\right) g}{6 \pi \eta_g} \left(\frac{C_1 M_1}{r_1} - \frac{C_2 M_2}{r_2}\right)$$

f III.154

III.4.3 The effective collection cross section

4.3.1 Introduction

The relative effective collection cross section P_{ct} is defined:

$$P_{ct} = P_{cc} P_{cs} \equiv \frac{r_e^2}{r_{12}^2} \equiv P_{cc} \frac{r_{max}^2}{r_{12}^2} ,$$

f III.155

where P_{cc} is the coalescence probability, P_{cs} is the relative effective collision cross section, and r_{max} is the radius corresponding to the effective collision cross-section.

Particle collision may not lead to particle coalescence. Rather than due to surface tension,

coalescence may be impeded by the presence of air between the particles, the evacuation of which may be hindered by the geometry of the drops (Pruppacher and Klett, 1997, p. 595 ff.). Thermodynamically particle recombination should be spontaneous since the recombined surface energy is lower than the sum of the surface energies of the two original drops. As small drops tend to be spherical, the coalescence probability of these tends to unity (Beard and Ochs, 1993). Only collisions between larger drops, means at least one drop is larger than approximatively 25·μm, tend to be ineffective, with values of coalescence probability down to less than 50% for rain drops hitting cloud drops of more than 40 micrometres.

The appropriate estimation of the collision cross-section is rather a fastidious task. Simply spoken the collision of two particles in the atmosphere is the result of the particles' inertia, which is disturbed by the friction force exerted by the flow field that interacts with the encountering particles. For this reason the ratio of inertia and friction force , that is the Reynolds number, is a characteristic figure of particle collision in turbulent flow. A first numerical approach to turbulent particle collision is the so-called superposition model (Pruppacher and Klett, 1997, p. 571 ff.). The simplification consists in assuming that each particle taken separately is exclusively influenced in its course through the flow field induced by the other particle. The reciprocity of particle interaction is thus neglected, while the frictional interaction of the respective flow field and the individual particle is taken into account. Their relative movement is obtained by stepwise superposition of the individual movement and ulterior adaptation of the individual flow field. The accuracy of the superposition model is limited in as much as the interactions among the common flow field and the respective trajectory are not negligible when the particles are close to each other, especially if these are of more or less equally large size. The model suggests that particles should pass rapidly through this zone of complex interaction, so that the action of the commonly perturbed flow field is limited. Quite a number of other conceptual models have been designed in order to estimate more accurately the interactions

Figure III.10: Streamlines of the Stokes flow field around a micrometre particle.

109

between the flow field and the particle trajectories (e.g. Schlamp et al., 1976; Klett and Davis, 1973; Lin and Lee, 1975). However, all these formalisations have in common that they are numerical computations of particular conditions of particle encounter. They comprise no analytical approach to particle trajectories as a function of particle velocity and size, the turbulent flow field as well as the anisotropy of the air due to temperature and density variation.

When solely aerosol particles are considered, there has been an inclination to assume that the relative effective collision cross section is equal to unity (e.g. Saffman and Turner, 1956; Pruppacher and Klett, 1997, p. 464 f.). These authors base this assumption on an experiment described in Manley and Mason (1952) showing that glass spheres of around 65 micrometres in diameter colliding in a viscous fluid. It is however known from precipitation scavenging theory (e.g. Loosmore and Cederwall, 2004) and cloud physics that the collision efficiencies of small drops differ substantially from unity by up to three orders of magnitude. For this reason the collision efficiency is parametrized in cloud models as a function of the respective drop size and air viscosity (e.g. Pinsky et al., 2001). Since cloud drops present a characteristic fall velocity as a function of their size, the relative effective collision cross-section is mostly not represented as a velocity function in cloud models. For the specific purpose of this study, however, the velocity function is essential since the individual effects of turbulent coagulation processes are to be investigated.

4.3.2 Derivation of a conceptual parametrization

At first the order of magnitude of the size of the particles and the consequences that can be drawn from this with respect to the relative effective cross-section need to be investigated. Due to their important liquid fraction marine aerosols, especially secondary particles, show a density that is comparable to the one of pure water (see above). For this reason data obtained from cloud droplet models to aerosol effective collision cross-section estimation may be applied. The size of marine aerosols should not exceed about 10 μm (see the parametrization of salt particle emission of Clarke et al., 2006). Larger aerosol particles are present in a negligible number concentration. This has an essential consequence to the flow regime around the considered particles. Since the Reynolds number of the flow around these particles is low, that is lower than 20, the flow is expected to be in the laminar, steady axis-symmetric regime,

so that the Stokes scheme of frictional drag modified by the Cunningham slip flow correction factor may be applied (Beard, 1976). The Stokes scheme is consistent with the turbulent aerosol flux formulas given in the previous sub-section.
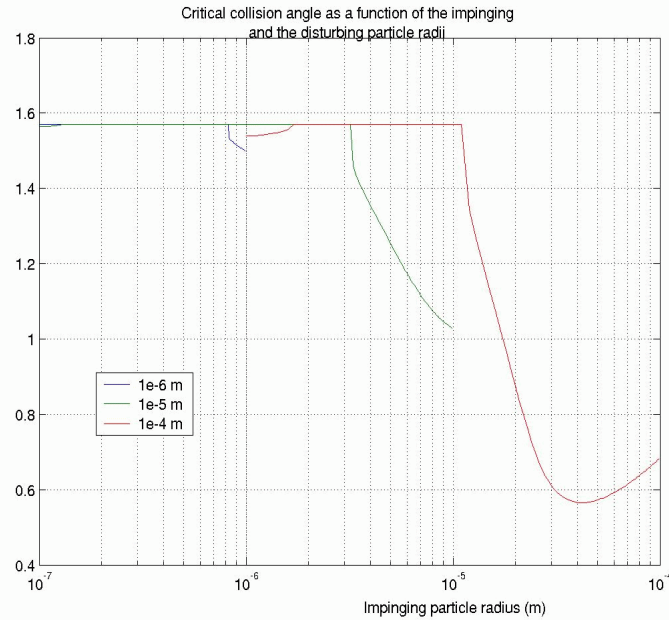
Figure III.11: Onset of relevance of inertia to particle collision in a Stokes flow field. In the absence of such influence the collision angle would be zero. Note that the collision angle is shown as a function of the radius of the impinging smaller radius under simplified model conditions (see text). The smaller radius is increased until reaching the larger particle size.

Let a small particle *p2* encounter a large particle *p1* in laminar flow. A first approximation would be to neglect the small particle influence on the flow field. The initial velocity of the small particle would be the corresponding final fall velocity, so that the relative velocity is the vectorial difference between the momentary velocity of the small drop evolving in the flow field induced by the larger particle minus the terminal fall velocity of this particle. The Stokes flow field is given by the following set of equations (Landau and Lifshitz, 1966, p. 70 ff.):

$$v_r = v_1 \cos\theta \left(1 - \frac{3}{2}\frac{r_1}{r} + \frac{1}{2}\frac{r_1^3}{r^3} \right)$$

$$v_\theta = -v_1 r \sin\theta \left(1 - \frac{3}{4}\frac{r_1}{r} - \frac{1}{4}\frac{r_1^3}{r^3} \right) \quad ,$$

f III.156

where v_r is the radial velocity and v_θ is the angular velocity of the induced flow field, v_1 is the

velocity of the larger particle relative to the flow field at infinite distance, r_1 the radius of particle $p1$ and r is the position vector in polar coordinates originating at the centre of $p1$. The resulting flow field is sketched in Figure III.10. Note that the flow is already notably influenced by the presence of the larger particle at a distance equal to several times its radius.

A first approximation of the effective radius for relatively small particles would be to assume that these move with the air current around the particle such that:

$$r_{max}^2 \simeq \delta^2 = r_{12}^2 \left(1 - \frac{3}{2} \frac{r_1}{r_{12}} + \frac{1}{2} \frac{r_1^3}{r_{12}^3} \right) \quad ,$$

f III.157

where δ is the impact parameter of the streamline whose apsidal distance is equal to r_{12}. This equation stems from the solution of the Stokes stream function equation set at the limits of infinite distance and of a polar angle equal to $\pi/2$, respectively (Pruppacher and Klett, 1997, p. 470).

Considering the flow field generated by the larger particle under terminal velocity assumption in the Stokes laminar flow regime that acts upon the inertial velocity of the smaller particle:

$$a_{f,N_1 \to N_2} = -\frac{6 \pi r_2 \eta_a}{M_2} C_2^{-1} (v_2 - v_{st}(v_r, v_\theta)) \quad ,$$

f III.158

where a_f is the friction force acceleration exerted on the smaller particle by the flow field induced by the larger particle and by its own movement relative to the air molecules. The local Stokes flow field vector v_{st} is given by Equation III.156.

Taking the critical impact parameter δ as initial value, numerical integration of the previous equation yields the collision angles displayed in Figure III.11. The figure shows three different curves corresponding to larger particles with radii of 1, 10 and 100 μm, respectively. Although these curves do not accurately represent the actual interaction process, that is two spheres moving in a commonly influenced flow field, some fundamental deductions can be drawn from the simplified model. Small particles do have a negligible inertia so that their movement follows the air streamlines as it is testified by the tangential impaction angle. Beyond a certain threshold particle size ratio, however, inertia becomes relevant, so that the smaller particles collide with the larger one at a rapidly increasing angle. The onset of the influence of inertia is abrupt since the critical particle tends to move nearly tangentially for quite a large portion of its trajectory. A slight inertial influence thus significantly modifies the collision angle, as it is

also demonstrated in Figure III.12 showing some of the corresponding particle tajectories until impaction.
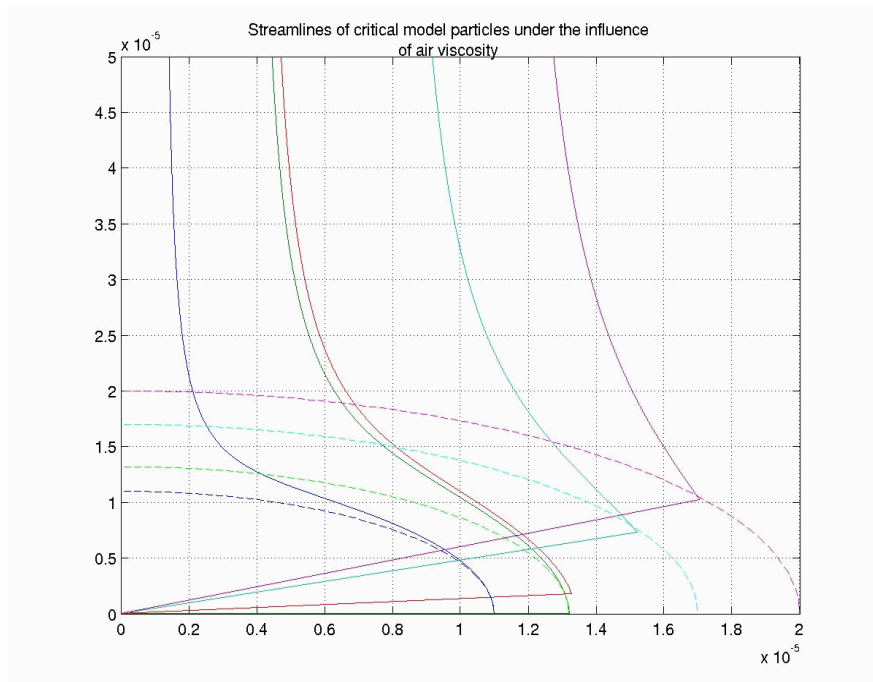
Figure III.12: Impact angle of particles whose impact parameter is equal to the critical one of a particle moving parallel to the streamlines (no inertia). The impact angle increases with the smaller particle radius along with the incidence of inertia. Particles showing no inertia would follow a tangential trajectory at the apsidal distance. The larger particle radius is 10 micrometres. The dotted lines indicate the virtual particle of radius $r_{12}=r_1+r_2$.

The precise location of the onset of inertial influence depends on both the size of the fixed particle and on the particles' relative size, so that the relative threshold radius r_2/r_1 decreases with r_1. In addition to the particle radius ratio and the larger particle radius, the hydrodynamic properties of the air, that is its viscosity, as well as the relative particle velocity should also be relevant to the onset of the influence of inertia on the particle trajectory. Thus a modified inverse Reynolds number adapted to the special conditions of the drag exerted onto a particle in the Stokes flow field may be defined. It is:

$$Re_{St,2}^{-1} = \frac{\beta r_1}{v_{12}} C_2^{-1} = \frac{6\pi \eta_a r_2 r_1}{M_2 v_{12}} C_2^{-1} \quad .$$

f III.159

The modified Reynolds number is known in literature as the Stokes number and recognised to

113

be relevant to the effective collision cross-section, for instance in relationship with aerosol precipitation scavenging efficiency through inertial impaction (e.g. Slinn, 1977). It permits quite well foreseeing the onset of inertia as is demonstrated by Figure III.13 in comparison with Figure III.11. The Stokes number threshold value is approximatively 5, 3, and 2, when the larger particle radius is set to 1, 10, and 100 μm, respectively. According to Beard (1976) the assumption of Stokes laminar flow is appropriate for particles subject to gravitational acceleration and at terminal velocity that are smaller than 19μm in radius.
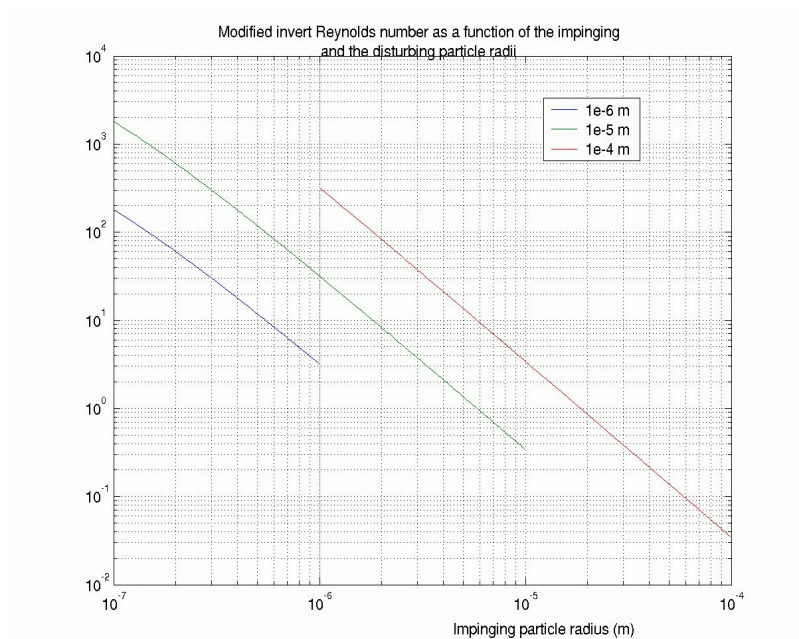
Figure III.13: Potential of the Stokes number to predict the onset of inertial influence on the effective cross-section of aerosol particle encounter. When compared to Figure III.11 it is apparent that the corresponding inverse Stokes number of inertial onset lies between 2 and 5, while the Stokes number varies over 5 orders of magnitude and the size of the particles varies over 4 orders of magnitude.

The above turbulent coagulation kernels stem from the laminar flow assumption for the Kolmogorov microscale. The simple model presented here consistently analyses the influence of inertia on particle encounter in laminar flow. In turn, the laminar flow assumption, from the consideration that on the Kolmogorov microscale the flow should be laminar, which is characterised by frictional kinetic energy dissipation. As it is indicated in Figure III.10 the range of particle-flow interaction in calm air is of the order of 5-10 times the particle radius. A particle of 10 μm in radius would therefore modify the flow field on a scale of 100 μm. The

Kolmogorov microscale being of the order of 10^{-2} m, the laminar flow assumption seems to be appropriate for the entire associated length scale of particle encounter. This conjecture, however, does not consider the true complexity of the turbulent flow field. The turbulent flow field does present spots of contrasting flow direction far below the Kolmogorov microscale. As a function of their inertia, collisions between particles of opposite flow direction may take place preferentially within these spots. The consequent encounters should be particularly effective since the related relative velocity should be larger than average. Pinsky et al. (1999) have investigated the issue of the complexity of the turbulent flow field. They found the typical turbulent collision cross-section not to be circular and coaxial, and to be larger than the values indicated by classical laminar flow investigations.

Another objection to the laminar flow assumption is that the turbulent flow field may be too variable in time on the Kolmogorov scale (Pruppacher and Klett, 1997, p. 471). To assess the pertinence of this objection the typical time scale of aerosol encounter needs to be investigated. Under steady state conditions it is (see Equation III.149):

$$t_i \propto \frac{r}{(\beta_1^{-1} - \beta_2^{-1}) a_K} \quad,$$

f III.160

where t_i is the typical interaction time.

Together with Equations III.145 and III.150 the typical ratio of the interaction time to the Kolmogorov microscale characteristic time of turbulent flow becomes:

$$\frac{t_i}{t_K} = A \rho_a \frac{6 \pi r_1}{M_1/r_1 - M_2/r_2} \frac{v_a^{0.75}}{\epsilon^{0.25}} \simeq A \frac{9 \rho_a}{2 \rho_1} \frac{v^{0.75}}{r_1 \epsilon^{0.25}} \cong 10^{-6} \frac{A}{r_1 \epsilon^{0.25}} \quad.$$

f III.161

Considering that the typical interaction length should be several times the larger particle radius, the proportionality factor A should be significantly larger than unity. For micrometre aerosol particles, with $0.1 < \epsilon^{0.25} < 1$, the above ratio tends to be larger than unity, especially in a highly turbulent boundary layer, so that the flux field varies during the interaction lapse. According to Pruppacher and Klett (1997) the influence of an evolving turbulent flow field on particle interaction has not yet been investigated, however attention needs to be drawn to the relatively recent work of Pinsky and Khain (2004), which investigates the incidence of the turbulent acceleration distribution on turbulent inertial coagulation. Although Pinsky and Khain assume a constant flow field, the anisotropy of turbulent acceleration introduces, in

addition to velocity variation, a further implicit temporal element. Their statistical study indicates that there is just a limited influence of the unsteadiness of turbulent acceleration on the collision efficiency. The collision efficiency is influenced, however, by the statistical variance of the turbulent flow acceleration.

The preceding excursus on effective collision has demonstrated the influence of turbulent flow field characteristics. The laminar flow assumption has allowed revealing the dominant role of the particles' individual and relative size, their inertia, their relative velocity and the drag exerted by the flow field. A conceptual parametrization comprising the previous elements to particle encounter in turbulent flow will now be formulated. It is based on model data of Pinsky et al. (2001). In this study a Stokes model for small particles is associated and weighed as a function of the Reynolds number with the flow model of Hamielec and Johnson (1962) for large particles. The flow field is assumed to be laminar on the scale of particle encounter, no turbulence related considerations are made. Particles move relative to the flow field at terminal velocity with gravity as driving force according to Beard (1976). The resulting stream function is assessed with the method of the superposition model.

Following extensive fitting experiments as a function of the relevant parameters the following parametrization proved to give consistent results for the relative effective collision cross section:

$$
\begin{aligned}
P_{cs} &= \left(Re_r \, a \, (Re_{St,1}^{-1} + Re_{St,2}^{-1})^{-1} + Re_r^{-1} b \frac{Re_1^{-1} \delta_1^2 + Re_2^{-1} \delta_2^2}{r_{12}^2 (Re_1^{-1} + Re_2^{-1})} \right) (Re_r + Re_r^{-1})^{-1} \\
&= \frac{Re_r}{Re_r + Re_r^{-1}} a \frac{v_{12}}{6 \pi \eta_a r_1 r_2} (M_1^{-1} C_1^{-1} + M_2^{-1} C_2^{-1})^{-1} + \frac{Re_r^{-1}}{Re_r + Re_r^{-1}} b \frac{\delta_1^2 M_1^{-1} C_1^{-1} + \delta_2^2 M_2^{-1} C_2^{-1}}{r_{12}^2 (M_1^{-1} C_1^{-1} + M_2^{-1} C_2^{-1})} \quad ,
\end{aligned}
$$

f III.162

where:

$$
Re_r = \frac{2 \rho_g r_{12} v_{12}}{\eta_g} \quad , \quad Re_i = \frac{2 \rho_g r_i v_i}{\eta_g} \quad ,
$$

f III.163

are the relative Reynolds number of encountering particles *p1* and *p2* on the characteristic scale r_{12} and the individual Reynolds number of particle *i*, respectively.

Attention should be drawn to the fact that the previous expression is conceptually close to the parametrizations used in relationship with precipitation scavenging (e.g. Slinn, 1977; Davenport and Peters, 1978). Compared to these expressions the first term stands for the

contribution of *impaction* while the second stands for *interception* (see below). Formally the expressions differ notably. While precipitation scavenging implies large raindrops moving onto much smaller aerosol particles, turbulent aerosol coagulation involves particles of more or less equal size. This fundamental difference might explain the formal opposition.
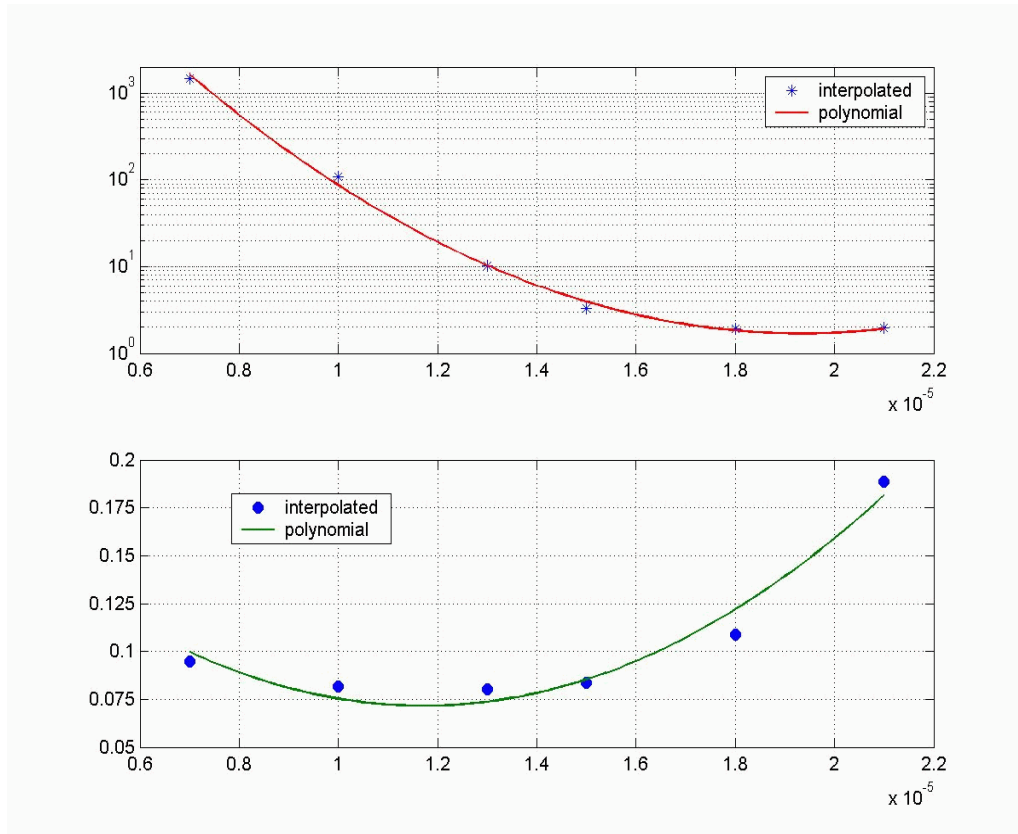
*Figure III.14: Dimensionless parametrization parameters **a** and **b** of Equation III.162 (**a**:upper panel, **b**:lower panel) as a function of the larger particle radius. The circles represent interpolation values based on data of Pinsky et al. (2001), the lines are obtained with second degree polynomial fittings to these points.*

The basic assumption of the previous equation is that, in accordance with the findings of Pinsky et al. (1999), impaction depends mainly on the particles' relative velocity and individual mass. When the relative velocity is close to zero the effective radius tends to its purely interceptive value. In this case the trajectories of the particles should resemble the one of simple air molecules in Stokes laminar flow. The limiting value should therefore be a simple function of Equation III.157. In accordance with the superposition model this function is weighed according to the respective Reynolds number of the particles. The best fitting function reproducing impaction behaviour was found to be the inverse of the sum of the

respective inverse Stokes numbers. The summation is in analogy again to the superposition model. This function is proportional to the relative velocity and increases with the individual mass and Cunningham factor of the particles. In order to quantify the relative importance of impaction and interception a weighing needs to be introduced that measures the influence of friction relative to inertia. This expression has to be representative for both particles. The characteristic velocity is the particles' relative velocity and not their individual velocity relative to the flow field. Particles showing a high velocity relative to the flow field show a high impactive potential. However, when the encountered particle has a similar velocity, the characteristic encounter time lapse increases to the point that through friction force the particles´ behaviour tends to become purely interceptive. The characteristic length is equal to the sum of the particle radii. The representative friction property is the one of the air medium. The parameters a and b have been assessed as a second degree polynomial function of the radius of the larger particle:

$$a = \exp(4.5265e10 \, r_1^2 - 1.7491e6 \, r_1 + 1.7422e+1)$$
$$b = 1.2711e9 \, r_1^2 - 2.9764e4 \, r_1 + 2.4580e\text{-}1 \qquad .$$

f III.164

The exponential function of coefficient a on the larger particle radius stems from the low Stokes number when the encountering particles are both small, as the related relative velocities are also very low. The fits of the two coefficients are displayed in Figure III.14. The interpolated values are obtained when Equation III.162 is fitted to the data of Pinsky et al. (2001). The second degree polynomial curves match well the interpolation values. Coefficient b is chosen not to be a constant, since this assumption would lead to inconsistent a-coefficients.

At high relative particle velocities Equation III.162 may yield relative effective radii larger than unity. This is not inconsistent with the model of Pinsky et al. (2001), since they also predict such figures for relatively large encountering particles. Values larger than unity are not consistent with the Stokes laminar flow assumption, so that such figures should not occur for corresponding Reynolds number values. An effective ratio larger than one should thus indicate that the range of validity of the parametrization has been exceeded.
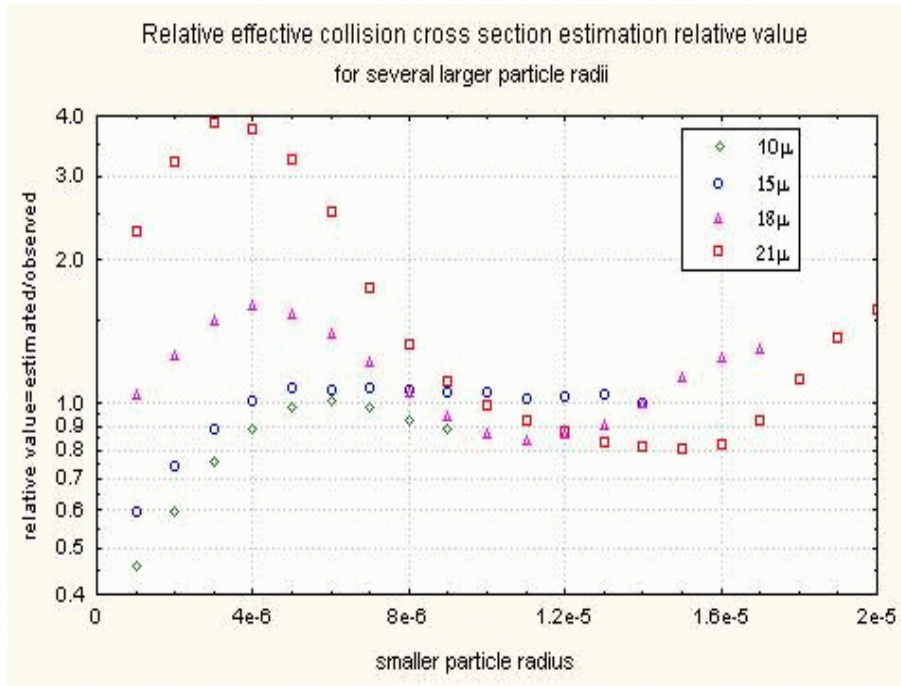
Figure III.15: Ratio of the effective cross-section, using the parametrization III.162, to the model data of Pinsky et al. (2001). For particles larger than 19 micrometres the parametrization performs poorly due to the limits of the Stokes laminar flow assumption. The seemingly poor performance for small impinging particles arises geometrically from the steep descent of the relative effective radius with decreasing radius (see Figure III.16).

Figure III.15 depicts the ratio of the parametrized effective cross-section to the Pinsky et al. (2001) data as a function of the radius of the smaller particle. It shows that large errors appear at small radii. A large error is inherent to the steep increase of the relative effective cross-section with particle radius for relatively small particles (see Figure III.16, or alternatively Pruppacher and Klett, 1997, p. 583, fig. 14-5). The parametrization formula tends to perform poorly when the larger particle radius is above 19 μm, which is the approximate limit of Stokes laminar flow (Beard, 1976). While the parametrization exclusively stems from the Stokes flow assumption, the study of Pinsky et al. (2001) associates the Stokes model to the flow model of Hamielec and Johnson (1962) for larger particles. The inconsistency between the model data and the parametrization should explain the poor performance above the size limit of 19 μm. It is also as an implicit indication for the consistency of the conceptual parametrisation scheme within the limits of the Stokes laminar flow solution.
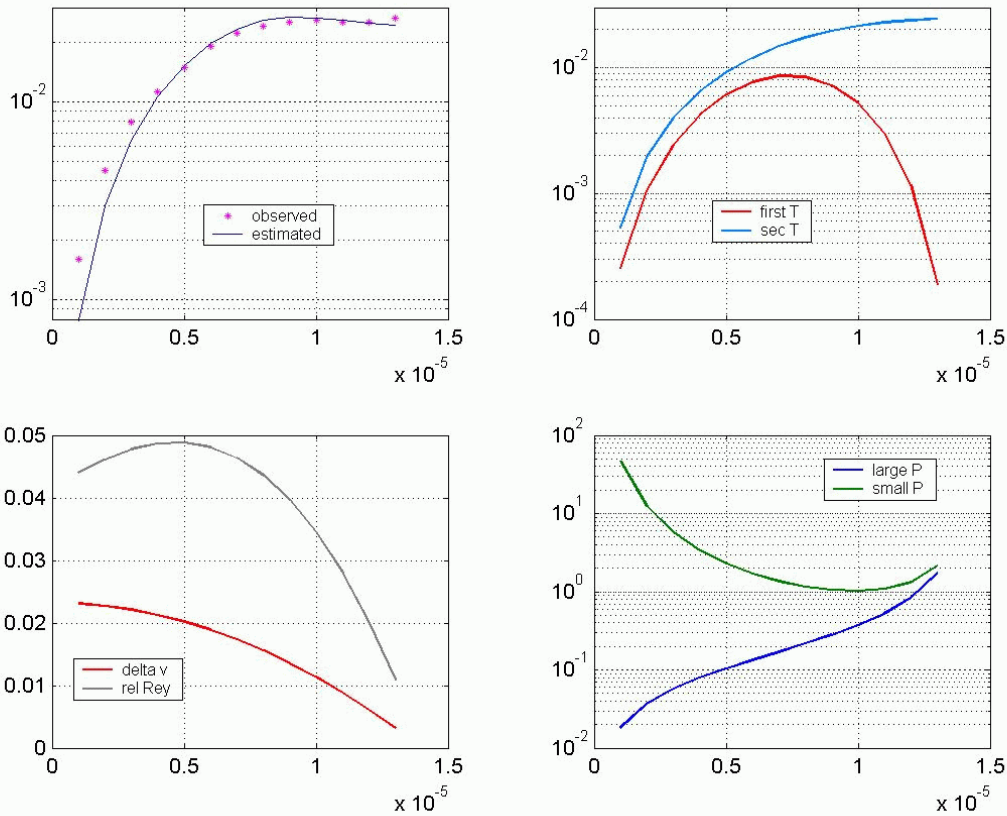
Figure III.16, panels from top left to bottom right: Parametrized effective collision cross-section compared to the data points of Pinsky et al. (2001); associated impaction (red curve) and interception (blue) term values; corresponding Cunningham slip factor corrected relative velocity (red) and relative Reynolds number (black); and inverse Stokes number for both the smaller (green) and the larger (blue) particles. All panels as a function of the smaller particle radius, the larger particle radius is 14 μm.

Figure III.16 depicts the performance of the parametrization along with some relevant associated variables, comparing estimated values to the data provided by Pinsky et al. (2001) for a larger particle of 14 μm radius. The consistency of Equation III.162 is confirmed further as the data for 14 μm particles has not been included during the interpolation of the parameters of the parametrization. The upper right panel shows that the interception term dominates the impaction term under gravitational settling conditions. It is interesting to note that according to the above consideration the effect of impaction decreases as the size of the particles becomes comparable while their relative velocity tends to zero.
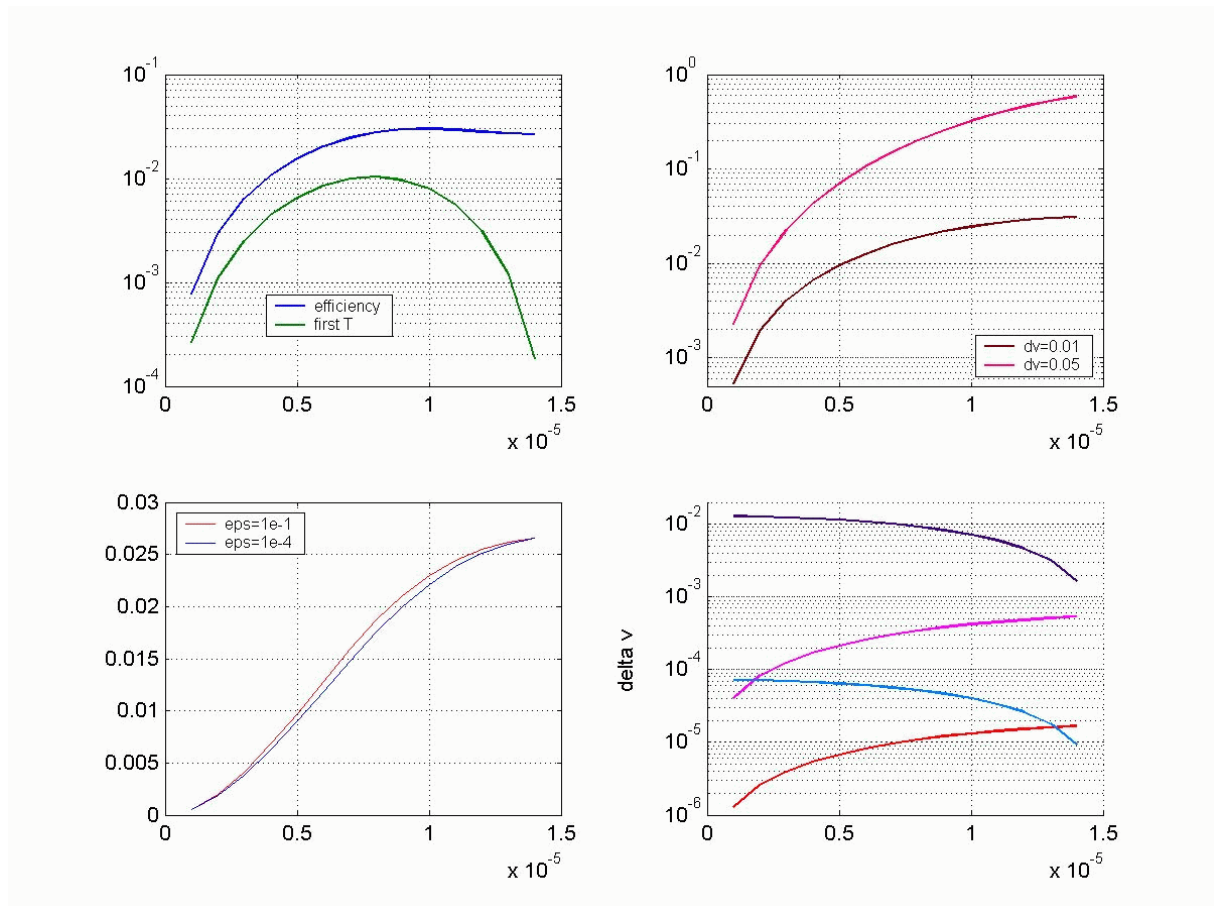
Figure III.17, panels from top left to bottom right: Relative effective collision cross-section for particles moving under gravitation force (blue) and magnitude of the impaction term (green); relative effective cross-section when the relative velocity is artificially held constant at 0.01 and 0.05 m/s (chestnut and pink, respectively), same variable for turbulent inertial coagulation for dissipation rates of 1e-1 and 1e-4 m²/s³ (red and blue, respectively); and relative particle velocities in case of turbulent shear (pink and red) and turbulent inertia (violet and blue) for the previous dissipation rates, respectively. All panels as a function of the smaller particle radius, the larger particle radius is 15 μm.

Figure III.17 depicts parametrized relative effective cross-sections in the context of the relative encounter velocity as a central input variable. The upper left panel compares the relative effective cross-section to the incidence of impaction to this value for gravitational coagulation. It shows that in analogy to the previous figure impaction tends to become negligible for comparably sized particles The upper right panel demonstrates the sensitivity of the effective cross-section to relative velocity variations. The lower curve displays the parametrized effective cross-section when the relative velocity is artificially held constant at 0.01 m/s, which is a typical value for gravitational settling. The second curve at 0.05 m/s

constant relative velocity shows notably higher results, more or less by one order of magnitude.

For gravitational coagulation the influence of impaction is pronounced, approximately contributing one third of the effective cross-section value (upper left panel). In case of turbulent inertial coagulation, for a turbulent energy dissipation rate variation from 0.0002 m^2/s^3, typical for calm air, to 0.2 m^2/s^3, typical for cumulonimbi, the influence of the relative velocity on the effective cross-section is quite limited, as it is shown in the lower left panel. The inertial coagulation relative velocity is one order of magnitude lower (lower right panel) than the typical gravitational value, thus decisively limiting its impactive potential. This result is in contradiction to the findings of Pinsky and Khain (2004) showing a relevant influence of the statistical variance of turbulent acceleration. The findings of Pinsky et al. (1999) have shown that the determination of a representative relative velocity in the turbulent flow field is rather a statistical issue. The formalism adopted in the previous sub-section to assess the representative relative particle velocity may be inappropriate. It could lead to an underestimation of the dependency of the effective collision cross-section on ambient turbulent conditions via the effective relative velocity. In case of turbulent shear the relative particle velocities are so low under any realistic turbulent energy state of the atmosphere that the influence of impaction is negligible and the associated curves of the effective relative cross-section are similar to the one of inertial coagulation in case of low energy dissipation.

Consequently it may be retained that under gravitational coagulation the relative effective cross-section is a function of both impaction and interception, with a tendency of dominance of the latter, while for both the cases of inertial and turbulent shear coagulation the dependency on the turbulent state of the air, in the limits of the present formalism to the variability of the characteristic relative velocity, is negligible. As a good approximation the parametrization Equation III.162 may therefore be reduced to the second term.

To assess the turbulent shear efficient collision cross-section an iterative formalism must be adopted; as a matter of fact a circle problem needs to be solved, for which the effective cross-section is also implicitly a function of the effective cross-section itself via the particle relative velocity. Let a small effective radius of say 1/10,000[th] the radius of the larger particle be considered. This particle size leads to a certain relative turbulent shear velocity, which in turn leads to an effective cross-section. This cross-section again leads to a certain relative velocity and so on until the relative velocity of the critical particle and the associated observed particle

match. Since the turbulent shear coagulation kernel is a cubic function of the sum of the particle radii, its expression in terms of the relative effective collection cross-section becomes:

$$K_\Gamma = \frac{4}{3}\Gamma P_{ct}^{1.5} r_{12}^3 \simeq \frac{4}{3} P_{cs}^{1.5} r_{12}^3 \frac{\epsilon^{0.5}}{v_a^{0.5}} \quad .$$

f III.165

III.4.4 Turbulent flow enhancement factor

Pruppacher and Klett (1997, p. 837) give the following approximate formula of the electrostatic enhancement factor E_T of coagulation in turbulent flow:

$$E_T = 1 - (4\pi\epsilon_0)^{-1} \frac{q_1 q_2}{r_1 + r_2} \left(\frac{M_1 M_2}{M_1 + M_2} \frac{v_{1,2}^2}{2} \right)^{-1} \quad .$$

f III.166

This formula is in direct analogy to Equation III.69 of Brownian coagulation enhancement in the free molecular regime. The above equations treat turbulent particle coagulation enhancement without considering the interaction between the encountering particles and the flow field, so that particles are virtually evolving in a vacuum. Neither the interaction of the collision efficiency and electric charge attraction forces (e.g. Tinsley et al., 2000) nor the effect of image forces are considered. Although the above formula is a gross estimation of the turbulent enhancement factor, according to Pruppacher and Klett (1997) it has proven to give accurate results in case of large and highly charged particles for which friction forces are negligible. Although this may not be assumed for charged aerosol particles the above formalism of turbulent coagulation enhancement is adopted here. Appropriate data to conduct a similar study leading to the conceptual parametrization Equation III.162 of uncharged particle interaction in turbulent flow was not at disposal at the time of this study.

Equation III.166 is used exclusively in case of attraction forces. In order to avoid negative values the following conceptual approach is adopted in case of repulsion in analogy to the molecular regime enhancement factor Equation III.119:

$$E_T = \exp\left(-(4\pi\epsilon_0)^{-1} \frac{q_1 q_2}{r_1 + r_2} \left(\frac{M_1 M_2}{M_1 + M_2} \frac{v_{1,2}^2}{2} \right) \right) \quad .$$

f III.167

III.4.5 Interaction between turbulent and Brownian coagulation

Brownian diffusion, turbulent and gravitational coagulation are simultaneous particle growth processes. Brownian diffusion has a purely fortuitous nature, while gravitation is essentially an ordered process, and turbulence may be regarded to be ordered on the Kolmogorov microscale. The velocity vector of an air parcel may be decomposed into a spatially averaged value and a local deviation. The coagulation processes have a specific counterpart in the particle velocity vector v_p, it is:

$$v_p = v'_B + \bar{u} + u' + \bar{v}_g + v'_g + \bar{v}_t + v'_t$$

$$\textbf{f III.168}$$

where the index B stands for Brownian motion, g stands for gravity and t for the turbulent flow velocity. The velocities v stand for the Kolmogorov microscale components of the velocity vector whilst $\bar{u}$ is the macroscale velocity of the air. There is a disordered element in the turbulent terms of the particle velocity vector as the particles do not move parallel to the flow field in turbulent acceleration (Pinsky et al., 1999).

Since the Brownian movement can be formally separated from the turbulent and the gravitational particle flow processes, it has no influence on the corresponding coagulation kernels. As Tinsley et al. (2000) point out, it is nevertheless possible that Brownian movement increases the effective radius of turbulent coagulation processes. This indirect effect should be pronounced for relatively small particles that are encountered by larger particles. Both the effective radius and the turbulent relative velocity of Aitken particles onto micrometre particles is low, so that the overall influence on the coagulation rate concerning should be limited, which will be confirmed in the following sub-section. However, it may not be stated that conversely there is no influence of turbulent coagulation on Brownian diffusion. According to Equation III.42 the Brownian motion mean velocity of a ten micrometre particle is of the order of 10^{-4} m/s. A typical turbulent or gravitational relative velocity is approximately 10^{-2} m s^{-1}, which is two orders of magnitude larger, and the associated particle mean free path according to Equation III.106 is of the order of 10^{-7} m. Consequently, Brownian motion may not effectively compensate particle removal through turbulent coagulation, which may thus modify the particle diffusion flux along with the particle concentration gradient. However, for a typical concentration of aerosol particles of 10^9 m^{-3}, the

mean distance between two particles is 10^{-3} m. This is approximately one order of magnitude larger than the typical length scale of particle interaction in turbulent flow. For this reason the encounter of two particular particles should not be influenced by the respective particle encounter history of these particles. Under typical atmospheric conditions, turbulent coagulation does not affect the concentration gradient of the respective particles and has thus no influence on the Brownian diffusion flux.

Saffman and Turner (1956) investigated the influence of the turbulent flow field relative velocity distribution on the coagulation kernel within a monodisperse aerosol population. Their findings indicate that jointly occurring turbulent inertial, gravitational and shear processes among particles with a given relative velocity distribution should result in the following formalism for the coagulation kernel:

$$K_T \simeq \sqrt{\sum_{i=1}^{3} K_i^2} \quad .$$

f III.169

Their basic assumption is:

$$\Phi_{p1 \leftrightarrow p2} = \pi \int r_e^2\{v_{12}\} N_1 N_2 v_{12} f\{\boldsymbol{v_{12}}\} d\boldsymbol{v_{12}} \simeq \pi r_e^2\{v=0\} N_1 N_2 \int v_{12} f\{\boldsymbol{v_{12}}\} d\boldsymbol{v_{12}}$$

f III.170

where $\Phi_{p1 \leftrightarrow p2}$ is the coagulation rate of $p1$ and $p2$ particles per unit volume, $\boldsymbol{v_{12}}$ is the vectorial relative velocity, and $f\{\boldsymbol{v_{12}}\} = \partial N / N \partial \boldsymbol{v_{12}}$ is an appropriate relative velocity density distribution.

In their study Saffman and Turner (1956) assumed that the effective radius is equal to the sum of the respective particle radii. As we have seen before, this assumption is inappropriate in the context of turbulent coagulation of aerosol particles. In addition Saffman and Turner (1956) assume that the relative velocity is normally distributed, so that the most probable relative velocity is zero. This assumption is certainly appropriate in case of gravitational and turbulent inertial coagulation among particles of equal size but it should be inaccurate under all other conditions. For these reasons the formalism of Equation III.169 is not retained here and the influence of the relative velocity distribution on the turbulent coagulation kernels while unsolved will be disregarded in this study.

III.4.6 Numerical comparison of turbulent and Brownian coagulation

Figure III.18 compares the individual Brownian diffusion and turbulent coagulation kernels as a function of the smaller particle radius. The radius of the larger particle is 19 μm. In the upper left panel the effective cross-section variation is included in the assessment of the turbulent coagulation kernels according to the parametrization III.162. The turbulent kinetic energy dissipation rate per unit mass is equal to $2 \cdot 10^{-4}$ m^2 s^{-3}, as an example for the cloud free boundary layer. The turbulent kernels share more or less the same pattern. This stems from their analogous formulation, diverging only in the intensity of the driving force. The gravitational force is more effective than turbulent acceleration, leading to a gravitational coagulation kernel that is three orders of magnitude larger under steady air conditions. The Brownian diffusion kernel tends to become dominant with decreasing smaller particle size. However, for the major fraction of the considered size spectrum of the smaller particle gravitational coagulation is the dominating process, except when the particles are almost of equal size, for which turbulent shear has an edge over Brownian motion.

The upper right and the lower left graphs depict the essential relevance of the effective cross-section to the turbulent coagulation kernels. In the upper right panel the relative effective cross-section is not considered. For comparison the relative effective cross-section is displayed in the lower left panel for gravitational and inertial coagulation. The relative cross-section of turbulent shear is not shown because it is nearly identical to the inertial one as the related relative velocities are quite low (see above). Without the relative effective cross-section the ordered process kernels are by several orders of magnitude larger and would be the dominating process of particle interaction over the whole considered smaller particle size range. The values of the effective cross-section for very small particles confirm the consistency of the parametrization stays outside of its derivation range. In analogy to the upper left panel, the lower right graph shows the individual coagulation kernels when the turbulent energy dissipation rate per unit mass is put equal to 0.2 m^2 s^{-3}. This situation is typical to a rather turbulent atmosphere, like within thunderstorm clouds. Without interference of the dissipation rate, the values of gravitational and Brownian diffusion coagulation are identical to the upper left graph. However, the values of turbulent shear and turbulent inertial coagulation, which depend on the square root and the cubic root of the power four value of the dissipation rate, respectively, are larger by approximately two orders of magnitude. Beneath
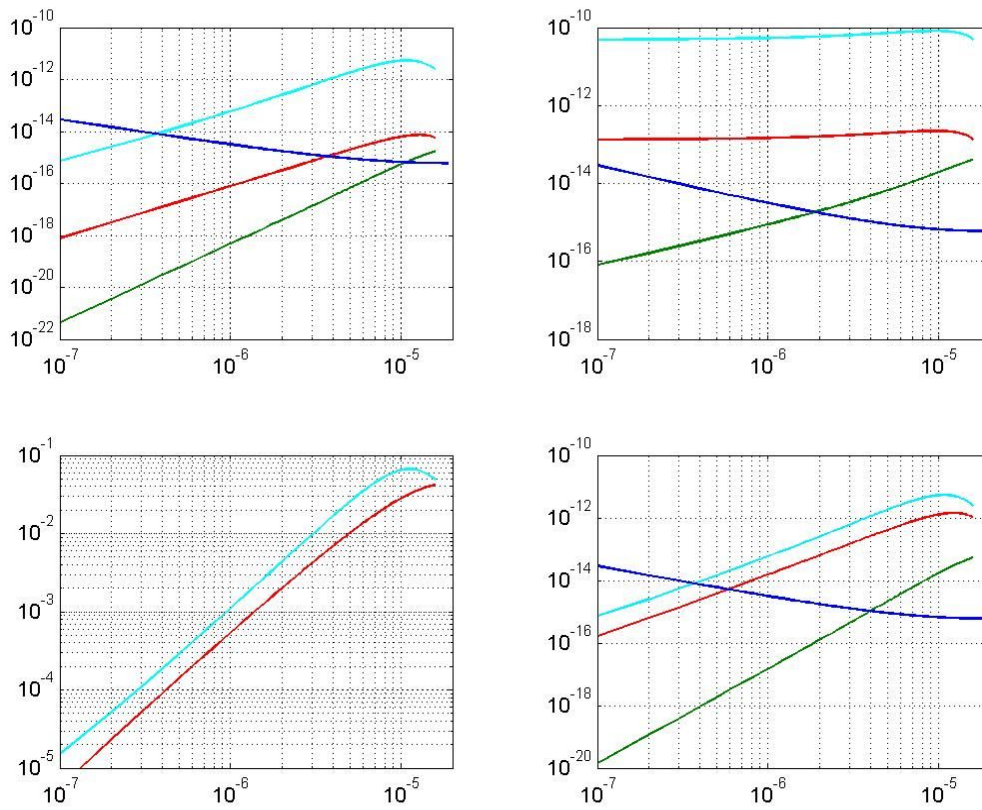
Figure III.18 : Gravitational (cyan), turbulent inertial (red), turbulent shear (green) and Brownian diffusion (blue) coagulation kernels for a larger particle of r=19·10⁻⁶ m. Results are shown as a function of the smaller particle radius, from up left to down right: Kernels for a dissipation rate ε=0.1 m² s⁻³, corresponding kernels assuming the relative effective cross-section is equal to unity, associated relative effective cross-section function assessed with Equation III.162, kernels for ε=10⁻⁴ m² s⁻³. Particles bear no charge; p=101,325 Pa, T=298.15 K.

gravitational coagulation, turbulent inertial coagulation has become a relevant process of particle interaction over much of the considered smaller particle spectrum as it is less than one order of magnitude smaller than the earlier process.

Figure III.19 is in analogy to the preceding except that the larger particle is of 1 μm only. The qualitative deductions to be made from this figure are mostly similar. Quantitatively, however, it is apparent that whatever the turbulent state of the atmosphere is, Brownian motion is the dominating process of coagulation as long as the effective cross-section is included. When hydrodynamic interaction between encountering particles is not considered, however, gravitational coagulation tends to become of equal importance to particle coagulation. This
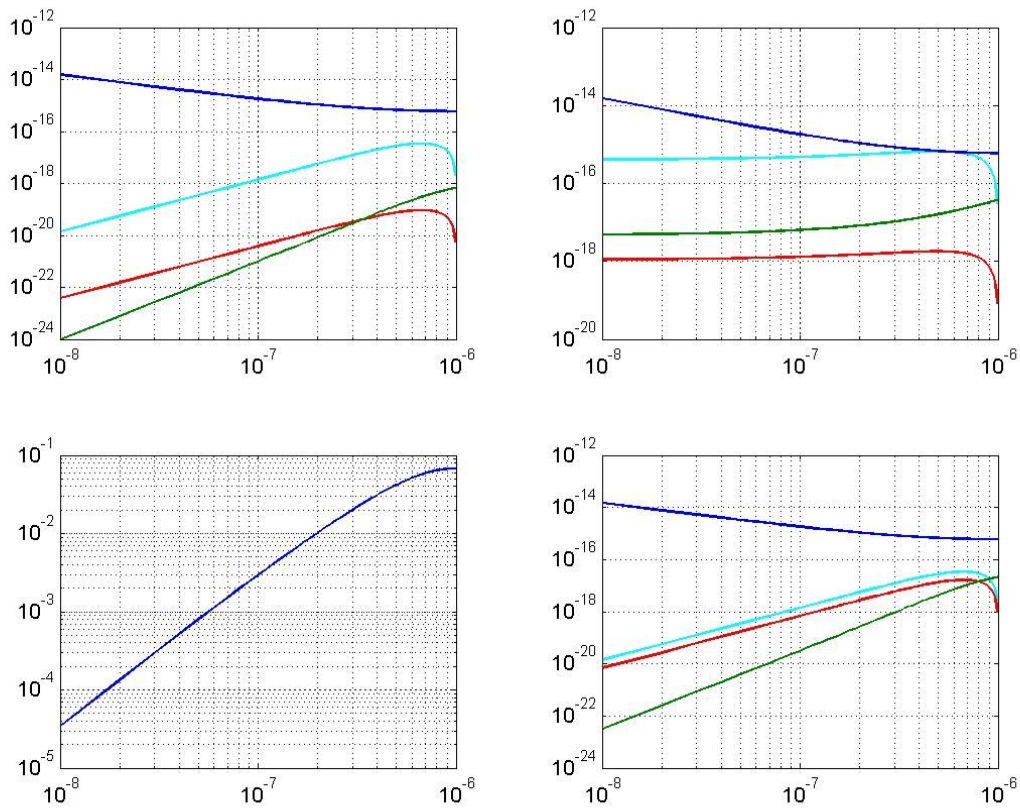
Figure III.19 : Gravitational (cyan), turbulent acceleration (red), turbulent shear (green) and Brownian diffusion (blue) coagulation kernels for a larger particle of 10^{-6} m radius. Results are shown as a function of the smaller particle radius, from up left to bottom right: Kernels for $\varepsilon=10^{-4}$ m^2 s^{-3}, same kernels with relative effective cross-section set to unity, corresponding effective cross-section assessed with Equation III.162, kernels for $\varepsilon=0.1$ m^2 s^{-3}. Particles bear no charge, p=101,325 Pa, T=298.15 K.

finding is consistent with other authors relating that turbulent processes tend to become relevant above micrometre size (e.g. Pruppacher and Klett, 1997, p. 472). Because of the low relative velocities involved (for gravitational coagulation these are of the order of 10^{-4} m s^{-1}) the relative effective cross-section values tend to be exclusively interceptive, and therefore indifferent of the process of turbulent coagulation. Consistently with the preceding figure, turbulent intertial coagulation is of the same order of magnitude as gravitational coagulation in the highly turbulent atmosphere. It is also noteworthy that turbulent shear plays a more important role in comparison to the preceding figure, hinging upon the fact that turbulent shear shows a more pronounced larger particle size dependence.

Both Figures III.18 and III.19 show that the influence of Brownian motion on the effective

cross-section should be irrelevant under most circumstances, as turbulent processes are negligible to particle interaction within the size range for which Brownian motion is effective. The influence of the actual turbulent flow field on both the turbulent inertial kernel and the effective collision cross-section is potentially relevant in those situations in which this process plays an important role, that is under conditions of strong turbulence such as in convective clouds.

IV. Unified model of aerosol and cloud droplet mechanics

IV.1 A box model for secondary aerosol formation and aerosol mechanics

IV.1.1 Introduction

The formalism of secondary aerosol particle nucleation and mechanics presented in the previous chapter has been encoded in Fortran 90. The inner-most subroutine calculates the activities of sulphuric acid and water in solution as a function of the mixing ratio of the constituents. It serves as an input to a second subroutine, which calculates both the binary nucleation rate and the ion-induced binary nucleation rate. Input parameters are atmospheric temperature, pressure, sulphuric acid concentration and relative humidity as well as the first dissociation constant of sulphuric acid estimated according to the method presented in the Appendix. The principal program routine has two main sections. Condensation and coagulation kernels as well as some associated parameters such as the equilibrium size of the aerosol particles in function of ambient temperature and moisture are calculated within the first part. The second unit tackles the temporal integration of particle growth using the parameters assessed within the first part as an input.

Some equations, especially the activity of water in solution, the critical composition of the particles and the equilibrium particle size, are solved via numerical integration or iteratively. In case of iterative evaluation, numerical divergence, especially in association with the Thomson equation, requires an approximate value to be estimated priorly by a trial and error sequence. The two closest values are retained and define the interval within which Newton iterations are performed. In case of divergence a new series of trial and error is undertaken to refine the interval.

The general particle growth differential equation set is solved with the explicit fourth order Runge-Kutta numerical integration method. The integration step is optimized dynamically according to integration error minimization criteria and within the growth dynamical limitations of the system. The mass balance equations of sulphuric acid and elementary ions are solved diagnostically with respect to their loss terms. Doing this mass loss within the

aerosol/sulphuric acid/ion system is reduced to a minimum. Semi-analytical solutions to the ion and sulphuric acid differential equations shall be presented. Elementary ions are assumed to evolve instantaneously to stable cluster size, so that these may be assimilated with the former within the aerosol growth model.

IV.1.2 General dynamic equations of aerosol particle growth

The general differential equation set of aerosol particle growth comprises the source and loss terms of nucleation, molecular and particle coagulation, and ion attachment (Raes and Janssens, 1986):

$$
\begin{aligned}
\frac{dN_i^q}{dt} =& \, J^q \frac{n_J - n_{i-1}}{n_i - n_{i-1}} \delta_{n_J \in [n_i, n_{i-1}]} + J^q \frac{n_{i+1} - n_J}{n_{i+1} - n_i} \delta_{n_J \in]n_i, n_{i+1}]} \\
&+ \frac{(K_B)_{i-1} N_{i-1} N_a}{n_i - n_{i-1}} \delta_{r_{i-1} < r_l} - \frac{(K_B)_i N_i N_a}{n_{i+1} - n_i} \delta_{r_i < r_l} \\
&+ \frac{(K_T)_{i-1} N_{i-1}}{n_i - n_{i-1}} \delta_{r_{i-1} > r_l} - \frac{(K_T)_i N_i}{n_{i+1} - n_i} \delta_{r_i > r_l} \\
&+ \sum_{l=qmin}^{qmax} \sum_{m=qmin}^{qmax} \sum_{j=1}^{i} \sum_{k=j}^{i} \frac{(K_p)_{j,k}^{l,m} N_j^l N_k^m}{1 + \delta_{j=k} \delta_{l=m}} \frac{(n_j + n_k) - n_{i-1}}{n_i - n_{i-1}} \delta_{n_j + n_k \in [n_{i-1}, n_i]} \delta_{l+m=q} \\
&+ \sum_{l=qmin}^{qmax} \sum_{m=qmin}^{qmax} \sum_{j=1}^{i} \sum_{k=j}^{i} \frac{(K_p)_{j,k}^{l,m} N_j^l N_k^m}{1 + \delta_{j=k} \delta_{l=m}} \frac{n_{i+1} - (n_j + n_k)}{n_{i+1} - n_i} \delta_{n_j + n_k \in]n_i, n_{i+1}]} \delta_{l+m=q} \\
&- N_i^q \sum_{l=qmin}^{qmax} \sum_{j=1}^{imax} (K_p)_{i,j}^{q,l} N_j^l \\
&+ A_{+,i}^{q-1} N_+ N_i^{q-1} \delta_{q>qmin} + A_{-,i}^{q+1} N_- N_i^{q+1} \delta_{q<qmax} \\
&- A_{+,i}^{q} N_+ N_i^{q} \delta_{q<qmax} - A_{-,i}^{q} N_- N_i^{q} \delta_{q>qmin}
\end{aligned}
$$

$$, $$

f IV.1

where n_i is the number of sulphuric acid molecules per particle i, K_B is the Brownian molecular regime condensation kernel, K_T is the Brownian transition regime condensation kernel, $(K_p)_{i,j}^{q,l}$ stands for the sum of the Brownian and the turbulent coagulation kernels between particles i and j of elemental charges q and l, respectively, and $A_{+,i}^q$ and $A_{-,i}^q$ are the respective attachment coefficients of a positively and a negatively elementarily charged ion.

The first line stands for the particle source function via nucleation, the second and the third line represent the balance of condensation, the fourth line stands for coagulation gains, the fifth and the sixth line express coagulation losses, whilst the seventh and the eighth line describe the gains and losses through ion attachment, respectively. δ_f is a binary coefficient,

which is $\delta_f=1$ when the boolean function f is true and $\delta_f=0$ when the function is false.

The basic concept of the general dynamic equation with respect to particle size discretisation is reflected by the presence of distribution factors. Particles are size discretised into classes according to their content of sulphuric acid. In each size class the central particle is believed to be representative to the whole class as to its dynamic evolution. Consequently condensation, coagulation and ion attachment kernels are calculated in conformance with the properties of this particular particle. The distribution factors share the condensation or coagulation product between the two adjacent classes according to their discretisation. Products of ion attachment do not have to be distributed since the number of sulphuric acid molecules is conserved.

Note that condensation is either in the free molecular or in the transition regime depending on the size of the concerned particles relative to the arbitrary radius r_l chosen to mark the limit between these two regimes (see above). The formalism of the coagulation terms ensures that each possible combination is only treated once. Due to the indistinguishableness of equal particles (Seinfeld and Pandis, 1998, p. 674 f.), growth fluxes involving such particles have to be divided by two, as it is indicated by the respective δ-function operators. The loss rate concerning particles of the same class is to be multiplied by the same factor as it involves the loss of two particles per combination, so that the indistinguishableness factor is cancelled out.

IV.1.3 Mass balance equations and their semi-analytical solution

1.3.1 The small ion continuity equation

The adopted elementary ion continuity equation is (e.g. Laakso et al., 2002):

$$\frac{d N_\pm}{dt} = 2\left(R_f\right)_\pm - \left(J_{tot}\right)_{ion} - \frac{c_{rec}}{2} N_\pm^2 - N_+ \sum_{q=qmin}^{qmax} \sum_{i=1}^{imax} A_{+,i}^q N_i^q - N_- \sum_{q=qmin}^{qmax} \sum_{i=1}^{imax} A_{-,i}^q N_i^q \quad ,$$

f IV.2

where $(R_f)_\pm$ is the elementary ion couple formation rate, and c_{rec} is the ion recombination coefficient, i.e. the ion-ion coagulation kernel.

The first term of the above equation stands for the mainly cosmic ray induced and thus height dependent ionization rate of the atmosphere. The second term represents the losses through ion-induced secondary nucleation, which according to Equation III.30 is proportional to the

concentration of ions itself. The third term stands for the recombination and consecutive neutralization of ions of opposite sign upon their encounter. The last two terms express the ion losses through the attachment of positive and negative ions, respectively, on aerosol particles. The number of positive and negative ions is insured to be identical by choosing identical properties relative to nucleation and ion attachment. For this reason the recombination rate is proportional to the square of half the total elementary ion concentration. Hoppel (1977) estimated the recombination coefficient to be $c_{rec}=1.4 \cdot 10^{-12} m^3 s^{-1}$. Assuming a typical earth surface ionization rate of $(R_f)_\pm = 2.5 \cdot 10^6 m^{-3} s^{-1}$, this figure leads to an equilibrium ion concentration $N_\pm \approx 2.67 \cdot 10^9 m^{-3}$ in the absence of aerosols and nucleation. The collision of a negative (positive) ion with an aerosol bearing *qmin* (*qmax*) charges leads to the loss of a negative (positive) small ion (note the missing binary delta factors), although for mass conservation reasons the aerosol particle number remains constant in the corresponding class.

The energy barrier between the stable ion cluster and the freshly nucleated ultrafine particle may vanish under certain conditions of ambient temperature, moisture and sulphuric acid content (Lovejoy et al., 2004). Close to these conditions the nucleation rate should tend to the encounter rate of stable cluster ions with a sulphuric acid molecule: the encounter of a stable cluster ion $I^{+/-}(H_2O)_n$ with a single sulphuric acid molecule is sufficient to produce a stable ultrafine aerosol particle, which will rapidly equilibrate to the ambient humidity. Thus the following limiting equation of the nucleation rate under stable conditions is obtained:

$$\left(J_{ion} \right)_{st} = E_B \pi r_{tot}^2 \sqrt{v_\pm^2 + v_a^2} N_a N_\pm$$

f IV.3 ,

where $(J_{ion})_{st}$ is the nucleation rate under stable growth conditions, $v_\pm$ is the mean ion velocity according to Equation III.140.

Due to its chemical specificity the above equation contains parameters for which it is difficult to find a representative value, such as the radius of the atmospheric ions and the associated ion velocity and enhancement factor. However, since the dependence on particle radius is close to square for both the enhancement factor and the collision cross-section, these effects should cancel each other more or less out. The main uncertainty resides thus in the estimation of a representative velocity. A further remarkable property of the above equation is that it is proportional to the ambient sulphuric acid concentration. Modgil et al. (2005) show a linear dependence of ion-mediated nucleation beyond a certain concentration (see Figure III.1) that may be associated with stable growth conditions (Lovejoy et al., 2004), whilst below this

threshold the dependence is much stronger, and thus reminiscent of unstable nucleation conditions (see above).

The nucleation rate as well as the attachment terms in the above equation require a complex system of differential equations involving the sulphuric acid continuity equation and the dynamic equations of aerosol growth to be solved. To allow for a simple analytical solution the aerosol particle concentrations as well as the proportionality faction of the nucleation rate to the ambient ion concentration have to be held momentarily constant. The ion concentration should be the limiting factor to the nucleation rate during nucleation events (Yu, 2002). The sulphuric acid concentration should show a stiffer behaviour so that it may be considered as a parameter during the integration interval. Keeping some variables constant allows finding a so-called semi-analytical solution of the small ion continuity equation. The mathematical formalism of the equation to be solved is:

$$\frac{dx}{dt} = -ax^2 - bx + c$$

.

f IV.4

The terms on the right hand side of the equation stand for ion recombination, combined nucleation and ion attachment, and ionization, respectively. It is possible to combine nucleation and ion attachment since the model number of cations and anions are equal.

This first order second degree equation is transformed into a second order first degree equation:

$$\frac{dx}{dt} = -a\left(\frac{w'}{aw}\right)^2 - b\frac{w'}{aw} + c \quad (1)$$

$$\frac{d\frac{w'}{aw}}{dt} = \frac{w''}{aw} + \frac{w'}{a}\left(\frac{-w'}{w^2}\right) \quad (2)$$

,

f IV.5

with:

$$x \equiv \frac{w'}{aw}$$

,

f IV.6

and thus

$$w'' + bw' - ac\, w = 0$$

.

f IV.7

This equation may be transformed into a system of two first order differential equations:

134

$$\frac{dw_1}{dt} \equiv \frac{dw}{dt} = w' \equiv w_2 \quad (1)$$

$$\frac{dw_2}{dt} = -bw_2 + ac\ w_1 \quad (2) \quad .$$

f IV.8

It admits general solutions of shape $C\ e^{\lambda t}$ for:

$$\lambda_{1,2} = -\frac{b}{2} \pm \sqrt{\frac{b^2}{4} + ac} \quad .$$

f IV.9

Switching back from w to x using Equation IV.6 yields:

$$x = a^{-1}\frac{\lambda_1 C_1 e^{\lambda_1 t} + \lambda_2 C_2 e^{\lambda_2 t}}{C_1 e^{\lambda_1 t} + C_2 e^{\lambda_2 t}} \quad .$$

f IV.10

With the initial condition $x(t=0)=x_0$ one finds the following link:

$$C_2 = \frac{a x_0 - \lambda_1}{\lambda_2 - a x_0} C_1 \quad ,$$

f IV.11

and finally:

$$x\{t+\delta t\} = \frac{\lambda_1 + \lambda_2 \dfrac{a x_0 - \lambda_1}{\lambda_2 - a x_0} e^{(\lambda_2 - \lambda_1)\delta t}}{a + a \dfrac{a x_0 - \lambda_1}{\lambda_2 - a x_0} e^{(\lambda_2 - \lambda_1)\delta t}} \quad .$$

f IV.12

With:

$$\lim_{\delta t \to \infty} \{x\{t+\delta t\}\} = \frac{\lambda_1}{a}$$

f IV.13

this function admits a stationary equilibrium solution. For the ion concentration to be stable under real conditions, the loss functions should thus be constant. This might be fulfilled when the nucleation rate is low, so that the losses are mainly due to large aerosol particles, whose number remains more or less constant. The expression IV.12 is a more accurate approximation to the atmospheric ion concentration than the frequently made assumption that the ionisation rate is in equilibrium with recombination, which denies significant nucleation as well as ion attachment losses. The transient solution of the ion continuity equation to this

situation *(b=0)* is formally similar to Equation IV.12, while the stable solution is equal to $(c/a)^{0.5}$. Ion attachment might become negligible after intensive scavenging

The complementary situation arises when ion recombination is negligible relative to the other loss processes *(a=0)*, that is when an important loss through nucleation or a huge aerosol population occurs. The solution to the modified differential equation is:

$$x\{t_0+\delta t\}=\frac{c}{b\{t_0\}}+A e^{-b\{t_0\}\delta t} \quad , \quad A=x_0-\frac{c}{b\{t_0\}} \quad .$$

f IV.14

The preceding relationship shows that when nucleation or attachment losses are very high the ion concentration should tendentially decrease exponentially.

1.3.2 Equation of continuity for sulphuric acid

The sulphuric acid continuity equation reads (e.g. Laakso et al., 2002):

$$\frac{dN_a}{dt}=\left(R_f\right)_a-n_J J_{tot}-n_{Jion}\left(J_{tot}\right)_{ion}+\sum_{i=1}^{imax} n_i \frac{dN_i^{q=0}}{dt}\delta_{n_j>n_{i-1}}$$
$$-N_a\sum_{i=1}^{imax} K_B N_i \delta_{r_i<r_l}-N_a\sum_{i=1}^{imax} K_T N_i \delta_{r_i>r_l} \quad ,$$

f IV.15

where *(Rf)a* is the atmospheric sulphuric acid formation rate.

The first term of the above equation represents the chemical formation of sulphuric acid in the atmosphere. In the marine atmosphere the dominant local source of sulphuric acid should be related to dimethylsulphide, which originates in marine plankton, and is constantly released to the atmosphere from the ocean surface and photochemically oxidized to sulphur dioxide (e.g. Seinfeld and Pandis, 1998). In turn sulphur dioxide is further oxidized via the cascade of reactions:

$$SO_2+HO\cdot\rightarrow HSO_3$$
$$HSO_3+O_2\rightarrow SO_3+HOO\cdot$$
$$SO_3+H_2O\rightarrow H_2SO_4 \quad ,$$

f IV.16
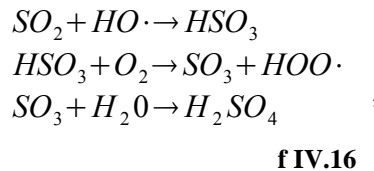
where the hydroxyl radical formation underlies the following pathway:

$$O_2 + h\nu \rightarrow 2O\cdot$$
$$O_2 + O\cdot \rightarrow O_3$$
$$O_3 + h\nu \rightarrow O_2 + O\cdot$$
$$H_2O + O\cdot \rightarrow 2HO\cdot$$
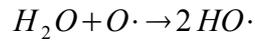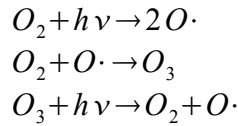
f IV.17

The sulphuric acid formation rate under purely marine conditions may be parametrized as a diurnal function (Yu and Turco, 2001; Clarke et al., 1998):

$$\left(R_f\right)_a = 10^{10} \sin\left(\frac{\pi}{\Delta t_d}(t - t_s)\right) ,$$

f IV.18

where t is local time, Δt_d is daylength, and t_s is time of sunrise. The formula reflects the photochemical dependence of the effectiveness of sulphuric acid synthesis via its linkage to the local solar parameters. The formation rate is limited photochemically by the disintegration of dimethylsulphide and the photochemical production of free hydroxyl radicals.

The second and the third term of the sulphuric acid continuity equation express the losses through homogeneous and heterogeneous binary nucleation, respectively. Note that this value includes the number of sulphuric acid molecules in the critical particle. The hypothesis that cosmic rays influence climate through changes in cloud properties assumes that ion nucleation should be considerably more effective than homogeneous nucleation, as shown by recent modelling results (Yu, 2006a, Yu, 2006b) and experiment (Svensmark et al., 2007). This translates into a higher number of sulphuric acid molecules in the critical homogeneous ultrafine particle (uncharged particles have to be larger to counterbalance the destabilizing surface tension effect), meaning that if a stable charged particle is neutralized through coagulation or ion attachment the resulting particle might become unstable, leading to its disintegration and the return of the contained sulphuric acid to the atmosphere. For this reason Laakso et al. (2002) added a supplementary term to their continuity equation, which is equivalent to the fourth term of the present continuity equation. One could argue that the authors thus inferred that every unstable particle would eventually disintegrate. However, this assumption is a misinterpretation of the concept of the nucleation rate. In fact a certain number of particles will disintegrate prior to reaching the homogeneous saddle point. The remaining fraction, however, will not disintegrate and will reappear *de facto* as part of the homogeneous nucleation flux following the related equilibrium assumption to the critical

137

cluster concentration. As a corollary, an additional amount of stable ionized particles will be formed through the attachment of ions on unstable neutral particles that exceed the charged stable size. These do not appear in the ion-induced nucleation rate, which exclusively consider cluster ion growth to stable size. However, as the net flow of unstable neutral particles should be negligible relative to the parallel flow of stable charged particles this additional pathway of stable particle formation may be neglected. The appropriateness of this assumption will be confirmed by the model results of ion-induced and homogeneous nucleation (see below).

The fourth and the fifth terms of the continuity equation of sulphuric acid represent the condensation losses. They are chosen to be consistent with the corresponding terms of the aerosol growth differential equations as to the particle size discretisation and the separation of the molecular and the transition regime.

The sulphuric acid continuity equation, as well as the dynamic growth equations of the particle size classes receiving the nucleation source function formally reduce to the following expression:

$$\frac{dy}{dt} = f\{y\} + B\{t\}x\{t\}$$

f IV.19

where x stands for the ion concentration and y represents the sulphuric acid (or aerosol particle) concentration. Note that $B\{t\}$ is negative within the sulphuric acid mass balance equation.

The mixed numerical and analytical solution to this equation is:

$$\int_{y\{t_0\}}^{y\{t_0+\delta t\}} dy \simeq f\{y\{t_0\}\}\delta t + B\{t_0\}\int_{t_0}^{t_0+\delta t} x\{t\} dt$$

f IV.20

Replacing $x\{t\}$ by the expression of Equation IV.12, one finds after integration:

$$\delta y \simeq f\{y\{t_0\}\}\delta t + B\{t_0\}\frac{\lambda_1}{a}\delta t + \frac{B\{t_0\}}{a} \ln \frac{a + a\frac{a x_0 - \lambda_1}{\lambda_2 - a x_0} e^{(\lambda_2 - \lambda_1)\delta t}}{a + a\frac{a x_0 - \lambda_1}{\lambda_2 - a x_0}}$$

f IV.21

IV.1.4 Numerical and semi-analytical integration

For the differential equation:

$$\frac{dy}{dt} = f\{y\{t\}\}$$

f IV.22

a particular explicit fourth order Runge-Kutta numerical solution is (e.g. Stöcker, 1995):

$$y\{t_0 + \delta t\} = y\{t_i\} + \frac{1}{6}\left(f\{y_0\} + 2f\{y_1\} + 2f\{y_2\} + f\{y_3\}\right)\delta t$$

f IV.23

where:

$$y_0 = y\{t_0\}$$
$$y_1 = y_0 + f\{y_0\}\frac{\delta t}{2}$$
$$y_2 = y_0 + f\{y_1\}\frac{\delta t}{2}$$
$$y_3 = y_0 + f\{y_2\}\delta t$$

f IV.24

In case of several interdependent variables y an equal number of differential equations has to be integrated in parallel.

The semi-analytical integration of:

$$\frac{dx}{dt} = f\{y\{t\}, x\{t\}\}$$

f IV.25

within the classical 4th order Runge-kutta formalism yields:

$$x\{t_0 + \delta t\} = x_0 + \frac{1}{6}\left(F\{\delta t, x_0, y_0\} + 2F\{\delta t, x_0, y_1\} + 2F\{\delta t, x_0, y_2\} + F\{\delta t, x_0, y_3\}\right)$$

f IV.26

where:

$$F\{\delta t, x_0, y_i\} = \int_{t_0}^{t_0 + \delta t} f\{x\{t\}, y_i\} dt$$

f IV.27

The solution is analytical regarding the x-variable whereas the time dependency of the y-variable is to be taken into account according to the Runge-Kutta formalism. For this reason

the x-variable goes into the analytical solution as an initial value at time increment t_0. The latter equation combined with Equations IV.24 delivers the three supporting intermediate y-values. The disparity between the analytical solution regarding the x-values and the numerical solution regarding the y-values underlines the semi-analytical nature of Equation IV.26. Note that the integration time step has vanished as a factor to become part of the semi-analytical solution.

In case that:

$$\frac{dy}{dt} = h\{y\{t\}\} + g\{F\{x\{t\}, y_i\}\}$$

,

f IV.28

the semi-analytical classical fourth order Runge-Kutta solution becomes:

$$y\{t_0 + \delta t\} = y\{t_0\} + \frac{\delta t}{6}\left(h\{y_0\} + 2h\{y_1\} + 2h\{y_2\} + h\{y_3\}\right)$$
$$+ \frac{1}{6}\left(G\{\delta t, x_0, y_0\} + 2G\{\delta t, x_0, y_1\} + 2G\{\delta t, x_0, y_2\} + G\{\delta t, x_0, y_3\}\right)$$

,

f IV.29

where:

$$G\{\delta t, x_0, y_i\} = \int_{t_0}^{t_0 + \delta t} g\{F\{x\{t\}, y_i\}\} \, dt$$

,

f IV.30

and:

$$y_1 = y_0 + h\{y_0\}\frac{\delta t}{2} + G\{\frac{\delta t}{2}, x_0, y_0\}$$
$$y_2 = y_0 + h\{y_1\}\frac{\delta t}{2} + G\{\frac{\delta t}{2}, x_0, y_1\}$$
$$y_3 = y_0 + h\{y_2\}\delta t + G\{\delta t, x_0, y_2\}$$

.

f IV.31

The fourth order Runge-Kutta numerical integration error may be assessed by (Stöcker, 1995):

$$R = \left| \frac{f\{y_2, t_0 + \frac{\delta t}{2}\} - f\{y_1, t_0 + \frac{\delta t}{2}\}}{f\{y_1, t_0 + \frac{\delta t}{2}\} - f\{y_0, t_0\}} \right|$$

.

f IV.32

This expression compares the numerical variability of the differential equation as inherent to the fourth degree Runge-Kutta integration to its variability over the time increment $\delta t/2$

according to the Newton method. When this ratio exceeds a certain value the time increment should be reduced. The stiffer the differential equation, the larger the ratio tends to be.

To ensure numerical stability the Courant criterion has to be respected, meaning:

$$a_i \delta t < 1 \quad \wedge \quad b_i \delta t < 1 \quad , \quad \frac{dy_j}{dt} = \sum_i^n a_i\{t\} y_j + c\{t\} - \sum_i^m b_i\{t\} y_j - d\{t\}$$
$$\Rightarrow \quad y\{t + \delta t\} > 0$$

f IV.33

where a_i and b_i group the terms proportional to the species number concentration y_j. Note that the coefficients may be time dependent.

Related to the present growth dynamical problem, the Courant criterion signifies that during the time increment of numerical integration a particle of species y_j must not be transformed more than once by the processes a_i and b_i, respectively. Although linked to numerical stiffness, the above criterion derives essentially from population dynamical considerations.

Numerical integration results reveal that the integration error increases from the smallest to the largest size class. This phenomenon is consistent from a growth dynamical position, as the number of coagulation growth terms, each of which contributes to the integration error, increases with size. Starting with zero aerosol particle concentration, the equation system shows extremely stiff behaviour, thus leading to a substantial relative initial error. The large initial error, however, is rapidly covered by the strong nucleation source function, as the associated aerosol concentrations grow from the infinitesimal range to several hundred million per cubic metre. While the integration increment is at first strongly limited by numerical stiffness, it is the population dynamical stability that is the limiting factor for explicit integration beyond the first couple of hundred simulated growth seconds. During the initial stiff phase Equation IV.32 is applied to the largest size class, later on the Courant criterion determines the time step as applied to the totality of the size classes. In order to avoid rounding errors the integration is executed in the double precision format.

According to Pirjola et al. (1998) the accuracy of the integration is strongly conditioned by the number of size classes. Numerical diffusion may result in a substantial artificial broadening of the aerosol spectrum. They show that when the number of particle size classes is set to 27, thus covering the size range of $5 \cdot 10^{-10}$ until 10^{-6} m, which is equivalent to some 7.8 classes per order of magnitude, numerical diffusion is satisfactorily reduced.

IV.1.5 Sea salt flux

1.5.1 Introduction

Although sea salt particles are a major constituent of the marine aerosol (see Figure II.21) there is still controversy on the size distribution of these. While earlier studies found the contribution of sea salt to the Aitken mode to be limited to high wind speed conditions (Clarke et al., 1987), more recent empirical investigations (Clarke, 2006) found a high number of ultrafine particles as small as 10 nanometres in diameter (dry particle radius, associated with 40% relative humidity) under average wind speed conditions.
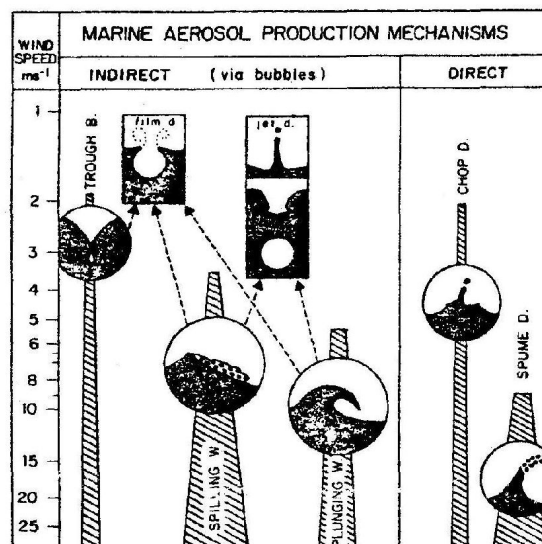
Figure IV.1: Indirect bubble and direct sea salt aerosol formation mechanisms. The relative importance of the mechanisms along with their wind speed dependence is indicated by the column width and length, respectively. Adopted from Monahan (1986).

Salt particles are released from the sea surface through various mechanisms (see Figure IV.1), some being direct, through the movement and subsequent fractionation of the water, others indirect, through released air bubbles in relationship with water motion (Monahan et al., 1986). Since the surface motion of the sea is at least partially driven by the atmosphere, the sea spray flux is a function of the wind velocity. As a surface process, the sea spray flux is expressed in units per surface area. The released droplets disperse vertically, adapting their

size to the ambient humidity conditions.

Sea salt aerosols are likely to interact considerably with the relatively small secondary aerosols and, because of their larger size, should play an essential role to the formation of cloud condensation nuclei. The typical marine aerosol distribution is bimodal (see above). The first mode, the Aitken mode, is commonly considered to be of secondary origin secondary, while the second mode is found to be a mixture of secondary and salt particles and assumed to be or have been activated as cloud nuclei (e.g. Pandis et al., 1994). Sea salt particles should therefore reduce the sensitivity of cloud microphysical properties to the variability of the secondary particles.

It is thus essential to consider sea salt emission and incorporation into the atmospheric aerosol as primary particles in the context of marine cloud condensation nuclei formation. Sea salt particles present effective hygroscopic properties (e.g. Zhou et al., 2001), and the incidence of this property to their size needs to be taken into account. However, in order to simplify considerably the aerosol growth formalism, sea salt will be chemically assimilated to sulphuric acid in this study. Two spectrally resolved parametrizations of sea salt particle emission as a function of the surface wind velocity are presented in this section. These will additionally to binary nucleation serve as a surface source function to aerosol formation.

1.5.2 Parametrization according to Monahan (1986)

The earlier parametrization by Monahan et al. (1982) and Monahan et al. (1986) of sea salt aerosol formation through ocean whitecaps is based on observations obtained under laboratory conditions in a simulation tank. Due to measurement constraints sea salt emission is assumed to be spectrally constrained to particles larger than *r≈0.1 μm* (solid particles at a relative humidity of 40%). It is:

$$\frac{d\Phi_s}{dr_{ws}} = W_i \frac{d\dot{Y}}{dr_{ws}} = \frac{W_i}{\tau}\frac{dY}{dr_{ws}} \simeq -\dot{W}_i \frac{dY}{dr_{ws}}$$

$$\text{,}$$

f IV.34

where Φ_s is the total flux of sea salt particles per unit surface, r_{ws} is the *wet* particle radius, Y is the total yield of sea salt particles per unit surface of the whitecap during the measurement time, and W_i and τ are the fraction of the surface covered by and the decay time of the aerosol releasing whitecap under laboratory conditions, respectively.

143

Now if it is assumed that:

$$\dot{W}_i = -a\,W_i$$

,

then it may be presumed that:

$$W = \sum_{i=1}^{n} W_i = \sum_{i=1}^{n} W_i\{t=0\}\,e^{-at_i}$$
$$\simeq -\int_{0}^{\infty} \dot{W}_i\{t=0\}e^{-at}\,dt$$
$$= -\frac{1}{a}\dot{W}_i\{t=0\}$$

Here it is assumed that the decay constant a is equal for all whitecaps, so that it is indifferent to the whitecap size. Essentially the above equations establishes a link between the single whitecap under laboratory conditions and the mean whitecap coverage fraction under natural conditions. Assuming that the oceanic sea salt aerosol flux is constant under given atmospheric conditions, one gets after comparison of Equations IV.34 and IV.36:

$$\frac{d\,\Phi_s}{dr_{ws}} = aW\frac{dY}{dr_{ws}}$$

Monahan et al. (1982) find $a \approx 0.283\ s^{-1}$.

The ocean fraction covered by whitecaps is assumed to follow the following wind velocity function (Monahan et al., 1982):

$$W = 3.84\cdot10^{-6}u^{3.41}$$

Based on their measurements, Monahan et al. (1986) find that an accurate parametrization of the spectrally resolved yield of salt particles per surface unit of the whitecap is:

$$\frac{dY}{dr_{ws}} = 1.26\cdot10^{-12}\ r_{ws}^{-3}\left(1+0.057(10^6\ r_{ws})^{1.05}\right)10^A$$
$$A = 1.19\,e^{-\left(\frac{0.380-\ln(10^6\ r_{ws})}{0.650}\right)^2}$$

This formula accounts for the heterogeneous distribution of the sea water droplets in the simulation tank.

1.5.3 Parametrization according to Clarke et al. (2006)

Clarke et al. (2006) estimate the sea salt particle yield of coastal breaking waves at a Hawaiian measurement site approximately 20 to 30 metres from the water edge. Their measurements indicate that the aerosol concentration below a height of 5 m is strongly variable over short time intervals corresponding to the successive arrivals of breaking waves, so that the productivity of the associated whitecaps may be inferred. Coastal breaking waves show two productive areas of aerosol release via bubble formation, a zone of plunging wave formation at the wave front and a zone of spilling wave formation behind the front. Assuming that the productivity of both zones is equal, the total release of sea salt particles through one breaking wave event reads:

$$Q_p = \int_{\tau_1} \Phi_{S,w} \left(A_{av} d\{t\} + w\{t\} \right) dl\, dt \simeq \Phi_{S,w} \left(A_m d + 0.5\, w_0 \right) dl\, \tau_1$$

f IV.40

where $\Phi_{S,w}$ is the sea salt source function per unit time and surface completely covered by bubbles, A_{av} is the mean fractional spilling area behind the front, d is the distance covered by the breaking wave upon formation to the shore line, w_0 is the initial width of the front, dl is the length increment of the braking wave along the shore line, and τ_1 is the duration of the breaking event.

The measured total quantity of released particles at the measurement site is:

$$Q_m = \int_h \int_{\tau_2} \Delta N_s v\, dl\, dt\, dz \simeq k\, \Delta N_s v\, h\, \tau_2\, dl$$

f IV.41

ΔN_S is the observed variation of the sea salt particle number concentration attributed to the breaking event, k is a corrective constant accounting for measurement height, v is the horizontal velocity of the wind, h is the height of the aerosol plume, and τ_2 is the duration of the sea salt concentration variation at the measurement site.

Assuming that the total quantity of salt particles released at the sea surface is transformed into a horizontal flux towards the measurement site, and that the corresponding time intervals are equal, the above equations may be equalled, yielding the surface source function of sea salt particles independently of the shore length increment and the duration of the breaking event. Clarke et al. (2006) thus find the spectrally resolved source function of the breaking wave whitecaps to follow the parametrization:

145

$$\frac{d\,\Phi_{S,w}}{d\log r_{ds}} = \sum_{i=1}^{3} A_i$$

$$with:\quad A_i = \sum_{j=1}^{6} a_{ij}\, r_{ds}^{\,j-1} \quad,$$

f IV.42

where r_{ds} is the dry (40% relative humidity) particle radius, $0.005 < r_{ds} < 4\ \mu m$.
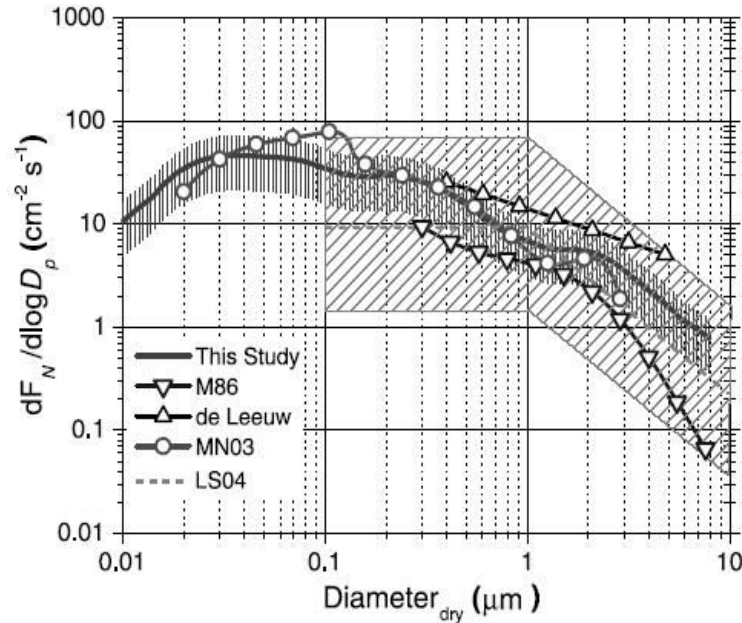
Figure IV.2: Comparison of the sea salt flux according to Clarke et al. (2006; =this study), laboratory estimations (Monahan et al., 1986; Martensson et al., 2003), model results fitted to measurements (de Leeuw et al., 2000) and mean observation derived estimations (Lewis and Schwartz, 2004). An error estimation to the measurements of Clarke et al. (2006) is also indicated. Wind speed is 9 m/s, results are spectrally resolved for dry particles (relative humidity r=0.4). Adapted from Clarke et al. (2006).

Clarke et al. (2006) assume that the mean sea salt source function of the coastal breaking wave productive area may be related to the mean open ocean surface source function in analogy to Equation IV.37. Their spectrally resolved source function is approximately two to three times more productive than the Monahan (1986) parametrization and yields an important quantity of particles of Aitken mode size (Figure IV.2).

IV.2 The one-dimensional model of aerosol cloud interaction

IV.2.1 Introduction

To simulate the interaction of the marine aerosol with cloud microphysical properties the preceding aerosol mechanical model was integrated into the one-dimensional version of the shallow cloud model (SCM) of Chlond et al. (2004). Originally, the model represents cloud microphysics leading to rain formation with the Kessler scheme (Kessler, 1969). Atmospheric moisture is subdivided in atmosphere gas phase, cloud liquid phase, and rain liquid phase rain moisture. Whilst the rain water content is determined prognostically, neither the cloud and rain droplet number concentration nor their size distribution are considered explicitly within the Kessler scheme. The cloud moisture content is assessed diagnostically considering total moisture, rain water and the saturation gas phase moisture. In order to use the additional information rendered by the aerosol box model an alternative scheme of aerosol/cloud droplet/raindrop interaction is derived in this study.

Vertical transport in the one-dimensional model is differentiated into a large scale, i.e. synoptic, and a small scale, i.e. subscale, flux. The subscale flux comprises turbulent transport from large Eddies down to the Kolmogorov microscale and assumed to be a diffusive process. The parametrized turbulent diffusion coefficients depend on the estimated energetic state of the atmosphere. The synoptic movement of the air is more or less balanced with cloud entrainment at the top of the boundary layer. Temperature is expressed in the conservative form of the liquid water potential temperature, which is equivalent to the temperature of the air when the totality of atmospheric moisture is evaporated regardless of the saturation pressure. All extensive quantities, such as atmospheric moisture, aerosol, ion, and sulphuric acid contents are expressed as mixing ratios relative to the dry air mass. These expressions are inappropriate to the aerosol growth formalism, which is related to the specific values exclusively.

The number of vertical levels of the one-dimensional model is deliberately fixed to 12 in this study, corresponding to a total height of 1200 metres. The model allows simulating the dynamical behaviour of aerosol growth in the totality of the vertical layer whilst the

computation time is restricted to limited figures. Sulphuric acid formation is assumed to be vertically homogeneous in terms of the mixing ratio, the ionization rate is assumed to increase linearly with height (Reiter, 1992). Along with the realistic temperature and moisture gradients height specific nucleation and growth rate gradients are generated, which tend to be levelled out by turbulent diffusion. The formalism of interaction between aerosol particles and cloud droplets, as well as of sulphuric acid scavenging through cloud droplets, assumes that cloud droplets follow the Khrigian-Mazin size density distribution. The cloud droplet number depends on the maximum supersaturation during aerosol particle activation as cloud condensation nuclei. Due to boundary layer convection water vapour and inactivated aerosol particles penetrate clouds continuously at their lower border. Conversely activated particles leave the cloud in the opposite direction. Water vapour supersaturation is maximal within penetrating air since there are no mature cloud droplets acting as effective sinks. In the present context of a vertical resolution of 100 metres, it is questionable whether aerosol particle activation may be appropriately represented. The cloud scavenges the subcritical particles in its vicinity so that the aerosol should tend to become vertically homogenized. As to particle population dynamics, the critical activation radius should therefore only be a moderate time function. However, turbulent diffusivity shows a pronounced vertical and temporal variability thus inducing a complex time dependency of the critical activation radius and requiring a high spatial resolution.

The Kessler scheme relies on a conceptual distinction between cloud droplets and raindrops based on size spectral considerations. In this context the raindrop liquid water amount increases through coagulation of cloud droplets onto raindrops, process qualified as accretion, as well as a result of coagulation among large enough cloud droplets, the products of which exceed the lower raindrop size limit, thus leading to an autonomous growth flux of cloud droplets to raindrops that is represented by the concept of autoconversion. The autoconversion rate is estimated according to an appropriate scheme of mutual cloud droplet interaction based on size moment considerations. The accretion rate is assessed with a kernel of cloud droplet raindrop interaction taking into account the size distribution of the latter and derived in analogy to the Kessler scheme.

For aerosols of the lowest cell gravitational settling is taken into account. Turbulent motion tends to zero next to the surface, and it may therefore be excluded as a direct deposition process as far as sea waves do not act as aerosol capturers. Settling through Brownian

movement is assumed to be negligible.

IV.2.2 Diagnostic assessment of the cloud liquid water content

The relationship between cloud liquid water, water vapour and rain water is given by:

$$Q_V = Q - (Q_C + Q_R)$$

f IV.43

where Q is the mixing ratio of the total atmospheric water [-], Q_V is the water vapour mixing ratio, and Q_C and Q_R are the cloud and the rain liquid water mixing ratios, respectively.

The cloud liquid water is corrected for the condensation heat release and the ensuing increase of the partial saturation pressure. It is:

$$Q_{sat}\{T_f\} = Q_{sat}\{T_i\} + \frac{dQ_{sat}}{dH}\Big|_{H\{T_i\}} \Delta H$$

f IV.44

where Q_{sat} is the saturation water vapour mixing ratio, H is the enthalpy of the air per total unit mass of the air, T_i is the air temperature prior to condensation, T_f is the temperature of the air after condensation of all excess water. When explicitly derived to temperature the preceding expression becomes:

$$Q_{sat}\{T_f\} = Q_{sat}\{T_i\} + \frac{dQ_{sat}}{dT}\Big|_{T_i} \frac{L_w}{c_p}\left((Q - Q_R) - Q_{sat}\{T_f\}\right)$$

f IV.45

where L_W is the water condensation enthalpy [J kg⁻¹] and c_P the air bulk heat capacity at constant pressure [J kg⁻¹ T⁻¹]. It is assumed that the heat capacity is constant and equal to the dry air value.

Solving for $Q_{sat}\{T_f\}$:

$$Q_{sat}\{T_f\} = Q_{sat}\{T_i\} \frac{1 + \dfrac{Q - Q_R}{Q_{sat}\{T_i\}} \dfrac{L_w}{c_p} \dfrac{dQ_{sat}}{dT}\Big|_{T_i}}{1 + \dfrac{L_w}{c_p} \dfrac{dQ_{sat}}{dT}\Big|_{T_i}}$$

f IV.46

with the Clausius-Clapeyron equation:

$$\frac{1}{Q_{sat}} \frac{dQ_{sat}}{dT} = \frac{1}{e_{sat}} \frac{de_{sat}}{dT} = \frac{m_w L_w}{R T^2} \quad ,$$

f IV.47

where e_{sat} is the saturation partial pressure of water vapour [Pa].

The cloud liquid water content upon condensation thus becomes:

$$Q_C\{T_f\} = \left(Q - Q_R - Q_{sat}\{T_f\}\right) .$$

f IV.48

The above quantity is transformed into its specific value using:

$$q_C = \frac{p_{tot}}{R T} \frac{m_a}{1 + Q_V \frac{m_a}{m_w}} Q_C \quad ,$$

f IV.49

where q_C is the specific cloud moisture [kg m^{-3}] and p_{tot} is the total pressure of wet air.

The mean volume radius of the cloud droplets then becomes:

$$r_C = \sqrt[3]{\frac{3}{4\pi} \frac{q_C}{\rho_w} \frac{1}{N_C}} \quad ,$$

f IV.50

where N_C is the cloud condensation nuclei number concentration.

IV.2.3 Maximum supersaturation and critical radius of aerosol activation

The Lagrangian variation rate of the water vapour mixing ratio within a rising air parcel reads:

$$\frac{d Q_V}{d t} = w \frac{\partial Q_V}{\partial z} + \frac{\partial Q_V}{\partial t} \quad ,$$

f IV.51

where w is the vertical velocity of the air parcel. Note the spatial derivative of the conservative mixing ratio is null, and the previous expression reduces to the second term of the right hand side. Transport variation of the water vapour mixing ratio is contained within the second term under the present diffusive approach to turbulence.

Within the framework of the boundary layer model the partial temporal derivative of the water vapour mixing ratio is:

$$\frac{\partial Q_V}{\partial t} = D \frac{\partial^2 Q_V}{\partial z^2} - \frac{\partial Q_V}{\partial t} \{cond.\}$$

f IV.52

where the first term on the right hand side stands for turbulent transport while the second term represents condensation losses. The contribution of turbulent transport is regarded to be relatively negligible, so that the total variation rate of the water vapour mixing ratio of a rising air parcel simplifies to the condensation losses.

In analogy the temperature variation rate of a rising air parcel is:

$$\frac{dT}{dt} \simeq w \frac{\partial T}{\partial z} + \frac{\partial T}{\partial t} \{cond.\}$$

f IV.53

This expression implies that turbulent and conductive heat exchange may be neglected on the considered time scale. The adiabatic temperature derivative is:

$$\frac{\partial T}{\partial z} = -\frac{g}{c_p}$$

f IV.54

where g is the gravitational acceleration.

The relevant vertical velocity of the air parcel may be estimated with:

$$w \simeq \sqrt{\frac{2}{3} E_{cin}}$$

f IV.55

where E_{cin} is the kinetic energy per unit air mass as given by the boundary layer model. Synoptic air motion is neglected in this formula.

The variation of temperature through condensation is:

$$\frac{\partial T}{\partial t} = -\frac{L_w}{c_p} \frac{\partial Q_V}{\partial t}$$

f IV.56

The mixing ratio variation of the water vapour content may be transformed into its specific counterpart using Equation III.48; the atmospheric pressure may be assumed to remain constant, so that:

$$\frac{\partial q_V}{\partial t} \{cond\} = \sum_{i=1}^{n} \sum_{q=1}^{m} \left(\phi_D^M \right)_{iq} N_i^q \delta_{r_i > r_l}$$

f IV.57

where ϕ^M_D is the diffusive condensation mass flux of water vapour onto particles of size class i and charge class q [kg s^{-1}]. Condensation in the free molecular regime, that is onto particles smaller than 10 nanometres in this study, is neglected.

The mass related diffusion flux is (Pruppacher and Klett, 1997):

$$\left(\phi^M_D\right)_{iq}=4\pi r_{iq} D_w\left(q_V-q_{sat}\{r_{iq}\}\right)$$

f IV.58 ,

with the perfect gas law:

$$q_{sat}\{r_{iq}\}=\frac{m_w}{R}\frac{e_{sat}\{r_{iq}\}}{T\{r_{iq}\}} \quad .$$

f IV.59

Equation III.62 yields for the diffusion coefficient of water vapour in air:

$$D_w=2.13\cdot10^{-5}\left(\frac{T}{273.15}\right)^{1.75}\left(\frac{101325}{p}\right) \quad .$$

f IV.60

For strong solutions the saturation pressure of a charged particle is assessed according to the Thomson equation (see Expression III.31):

$$e_{sat}\{r_{iq}\}=e_{sat}\{r_\infty,\alpha_{w,l}=1\}\alpha_{w,l}e^{\left(\frac{2m_w\sigma}{RT\rho_{s,w}r_{iq}}\left(1-\frac{q^2}{64\pi^2\epsilon_0\sigma}\left(1-\frac{1}{\epsilon_r}\right)\frac{1}{r_{iq}^3}\right)\left(1+\frac{X_s}{\rho_{s,w}}\frac{d\rho_{s,w}}{dX_s}\right)\right)}$$

f IV.61 ,

where $\rho_{s,w}$ is the density of the particle solution.

The latter expression is obtained with Equations III.34 and III.35 combined to VII.14 and letting:

$$e_{sat}\{r_{iq}\}=e\{r_{iq}\}$$

f IV.62

under local equilibrium conditions between the gas and the liquid phase at particle surface.

The liquid phase of activated particles is considered to be dilute to the point that Expression IV.61 may reduce to the following shape (Puppacher and Klett, 1997):

$$e_{sat}\{r_{iq}\}=e_{sat}\{r_\infty\}\ \exp\left(\frac{A}{r_{iq}}-\frac{B}{M_{iq}/M_{s,iq}-1}\right) \quad ,$$

f IV.63

where A and B are the curvature, that is the surface tension, and the hygroscopicity parameter,

respectively. The parameter A depends on the surface tension of pure water, which is approximatively a linear temperature function (Jacobson, 1999, p. 428). According to Hänel (1987) it follows:

$$A = 5.087\text{e-}7\,T^{-1} - 6.630\text{e-}10$$

f IV.64

Still, the variation of particle density through water vapour condensation may be neglected for a dilute solution:

$$\frac{d\,\rho_{s,w}}{d\,r}\{r \to r_{min}\} \cong \frac{d\,\rho_w}{dr} = 0 \quad,$$

f IV.65

where $\rho_{s,w}$ is the density of the salt solution, ρ_w is the density of the pure water solution and r_{min} is the critical activation radius.

The equivalent critical activation radius at 99% relative humidity should not be much less than 50 nanometres. The corresponding minimum number of elementary charges to induce a 5% variation of the surface saturation pressure would not be less than 30 according to Equation IV.61. For the same particle bearing five elementary charges the induced relative variation of the saturation pressure would be 0.1%. However, particles of comparable size rarely bear more than a couple of charges (Pruppacher and Klett, 1997; compare also with Figure V.37 below). As a corollary, the direct influence of particle charge on the process of particle activation should be limited. These findings contrasts with experimental evidence of Chen et al. (2000) showing that the activation of charged particles is enhanced. The chemically indifferent Thomson equation does not allow explaining this phenomenon.

Deriving Equation IV.63 it has been assumed that the fractional activity of diluted solutions is:

$$\ln \alpha = -(a+b)\frac{n_s}{n_w} \quad.$$

f IV.66

Thus, the parameter B is:

$$B = (a+b)\frac{m_w}{m_s} \quad,$$

f IV.67

where $a+b$ is the sum of anions and cations the solute dissociates into, and m_S and m_w are the molecular masses of the solute and pure water, respectively.

In order to close the equation system of condensation growth of cloud droplets the temperature at the surface of the drop needs to be assessed. The rate of heat release at the surface of the droplet is proportional to the rate of droplet mass increase. Assuming equilibrium at the droplet surface between the heat released through condensation and the diffusive transport of heat leads to:

$$\frac{dH_{iq}}{dt} = -L_w \frac{dM_{iq}}{dt} \quad .$$

f IV.68

This pseudo-equilibrium assumption is in analogy to the formalism that leads to the expression of the nucleation rate as a function of the equilibrium concentration of the critical cluster.

According to Pruppacher and Klett (1997) the latent heat enthalpy of water follows the following temperature function for 253<T<313 K:

$$L_w = 2499.1e3 - 2.35e3 \cdot (T - 273.15) \quad .$$

f IV.69

The flux of thermal energy reads in analogy to equation IV.58:

$$\frac{dQ_{iq}}{dt} = 4\pi r_{iq} k_{aw} (T\{\infty\} - T\{r_{iq}\}) \quad ,$$

f IV.70

where k_{aw} is the thermal conductivity of moist air [J K^{-1} m^{-1} s^{-1}].

Assimilating the thermal conductivity of moist air to the one of dry air:

$$k_a = 2.38e\text{-}2 + 7.12e\text{-}5(T - 273.15) \quad .$$

f IV.71

The combination of Equations IV.68 and IV.70 leads to:

$$T\{r_{iq}\} = T\{\infty\} + \frac{L_w \rho}{k_a} r_{iq} \frac{dr_{iq}}{dt} \quad .$$

f IV.72

During particle activation cloud droplet coagulation may be neglected as it is relatively slow. Supersaturation increases until a maximum value prior to decreasing again as water vapour consumption increases with growing droplet size. The critical activation radius is then given by the following system:

154

$$s_{max} \equiv \frac{e_{sat}\{r_{min}\}}{e_{sat}\{r_\infty\}} = f\{r_{min}, r_{s,min}\} \quad (1)$$

$$\frac{d\,s}{dr_{iq}}\Big|_{r_{iq}=r_{min}}^{s=s_{max}} = 0 \qquad\qquad (2) \quad,$$

f IV.73

where s_{max} is the maximum supersaturation, r_{min} is the critical activation radius under given conditions and $r_{s,min}$ is the corresponding dry particle radius. Equation (1) is a modification of IV.63.

This system (Hänel, 1987) yields the wet radius of the particular particle whose maximum water surface pressure during condensation growth is equivalent to the actual air maximum supersaturation obtained under given conditions of the aerosol spectrum and air temperature variation; using Equation IV.65:

$$r_{min} = \frac{AB}{3\ln s_{max}} \frac{1 - \frac{3}{B}\ln s_{max} + \sqrt{1 + \frac{3}{B}\ln s_{max}}}{B - \ln s_{max}} \quad.$$

f IV.74

The corresponding critical solute mass follows immediately from Equation IV.63:

$$M_{s,min} = \frac{4}{3}\pi r_{min}^3 \rho_w \left(B\left(\frac{A}{r_{min}} - \ln s_m\right)^{-1} + 1 \right)^{-1} \quad.$$

f IV.75

For the number of activated particles to be transient in the framework of discrete size classes within the aerosol growth model, two additional size classes are introduced, each containing the particle fraction that is not activated of the size classes that are adjacent to the critical size. Upon first activation the particles are distributed proportionally, as with the coagulation distribution factors within the nodal scheme of aerosol size discretisation (see Equation IV.1). For size class n_i, where $n_i < n_{min} < n_{i+1}$, it is:

$$N_i^{act} = N_i^{tot} \frac{n_{i+1} - n_{min}}{n_{i+1} - n_{i-1}} \quad, \quad N_i^{nact} = N_i^{tot} - N_i^{act} \quad.$$

f IV.76

The number of activated particles in size class $i+1$ is calculated in analogy.

When the critical radius increases in time it is proceeded as follows for the size class i:

$$N_i^{nact}\{t+\delta t\} = N_i^{nact}\{t\} + N_i^{act}\frac{n_{min}\{t+\delta t\} - n_{min}\{t\}}{n_{i+1} - n_{min}\{t\}}$$

$$N_i^{act}\{t+\delta t\} = N_i^{act}\{t\} + \left(N_i^{nact}\{t+\delta t\} - N_i^{nact}\{t\} \right)$$

f IV.77

For the size class $i+1$ the redistribution is made in analogy. When $n_{min}\{t+\delta t\}$ exceeds $n_{i+1}\{t\}$ all remaining particles in the size class i are deactivated and particles in size class $i+2$ are activated following Equation IV.76. In case that the critical radius decreases in time, or when $n_{min}\{t+\delta t\} < n_i\{t\}$ in particular, the redistribution is realised conversely.

IV.2.4 Aerosol – cloud droplet and cloud – cloud droplet interaction

Physically, cloud droplets are large aerosol particles, to which the theory related to condensation, coagulation and ion attachment developed in the previous chapter applies. The difficulty resides in finding an appropriate linearisation of the growth mechanism to which a representative cloud droplet radius may be associated:

$$\phi_{PROC}\{N_C \to N_i^q\} = \int_0^\infty f_{PROC}\{r_C\}\frac{\partial N_C}{\partial r_C}dr_C \simeq \int_0^\infty (A r_C^i + B)\frac{\partial N_C}{\partial r_C}dr_C \equiv A r_{Ci}^i N_C + B N_C$$

f IV.78

where f_{PROC} is the considered growth process, and r_{Ci} is the i-th moment of the cloud droplet size density distribution.

Pruppacher and Klett (1997, p. 26f) relate that many cloud droplet distributions follow the Khrigian-Mazin distribution:

$$n_C \equiv \frac{\partial N_C}{\partial r_C} = A r_C^2 e^{-Ba}$$

f IV.79

The moment integrals of this distribution are:

$$\int_0^\infty r_C^i n_C dr_C = \frac{A\Gamma\{i+3\}}{B^{i+3}} = r_{Ci}^i N_C$$

f IV.80

where $\Gamma\{x\}$ is the Gamma function, which has the following remarkable properties:

$$\Gamma\{x\}=(x-1)\cdot\Gamma\{x-1\}$$
$$\Gamma\{1\}=1 \ , \ \Gamma\{0.5\}=\sqrt{\pi} \ .$$

f IV.81

From Equation IV.80 applied to the i-th and the 0-th moment one finds for the i-th moment mean radius:

$$r_{Ci}=B^{-1}\left(\frac{\Gamma\{i+3\}}{2}\right)^{1/i} \ .$$

f IV.82

One may thus define:

$$\beta_i=\frac{r_{Ci}}{r_{C3}}=2^{(i-3)/3i}\cdot\frac{(\Gamma\{i+3\})^{1/i}}{(\Gamma\{6\})^{1/3}} \ .$$

f IV.83

Equation IV.80 yields for the cloud droplet number:

$$N_C=\int_0^\infty n_C\,dr_C=2\frac{A}{B^3} \ ,$$

f IV.84

and the cloud water content is:

$$q_C=\frac{4}{3}\pi\rho_w\int_0^\infty r_C^3 n_C\,dr_C=\frac{4}{3}\pi\rho_w 5!\frac{A}{B^6} \ .$$

f IV.85

Combining Equations IV.84 and IV.85 one finds:

$$A=40\pi\rho_w\frac{N_C^2}{q_C}$$
$$B=\left(80\pi\rho_w\frac{N_C}{q_C}\right)^{1/3} \ .$$

f IV.86

According to Equation IV.83 each moment integral may be expressed as a function of the mean volume radius (Equation IV.50) and the appropriate weighing coefficient β_i. Thus, in case of Brownian condensation in the diffusion regime (Equation III.48) one finds for the mean flux of sulphuric acid molecules onto a cloud droplet:

$$\phi_{D,\,p_a\to p_c}\simeq 4\pi\beta_1 r_{C3}D N_a \ .$$

f IV.87

It has been assumed that the transition factor tends to unity for the relevant part of the cloud

droplet size spectrum.

The cloud droplet – aerosol Brownian coagulation kernel (see Equation III.95) is:

$$K_{PD,p_i,p_c} \simeq \frac{2kT}{3\eta_g} E_{PD}\{r_i, r_{C3}\} \left(2 + \beta_{-1}^{-1} \frac{r_i}{r_{C3}} + \beta_1 \frac{r_{C3}}{r_i} \right) .$$

f IV.88

Here the enhancement factor has been assumed to be close to unity and fairly constant for the relevant cloud droplet size range, so that the representative enhancement factor may be associated with the mean volume radius. Again cloud droplets should be large enough for the flux to be purely diffusive.

For a cloud droplet population that is discretised according to its solute content, one finds for the Brownian coagulation kernel among cloud droplets in the diffusion regime:

$$\Phi_{PD,P_c \leftrightarrow P_c'} = \frac{2kT}{3\eta_g} \int_0^\infty \int_0^\infty E_{PD}\{r_C, r_C'\} \left(2 + \frac{r_C'}{r_C} + \frac{r_C}{r_C'} \right) \frac{\partial N_C}{\partial r_C} \frac{\partial N_C'}{\partial r_C'} d r_C' d r_C ,$$

f IV.89

where N_C' and N_C are the total cloud droplet concentrations in the respective solute mass class. Note that the indistinguishableness of cloud droplets of the same solute content class is inherently contained in the above relationship.

When cloud droplets follow the Khrigian-Mazin distribution one finds:

$$\Phi_{PD,P_c \leftrightarrow P_c'} \simeq \left(1 + \delta_{C=C'}\right)^{-1} \frac{2kT}{3\eta_g} E_{PD}\{r_{C3}, r_{C'3}\} \left(2 + 2 \frac{\beta_1}{\beta_{-1}} \right) N_C N_C' .$$

f IV.90

When in analogy to Equation IV.88 the radius dependence of the enhancement factor is neglected, the flux of cloud droplets onto ions reads according to Equation III.138:

$$\phi_{PD,p_c \rightarrow ion} \simeq 4\pi E_{PD}\{r_{ion}, r_{C3}\} \beta_1 r_{C3} D_{ion} N_C .$$

f IV.91

Turbulent coagulation between aerosols and cloud droplets is related to the effective collision cross-section, which is a complex function of both the smaller and larger particle radius. The relevant part of the cloud droplet spectrum should be relatively narrow and limited to the order of say 10 to 50 micrometres. When the effective cross sections related to this size range are compared (Pinsky et al., 2001) one finds their particle size dependence to be limited as soon as the size difference to the smaller particle is of more than one order of magnitude. For

this reason, as far as aerosol cloud droplet interaction are considered, one may neglect as a first approximation the dependence of the effective cross section on the cloud droplet radius:

$$\frac{\partial P_{cs}\{r_i, r_C\}}{\partial r_C} \simeq 0 \quad .$$

f IV.92

In analogy to diffusive coagulation the turbulent enhancement factor is assumed to be close to unity for relatively large particles, and therefore fairly constant. Further, if the particle cross section is approximated through the larger particle radius since $r_{C3} \gg r_i$ one finds for the turbulent shear flux of cloud droplets onto an aerosol particle in accordance with Equations III.141 and III.162:

$$\phi_{\Gamma, p_c \to p_i} \simeq \frac{4}{3} \Gamma P_{ct}^{3/2}\{r_i, r_{C3}\} E_T^{3/2}\{r_i, r_{C3}\} \beta_3^3 r_{C3}^3 N_C \quad .$$

f IV.93

For the turbulent inertial flux one finds under the additional assumption that the Cunningham constant is equal to unity (see Equations III.148 and III.151):

$$\phi_{I, p_c \to p_i} \simeq \frac{2}{9} \pi \left(\frac{\rho_w}{\rho_g} - 1 \right) \frac{\epsilon^{0.75}}{\nu_g^{1.25}} P_{ct}\{r_i, r_{C3}\} E_T\{r_i, r_{C3}\} \beta_4^4 r_{C3}^4 N_C \quad .$$

f IV.94

The gravitational flux of cloud droplets onto an aerosol particle is in analogy to the preceding according to Equation III.154:

$$\phi_{G, p_c \to p_i} \simeq \frac{2}{9} \pi \left(\frac{\rho_w}{\rho_g} - 1 \right) \frac{g}{\nu_g} P_{ct}\{r_i, r_{C3}\} E_T\{r_i, r_{C3}\} \beta_4^4 r_{C3}^4 N_C \quad .$$

f IV.95

In case of cloud droplet – cloud droplet interaction Equation IV.92 does not hold any more. The particles' relevant radius is of the same order of magnitude and the efficiency is a strong size function. The parametrization of turbulent collision efficiency Equation III.162 is not appropriate for cloud droplet collisions since it holds for particles smaller than approximately 20 micrometres only. Moreover it is useful to find a relatively simple formulation of the effective collision cross section that is analytically integrable as a moment of the cloud droplet distribution according to Equation IV.80. Long (1974) provides the following formulation of the collision efficiency as a function of the larger and the smaller particle radius:

$$P_{cs} = k_1 r_1^2 \left(1 - \frac{k_2}{r_2}\right) ,$$

f IV.96

where $k_1 = 4.5 \cdot 10^8 \ m^{-2}$ and $k_2 = 3 \cdot 10^{-6} \ m$. Note that in the previous expression r_1 stands for the larger particle radius.

This formula assumes that the larger particle radius is inferior to 47 micrometres and the smaller particle radius has a minimum radius of 3 micrometres. The corresponding particle size range should essentially cover the relevant part of the cloud droplets spectrum under oceanic conditions (see Pruppacher and Klett, 1998, p. 10 ff.). Consistently with turbulent coagulation among aerosol particles the coalescence probability is assumed to be equal to unity. Hence one finds for the turbulent coagulation flux among cloud droplets:

$$\Phi_{T, p_c \leftrightarrow p_c} = \int_0^\infty \int_0^{r_1} K_T\{r_1, r_2\} n_1 n_2 \, d r_2 d r_1$$
$$\simeq \int_{k_2}^{k_1^{-1/2}} \int_{k_2}^{r_1} K_T\{r_1, r_2\} n_1 n_2 \, d r_2 d r_1 \quad .$$

f IV.97

With Equations III.141 and III.165 and the assumption of a constant near unity turbulent enhancement factor, the previous relationship lead to the following expression in case of turbulent shear:

$$\Phi_{\Gamma, p_c \leftrightarrow p_c} = \frac{4}{3} \Gamma k_1^{3/2} E_T^{3/2}\{r_{C3}, r_{C3}\} \int_{k_2}^{k_1^{-1/2}} F\{r_1\} n_1 dr_1$$
$$F\{r_1\} = \int_{k_2}^{r_1} r_1^3 \left(1 - \frac{k_2}{r_2}\right)^{3/2} (r_1 + r_2)^3 n_2 dr_2 \quad .$$

f IV.98

With the approximation:

$$(1-x)^{3/2} \simeq (1-x) \ (1 - 0.5 \, x - 0.125 \, x^2 - 0.0625 \, x^3 - 0.0390625 \, x^4)$$
$$\simeq 1 - 1.5 \, x + 0.375 \, x^2 + 0.0625 \, x^3 + 0.0234375 \, x^4$$
$$\equiv 1 - c_1 x + c_2 x^2 + c_3 x^3 + c_4 x^4 \qquad ,$$

f IV.99

and (Gradshteyn and Ryzhik, 1965):

$$\int_a^b x^n e^{-cx} dt = \left[-e^{-cx} \sum_{k=0}^{n} \frac{n!}{k!} \ c^{k-n-1} x^k \right]_a^b$$

$$\int_a^b x^{-1} e^{-cx} dt = \left[Ei\{-cx\} \right]_a^b$$

$$\int_a^b x^{-n} e^{-cx} dt = \left[-e^{-cx} \sum_{k=1}^{n-1} \frac{(k-1)!(-c)^{n-k-1}}{(n-1)! \, x^k} + \frac{(-c)^{n-1}}{(n-1)!} Ei\{-cx\} \right]_a^b$$

,

f IV.100

with:

$$Ei\{x\} = \int_{-\infty}^x t^{-1} e^{-t} dt = C + \ln|x| + \sum_{k=1}^{\infty} \frac{x^k}{k \cdot k!}$$

f IV.101

being the exponential integral. $C \approx 0.577216$ is the Euler Constant.

Although Equation IV.98 may thus be solved analytically, it may seem preferable to solve the Equation numerically for computational reasons.

The analogous equation of turbulent inertial cloud droplet interaction is:

$$\Phi_{I, p_c \leftrightarrow p_c} \simeq \frac{2\pi}{9} \left(\frac{\rho_w}{\rho_g} - 1 \right) \frac{\epsilon^{0.75}}{\nu_g^{1.25}} E_T\{r_{C3}, r_{C3}\} \int_{k_2}^{k_1^{-1/2}} \int_{k_2}^{r_1} k_1 r_i^2 \left(1 - \frac{k_2}{r_2} \right) (r_1 + r_2)^2 (r_1^2 - r_2^2) n_1 n_2 dr_2 dr_1$$.

f IV.102

The gravitational flux among cloud droplets is:

$$\Phi_{G, p_c \leftrightarrow p_c} \simeq \frac{2\pi}{9} \left(\frac{\rho_w}{\rho_g} - 1 \right) \frac{g}{\nu_g} E_T\{r_{C3}, r_{C3}\} \int_{k_2}^{k_1^{-1/2}} \int_{k_2}^{r_1} k_1 r_i^2 \left(1 - \frac{k_2}{r_2} \right) (r_1 + r_2)^2 (r_1^2 - r_2^2) n_1 n_2 dr_1 dr_2$$.

f IV.103

Note that the two preceding equations are proportional and may also be solved analytically.

In the context of cloud droplet discretisation according to their solute content, the respective turbulent coagulation flux of activated particles of class i onto activated particles of class j is:

$$\Phi_{T, p_i \leftrightarrow p_j} = \int_{k_2}^{k_1^{-1/2}} \int_{k_2}^{r_i} k_1 r_i^2 \left(1 - \frac{k_2}{r_j} \right) K_T\{r_i, r_j, P_{ct} \equiv 1\} n_i n_j dr_i dr_j$$
$$+ \int_{k_2}^{k_1^{-1/2}} \int_{r_i}^{k_1^{-1/2}} k_1 r_j^2 \left(1 - \frac{k_2}{r_i} \right) K_T\{r_i, r_j, P_{ct} \equiv 1\} n_i n_j dr_i dr_j$$.

f IV.104

161

IV.2.5 The rainwater content

The rainwater mixing ratio is determined prognostically according to the Kessler scheme (Kessler, 1969). The equivalent local specific tendency is defined as follows:

$$\frac{\partial q_R}{\partial t}=\frac{\partial q_R}{\partial t}\{auto\}+\frac{\partial q_R}{\partial t}\{acc\}+\frac{\partial q_R}{\partial t}\{eva\}+\frac{\partial q_R}{\partial t}\{sed\}$$,

f IV.105

where the first term on the right hand side stands for the rainwater increase through autoconversion, the second term refers to the accretion flux, the third term represents the rainwater loss through evaporation in relationship with unsaturated air, and the last term expresses the loss of rainwater through raindrop sedimentation. Rainwater sedimentation is treated as a local tendency since in the context of the shallow cloud model of Chlond et al. (2004) raindrops are assumed to move independently of the local air velocity.

The raindrop size distribution is presumed to follow the Marshall-Palmer distribution:

$$\frac{dN_R}{dr_R}=N_0 e^{-\lambda r_R}$$,

f IV.106

where:

$$\lambda=\left(\frac{8\pi\rho_w N_0}{q_R}\right)^{0.25}$$,

f IV.107

and $N_0=2\cdot 10^7\ m^{-4}$.

The moment integrals of this function read:

$$P^{(k)}=\int_0^\infty r^k N_0 e^{-\lambda r}\,dr=\frac{N_0\Gamma\{k+1\}}{\lambda^{k+1}}$$,

f IV.108

where $\Gamma\{x\}$ is the Gamma function.

Under gravity raindrops are assumed to fall strictly vertically at constant, i.e. terminal velocity. In the original Kessler scheme the terminal fall velocity is a linear function of the square root of the raindrop radius:

$$v_{Rg,r} = a\sqrt{2\,r_R}$$

f IV.109 ,

where $a = 130\ m^{0.5}s^{-1}$ is an empirical proportionality factor.

The mean volume falling velocity is:

$$v_{Rg3} = q_R^{-1}\int_0^\infty v_{Rg,r}\frac{4}{3}\pi\,r_R^3\rho_w\frac{dN_R}{dr_R}dr_R \ .$$

f IV.110

The sedimentation rate is:

$$\frac{\partial q_R}{\partial t}\{sed\} = -238.19\left(\rho_w N_0\right)^{-0.125}\frac{\partial q_R^{1.125}}{\partial z} \ .$$

f IV.111

The evaporation rate is parametrized proportionally to the saturation deficit of the air. It is a power function of the air density and the specific rainwater content:

$$\frac{\partial q_R}{\partial t}\{eva\} = 0.0485\left(\rho_a q_R\right)^{13/20}\left(q_V - q_{sat}\right) \ .$$

f IV.112

The Kessler scheme does not require knowledge on the cloud droplet number concentration. The information on the actual cloud droplet number provided by the aerosol-cloud droplet growth dynamical system may not be used unless appropriate formulations of the related accretion and autoconversion rates are found.

2.5.1 The accretion rate

The accretion rate conveys the integrated flux of raindrops onto both cloud droplets and aerosol particle, so that for a single particle:

$$\begin{aligned}\Phi_{N_R\to N_i} &= \int_{N_R} P_{ct}\{r_R,r_i\}\ \pi(r_R+r_i)^2\ v_g\{r_R,r_i\}\ dN_R\\ &\simeq P_{ct}\{r_i,r_{R3}\}\int_{N_R}\pi\,r_R^2 v_{Rg}\{r_R\}dN_R\end{aligned}$$.

f IV.113

In the previous relationship it is assumed that the exclusive driving force of aerosol/cloud droplet raindrop encounter is the relative terminal gravitational fall velocity. This is in accordance with the above investigation on turbulent coagulation, which showed that with increasing radius of the larger particle, gravitational coagulation tends to become the

dominant process. Since the size difference between the largest aerosol particle/cloud droplets and the relevant raindrops is very large, the smaller particle radius may be neglected in relationship with the particle collision cross section and the relative velocity. Conversely, the effective relative collection cross section may be approximated to be exclusively a function of the smaller particle size. As a matter of fact, the part of the raindrop spectrum that is relevant to the Expression IV.113 is relatively narrow. Further, the dependency of the collection cross-section on the larger particle radius is very low when the smaller particle is several orders of magnitude smaller (Pinsky et al., 2001), so that the mean raindrop volume radius may serve for its evaluation.

For typical cloud droplets the relative effective cross-section is close to unity. Using Equation III.108 the total flux of raindrop particles onto a cloud particle thus becomes:

$$\phi_{N_R \rightarrow N_C} = \Gamma\{3.5\} \sqrt{2}\, a \left(\pi N_0\right)^{0.125} \left(\frac{q_R}{8 \rho_w}\right)^{0.875} .$$

f IV.114

For aerosol particles, however, the relative effective collision cross section may considerably differ from unity, and may not be neglected although it is only a week function of the raindrop size. The mean volume radius of Marshall-Palmer distributed raindrops is:

$$r_{R3} = \sqrt[3]{\frac{3 q_R}{4\pi \rho_w N_R}} .$$

f IV.115

Equation IV.108 yields for *k=1*:

$$N_R = \frac{N_0}{\lambda} .$$

f IV.116

The parametrization of the effective cross section of aerosol-aerosol and aerosol-cloud droplet coagulation presented in this study formally accounts for inertial impaction and interception. The negligence of Brownian motion is appropriate as turbulent processes should be relevant when Brownian motion is negligible and conversely (see section III.4.5). In case of aerosol scavenging through raindrops, however, gravity tends to be the driving force of particle encounter indifferently of aerosol size, so that the effective cross-section may be considerably enlarged by Brownian motion. Additional processes that modify the effective cross section are thermophoresis, diffusiophoresis and electrostatic attraction (Pruppacher and Klett, 1997). Moreover, these processes should have a relevant contribution to the accretion flux as such,

independently of the effective collision cross-section of gravitational coagulation. The resulting collision efficiency may be represented by the sum of the individual process actions (Slinn, 1977, Loosmore and Cederwall, 2004, and Andronache et al., 2006):

$$P_{ct} = \sum_{i=1}^{5} P_{ct,i} \quad .$$

f IV.117

The inertial impaction efficiency is expressed by (Slinn, 1977, Loosmore and Cederwall, 2004):

$$P_{ct,IP} = \left(\frac{Re_{St,p} - Re_{St,R}^*}{Re_{St,p} - Re_{St,R}^* + 2/3} \right)^{3/2} \left(\frac{\rho_p}{\rho_w} \right)^{1/2} ,$$

f IV.118

where $Re_{St,p}$ is the Stokes number of the aerosol particle according to Equation III.159 and $Re_{St,R}^*$ is the so-called critical Stokes number defined by:

$$Re_{St,R}^* = \frac{1.2 + \dfrac{1}{12} \ln(1 + Re_R)}{1 + \ln(1 + Re_R)} ,$$

f IV.119

where Re_R is the Reynolds number of the raindrop.

The concept of the critical Stokes number is introduced by Slinn (1974). It reflects that inertial collision is assumed to be impossible whenever the smaller particle Stokes number is smaller than a critical value, which is related to the raindrop size.

The interception collection efficiency is given by (Slinn, 1977, Loosmore and Cederwall, 2004, Andronache et al., 2006):

$$P_{ct,IT} = 4 \frac{r_p}{r_R} \left(\frac{\eta_a}{\eta_w} + (1 + 2 Re_R^{0.5}) \frac{r_p}{r_R} \right) \quad .$$

f IV.120

The dynamic viscosity of the air is evaluated with Equation III.101. The viscosity of pure water may be assessed using (Pruppacher and Klett, 1997, p. 93f):

$$\eta_w = 1.76\text{e-}3 \cdot \exp\left(\sum_{i=1}^{3} c_i (T - 273.15)^i \right), \quad T > 273.15\,K$$
$$c_1 = -3.5244\text{e-}2, \quad c_2 = 4.7163\text{e-}4, \quad c_3 = -6.0667\text{e-}6$$

f IV.121

Comparing the latter expressions of impaction and interception collection efficiency to the

parametrization III.162 of the effective cross section of turbulent coagulation among aerosol and cloud droplets, it appears that the approach of Slinn does not represent impaction and interception efficiency as concurrent and therefore competing processes. Considering their simultaneousness Davenport and Peters (1978) have assumed these processes to be linear. Similarities between the parametrization of turbulent coagulation and the above expressions include that the turbulent the impaction efficiency is commonly a function of the Stokes number whilst interception is mainly a function of the ratio of the particle radii. For aerosol scavenging a weighing as to the relative influence of the smaller and the larger particle is unnecessary since the influence of the raindrop is clearly dominant.

Brownian diffusion, thermophoresis, diffusiophoresis and electrostatic interaction may be seen to be independent processes exclusively. In order to incorporate these processes into Equation IV.117 the ratio of the respective process to the gravitational accretion flux has to be evaluated, it is (Davenport and Peters, 1978):

$$P_{ct,i} = \frac{\int\limits_{N_R} 4\pi r_R^2 \frac{D_i}{r_R} dN_R}{\int\limits_{N_R} \pi r_R^2 v_R dN_R} \simeq \frac{4 v_i}{v_R} \quad ,$$

f IV.122

where D_i is the diffusion coefficient associated to the considered process i. This relationship is equivalent to the ratio of the raindrop surface to the raindrop cross-section weighed with the respective flux velocity. The velocity v_i is the drift velocity resulting from the equilibrium of the considered driving force and the friction force exerted by the gaseous medium.

The effectiveness of the diffusive processes tends to be somewhat higher by the additional turbulent driving energy in the atmospheric boundary layer. The ratio of the convective diffusion constant to the purely Brownian diffusion constant is given by the Sherwood number. According to Skelland (1974, p. 276) it takes the following shape when $20<Re_R<2000$:

$$Sh_R \simeq 1 + 0.4 Re_R^{1/2} X_i^{1/3}$$

f IV.123 ,

where X_i is the ratio of the respective process to the cinematic viscosity acceleration exerted on the aerosol particle.

In case of Brownian diffusion and diffusiophoresis X is given by the respective Schmidt number of the considered aerosol particle:

$$Sc_i = \frac{\nu_a}{D_i} \quad .$$

f IV.124

For thermophoresis the ratio X is equal to the Prandtl number:

$$Pr = \frac{c_p \eta_a}{k_a} \quad ,$$

f IV.125

where c_p is the heat capacity of the air at constant pressure, and k_a is the heat conductivity of the air. According to Jacobson (1999) $c_p = 1004.67 \ J \ K^{-1} \ kg^{-1}$ at 298.15 K for dry air.

Combining Equations IV.122, IV.123 and IV.124 the Brownian diffusion equivalent collection efficiency is expressed by (Slinn, 1977, Loosmore and Cederwall, 2004, and Andronache et al., 2006):

$$P_{ct,D} = \frac{4}{Re_R Sc_p} \left(1 + 0.4 \, Re_R^{1/2} \, Sc_p^{1/3} \right) \quad ,$$

f IV.126

where Sc_p is the Schmidt number of the aerosol particle.

The diffusion coefficient of the aerosol particle is calculated according to Equation III.94 multiplied by the slip correction factor according to III.98. Note that Loosmore and Cederwall (2004) and Andronache et al. (2006) have retained a slightly different expression of the Sherwood number. For consistency reasons with the following equations the preceding formulation is adopted however.

The drift velocity related to thermophoresis is resulting from the equilibrium between the Stokes friction force and the thermal diffusion force, it is (Waldmann, 1959; Davenport and Peters, 1978):

$$v_{TP} = \frac{C_p \left(2 k_a + 5 \frac{\lambda_g}{r_p} k_w \right)}{\left(1 + 3 \frac{\lambda_g}{r_p} \right) \left(2 k_a + k_w + 5 \frac{\lambda_g}{r_p} k_w \right)} \frac{k_a}{5 p} \frac{T\{\infty\} - T\{r_R\}}{r_R} \quad ,$$

f IV.127

where C_p is the Cunningham slip flow correction factor of the scavenged particle, λ_g is the mean free path of an air molecule, p is the atmospheric pressure, k_a is the thermal conductivity of the air and k_w is the thermal conductivity of liquid water. According to Jacobson (1999, p. 12) $k_w = 0.6 \ J \ K^{-1} m^{-1} s^{-1}$ at $T = 298.15 \ K$.

Combining Equations IV.122, IV.123, IV.125, and the preceding one finds for the thermophoretic equivalent collection efficiency (Davenport and Peters, 1978, Andronache et al., 2006):

$$P_{ct,TP} = 4 \frac{v_{TP}}{v_R} \left(1 + 0.4 \, Re_R^{1/2} \, Pr^{1/3} \right) \quad .$$

f IV.128

The driving temperature gradient of thermophoresis may be assessed combining Equations IV.72, IV.107, IV.112, and IV.115:

$$\frac{T\{\infty\} - T\{r_R\}}{r_R} = \frac{L_w \rho_w}{k_a} \frac{\partial r_R}{\partial q_R} \frac{\partial q_R}{\partial t} \{eva\}$$

$$= 0.0485 \left(\rho_a q_R \right)^{13/20} \frac{L_w}{k_a} \sqrt[3]{\frac{3}{4} \left(\frac{8 \rho_w^9}{\pi^3 N_0^3} \right)^{0.25}} \frac{\left(q_{sat} - q_V \right)}{4 q_R^{0.75}} \quad .$$

f IV.129

The diffusiophoretic drift velocity is according to Davenport and Peters (1978):

$$v_{DP} = \frac{T\{\infty\} D_w}{p} \sqrt{\frac{m_w}{m_a}} \frac{\dfrac{e_{sat}}{T}\{r_R\} - \dfrac{e}{T}\{\infty\}}{r_R} \quad ,$$

f IV.130

where D_w is the molecular diffusion constant of water vapour in the air.

In analogy to thermophoretic accretion one finds for the diffusiophoretic equivalent collection efficiency:

$$P_{ct,DP} = 4 \frac{v_{DP}}{v_R} \left(1 + 0.4 \, Re_R^{1/2} \, Sc_w^{1/3} \right) \quad ,$$

f IV.131

where Sc_w is the Schmidt number of water vapour molecules in the air.

The electrostatic attraction force is treated here as an independent process. The electrostatic accretion flux may therefore be regarded to be fully diffusive in case of small aerosol particles impinging on a large raindrop. Applying Equation IV.117 yields (Davenport and Peters, 1978, Andronache et al., 2006):

$$P_{ct,E} = 4 \frac{C_p q_R q_p}{24 \pi^2 \epsilon_0 \eta_a r_R^2 r_p v_R} \quad .$$

f IV.132

Note that in the previous expression the Sherwood factor has not been included since

turbulent diffusion is considered to be a disjunct process.

The mean electrostatic charge of a raindrop particle depends on the atmospheric conditions. According to Pruppacher and Klett (1997, p. 807) the mean absolute charge of a raindrop is for weakly charged warm clouds:

$$q_R = 6.6 \cdot 10^{-11} \, r_R^{1.3}$$

f IV.133

Combining Equations IV.114 and IV.117 according to the assumptions of IV.113 the flux of raindrops onto an aerosol particle becomes eventually:

$$\phi_{N_R \to N_i^q} = \sum_{j=1}^{5} P_{ct,j}\{r_{R3}, r_{iq}\} \cdot \phi_{N_R \to N_i^q}\{P_{ct} \equiv 1\}$$

f IV.134

Note that the unit collection efficiency accretion flux of raindrops onto aerosol particles is in analogy to Equation III.113 and that the effective collision cross-section is approximated by its mean raindrop volume equivalent.

The total accretion rate of raindrops onto aerosol particles and cloud droplets thus becomes:

$$\frac{\partial q_R}{\partial t}\{acc\} = \frac{4}{3}\pi \sum_{i=1}^{n_{crit}} \sum_{q=1}^{m} \phi_{N_R \to N_i^q} r_{iq}^3 \rho_{iq} X_{w,iq} N_i^q + \frac{4}{3}\pi \, \phi_{N_R \to N_C} r_{C3}^3 \rho_w N_C$$

f IV.135

Originally the Kessler scheme accretion rate is proportional to the specific cloud water content and a 0.875-power function of the air rainwater content. The above formula keeps these characteristics since it relies on analogous assumptions that have been extended to the discrete aerosol distribution.

2.5.2 The autoconversion rate

Essentially, precipitation is the resultant of cloud droplet encounter and coalescence. The formation of precipitation may not be accurately represented without considering the statistical properties of the turbulent flow field at the scale of particle interaction. The formation of particles of raindrop size under average conditions is so slow that the related precipitation yield is negligible. In the framework of the present shallow cloud model of Chlond et al. (2004) including explicit aerosol cloud droplet interaction it is not computationally reasonable to implement an explicit scheme of droplet coalescence/turbulent

flow field interaction. A fully microphysical scheme of aerosol cloud droplet interaction and precipitation formation would require a bi-dimensional discretisation of the particle both as a function of their solute and water content. For this reason a conceptual approach to rain formation is the method of choice. The basic idea behind the concept of autoconversion is that the precipitation formation process may be represented by the general tendency of the droplets to encounter, that is the integrated coagulation mass flux among cloud droplets. Autoconversion is thus not a physical flux of small cloud particles that become raindrops, it is merely a formal representation of the transformation of cloud water to rainwater. As such it is disconnected with the scheme of cloud droplet interaction based on average size and velocity conditions adopted here, and consistently has no direct incidence on their number and spectral distribution. It does have an indirect incidence, however, through the cloud water mass balance.

Kessler (1960) defined autoconversion as:

$$\frac{\partial q_R}{\partial t}\{auto\} \propto \left(q_C - q_C^*\right)\delta_{q_c > q_c^*} \quad ,$$

f IV.136

where q_C^* stands for a certain critical cloud water content below which autoconversion is ineffective.

The concept that precipitation does not occur below a certain threshold may not be appropriate. Liu et al. (2006a) show that the rain water production rate does strongly decrease below a certain threshold of cloud water content but does not cease sharply. Consequently a more appropriate ansatz to the autoconversion rate would be (Liu and Daum, 2004):

$$\frac{\partial q_R}{\partial t}\{auto\} \equiv f\left\{\Phi_{COAG}, g\left\{q_C, q_C^*\right\}\right\} \equiv \Phi_{COAG} \cdot g\left\{q_C, q_C^*\right\} \quad ,$$

f IV.137

where Φ_{COAG} is the total coagulation mass flux among cloud droplets and $g\{x\}$ is the autoconversion threshold function.

The coagulation mass flux of cloud droplets r onto collector droplets R that is relevant to autoconversion is generally defined:

$$\Phi_{COAG} = \int_{\Delta R} \frac{\partial N_R}{\partial R} dR \int_{\Delta r} K\{R, r\}\left(M\{r\} + M\{R\}\right)\frac{\partial N_r}{\partial r} dr \quad .$$

f IV.138

Liu and Daum (2004) integrate the preceding equation over the whole cloud droplet spectrum,

which means that the autoconversion rate is formulated as a function of the total coagulation flux of the cloud droplets:

$$\Phi_{COAG} = \int_0^\infty \frac{\partial N_R}{\partial R} dR \int_0^R K\{R,r\}\left(M\{R\}+M\{r\}\right)\frac{\partial N_r}{\partial r} dr$$
$$= 1/2 \int_0^\infty \frac{\partial N_R}{\partial R} dR \int_0^\infty K\{R,r\}\left(M\{R\}+M\{r\}\right)\frac{\partial N_r}{\partial r} dr \quad .$$

f IV.139

Some authors (e.g. Wood and Blossey, 2005, in their comment on Liu and Daum, 2004) criticize the ad hoc character of this formulation and argue that it is more appropriate to define a critical separation radius between cloud droplet and raindrop size. However, this approach entails a high sensitivity of the autoconversion rate on the separation size, for which there is no specific criterion of choice. For this reason the clear formulation of Liu and Daum (2004) is chosen in this study that seems to produce accurate results (Liu et al., 2006a).

Liu and Daum (2004) assume that the latter equation is determined by those circumstances when $R>>r$ and $r>>R$ so that $K\approx K\{R\}$ and $K\approx K\{r\}$, respectively, yielding:

$$\Phi_{COAG} = q_C \cdot \int_0^\infty K\{R\}\frac{\partial N_R}{\partial R} dR \quad .$$

f IV.140

According to Long (1974) the coagulation kernel of particles of less than 50 μm should follow:

$$K\{R\} = a_K R^6 \quad ,$$

f IV.141

with $a_K \approx 1.9e17 \ m^{-3} \ s^{-1}$.

Combining the two preceding equations and integrating according to the assumed cloud droplet gamma distribution leads to:

$$\Phi_{COAG} = a_K N_C R_{C6}^6 q_C \quad ,$$

f IV.142

and finally through the link between R_6 and R_3 established by Equation IV.83:

$$\Phi_{COAG} = \left(\frac{3}{4\pi\rho_w}\right)^2 a_K \beta_6^6 N_C^{-1} q_C^3 \quad .$$

f IV.143

According to Liu et al. (2006, 2006a) the general shape of the autoconversion threshold function is:

$$g\{q_C, q_C^*\} = 1 - e^{-\left(\frac{q_C}{q_C^*}\right)^b} ,$$

f IV.144

where *b* essentially is an empirical parameter.

Sundqvist (1978) originally suggested *b=2*. For this reason the previous formulation of the threshold function is also called *generalized Sundqvist-type threshold function*.

Ideally, the critical cloud water content is a remarkable quantity. A cloud contains droplets that tend to evaporate whilst others tend to grow through condensation and/or coagulation. It seems reasonable that in a cloud that yields precipitation the radius delimiting growing from evaporating particles should be lower than its mean volume value. Consequently, a remarkable quantity in relationship with precipitation formation is the droplet size for which mass gains through coagulation and condensation equal the losses through evaporation (Liu et al., 2004):

$$\phi_{cond}\{r_C^*\} + \phi_{coag}\{r_C^*\} = \phi_{eva}\{r_C^*\}$$

f IV.145

where ϕ_i is the molecular occurrence frequency of the respective process [s⁻¹], and r_C^* is the critical radius in relationship with the autoconversion threshold function.

In accordance with the formulation of IV.142:

$$\phi_{coag}\{r_C^*\} = a_K r_C^{*6} \frac{q_C}{M_{H2O}} .$$

f IV.146

The evaporation frequency may be formulated as a function of the condensation frequency:

$$\phi_{eva} = \phi_{cond} \ e^{\left(\frac{q_C}{M_{H2O} N_C}\right)^{-1}} \simeq \left(1 + \frac{M_{H2O} N_C}{q_C}\right) \phi_{cond} .$$

f IV.147

To derive this relationship McGraw and Liu (2003) have assumed the droplets to be in equilibrium in respect of evaporation and coagulation:

$$\phi_{cond,i} N_i = \phi_{eva,i+1} N_{i+1} .$$

f IV.148

The droplets are assumed to observe the following distribution that is in analogy to the Marshall-Palmer distribution (see eq. IV.106):

$$N_i = \frac{N_C}{i_C} e^{-\left(\frac{i}{i_c}\right)} \quad ,$$

<div align="center">**f IV.149**</div>

where i is the number of water molecules in the droplet.

Formula IV.147 follows directly from the combination of Equations IV.148 and IV.149. Equations IV.145, IV.146 and IV.147 yield for the critical radius:

$$r_C^* = \left(\frac{M_{H2O}^2}{a_K} \phi_{cond}\{r_C^*\} \frac{N_C}{q_C^2} \right)^{1/6} .$$

<div align="center">**f IV.150**</div>

To determine the critical condensation frequency have conjectured that the cloud droplet mean volume radius equals the critical radius at the onset of relevant drizzle formation. In addition Liu et al. (2004) made the following assumption:

$$\phi_{cond}\{r_C^* \equiv r_{C3}\{N_C^\circ, q_C^\circ\}\} \simeq \phi_{cond}\{r_C^*\{N_C, q_C\}\} \simeq const$$

<div align="center">**f IV.151**</div>

where N°C and q°C denote the cloud droplet and water concentrations when the mean volume radius is supposed to be equal to the critical radius.

The empirical findings of Liu et al. (2004) for the mean condensation frequency are normally distributed, which is an indication that the assumptions leading to the expression of the critical radius are not inconsistent, the mean value is $\phi_{cond}\{r_C^*\} \approx 1.15e23 \ s^{-1}$.

Finally the ratio of the cloud water content to its critical counterpart in the context of the autoconversion threshold function is Liu et al. (2004):

$$\frac{q_C}{q_C^*} = \frac{3}{4\pi} \cdot \frac{a_K^{0.5}}{\rho_w M_{H2O} \phi_{cond}^{0.5}} \cdot N_C^{-1.5} q_C^2 .$$

<div align="center">**f IV.152**</div>

IV.2.6 Turbulent diffusion scheme

Turbulent convective circulation determines the parameters of aerosol and cloud droplet growth, such as atmospheric moisture, secondary aerosol condensables, particle number concentration, temperature, and convective cooling rate. In the shallow cloud model of Chlond et al. (2004) turbulent convection is represented as a diffusion process. It is:

$$\frac{\partial Q_i}{\partial t}\{conv\}=-\frac{\partial \overline{Q'_i w'}}{\partial z}\equiv\frac{\partial}{\partial z}D_{BL}\frac{\partial Q_i}{\partial z} \quad,$$

f IV.153

where Q_i is the mixing ratio value of the considered quantity, w is the vertical velocity of the air, D_{BL} is the turbulent diffusion coefficient and z stands for the vertical dimension.

The complete partial temporal derivative of the quantity Q_i in the shallow cloud model comprises:

$$\frac{\partial Q_i}{\partial t}=\frac{\partial Q_i}{\partial t}\{conv\}+\frac{\partial Q_i}{\partial t}\{had\} \quad.$$

f IV.154

The additional second term on the right hand side of the previous expression refers to the so-called large scale subsidence corresponding to the regional circulation of the air in the Hadley cell. It reads:

$$\frac{\partial Q_i}{\partial t}\{had\}=-\frac{\partial U_{had}Q_i}{\partial z} \quad,$$

f IV.155

where U_{had} is the mean synoptic vertical air velocity. Note that the large scale vertical velocity is negative in subsidence regions.

The large scale subsidence velocity is comprised in the following conceptual decomposition of the vertical velocity:

$$v_z\equiv U_{had}+\overline{w}+w'$$

f IV.156 ,

representing the synoptic (10^6 m), the convective cell (10^3-10^4 m) and the turbulence (10^{-2}-10^2 m) length scales, respectively, as the main scales of interest to cloud modelling when exception of the Kolmogorov microscale is made. In the one-dimensional model the mean convective velocity is not defined.

The discrete approximation to Equation IV.154 is:

$$Q_i^{\{t+\delta t\}}=Q_i^{\{t\}}-\left(U_{had}^{\{z+\frac{\delta z}{2}\}}Q_i^{\{t,z+\frac{\delta z}{2}\}}-U_{had}^{\{z-\frac{\delta z}{2}\}}Q_i^{\{t,z-\frac{\delta z}{2}\}}\right)\frac{\delta t}{\delta z}$$
$$+\left(D_{BL}^{\{t,z+\frac{\delta z}{2}\}}\left(Q_i^{\{t,z+\delta z\}}-Q_i^{\{t,z\}}\right)-D_{BL}^{\{t,z-\frac{\delta z}{2}\}}\left(Q_i^{\{t,z\}}-Q_i^{\{t,z-\delta z\}}\right)\right)\frac{\delta t}{\delta z^2} \quad,$$

f IV.157

with:

$$X^{\{z\pm\frac{\delta z}{2}\}}=\frac{X^{\{z\pm\delta z\}}+X^{\{z\}}}{2}$$

,

f IV.158

where δt and δz are the time and vertical increments, respectively.

At the upper limit of the cloud the turbulent diffusion coefficient should be consistent with the entrainment velocity w_E, which defines the vertical displacement of the inversion:

$$D_{BL}^{\{inv\}}=\frac{w_E}{\delta z}$$

.

f IV.159

The vertical entrainment velocity w_E may be assessed from the temporal derivative of the liquid water potential temperature Θ_l (Duynkerke et al., 2004):

$$\frac{\partial\Theta_l}{\partial t}=\frac{\partial}{\partial z}\left(w_E\Theta_l+\overline{w'\Theta'_l}\right)+\frac{\partial\Theta_l}{\partial t}\{had\}+\frac{\partial\Theta_l}{\partial t}\{lw\}$$

.

f IV.160

The fourth term on the right hand side results from longwave cooling at the upper cloud limit. According to Duynkerke (2004) the previous expression is balanced to a first approximation, while convective heat transport and large scale subsidence are negligible. Equation IV.160 thus yields:

$$w_E=C\;\frac{\dfrac{\partial\Theta_l}{\partial t}}{\dfrac{\partial\Theta_l}{\partial z}}$$

,

f IV.161

where C [-] is an arbitrary proportionality factor close to unity.

IV.2.7 Cloud droplet mass balance equation

The modelled aerosol particles are activated with respect to sulphuric acid and their condensation growth is limited by its abundance. Cloud droplets, however, are activated to both sulphuric acid and water vapour. As the atmospheric moisture content is typically around ten orders of magnitude larger than the content of sulphuric acid, their size is essentially a function of the condensed water mass. For the purpose of aerosol growth simulation the particles are spectrally resolved according to their sulphuric acid content. This is still useful

when dealing with cloud droplets, for which in-cloud residence time is rather limited. Simulating aerosol trajectories in the atmospheric boundary layer, Feingold et al. (1996) have estimated the typical integrated cloud residence time of an aerosol to be about 12 minutes per hour. Rapid coalescence within the cloud modifies the sulphuric acid content of the droplets. The aerosol particles are thus cloud processed, which results in a modification of their activation properties. Reliable information on aerosol activation is only obtained when cloud droplets are discretised with respect to their sulphuric acid. This information will in turn be most valuable to the evaluation of the following processing cycle. As coalescence is essentially a size dependent process and droplet size is mainly determined by their water content, the cloud droplet spectrum should ideally also be size resolved as a function of solute content. Aerosol activation does not produce a monodisperse cloud droplet population as determined by the solute content. The substantial heterogeneity of the atmosphere on relatively small length scales produces a continuous particle size spectrum at fixed solute content. Hence, the following scheme is adopted to simulate concurrent solute and solvent mass variation of cloud droplets: During activation cloud droplets remain in their respective solute content class. Upon activation cloud droplets are redistributed within the solute content resoled particle spectrum due to coalescence among cloud droplets as well as coagulation between aerosol particles. Within their respective solute content class cloud droplets are assumed to follow the Khrigian-Mazin density function with respect to their size. Their class specific mean radius is assessed through the solution of a total mass balance equation. Coalescence is assumed to be conservative with respect to the size density distribution. Discrepancies between the prognostic total particle water content and the diagnostic cloud water content are imputed to instant evaporative or condensation size adaptation to the local saturation water vapour pressure. Concurrent sulphuric acid condensation is conditioned by the class specific cloud droplet mean size, which in turn depends on both the ambient moisture conditions and the mean class specific coagulation background of the particles. As the solution should be dilute, its equilibration with respect to the ambient moisture content is neglected.

This leads to the following mass balance equation with respect to the prognostic processes:

$$\frac{d\,q_C^{iq}}{dt} = \frac{d\,q_C^{iq}}{dt}\{coag\} + \frac{d\,q_C^{iq}}{dt}\{cond\} + \frac{d\,q_C^{iq}}{dt}\{att\} + \frac{d\,q_C^{iq}}{dt}\{acc\} \quad .$$

f IV.162

The terms on the right hand side stand for the processes of coagulation/coalescence, solute

condensation, ion attachment and accretion, respectively. Note that the condensation term refers to sulphuric acid condensation exclusively Condensation and ion attachment do not relevantly modify the mass of the single particle. It is their influence on the total mass of the solute class through particle transfer that is rendered by the above equation. The coagulation, condensation and ion attachment mass fluxes are assessed in accordance with the general particle dynamic growth Equation IV.1 combined with the appropriate moment or bi-moment kernel according to the expressions of section IV.2.4. Equation IV.134 serves to evaluate the accretion rate mass loss.

As an example, the water mass flux onto a solute class iq due to these droplets interacting with cloud droplets of the class jp in the context of process f is to a first approximation:

$$\frac{dq_C^{iq}}{dt}\Big|_{jp}^{a_i+a_j<a_{i+1}} = \frac{a_{i+1}-(a_i+a_j)}{a_{i+1}-a_i} \int_0^\infty \int_0^\infty \left(M^{jp}+M^{iq}\right) f\{r_{iq},r_{jp}\} \frac{\partial N_j^p}{\partial r_{jp}} \frac{\partial N_i^q}{\partial r_{iq}} dr_{jp} dr_{iq}$$

$$\simeq \frac{a_{i+1}-(a_i+a_j)}{a_{i+1}-a_i} \left(M_{C3}^{jp}+M_{C3}^{iq}\right) \int_0^\infty \int_0^\infty f\{r_{iq},r_{jp}\} \frac{\partial N_j^p}{\partial r_{jp}} \frac{\partial N_i^q}{\partial r_{iq}} dr_{jp} dr_{iq} \quad .$$

f IV.163

This expression implies that the mean volume mass is the representative mass of particle interaction. This approximation is made for all mass balance relevant processes to save computation time. Without this approximation mass flux specific kernels would have to be assessed whenever a continuous cloud droplet size spectrum is involved. The inaccuracy related to this assumption adds to more far-reaching approximations of the present scheme of aerosol cloud droplet interaction, such as the assumption of cloud droplets to follow solute class specific conservative size distributions, instantaneous equilibration of the prognostic and the diagnostic cloud water content, and rainwater formation parametrization, and should therefore not be of extensive relevance.

Considering Equation IV.58, and assuming that the particle density variability is negligible, yields for the temporal derivative of the radius of a cloud droplet through condensation:

$$\frac{dr_p}{dt} \simeq \frac{D_w}{\rho_{s,w} r_p} \left(q_V - q_{sat}\{r_p\}\right) \quad .$$

f IV.164

Hence, the temporal particle surface (S_p) derivative yields:

$$\frac{dS_p}{dt} = \frac{8\pi D_w}{\rho_{s,w}} \left(q_V - q_{sat}\{r_p\}\right) \quad .$$

f IV.165

For activated particles the following approximations are appropriate:

$$\rho_{s,w} \simeq \rho_w$$
$$q_{sat}\{r_p\} \simeq q_{sat}\{r_\infty\} \quad .$$

f IV.166

The right hand side of expression IV.165 is thus particle indifferent, leading to the following relationship between the surface of particles i and j at subsequent points of time:

$$(S_i - S_j)|_{t+dt} = (S_i - S_j)|_t \quad .$$

f IV.167

The total cloud liquid water is:

$$\sum_{i=1}^{n} \sum_{j=1}^{m} \frac{4}{3} \pi \rho_w \int_0^\infty r_{iq}^3 \frac{\partial N_i^q}{\partial r_{iq}} dr_{iq} = \sum_{i=1}^{n} \sum_{j=1}^{m} \frac{4}{3} \pi \rho_w \left(\frac{S_{C3}^{iq}}{4\pi} \right)^{3/2} N_i^q = q_C \quad .$$

f IV.168

Combing Equations IV.167 and IV.168 yields for the mean surface of a cloud droplet S_p of a particular solute content in the context of continuous and class specific cloud droplet size distributions:

$$S_p|_{t+dt} = \left(\frac{6\sqrt{\pi} \dfrac{q_C|_{t+dt}}{\rho_w}}{\displaystyle\sum_{i=1}^{n} \sum_{j=1}^{m} \left(1 - \frac{(S_p - S_{C3}^{iq})|_t}{S_p|_{t+dt}} \right)^{3/2}} \right)^{2/3} \quad .$$

f IV.169

This expression may be solved iteratively. Following each time increment the prognostic cloud droplet mean surface may thus be adapted to its new equilibrium value according to the total diagnostic cloud water content determined with Equation IV.48.

V. Results and Interpretation

V.1 Ion-Induced Nucleation

V.1.1 Liquid water activity in the H_2SO_4/H_2O system

The dependence of the fractional particle water activity on the sulphuric acid mass fraction is depicted by Figure V.1. According to Equation VII.49 the fractional activity of water is equal to the activity coefficient on the molal base.

Molal activity coefficient of water as a solvent of sulfuric acid

as a function of the sulfuric acid mass fraction
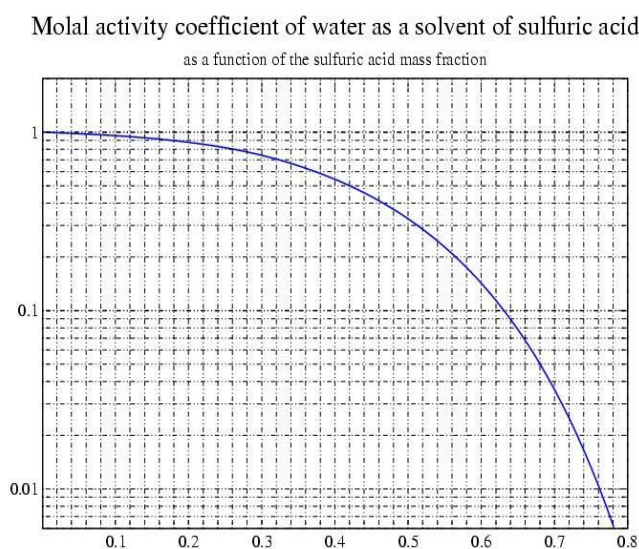
Figure V.1: The fractional activity of water [-] as a function of the mass fraction of sulphuric acid in solution [-] at T=288.15 K.

Relatively weakly conditioned for diluted solutions, it appears that the activity of water eventually tends to an exponential function of the sulphuric acid. This strong dependence reflects the pronounced affinity of sulphuric acid for water molecules. The hygroscopic property of sulphuric acid renders water evaporation almost impossible and is linked to the distinct acidic property of sulphuric acid. Sulphuric acid dissolved in water dissociates almost entirely, and the evaluation of both the Henry and the first disintegration constant is thus

impeded by a very low saturation vapour pressure. These values are essential inputs to the activity of sulphuric acid, which in turn determines the nucleation rate of secondary aerosol particles in the H_2SO_4/H_2O system (see Equation III.31 and Section VII.1).
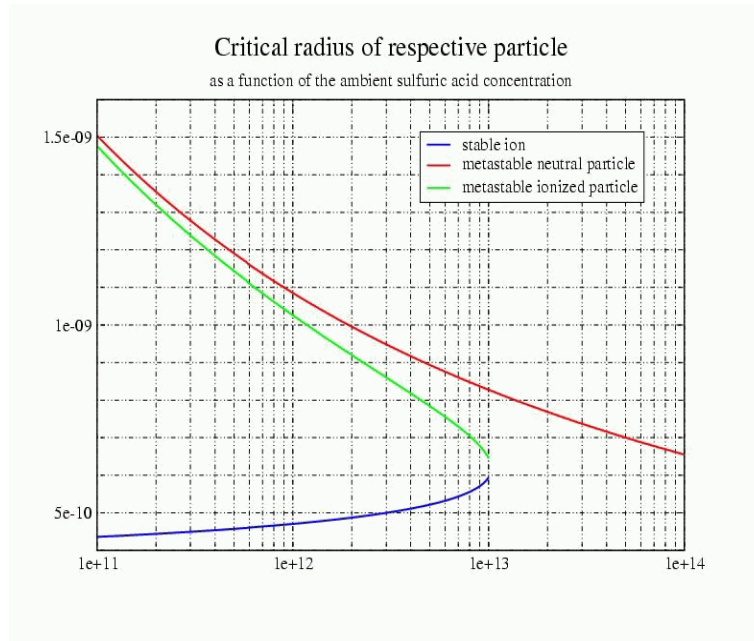
Figure V.2: Characteristic radii of classical and ion-induced nucleation [m] as a function of the atmospheric number concentration of sulphuric acid [m^{-3}] for T=288.15 K, r=0.8 and K1=7.94·10^9 mol/kg.

V.1.2 The critical radius

Figure V.2 compares the modelled critical radii of classical and ion-induced nucleation in the in the H_2SO_4/H_2O system as a function of the molecule number concentration of sulphuric acid in the gas phase. The relative humidity is held constant at 80% and temperature is 288.15 K. The upper curve depicts the critical radius of classical binary nucleation. The ion-induced critical radius is shown by the curve on the left hand side just below the former, and finds its analytical counterpart in the stable cluster radius that is shown still below. With increasing ambient sulphuric acid concentration the stable cluster radius tends to the critical nucleation radius, and beyond this merging point both variables are not defined any more.

The depicted situation may be described as follows. The lower the concentration of sulphuric

acid, the more improbable is it for unstable particles to overcome the increasing size gap between the stable ion cluster and the critical nucleus. The widening of the gap is mainly due to the critical radius, the stable ion radius not varying a lot. The changing of the critical radius with the atmospheric sulphuric acid concentration is determined by the concurrent variation of the sulphuric acid and the water vapour pressures over the particle solution, which are interdependent in a binary mixture. When the atmospheric sulphuric acid concentration reaches a threshold, the unstable particle range vanishes and cluster ions grow freely.
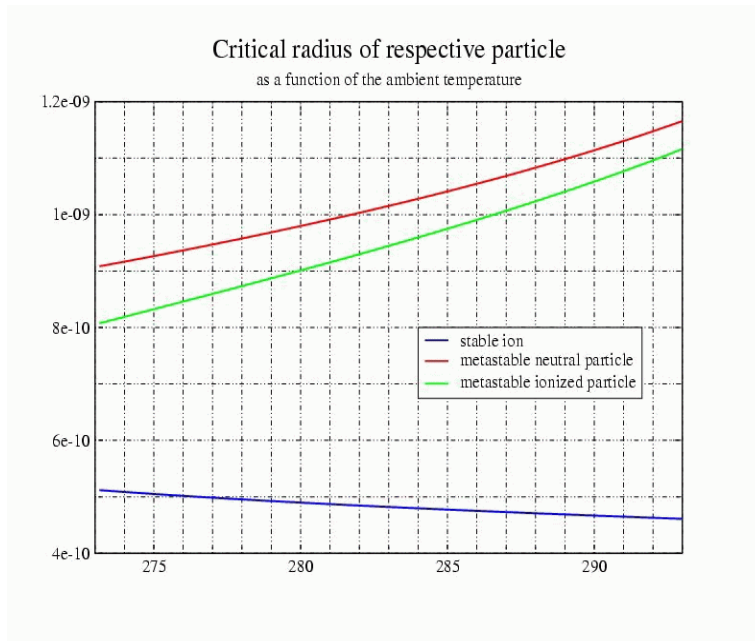
Figure V.3 : Characteristic radii of classical and ion-induced nucleation [m] as a function of atmospheric temperature [K] for [H2SO4]=10^{12} m^{-3}, r=0.8 and K1=7.94·10^9 mol/kg.

When one compares the classical to the ion-induced critical radius, it appears that the main incidence of electrostatic charge does not consist in the lowering of the critical radius but in the narrowing of the unstable cluster size range by the stable cluster ion. The findings of Figure V.2 are both qualitatively and quantitatively similar to those of Laakso et al.(2002), except for the stronger dependence of the critical radius on ambient sulphuric acid. Quantitative differences between the results presented here and those of Laakso et al. (2002) may be imputed to the particular respective representation of sulphuric acid activity in the liquid phase. Laakso et al. (2002) referred to relate the vapour pressure above particle solution to the pure species vapour pressure, while this study determines the sulphuric acid activity

181

directly based on activity data on its dissociation products (see Appendix).

Figure V.3 shows that the positive temperature dependence of the critical radius is fairly pronounced, as a temperature decrease of 30 degrees corresponds to a modelled decrease of the critical particle radius of nearly 30%. Figure V.4 depicts the relationship of the characteristic radii and relative humidity. Ambient humidity directly conditions the particle water vapour pressure, and thus the critical radius. Moreover, the critical nucleation radius is conditioned by the interaction of the water and sulphuric acid activity in the binary solution, resulting in an implicit dependence of the critical radii on ambient humidity via the action of sulphuric acid. Note that the variation of the critical nucleation radius within a realistic humidity range is of similar magnitude than the corresponding variation as a function of ambient sulphuric acid concentration or temperature.
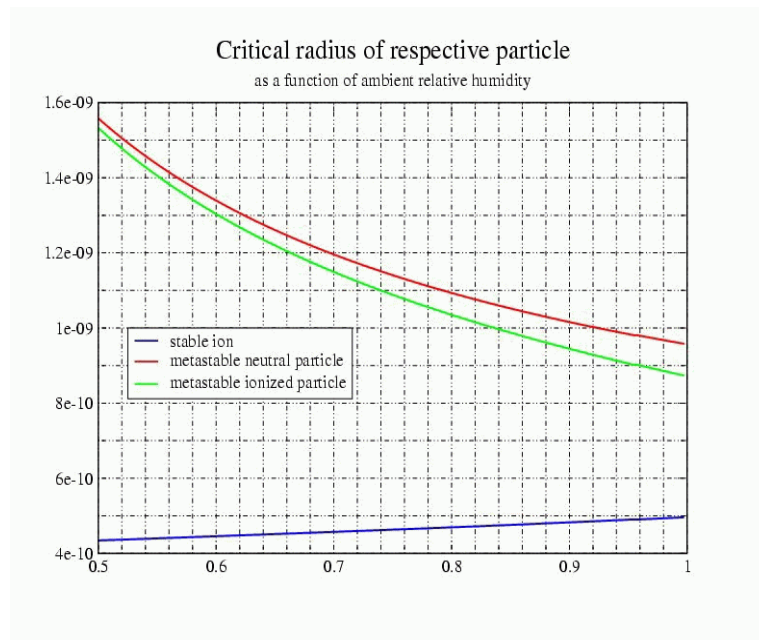
Figure V.4 : Characteristic radii of classical and ion-induced nucleation [m] as a function of the atmospheric relative humidity [-] for [H2SO4]=10^{12} m^{-3}, T=288.15 K, and K1=7.94·10^9 mol/kg.

Figure V.5 depicts the variation of the characteristic radii within range of uncertainty of the sulphuric acid first dissociation constant; note that the dissociation constant is in fractional units. It clearly appears that while the stable ion radius is almost constant the critical nucleation radii show a moderate quasi-linear dependence on the dissociation constant. When the dissociation constant is relatively low the tendency of sulphuric acid to evaporate increases

along with its activity in solution (see Equation VII.38). This particle destabilizing effect increases in consequence the critical particle radius. The uncertainty inherent to the first dissociation constant adds to the formal assumptions that led to binary nucleation rate according to Stauffer (1976). It is representative to the so-far lack of reliable data on the sulphuric acid vapour pressure over aqueous solutions due to the distinct hygroscopic property of sulphuric acid.
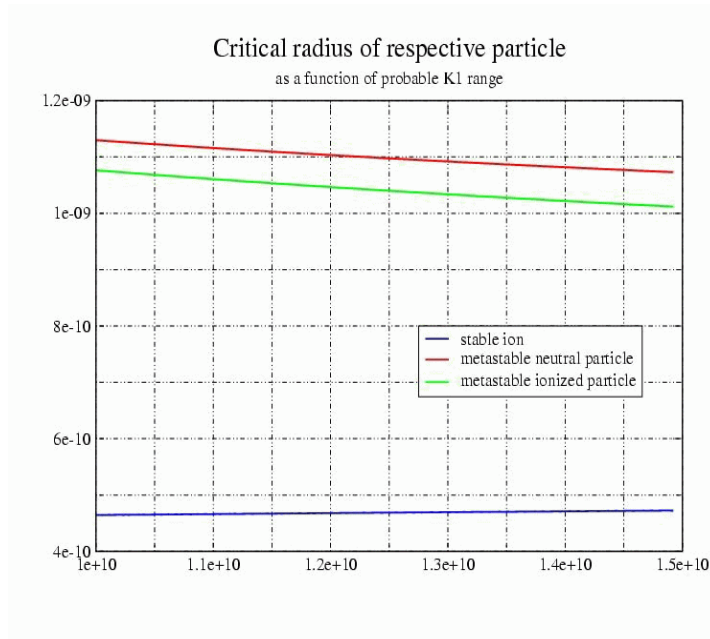
Figure V.5 : Characteristic radii of classical and ion-induced nucleation [m] as a function of the sulphuric acid first dissociation constant on the fractional base [-], for [H2SO4] =10¹² m⁻³, r=0.8, and T=288.15 K.

V.1.3 The nucleation rate and its associated variables as a function of atmospheric sulphuric acid

In this section model results of the binary sulphuric acid/ water nucleation rate are presented in the framework of classical (homogeneous), ion-induced (heterogeneous) and dipole-ion interaction enhanced heterogeneous nucleation according to Equation III.78.

Figure V.6 depicts the strong sensitivity of the nucleation rate to the atmospheric sulphuric acid concentration for both enhanced ion-induced and homogeneous nucleation. Values for

ion-induced nucleation are not shown since they are too close to the enhanced ones to be resolved on the chosen logarithmic scale. Depending on the critical radius, the enhanced nucleation rate is up to one order of magnitude larger as it is depicted by Figure V.7, which shows the respective condensation enhancement factors of both sulphuric acid and water, and the corresponding critical particle radius as a function of atmospheric sulphuric acid.
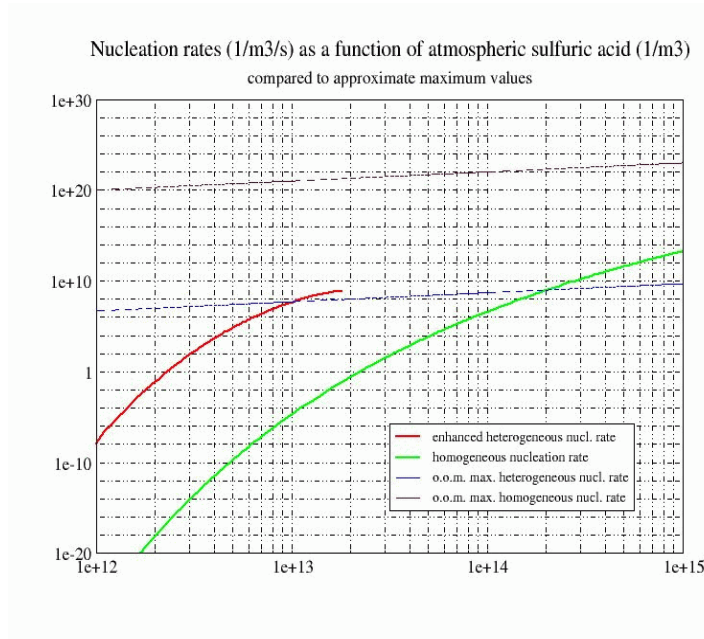
Figure V.6: Nucleation rate [m⁻³ s⁻¹] as a function of the ambient number concentration of sulphuric acid [m⁻³] at T=288.15 K, r=0.8, and K1=7.94·10⁹ mol/kg. The free ion concentration is 2·10⁹ m⁻³.

Figure V.6 also shows the approximate maximum homogeneous and heterogeneous nucleation rates according to Equation IV.3. This equation stems on the assumption that the combination of one ion and one sulphuric acid molecule leads to the formation of a stable particle, or in case of homogeneous nucleation, that the combination of one sulphuric acid molecule and one water molecule is thermodynamically stable. It serves as an indicator to the accuracy and consistency of Stauffer´s (1976) binary nucleation scheme, as with decreasing stable particle size the nucleation rate should tend to its mechanical counterpart, meaning that:

$$\lim_{\Delta \Delta_f G \to 0} Z\, R_{av}\, N_{\pm}\, e^{-\frac{\Delta \Delta_f G}{kT}} = R_b\, N_{\pm} \quad .$$

f V.1

Equation III.15 implies that for species *b* standing for the acid and *a* for water, the growth angle has to tend to $\phi=\pi/2$, meaning that $R_{av}=R_b$ holds at the limit between stable and unstable ambient cluster growth conditions, as for stable conditions particle growth is limited exclusively by sulphuric acid. Since the determination of the growth angle is based on bulk properties, the previous relationship may also indicate their appropriateness in relationship with particles as small as cluster ions. Figure V.6 shows that the relationship V.1 holds within an order of magnitude, which is an astonishingly precise result considering the sensitivity of the mean growth angle equation at the limit between stable and unstable growth (see below).
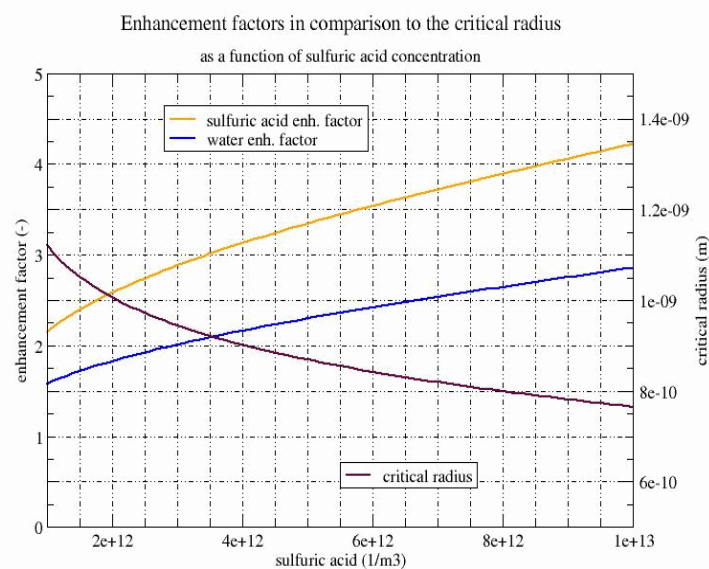
Figure V.7: Comparison of the condensation enhancement factor and the critical radius as a function of ambient sulphuric acid for T=288.15 K, r=0.8, and K1=7.94·10⁹ mol/kg.

The model results indicate that ion-induced nucleation is, when defined, potentially around ten orders of magnitude more important than homogeneous nucleation. Ion-induced nucleation is a function of both ambient cluster ions and sulphuric acid, while classical binary nucleation is exclusively a function of the latter. In order to assess properly the consequences of the double dependence of ion-induced secondary particle formation to its efficiency, it is useful to consider the integral of the nucleation rate over a small time period according to Equation IV.12 at two limiting situations.
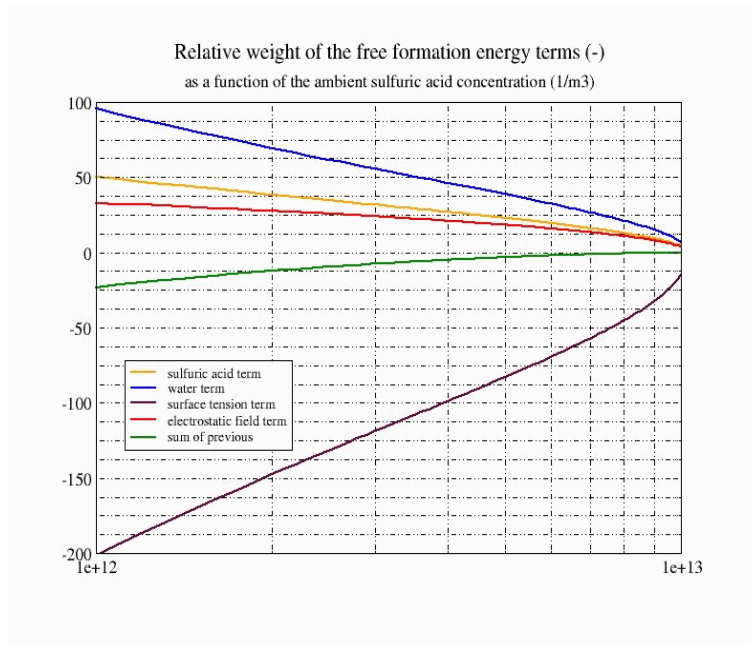
Figure V.8: Negative and normalized free formation energy of the critical particle and the associated individual terms of the Thomson equation as a function of the atmospheric concentration of sulphuric acid [m⁻³] at T=288.15 K, r=0.8, and K1=7.94·10⁹ mol/kg.
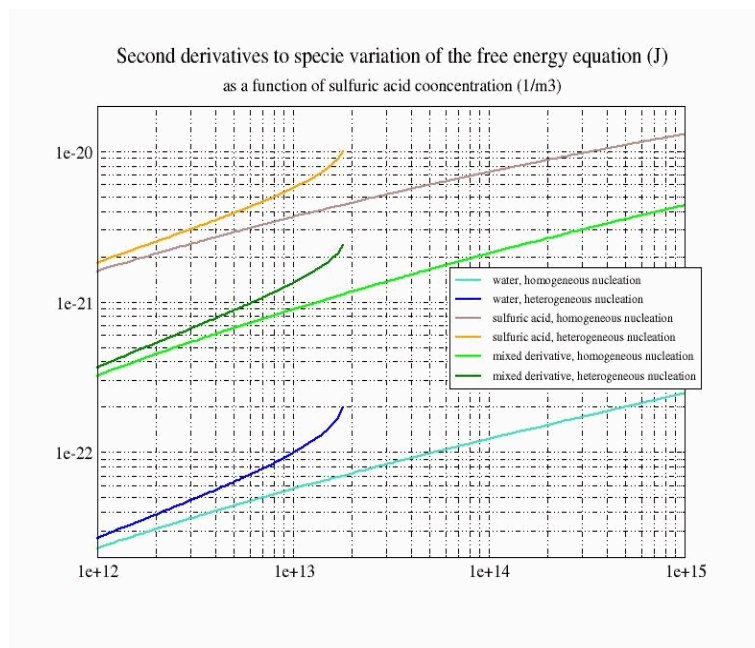
Figure V.9: Second derivatives of the Gibbs free formation energy of the critical particle to the respective condensing species number per particle [J] as a function of the atmospheric concentration of sulphuric acid [m⁻³] at T=288.15 K, r=0.8 and K1=7.94·10⁹ mol/kg.

186
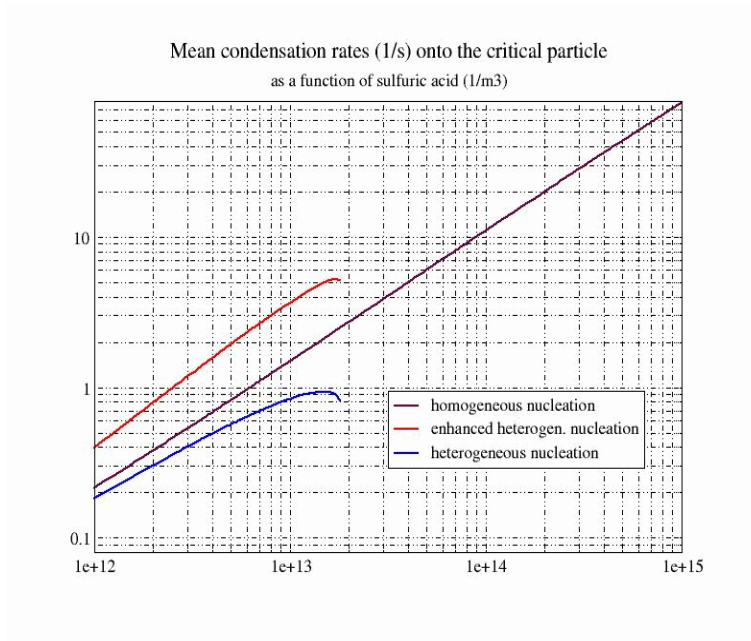
Figure V.10: Mean condensation rate of water and sulphuric acid molecules onto the critical particle [s⁻¹] as a function of the ambient sulphuric acid concentration [m⁻³] at T=288.15 K, r=0.8 and K1=7.94·10⁹ mol/kg.
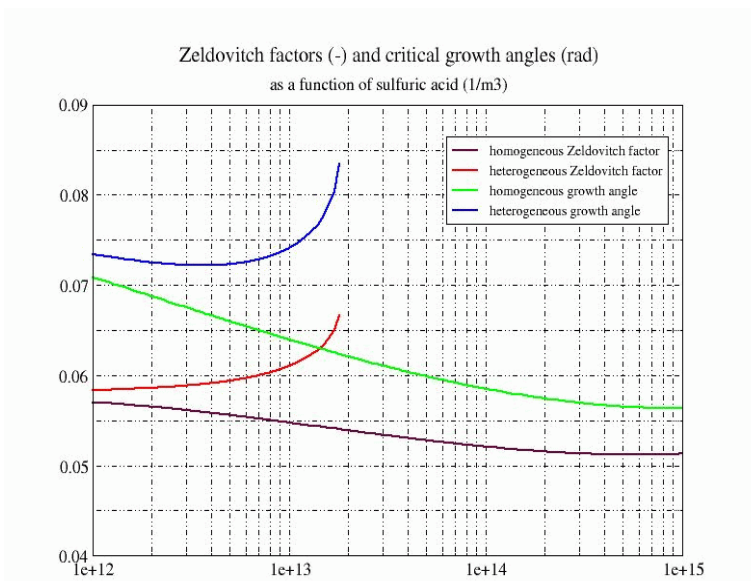
Figure V.11: Zeldovich non-equilibrium factor and critical growth angle as a function of the ambient sulphuric acid concentration [m⁻³] at T=288.15, r=0.8 and K1=7.94·10⁹ mol/kg.

187

When the atmospheric sulphuric acid concentration is low, the quantity of nucleated particles formed will be low, but the only possibility for homogeneous nucleation to be the dominant process is that the free ion concentration is extremely low. In the absence of a high ion consuming process, such as nucleation, this is improbable, so that when the nucleation rate is limited by sulphuric acid, ion-induced nucleation should be the dominant process under all circumstances. When the ion-induced nucleation rate is high, the free ion concentration may drop dramatically, but according to Equation IV.14:

$$\lim_{b,t\to\infty} \frac{c}{b} + A e^{-bt} = \frac{c}{b} = x \ \Rightarrow \ bx = c \ ;$$

f V.2

so that the nucleation rate, when strongly limited by the ambient cluster ion concentration, may not be inferior to the ion formation rate, which is of the order of 10^6 to 10^7 m^{-3}s^{-1}. For these reasons homogeneous nucleation may exclusively become the dominant nucleation process when the ambient sulphuric acid concentration is high enough for the ion-induced nucleation rate to be limited by the ion formation rate, while homogeneous nucleation is limited only by the ambient sulphuric acid formation rate, which is of the order of 10^9 to 10^{13} m^{-3}s^{-1}. As Figure V.6 suggests heterogeneous nucleation should be dominant as long as the atmospheric sulphuric acid concentration is below approximately 10^{14} m^{-3}. This is an important result for this study, as it shows, still to the extent of the validity of the ion-induced nucleation theory, that heterogeneous nucleation should be the key process of secondary particle formation under typical marine conditions, to the exclusion of an unknown formation mechanism.

Now a closer look is taken at the variables associated to the nucleation rate, namely the Zeldovich factor, the mean condensation rate and the stable particle Gibbs free formation energy variation. Both the Zeldovich factor and the mean condensation rate are functions of the individual condensation rates of sulphuric acid and water vapour, and of the second derivatives of the Gibbs free formation energy of the critical clusters to the number of sulphuric acid and water molecules per particle. Figure V.8 depicts the dependence of the free formation energy variation, as well as of the individual terms of the Thomson equation, on the ambient sulphuric acid concentration. Note that following Equation III.30 the negative values of these variables are shown and that these are normalised by *kT*. Further, the respective negative and normalised contribution of the stable cluster ion is subtracted from the individual terms. It appears that this function is negative for the entire sulphuric acid range for which

ion-induced is defined, while it tends to null when the threshold value of stable particle growth is reached, as it has already been inferred by Equation V.1.
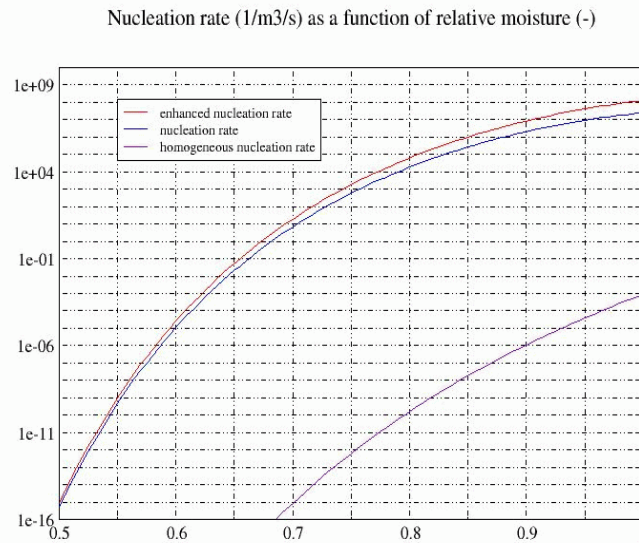
Figure V.12: Nucleation rate [$m^{-3}s^{-1}$] as a function of the ambient relative humidity at T=288.15 K, [H2SO4]=10^{12} m^{-3}, and K1=7.94·10^9 mol/kg. The free ion concentration is 2·10^9 m^{-3}.

This finding confirms the accuracy of the model results, as the energy barrier to stable ultrafine particle formation should vanish at this point. The Thomson equation suggests that the energy barrier is caused by the surface tension of the considered particle. Both the sulphuric acid and the water vapour condensation terms are negative, implying that the respective species' pressure over a flat surface is lower than the ambient pressure. This feature stresses the metastable character of the critical particles via their tendency to grow further as their surface tension is reduced with increasing size. While the surface tension generally has an impeding influence on particle growth, the saddle point materializes the threshold beyond which energy release through condensation surpasses energy consumption through surface increase. The inverse particle radius dependence of the electric field variation term adds to the growth tendency of ultrafine particles, although its contribution is decreasing with size. Figure V.8 shows that with decreasing critical radius the absolute values of the terms of the Thomson equation become smaller. However, the variability of the surface tension is the most pronounced, so that the energy barrier tends to vanish with increasing ambient sulphuric acid

concentration.

The second derivatives of the free formation energy of homogeneous and heterogeneous critical binary particles to their respective molecule number per particle are shown in Figure V.9. It appears that the second derivative to the number of water molecules is one to two orders of magnitude lower than the derivative to sulphuric acid and the mixed derivative. This appears plausible since the number of water molecules in the critical particle is higher (see below). The water activity is sensitive to a variation of the number of sulphuric acid molecules in strong sulphuric acid solutions and thereby modifies the free formation energy more effectively.
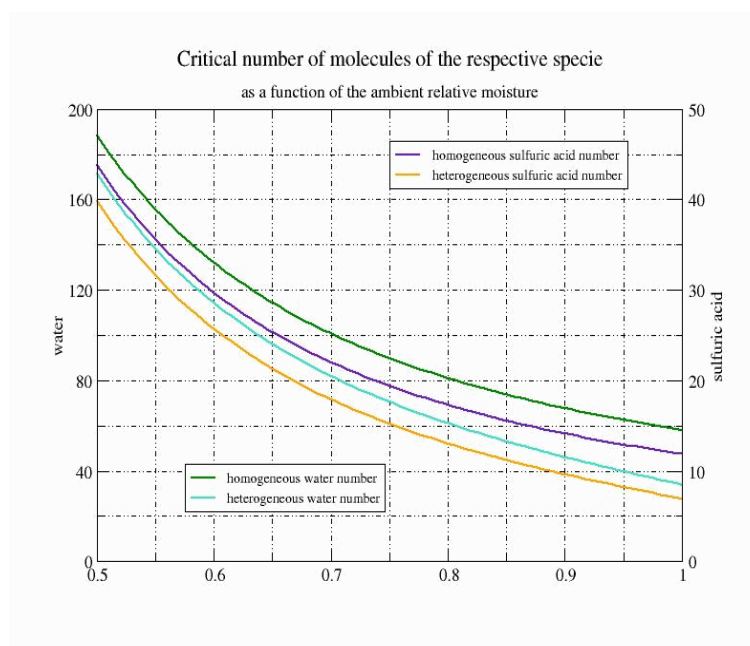
Figure V.13: Critical number of sulphuric acid and water molecules per particle, respectively, as a function of the ambient relative humidity at T=288.15 K, [H2SO4]=10^{12} m^{-3}, and K1=7.94·10^9 mol/kg.

Because of the inverse radius function of the charge specific term of the Thomson equation, the Gibbs free energy derivatives of the critical charged particle tend to the corresponding homogeneous figure with decreasing sulphuric acid pressure. As a corollary, when the critical radius tends to the threshold of stable particle growth, the difference between the Gibbs energy derivatives of the two particle formation mechanisms is maximal.

The mean condensation rate onto the critical particles is given by Equation III.15 and shown in Figure V.10 as a function of the ambient sulphuric acid number concentration. It is a

function of the individual condensation rates and the growth direction angle in the virtual sulphuric acid water vapour phase plane at the saddle point. The growth direction angle and the Zeldovich factor are depicted for both nucleation mechanisms in Figure V.11. The growth angle ϕ is assessed such that variable b of Equation III.11 stands for the acid, whilst variable a stands for water, so that ϕ is the angle between the growth axis and the water axis. Concerning the mean condensation rate, both terms of the denominator of Equation III.15 should be relevant at saddle point   except when close to the stable growth threshold; since the high net growth rate in the a-direction ($sin\phi \approx 0$) is compensated by the high condensation rate of water, which is proportional to its atmospheric concentration, and conversely. Thus, the mean condensation rate should increase with ambient sulphuric acid through the linear function of the condensation rate and decrease through the complex effect of the critical angle variation. As it may be inferred from Figure V.10, the first effect is dominating the vast majority of the considered range of sulphuric acid concentration. Only when the critical radius tends to its threshold value does the variation of the mean growth angle make the mean condensation rate decrease and tend to the sulphuric acid condensation rate, as predicted by Equation V.1.

When the Zeldovitch factor is compared to the critical growth angle it appears that both variables are numerically similar (Figure V.11). According to Stauffer (1976), when the domination of water vapour condensation is considered, the growth angle may be approximated by:

$$\tan \phi \simeq - \frac{D_{ww}}{D_{aw}} \text{ ,}$$

f V.3

where indexes a and w stand for the acid and water, respectively.

When the growth angle is close to zero the Zeldovich factor as given by Equation III.18 may be approximated by:

$$Z \simeq - \frac{D_{ww}(1-\phi)^2 + D_{aa}\phi^2 + 2 D_{aw}(1-\phi)\phi}{\sqrt{-D_{aa}D_{ww} + D_{aw}^2}} \text{ .}$$

f V.4

Considering that D_{ww} is several orders of magnitude smaller and assuming that if D_{aw} or D_{aa} is multiplied by the growth angle it is of the same order of magnitude than D_{ww}, the preceding equation rereads:

$$Z \simeq \frac{D_{ww} + 2\,D_{aw}\,\phi}{D_{aw}} \quad .$$

f V.5

Replacing the growth angle by the expression of Equation V.3 considering that $\tan\phi\big|_{\phi\simeq 0} \simeq \phi$, one finds the identical expression for the Zeldovich factor.
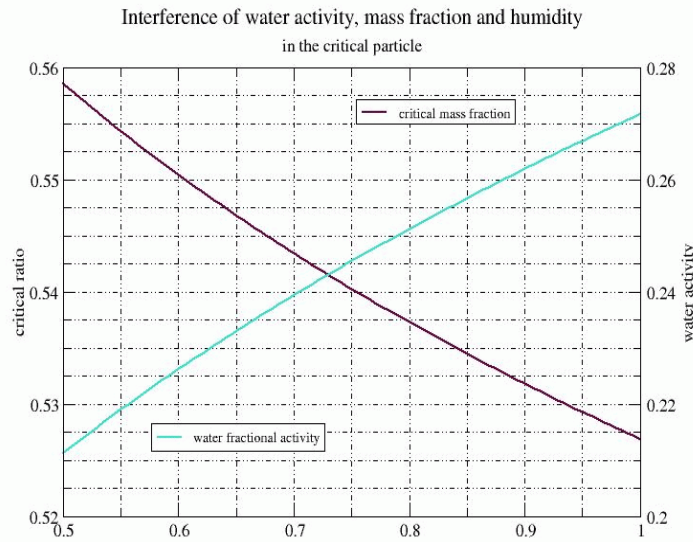
Figure V.14: Comparison of the mass fraction of sulphuric acid (X_a) within the critical particle and the corresponding water fractional activity as a function of the relative ambient humidity, at T=288.15 K and [H2SO4]=10^{12} m^{-3}, and K1=7.94·10^9 mol/kg.

V.1.4 The nucleation rate as a function of temperature, humidity, and the first dissociation constant of sulphuric acid

In this subsection the influence of temperature, relative humidity and the first dissociation constant of sulphuric acid on the nucleation rate is investigated. The concentration of sulphuric acid remains fixed at 10^{12} m^{-3}.

Figure V.12 depicts the increasing sensitivity of the nucleation rate to the ambient water vapour pressure with decreasing relative humidity. This pattern is in analogy to the sensitivity with respect to ambient sulphuric acid. It is a complex function of the variation of the water

192

vapour pressure, the critical particle radius, the particle solution composition and the species' activity coefficient.
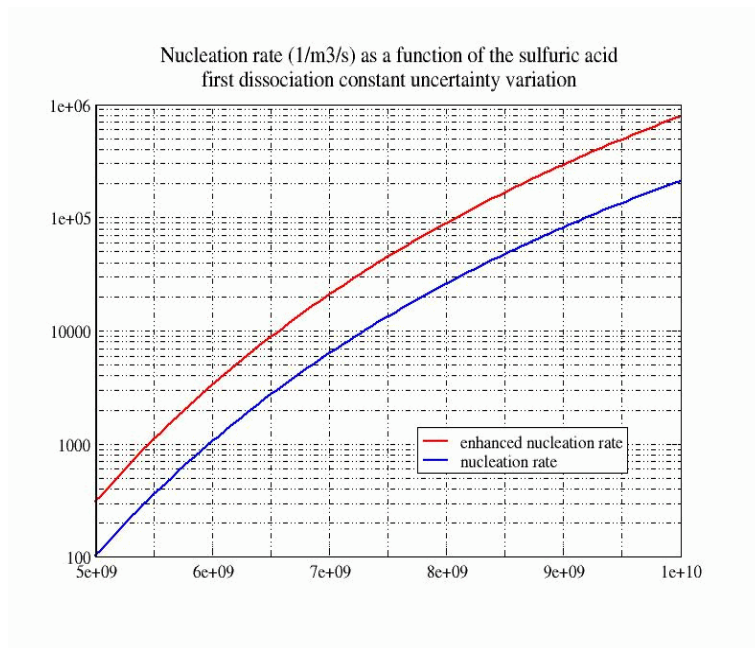
Figure V.15: Nucleation rate [s^{-1} m^{-3}] as a function of the first dissociation constant of sulphuric acid [mol kg^{-1}] at T=288.15 K, r=0.8 and [H2SO4]=10^{12} m^{-3}. The ion concentration is $2·10^9$ m^{-3}.

Figure V.13 compares the number of sulphuric acid and water molecules within the critical particle solution as a function of relative humidity. It shows that the number of water and sulphuric acid molecules in the critical particle is anticorrelated with relative humidity, as it evolves in parallel to the particle critical size. Consistently the critical number of molecules is lower for ion-induced nucleation than for homogeneous nucleation. As it is revealed in Figure V.14, the critical mass fraction of sulphuric acid is not a constant. Actually, the total mass relative quantity of sulphuric acid decreases with relative humidity along with particle size, and the solution becomes more dilute. The activity of water in the particle solution varies in consequence. The nucleation rate is positively correlated with relative humidity (see Figure V.12) while the critical particle radius along with the related Gibbs free formation energy variation of the critical cluster is anticorrelated. When the critical radius decreases, the formerly critical particle lies within the stable part of the particle composition phase plane. When particle size is reduced at constant activities, the relative importance of the surface tension term to the Thomson equation increases, so that the formation energy of a smaller

critical particle would be higher. However, the concurrent variation of the activities may invert this tendency, as the relative importance of the phase transition terms may actually increase when the ambient pressure of the condensables is increased. The corresponding critical particle composition varies in consequence according to Equation III.37, as for a non-linear function $f\{x\}=y$, $x_1 \neq x_2$ generally implies that $y_1 \neq y_2$. The critical radius, critical particle composition, ambient vapour pressures and temperature thus generally form a unique combination of conditions that determines the nucleation rate.
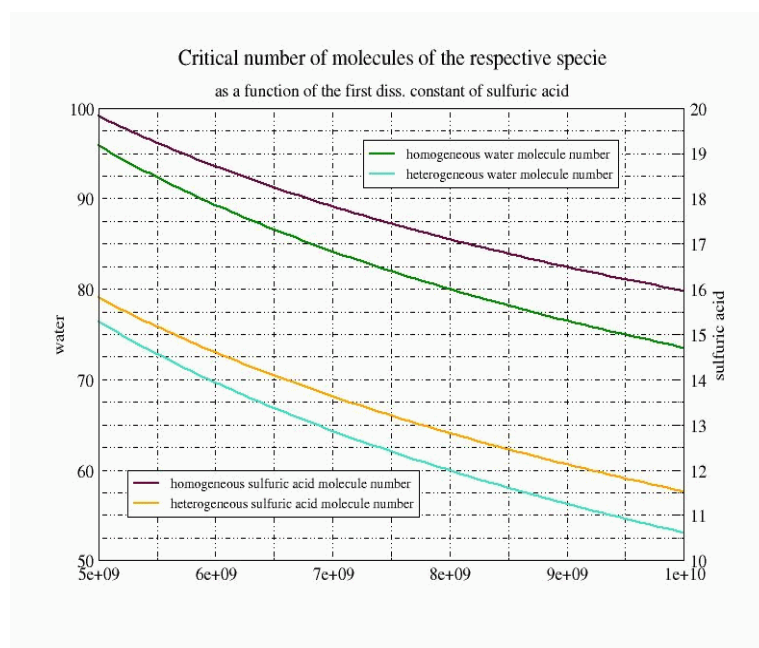
Figure V.16: Number of sulphuric acid and water molecules in the critical particle as a function of the first dissociation constant of sulphuric acid [mol kg^{-1}] at T=288.15, r=0.8, and [H2SO4]=10^{12} m^{-3}.

The first sulphuric acid dissociation constant plays a particular role in this study in as much as it is subject to an uncertainty equivalent to more or less half an order of magnitude. The precise value is so unsure that standard reference manuals (e.g. Lide, 2003) do not even indicate an approximate value. The present approximation is derived from a formula given by Ayers (1980), which is based on measurement data of the vapour pressure of pure liquid sulphuric acid as a function of temperature combined to thermodynamic data on the binary water sulphuric acid mixture provided by Giauque (1960). It is consistent with the empirical data of Marti (1997) of the vapour pressure of diluted sulphuric acid. It is referred to Appendix II. for more details on the estimation of the first dissociation constant of sulphuric

acid. Figure V.15 shows that the variability of the ion-induced nucleation rate due the uncertainty related to the first dissociation constant is equivalent to up to three orders of magnitude. It is the critical radius of the particle that, via its influence on the free formation energy, is the triggering factor, as it is demonstrated by Figure V.5.
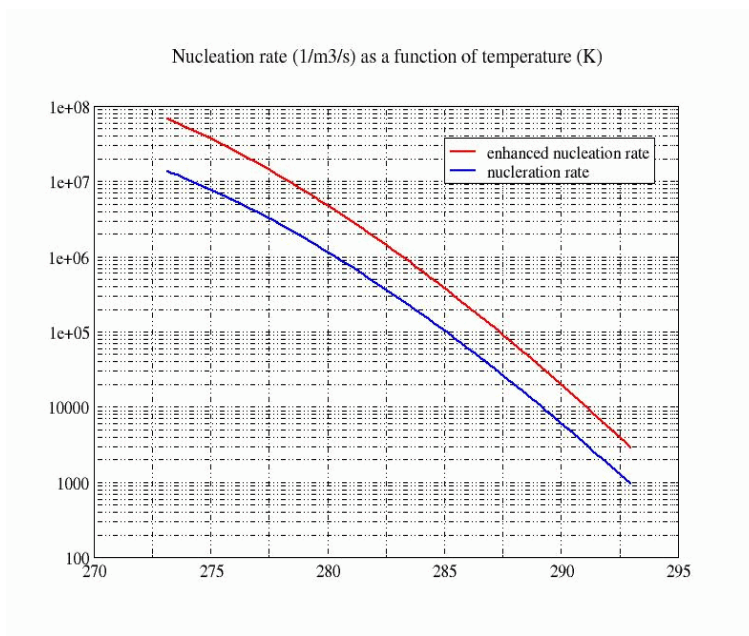
Figure V.17: Nucleation rate [m⁻³s⁻¹] as a function of the ambient temperature [K] at r=0.8, [H2SO4]=1e-12 m⁻³, and K1=7.94·10⁹ mol/kg. The stable cluster ion concentration is 2·10⁹ m⁻³.

Figure V.16 shows that the number of sulphuric acid molecules within the critical particle varies consistently when the dissociation constant varies from $5 \cdot 10^9$ to 10^9 mol/kg. The linear dependence of the number of critical molecules as a function of the dissociation constant is reminiscent of the linear variation of the critical radius as depicted in Figure V.5. In opposition to the preceding example of critical radius variation as a function of humidity, the activity of water in solution is positively correlated with the critical particle radius, so that the particle solution becomes stronger with decreasing radius (not shown). This opposite behaviour of the particle solution with respect to the critical radius and the nucleation rate shows that the primary response element of the binary nucleation system to a modification of the ambient parameters is the critical radius. The activity variation may thus add further to the induced tendency, but it may also have an opposite effect.

Figure V.17 depicts the temperature sensitivity of the nucleation rate. Considering Equations III.30 and III.31 one finds that the explicit incidence of temperature on the phase transition terms of the Thomson Equation is levelled by the temperature dependence of the gas particle mean kinetic energy. The same kinetic energy confers to the normalized surface tension and electric field variation terms an inversely proportional dependence, so that the nucleation rate would be positively correlated with temperature.
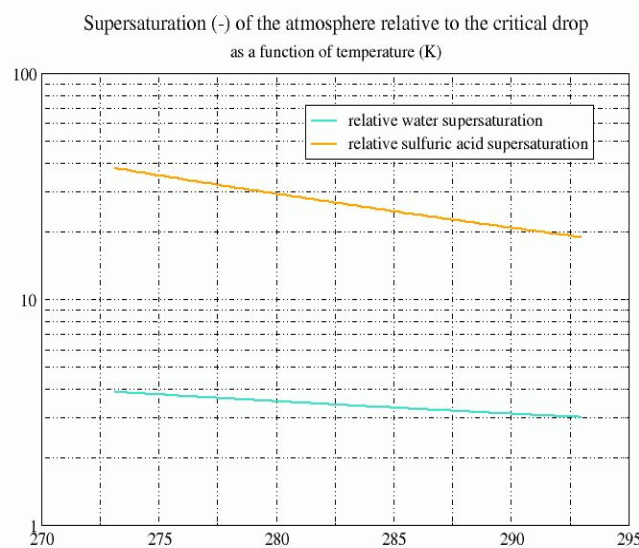
Figure V.18: Ratio of vapour pressure in the atmosphere to the pressure over a flat surface of the critical particle solution of sulphuric acid and water, respectively, as a function of temperature, for r=0.8, [H2SO4]=10^{12} m^{-3}, and K1=7.94·10^9 mol/kg.

However, Figure V.3 has shown that the particle critical radius variation is more important than the corresponding temperature variation, so that the normalized surface tension term tends to increase with temperature. A larger particle critical radius implies that the phase transition terms should vary in consequence. However, it is the interaction of ambient conditions, the critical radius and the critical particle composition that eventually determines the incidence of temperature on the nucleation rate. As it is depicted in Figure V.18 the degree of saturation of ambient air relative to a flat solution of critical particle composition is markedly anticorrelated with the critical radius. As a result the radius induced variation of the

196

phase transition terms is neutralised by the variability of the particle vapour pressures, so that eventually the surface tension term lets the nucleation energy barrier increase with temperature. The mechanical corollary to stable particle formation is that the higher temperature causes more frequent molecule particle encounters, but that the resulting particles are thermodynamically much more unstable in terms of their tendency to evaporate, so that the net particle growth flux is lowered.

Contour plots V.19 and V.20 summarize the variability of ion-dipole interaction enhanced ion-induced nucleation as a function of both atmospheric sulphuric acid and water vapour, and sulphuric acid and temperature, respectively. Note that the nucleation rate at the threshold of stable particle growth is correlated with temperature while it is anticorrelated with humidity. This stems from the threshold nucleation being a linear function of the corresponding sulphuric acid number concentration.
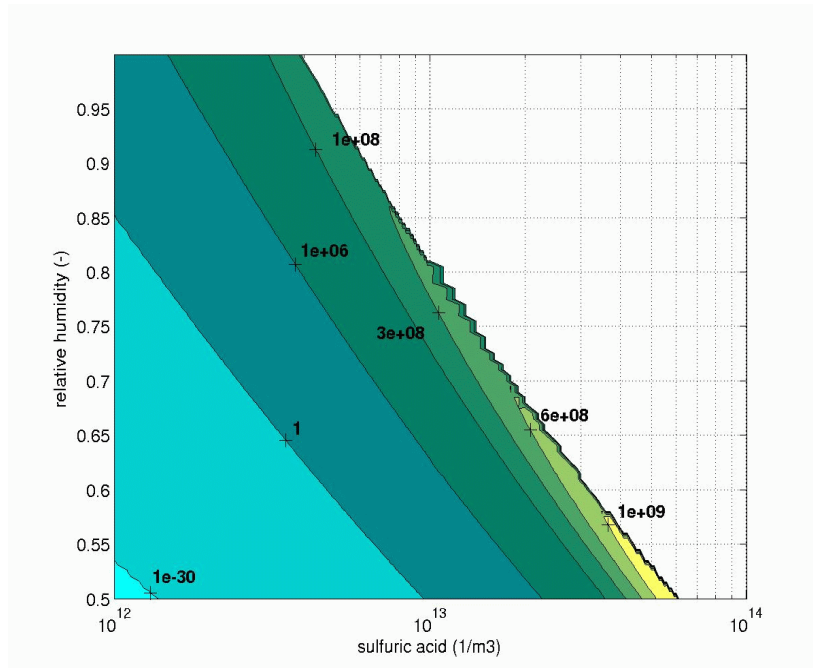
Figure V.19: Isopleths of the ion-induced enhanced nucleation rate [m⁻³s⁻¹] as a function of the atmospheric sulphuric acid number concentration and relative humidity, at T=288.15 K and K1=7.94·10⁹ mol/kg. The assumed ion concentration is 2·10⁹ m⁻³.
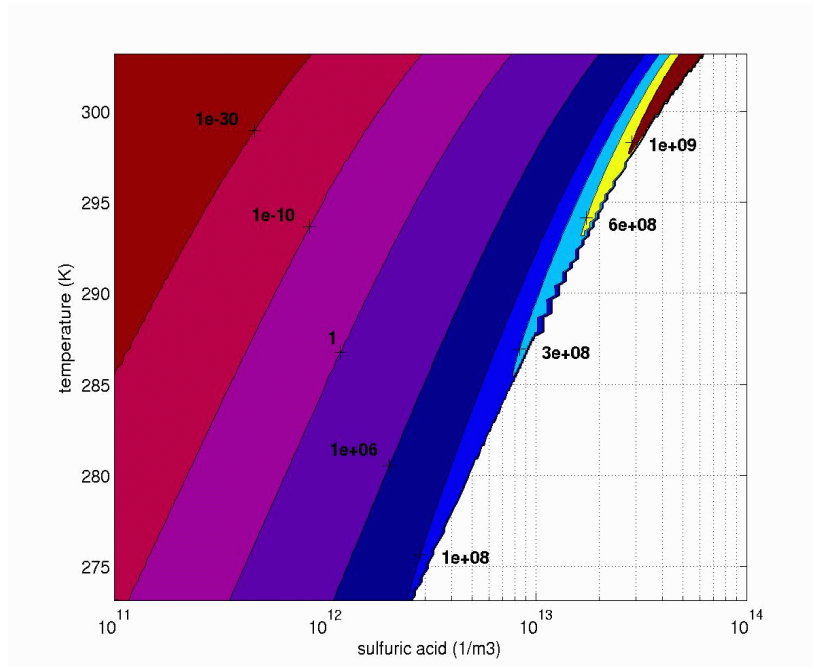
Figure V.20: Same as preceding as a function of temperature and the sulphuric acid number concentration, for r=0.8 and K1=7.94·10⁹ mol/kg.

V.2 Secondary aerosol growth dynamics

V.2.1 Introduction

The box model of aerosol mechanics allows simulating the dynamics of particle growth, nucleation, ambient sulphuric acid and free ions, with temperature, air density, humidity, and the ionisation and sulphuric acid formation rates as input parameters. Both homogeneous and heterogeneous nucleation serve as source function to secondary aerosol. Alternatively sea salt particles may be injected into the system. The specific chemical nature of these is neglected, so that they are assimilated to the secondary particles. The box model may not represent the spatial specificities of aerosol formation and growth, and the ensuing mixing patterns.

The main purpose of the zero-dimensional model of aerosol growth is the exploration of growth dynamical patterns of secondary aerosols, especially as related to aerosol mechanics, ionisation and sulphuric acid formation, nucleation, and primary and secondary particle interaction. Constant atmospheric parameters, the absence of background aerosols, aerosol transport, as well as cloud aerosol interaction processes ensure that the number of relevant elements is reduced to a minimum. Simulation results without ion attachment allows determining the relative part of condensation and coagulation to aerosol growth. The subsequent inclusion of ion attachment shows the nature of the contribution of this process, while the injection of sea salt aerosols yields an evaluation of primary and secondary particle interaction. Finally the sensitivity of particle growth dynamics to sulphuric acid formation and the ionisation rate is investigated in their relationship to the indirect sun aerosol cloud climate interaction theories.

V.2.2 Aerosol growth dynamics without ion attachment

In this subsection general aerosol growth dynamical properties are shown and scrutinised as to their process relative patterns. Ion attachment is excluded in a first step, so that the relative part of condensation and coagulation may be investigated without disturbing third part effects. Simulations are carried out under the conditions specified in the caption of Figure V.21, and are supposed to be representative to tropical marine conditions.

Figure V.21 depicts simulation results of the particle charge integrated aerosol distribution at discrete time steps. The aerosol spectrum after twelve simulated hours at 12 pm. local time, while representative to the aerosol distribution at night, is mono-modal while the remaining daytime representative spectra are bimodal. A look on Figure V.22 shows that the nucleation rate is an extremely sensitive time function, with figures rapidly dropping to zero at night. This pattern follows from the parametrization of atmospheric sulphuric acid formation adopted here (see Equation IV.18), as it is demonstrated by Figure V.23 showing that ambient sulphuric acid and nucleation evolve in parallel. The ultrafine particles grow rapidly, so that when nucleation falls short, the freshly nucleated particles vanish shortly after, resulting in the 12 hour mono-modal particle distribution. The ultrafine particle mode is thus conditioned by the nucleation as a process and source function and will consecutively be addressed to as the *nucleation mode*.
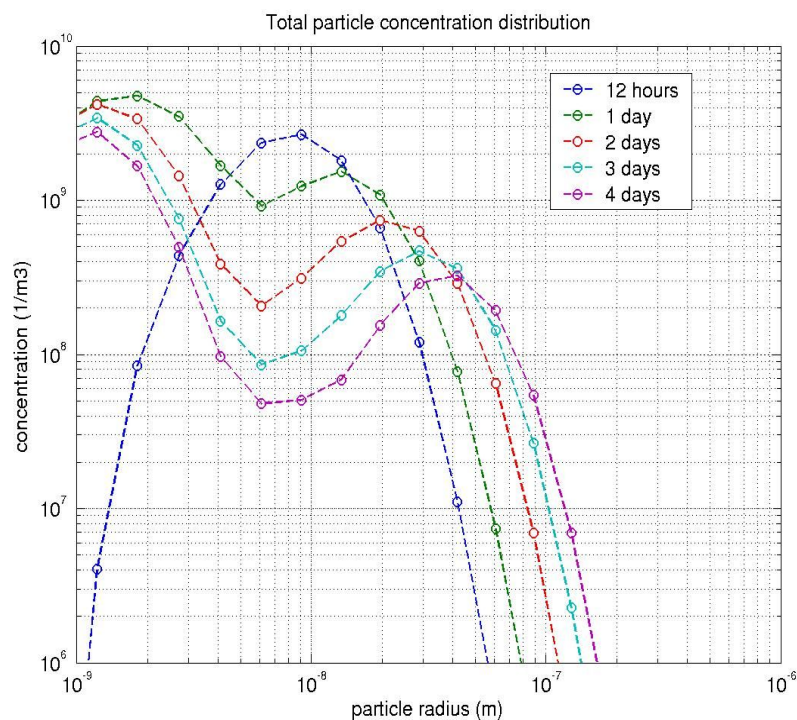
Figure V.21: Modelled particle spectrum at daily time intervals, 12 hour spectrum for comparison. Simulation initial conditions: start at 12 am., sulphuric acid concentration 10^{13} m^{-3}, formation rate 10^{10} s^{-1} m^{-3}, ions $2 \cdot 10^9$ m^{-3}, formation rate $2.5 \cdot 10^6$ ion pairs s^{-1} m^{-3}, temperature 293.15 K, atmospheric pressure 1013.25 hPa, relative humidity 0.8. No background aerosol and sea salt emission. Ion attachment is excluded as a growth process.

On the following day (see 1 day distribution on Figure V.21) a new nucleation burst event induces a new nucleation mode, which is by then separated from the mode nucleated on the preceding day. The bimodal shape is therefore primarily conditioned by the discontinuity of nucleation. However, the daily succession of nucleation bursts does not lead to an equivalent number of particle modes. Apart from the freshly nucleated particles, the secondary aerosols seem to gather in a unique mode, which is consequently designated as the *(secondary particle) accumulation mode* (Pandis et al., 1994). The absence of a succession of particle modes may thus not be explained by the nucleation discontinuity, but rather points to another dynamical effect. Further investigations will reveal the supplementary elements that determine the bimodality of the secondary aerosol.

Heterogeneous nucleation is the dominant process of new particle formation during the entire simulation time interval (Figure V.22). The ion-induced nucleation rate tends to a plateau during the daytime nucleation bursts. The maximum nucleation rate happens to correspond to the ion formation rate, which acts as a limiting factor, as stated in the previous section. Under this circumstance homogeneous nucleation may become relevant, as it is confirmed during the nucleation burst on the first day, when the classical binary rate attains up to one tenth of the ion-induced particle formation rate. Note that the excess of atmospheric ions is consumed at the onset of nucleation, so that the nucleation rate may initially exceed the ionisation rate for a relatively brief period of time. The ion concentration, depicted in Figure V.24, shows in analogy to ambient sulphuric acid numerically stiff behaviour with rapid transition from night time recombination loss dominated to the daytime nucleation loss dominated pseudo-equilibrium. Since the nucleation rate reaches about *1 s^{-1}* per free ion in the vicinity of the stable growth threshold value, the daytime pseudo-equilibrium concentration in the absence of ion attachment and relevant recombination would be according to Equation IV.4 *c/a=5·10^6 m^{-3}* for *(R$_f$)$_\pm$=0.5c=2.5·10^6 m^{-3}s^{-1}*.

Figure V.25 shows the relative aerosol concentration distribution resulting from two different ion formation rates. Although ratio of the high to the low ionisation rate is 2.5, the corresponding ratio of the number concentration of the freshly nucleated aerosols is less than 2.5. With increasing size the ratio further decreases, reaching figures below unity, whilst it is close to unity in the vicinity of the maximum of the accumulation mode. However, the ratios below unity do not significantly influence the total particle number as the absolute particle number that they are associated with is negligible.
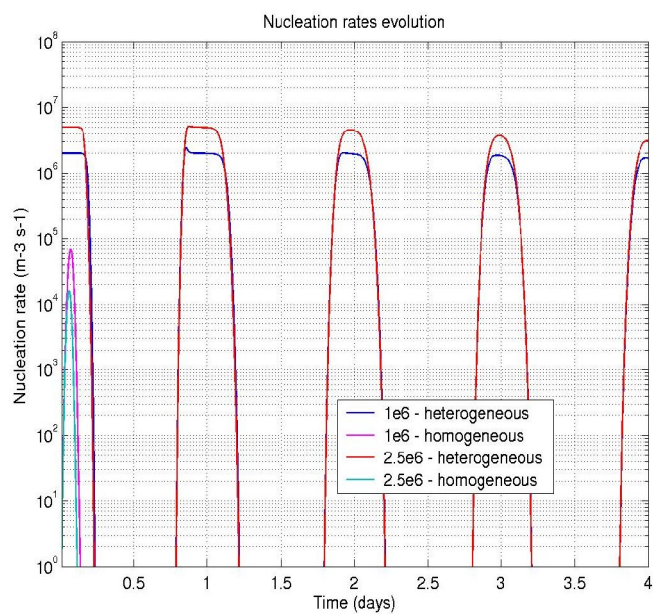
Figure V.22: Ion-induced and classical binary nucleation rate as a time function for two ionization rates [m⁻³ s⁻¹]. Conditions see Figure V.21. Note that the maximum ion-induced nucleation rate is equal to double the ionization rate.
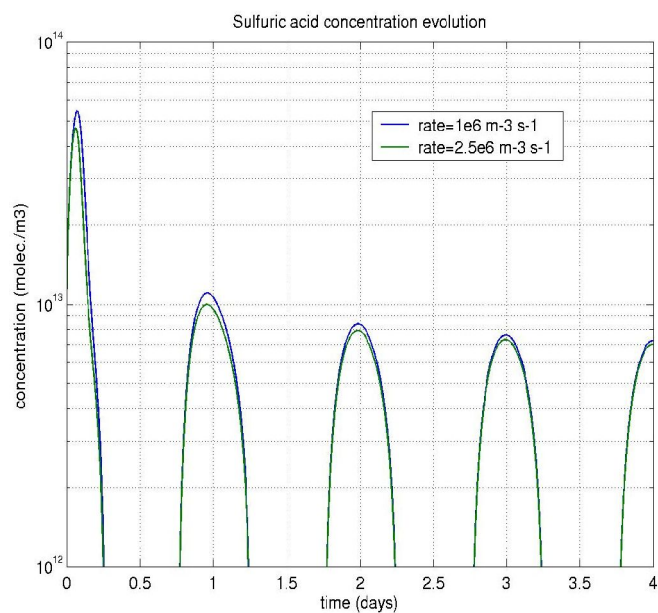
Figure V.23: Variability of the modelled sulphuric acid concentration. Results for two ionisation rates are shown. For simulation conditions see Figure V.21.
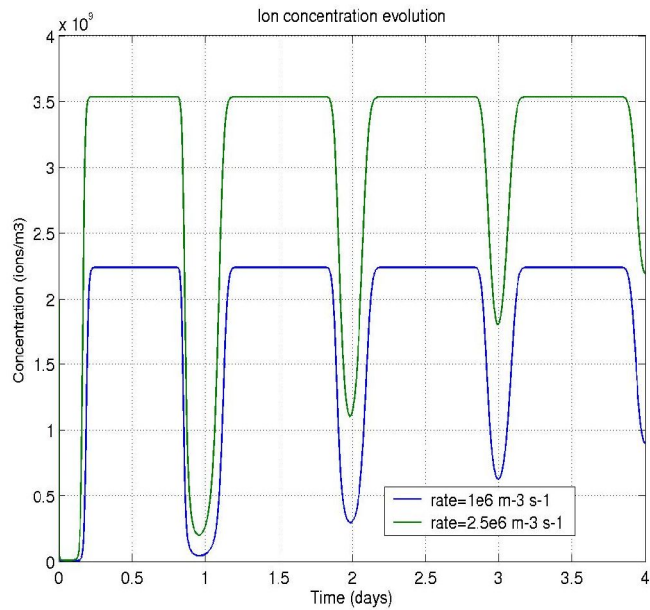
Figure V.24: Cluster ion concentration as a time function for two ionisation rates. Simulation conditions according to the commentary to Figure V.21.
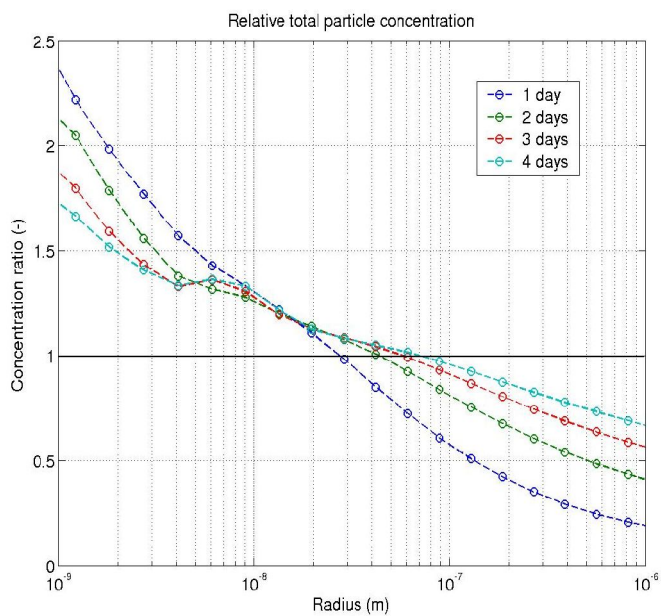
Figure V.25 : Relative aerosol spectrum of the secondary aerosol obtained with an ionisation rate of $2.5 \cdot 10^6$ s^{-1} m^{-3} to the 10^6 s^{-1} m^{-3} ionisation rate distribution. Simulation conditions see Figure V.21.
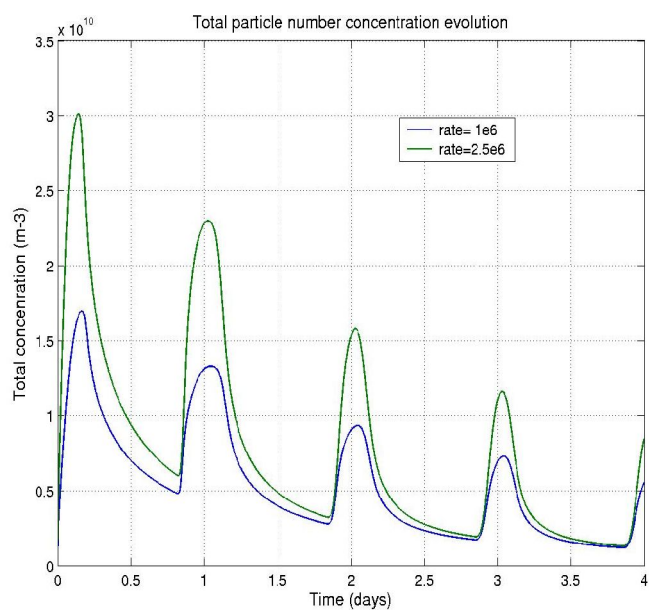
Figure V.26:. The total particle number in the system is compared for two different ion pair formation rates. Simulation conditions are given in Figure V.21
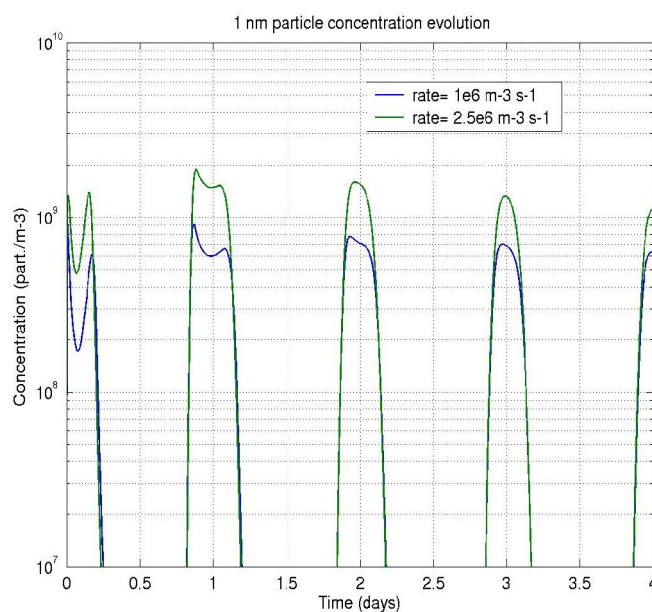
Figure V.27: Simulated approximately 1 nanometre size particle number concentration. Particle charge is one negative elementary charge, number of sulphuric acid molecules per particle is 10. Results are displayed for two ionisation rates. Other simulation conditions see Figure V.21.

204
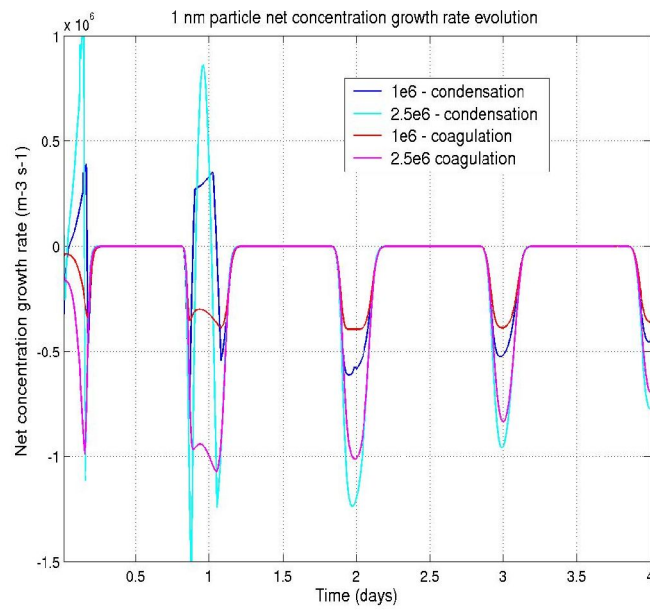
Figure V.28: Net particle flux related to the processes of condensation and coagulation. Simulation conditions see Figure V.21 and preceding.
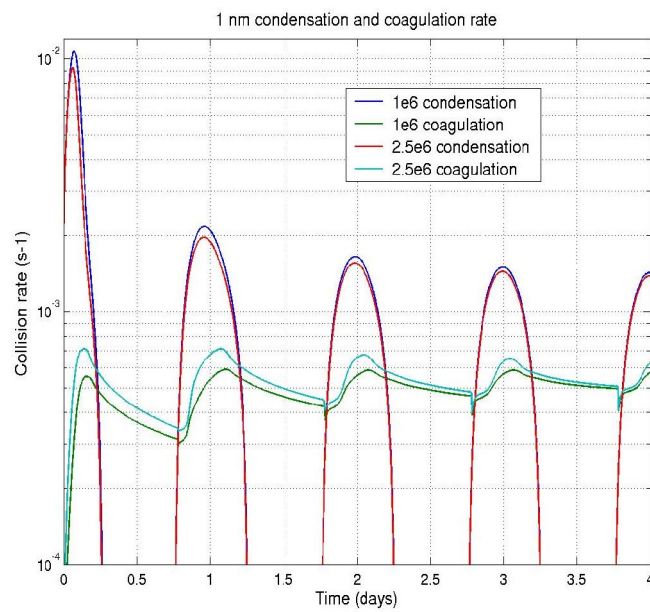
Figure V.29: Frequency a 1 nanometre particle experiences condensation and coagulation. Simulation conditions see Figures V.21.

In principle both condensation and coagulation might induce a pattern of differential aerosol growth as a function of the nucleation rate. The continuously decreasing ratio may indicate an effective particle number reducing process, i.e. coagulation, whose effectiveness increases with increasing particle number. Condensation is a particle number conserving process but depends on ambient sulphuric acid. A decreasing ratio might thus result from a slower particle growth velocity, as a higher number of nucleated particles tends to consume a higher amount of sulphuric acid, so that a lower amount is available to the individual particle. The relative incidence of these mechanisms will now be investigated.

Now, let coagulation alone be assumed to cause the observed *differential* particle number reduction. As the reduction potential of coagulation is proportional to the particle concentration itself, the pure coagulation scenario would make the particle ratio continuously decrease and asymptotically tend to unity with increasing size. Coagulation could by no means let the observed ratio become smaller than unity. Since the ambient sulphuric acid concentration is not affected in a major way by the nucleation rate, it seems that it is the interaction of condensation and coagulation that is responsible for the observed differential particle number reduction. Via condensation the time required for the particles to reach a certain size will be negatively correlated with the total aerosol number, which in the meantime will be more effectively reduced by coagulation. As time goes on, the regulating effect of coagulation will make the aerosol number tend to an equal number, so that with increasing aerosol size the sulphuric acid consumption, and therefore also the nucleation rate, tend to become levelled.

The preceding description characterizes the aerosol growth system as an effectively damped system, for which the sinusoidal parametrization of atmospheric sulphuric acid formation acts as a time dependent forcing that induces undulation. The effective interaction mechanism of coagulation and condensation tends to make the system evolve to a similar evolution independently of the initial particle input. Within the simplified five-dimensional phase space built up by the sulphuric acid and small ion number, the particle total number (see Figure V.26) and mean size, and the sulphuric acid formation rate, the prospective evolution of the system is reminiscent to a time inverted saddle-focus around the mean particle size axis (e.g. Nicolis, 1995, p. 89). To illustrate the damping potential of combined coagulation and condensation, let the following system be considered:

$$(1) \quad \frac{dx}{dt} = -axy - bx + cy$$

$$(2) \quad \frac{dy}{dt} = -axy + d \quad ,$$

f V.6

where x and y are the aerosol particle and the sulphuric acid number concentration, respectively, the parameters a and b stand for the effectiveness of condensation and coagulation, respectively, c is the assumed proportionality constant of nucleation to sulphuric acid, and d is the sulphuric acid formation rate.

The previous system presents one physical node:

$$(1) \quad y_0 = \frac{d}{ax_0}$$

$$(2) \quad x_0 = -\frac{d}{2b} + \sqrt{\left(\frac{d}{2b}\right)^2 + \frac{cd}{ab}} \quad .$$

f V.7

The previous equation expresses that the stable concentration is a function of the ratio of the source to the sink terms. The non-linear dependence on the product of condensation and coagulation effectiveness reflects the incidence of the interaction of these processes in letting the particle concentration tend to a non-zero equilibrium concentration.

Linear stability analysis leads to the Jacobian:

$$J_{xy} = \begin{pmatrix} -ay - b & -ax + c \\ -ay & -ax \end{pmatrix} \quad .$$

f V.8

The elements of this matrix are strictly negative at the limit of the node, except for the upper right element, for which it may be shown that:

$$(-ax + c)\big|_{x_0} > 0 \Leftrightarrow \left(\frac{cd}{ab}\right)^2 > 0 \quad .$$

f V.9

The nucleation rate term thus presents an intrinsic tendency to produce instability. The eigenvalues of the Jacobi matrix are:

$$\lambda_{1,2} = -\frac{a}{2}(x+y) - \frac{b}{2} \pm \sqrt{\left(\frac{a}{2}(x+y) + \frac{b}{2}\right)^2 - (abx + acy)} \quad .$$

f V.10

At the limit of the node the real part of the eigenvalues are strictly negative, while the existence of an imaginary part is subject to the condition:

$$x_0\left(ax_0+\frac{d}{x_0}+b\right)^2-4\left(abx_0^2+cd\right)<0 \quad .$$

f V.11

This expression shows that the Equation System V.7 may present intrinsic damped oscillation behaviour in the vicinity of the stable node. Expression V.9 underlines anew that the simultaneity of condensation and coagulation conditions the fundamental dynamical properties of the system. The stability analysis of the simplified aerosol growth system has allowed rendering its predicted convergence property plausible, when abstraction is made of ion concentration and mean particle size. Apart from the time-dependent forcing, additional oscillation might arise intrinsically through the interaction of the growth processes. The convergence property of the aerosol growth system with respect to its particle number will be further investigated in this section. The aerosol growth system sketched in this paragraph may be oversimplified in as much as the continuous size distribution of aerosol has not been considered. The size differential incidence of coagulation and condensation will now be investigated, taking the 1, 10 and 100 nanometre particles as representative examples of the secondary aerosol spectrum.

Figure V.27 depicts the modelled 1 nanometre particle concentration as a time function. It shows the pronounced modulation of freshly nucleated particles through nucleation, which is in turn conditioned by the undulating sulphuric acid formation rate. The small particle end of the aerosol spectrum constitutes the bulk of the total particle number (see Figure V.26), letting these two variables largely evolve in parallel. In agreement with the convergence hypothesis, the total particle number variability is damped, as the ambient sulphuric acid concentration, which determines the nucleation rate, is more and more conditioned by the larger secondary particles. Due to the interaction mechanism of condensation and coagulation and the consequent convergence of the nucleation rate, the number of larger particles is increasingly independent of the ionisation rate, and so is the total particle number.

Figure V.28 shows the evolution of the net condensation and coagulation flux relative to the 1 nm particle bearing one elementary charge. Initially the simultaneous net condensation and coagulation losses are overcompensated by the nucleation flux, leading to a steady increase of the particle concentration. This tendency is abruptly inverted when the critical nucleation

radius becomes inferior to 1 nanometre. This phenomenon has several causes. First, following nucleation theory it would be consistent that in the vicinity of the saddle point the net particle flux is continuous. As the model particle concentration below critical size is zero and not at equilibrium concentration, however, it will take a certain amount of time for the corresponding concentration to build up. Consequently, an artificial momentary particle flux disruption is produced that will lead to a decrease of the particle concentration in the adjacent supracritical size classes. The rapid population build up in the freshly stabilized particle classes is testified for by the fast subsequent increase of the net condensation flux. The continuous increase of the coagulation losses further expresses the total particle number increase. Second, stable particles are subject to coagulation, and therefore progressively reduced with increasing size. The particle growth flux thus tends to decrease with increasing distance to the critical size, whilst the respective critical size bin tends to show maximum particle concentration. Third, with increasing distance to the critical radius an increasing part of the growth flux will be lead over the neutral classes, thus reducing the concentration of the single charged particles. During the consecutive nucleation bursts the maximum size difference between the critical and the nanometre particle is less pronounced, and the intermediate abrupt decrease of the nanometre particle concentration tends to vanish. Comparing the net condensation and coagulation fluxes as a function of the ionisation rate, it appears that both the net condensation flux and particle concentration are positively correlated with the ionisation rate. However, it should be noted that the corresponding net coagulation losses are also higher.

Figure V.29 shows the occurrence frequency of condensation and coagulation involving an elementary charged nanometre particle as a time function. As condensation is proportional to the sulphuric acid number concentration, it shows the pattern of sulphuric acid variability. The coagulation rate, in turn, is correlated with the particle total number, as it is demonstrated through comparison with Figure V.26. As due to the particle number convergence mechanism, the individual condensation rate is higher in case of a low ionisation rate while the coagulation rate is lower. In case of a high ionisation rate the survival probability of a small particle is lowered along with the associated condensation growth rate. The little ticks related to the onset of a nucleation burst provide an interesting example of a numerical artefact and growth dynamical hysteresis.
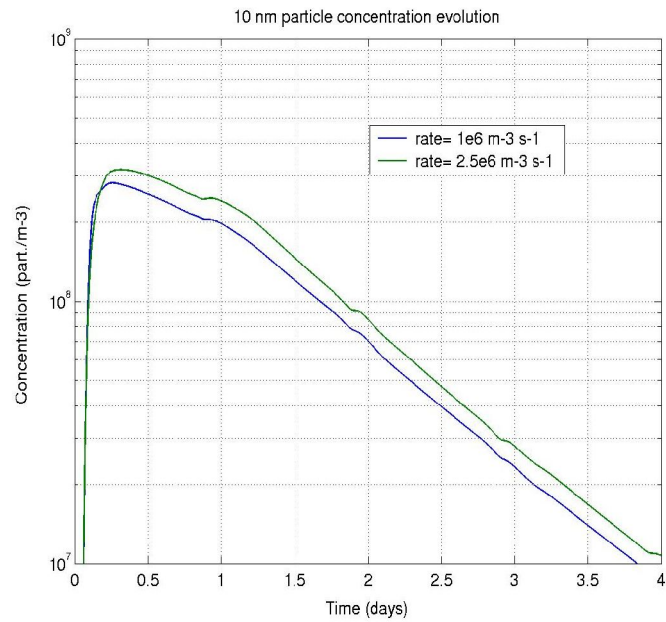
Figure V.30 : Evolution of the number concentration of the 10 nanometre particles, according to the closest size bin. Other parameters see Figure V.21.
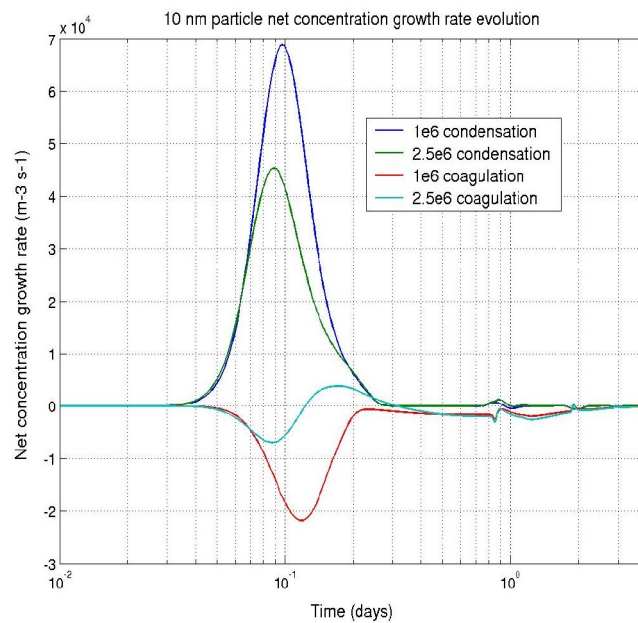
Figure V.31: Net condensation and coagulation flux of the 10 nanometre particles. Simulation conditions see Figure V.21. Particle charge is one negative elementary charge.
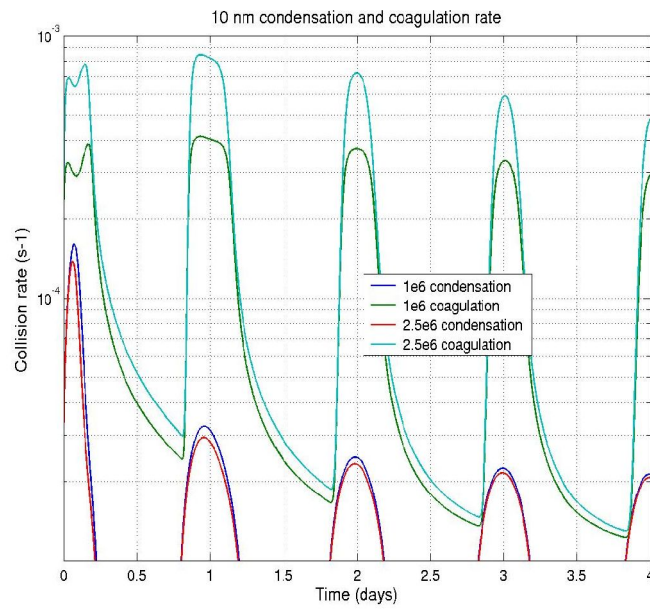
Figure V.32: Frequency the 10 nanometre particle experiences condensation and coagulation, respectively. Simulation conditions see previous.
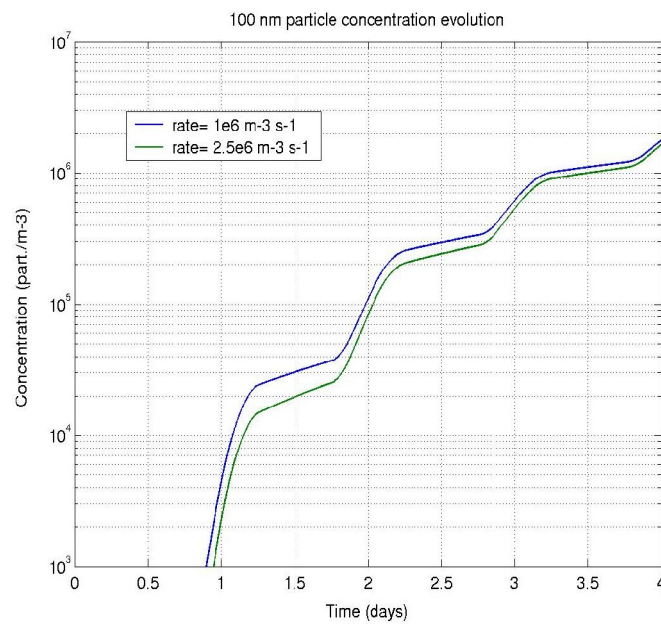
Figure V.33 : Evolution of the 100 nanometre particle number concentration. The particle charge is one negative elementary charge. Other simulation parameters see Figure V.21

211
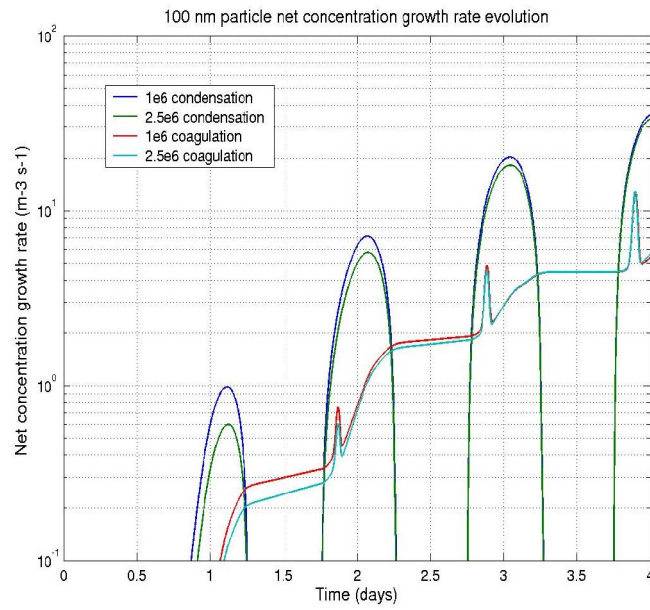
Figure V.34: Net condensation and coagulation flux of the 100 nanometre particles. Simulation parameters see Figure V.21.
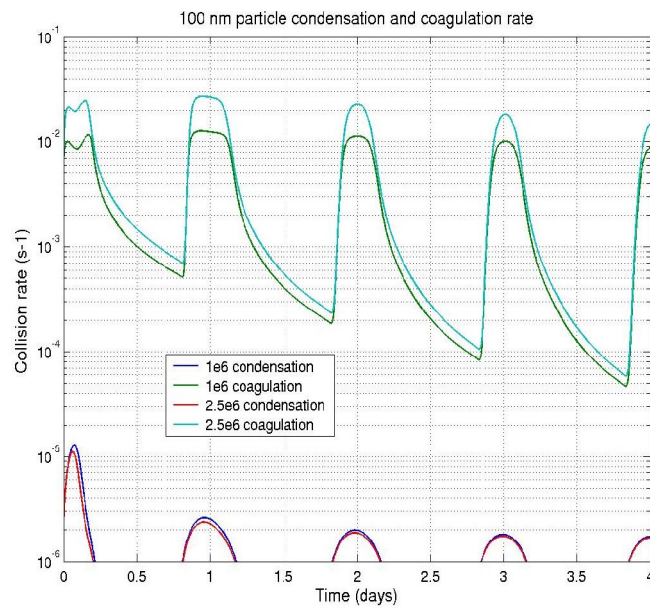
Figure V.35: Experience frequency of condensation and coagulation of a 100 nanometre particle. Simulation conditions see Figure V.21.

As the critical radius decreases to nanometre size, the coagulation rate becomes an increasing function of the nanometre particle number concentration due to their increasing number. However, because of the criterion of indistinguishableness in relationship with coagulation among equal particles, the related coagulation kernel is approximately half the one of the contiguous size bins. As a consequence the coagulation probability tends to drop down abruptly as the critical radius, and therefore the bulk of the nucleation mode particles are within the nanometre particle size class. With increasing critical radius the nanometre particle coagulation rate is less conditioned by their own concentration, but rather by the already constituted broad nucleation mode, thus leading to the observed growth dynamical hysteresis.

Figure V.30 depicts the elementarily charged particle number concentration within the first size class whose nodal particle is larger than 10 nanometres. The 10 nanometre concentration attains a maximum after a fast build up transition and then continuously declines exponentially with slight interruptions during the nucleation events. When one compares with Figure V.21 one may see that the maximum is more readily reached than the point at which the peak of the nucleation mode is located at 10 nanometre size. Figure V.31 shows the net coagulation and condensation growth rates. Note that the time axis is on the logarithmic scale to stress the quick initial variation of the variables, standing for the disequilibrium the particle growth system is in at the onset of secondary particle formation. The initial rapid particle number increase is dominated by the disequilibrium of the condensation flux that ensues from the particles still being concentrated in the smaller classes. During the second nucleation burst the disequilibrium is much less pronounced. Both the condensation and coagulation net fluxes are lower since the aerosol spectrum build up is in a far more advanced stage. Coagulation is the dominating process of particle number decay, as it is testified by the negative net coagulation flux while the condensation flux is more or less at equilibrium.

In opposition to the 1 nanometre particles, the most frequent 10 nanometre particle growth process is coagulation, as expressed by Figure V.32. In analogy, the coagulation frequency shows the pattern of the total particle number, while the condensation frequency reflects the diurnal variability of the sulphuric acid concentration. Coagulation frequency peaks show the same top deformation as the one nanometre particle number concentration (see Figure V.29), stressing the relative contribution of ultrafine particles to coagulation involving 10 nanometre particles. In accordance with the convergence mechanism of aerosol number sketched above, the lower ionization rate condensation frequency is more higher while the coagulation rate is

positively correlated. Paradoxically the net condensation growth flux is anticorrelated with the ionisation rate at the onset of particle formation, while the situation is inverted as of the second nucleation burst. This contrasts with the 1 nanometre net flux, which is correlated with the ionisation rate during the entire simulation period. The correlation inversion may be explained considering the shape of the particle distribution. The nucleation rate correlates with the ionisation rate, leading to a higher amount of ultrafine particles. However, the higher amount of particles consumes more sulphuric acid, so that the individual condensation growth rate. The effect of the lower individual growth rate adds up, leading to a decreasing particle relative concentration with increasing size distance to the critical ratio (Figure V.25). The net flux is therefore correlated with the ionisation rate at critical size, while beyond a certain size the flux is anticorrelated. As a result the condensation growth displacement of the nucleation mode maximum is slower in case of a high ionisation rate and the net condensation growth flux is initially anticorrelated. When the slower nucleation mode attains the observed particle size, the trend inverses. Although the individual condensation rate is still lower, the net condensation flux is higher due to the still higher amount of particles. Coagulation is not effective enough at 10 nanometre size to have levelled the particle number to equal values indifferently of the nucleation rate.

Figure V.33 shows that the 100 nanometre particle concentration is increasing over the whole simulation interval. Figure V.35 depicts that coagulation is the primary process at the single particle level. However due to the strong particle number size gradient the net condensation flux is much less balanced than the total particle number influenced coagulation flux, and condensation tends to be the dominant process of particle number increase (Figure V.34).Due to the convergence property of aerosol particle dynamics, and as the particle concentration is in the build up phase during the whole simulation period, both the net condensation flux and individual frequency are anticorrelated with the ionisation rate. Interestingly the net coagulation flux and the individual coagulation rate show divergent behaviour. While the coagulation frequency is correlated with the total particle number and thus the ionisation rate, the initial net coagulation flux is anticorrelated. This shows a certain spectrum geometry dependence of the coagulation flux, in analogy to the one of condensation. Due to the particle size dependence of the coagulation kernel the absolute coagulation flux tends to be dominated by encounters between particles contrasting by their respective size. The net coagulation flux, however, tends to be dominated by encounters between similarly sized particles via its

214

dependence on the local particle number gradient. For this reason it is initially anticorrelated with the ionisation rate for accumulation mode particles. The weaker dependence of coagulation within the accumulation mode on nucleation mode particles also explains the less pronounced first day peak deformation of the coagulation frequency, when compared with the 10 nanometre particle coagulation frequency, as a result of the variation of the critical radius.

V.2.3 Ion attachment and ambient temperature influence

In this subsection the influence of ion attachment on particle growth dynamics is explored in comparison with the results of the previous sub-section. The sensitivity of the aerosol spectrum to temperature is also investigated.

Figure V.37 shows the typical particle distribution as a function of their electrostatic charge within their respective size class. Encounters between particles bearing a certain amount of elementary charges of equal sign are very improbable. For ultrafine particles the charge limit is therefore attained with one elementary charge. Moreover, there is a size specific charge limit beyond which additional charge leads to the disruption of the particle (Pruppacher and Klett, 1997). As the critical number of equal charges is not assessed in this study, a negligibly small number of overcharged particles remains. With increasing size the repulsion effect is vanishing within the charge number interval considered here, so that the particles tend to become uniformly distributed.

Figure V.36 depicts the particle distribution with ion attachment relative to the same distribution without ion attachment. The incidence of ion attachment on the smaller particle concentration is high, whereas the larger particle fraction, of say more than 30 nanometres, shows no major change. According to the above considerations, ion dipole interaction has no substantial influence on the condensation kernel of particles larger than 10 nanometres. However, the particle coagulation kernels show a significant asymmetry, meaning that inhibited collision of equally charged particles tends not to be counterbalanced by enhanced coagulation between oppositely charged particles. The net effect of particle charge on their growth velocity is therefore negative to indifferent, depending on their respective charge and size. As ion particle encounter between oppositely charged particles is more probable, as far as their encounter frequency is charge limited, ion attachment will reduce the average particle charge in the Aitken mode (Figure V.38).

215
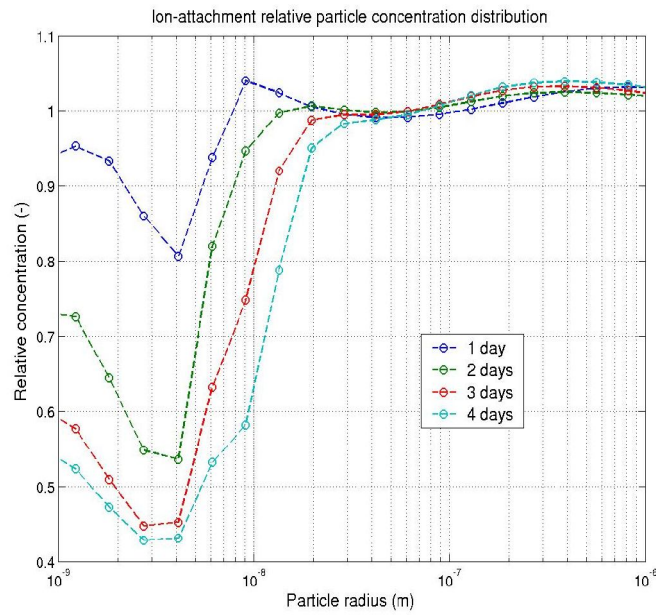
Figure V.36: Particle distribution when ion attachment is included relative to the results obtained when this process is neglected. Simulation conditions similar to those of Figure V.21.
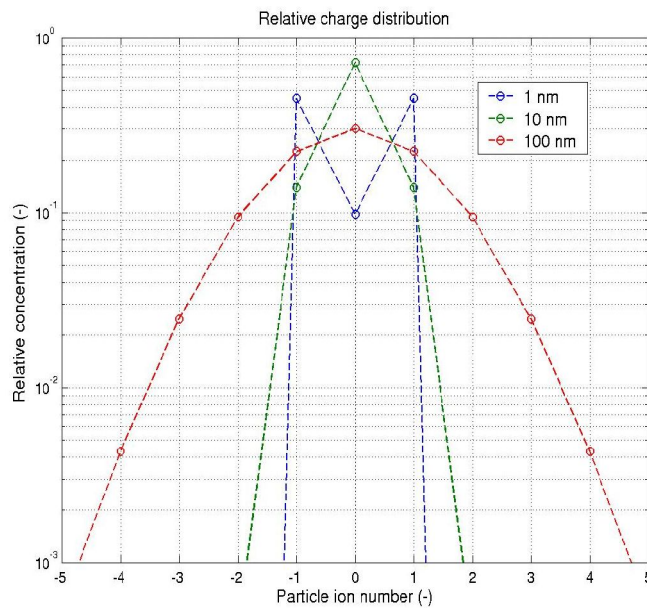
Figure V.37: Number of particles in the respective charge class relative to the total number of particles in the corresponding size class. The charge distribution tends to become more homogeneously distributed when particle size increases. Simulation conditions are those of Figure V.21. Ion attachment is included.
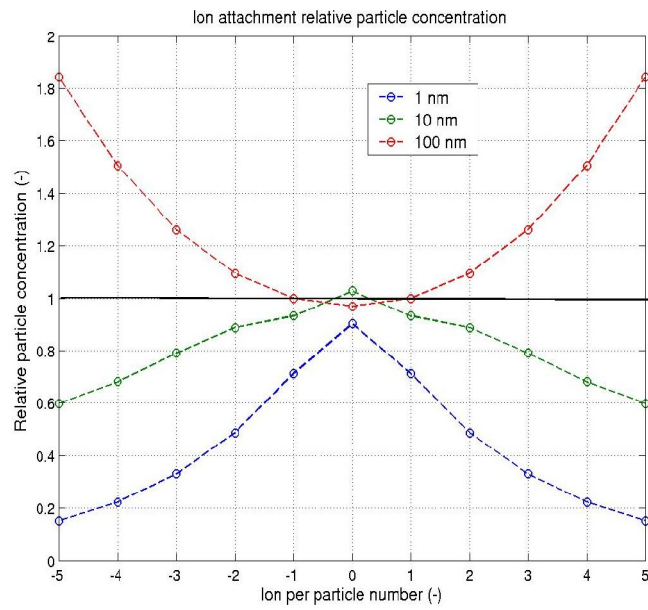
Figure V.38: Charge class resolved particle number distribution relative to the corresponding values when ion attachment is neglected. Ion attachment reduces the mean charge of small aerosols while it precipitates the charge homogenisation of larger particles. Simulation conditions according to Figure V.21.
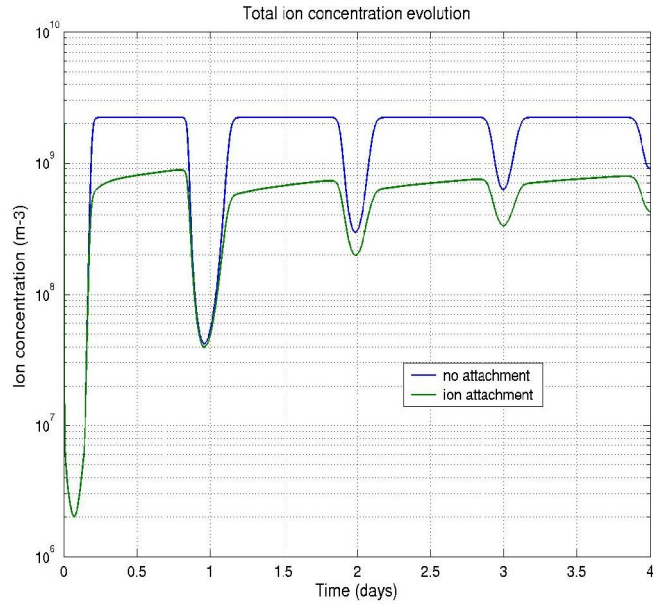
Figure V.39: Total ion concentration when ion attachment is included compared to simulation results without this process. Simulation conditions see Figure V.21.

The net growth rate of ultrafine particles is thus enhanced, so that their relative concentration as depicted by Figure V.36 is below unity. As a corollary, enhanced growth results in a slightly enhanced particle concentration in the larger particle range of above 0.1 micrometres. The charge distribution within the larger particle size classes, although potentially indifferent to particle charge within the assumed range, is still reminiscent of the smaller size class distributions. Ion attachment leads to more rapid levelling of charge distribution within these size classes. Consequently, the relative concentration within these classes of above 100 nanometres tends to be above unity for charged particles, while the uncharged particle number tends to be diminished (Figure V.38).
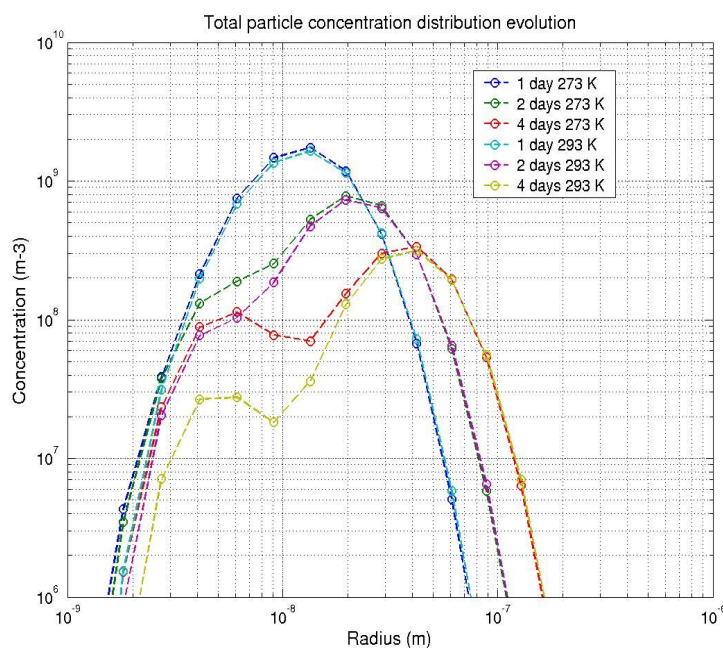
Figure V.40: The incidence of temperature on the aerosol particle distribution. Simulation starts at 6 a.m., initial sulphuric acid concentration is null, the formation rate is 1e10 m^{-3} s^{-1}, the initial ion concentration is in equilibrium with ion recombination, the ion pair formation rate is 1e6 m^{-3} s^{-1}, atmospheric pressure is 1013.25 hPa, temperature is equal to 273.15 and 293.15 K respectively, relative humidity is 80 % in both cases. Ion attachment is included, salt particle emission excluded. The results are displayed for each day at 6 a.m. except on the first day for which display time is 18 p.m..

Figure V.39 depicts the incidence of ion attachment onto aerosol particles on the stable cluster ion concentration. Generally, as it is obvious from the ion balance Equation IV.2, their concentration decreases due to the ion consumptive attachment process. At night-time, when

no nucleation takes place, the ion concentration is no longer an equilibrium between recombination and ionization rate. According to the dynamical stiffness properties of the ion continuity equation, it is in transient equilibrium with the total particle concentration, whose incidence is of similar order of magnitude as for cluster ion recombination. Although due to competing attachment the ion concentration tends to be comparatively low after each daytime nucleation event, and the total amount of nucleated particles is consecutively decreasing, the night-time ambient ion concentration is lower on day 2 than on day one before it tends to increase again. This shows that the ion abundance is a complex function of the particle size dependent ion removal potential and the particle spectrum.

Figure V.40 compares the aerosol spectra at multiples of 24 hour intervals relative to respective ambient temperature. The initial time is 6 o'clock local time, so that the aerosol distributions shown are typical night-time spectra, in opposition to the previous mid-nucleation daytime spectra. The distribution after one day is reminiscent to the 12 hour distribution of Figure V.21, as particles are gathered into a unitary mode. It is only on the following day that the bimodal particle distribution is about to become obvious. The smaller mode may not be explained exclusively through nucleation, as it is separated both by time and size from the critical nucleation radius. Comparing its characteristic radius of about 10 nanometres to the size relevant growth processes as expressed by Figures V.29, V.32 and V.35 it may be interpreted as the resultant of the strong decrease of the condensation velocity, while coagulation has not yet become predominantly effective. As it follows from condensation within the nucleation mode, this mode will be addressed to as the *condensation mode*. It should be noted that during nucleation bursts, the condensation mode is assimilated by the nucleation mode due to the high condensation growth velocity of ultrafine particles. When Figures V.25 and V.40 are compared, one may see that the variation of particle number concentration with temperature is reminiscent to the variation with the ionisation rate. Ultrafine particle concentration is anti-correlated with temperature via the nucleation rate, while the correlation tends to become inverted with increasing size. However, the transient correlation inversion with particle size may not be explained any more by sulphuric acid aerosol growth dynamical interaction, as the sulphuric acid concentration is correlated with the nucleation rate upon temperature variation (not shown). It is the temperature variation that explicitly acts on the growth dynamics via the temperature dependence of the condensation and coagulation kernels. Both condensation and coagulation growth of the particles is

enhanced. High temperature coagulation yields less ultrafine particles, but also enhanced condensation, so that the overall effect on the sulphuric acid concentration is negative.

V.2.4 Model validation

2.4.1 Simulation of aerosol growth with sea salt particle injection

The primary aim followed in this sub-section is not to reproduce the marine aerosol population but to study the effect of an increasingly large primary aerosol on secondary particle growth dynamics. This effect is investigated at the instance of sea salt particles, using the Monahan (1986) parametrization as a source function to sea salt emission. For their larger part sea salt particles already have cloud condensation nucleus size when they are emitted into the atmosphere. Their effects on the nucleation rate and the secondary particle spectrum should thus be similar to the ones of a continental dust aerosol. Sea salt particle formation is a surface process. To ensure a quick build up of the primary aerosol it is assumed that 10% of the emitted particles gather in a 1 metre vertical portion of the atmosphere.

Figure V.41 depicts the progressive appearance of the sea salt particle mode. A comparison with the preceding Figure V.40 shows that the coagulative influence of the sea salt mode is such that the residual night-time condensation mode has entirely vanished, while the secondary particle accumulation mode is sensibly less pronounced and displaced to the smaller particle side. Ultrafine particle growth and nucleation are reduced by the relatively low ambient sulphuric acid concentration (Fig. V.43). On the fifth simulated day the nucleation rate is restricted to negligible figures due to the sulphuric acid absorbing sea salt particles. The coagulative capacity of the sea salt particles is also apparent in the high to low ionisation rate relative aerosol spectrum depicted in Figure V.42. Within the salt particle mode the ratio is very close to unity thus demonstrating the overwhelming dominance of sea salt within this mode. When compared with V.25, it appears that the area of massive positive correlation between the ionisation rate and the relative particle number is driven back to the ultrafine particle range. Since nucleation tends to be effectively impeded the area of significant positive correlation is restricted to the secondary accumulation mode. Due to the salt particle mode, the area of negative correlation tends to become suppressed in conjunction with the relative displacement of the high nucleation rate accumulation mode maximum to the

larger particle side (relative particle spectrum geometry, see above).
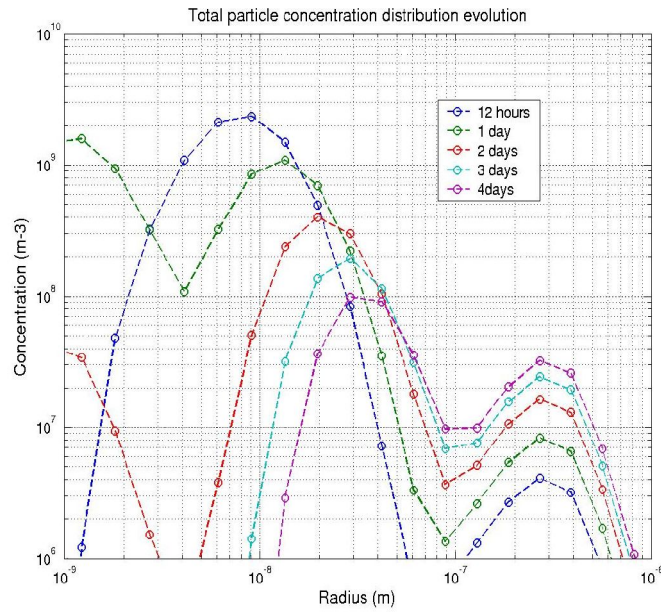
Figure V.41: Ion-induced secondary aerosol spectrum with conjoint sea salt particle emission according to Monahan (1986). Simulation conditions of Figure V.21.
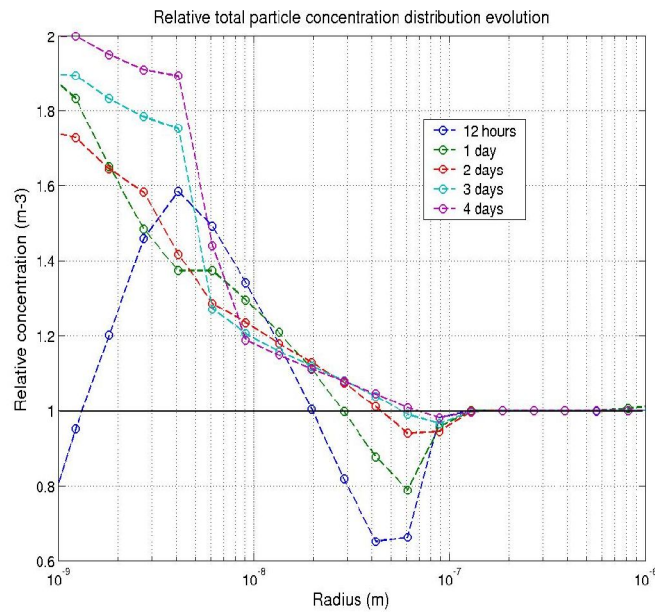
Figure V.42: Aerosol spectrum obtained with an ionisation rate of $R_f=2.5\cdot10^6$ $m^{-3}s^{-1}$ and sea salt injection relative to the one of the preceding figure ($R_f=10^6$ $m^{-3}s^{-1}$). Simulation conditions are those of Figure V.21
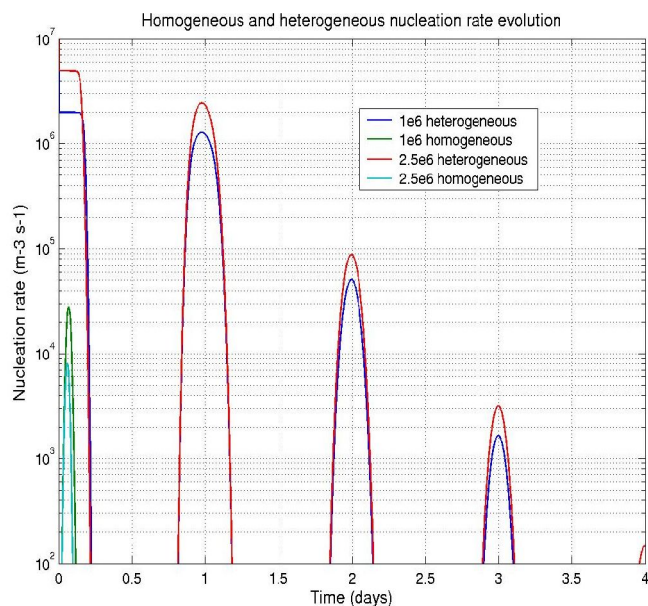
Figure V.43: Ion-induced and classical homogeneous nucleation rate as a time function when sea salt is injected into the secondary particle system. The results are given for an ionization rate of 10^6 and $2.5 \cdot 10^6$ ion pairs per time and volume unit, respectively.

Figure V.44 compares the results obtained with the aerosol box model to marine aerosol data from Quinn et al. (1993). The selected data should present a certain degree of extraneous influence as it was obtained within air coming from aloft and from the continent.. Nevertheless, it shows the typical marine bimodal distribution (Pandis et al., 1994) and is chosen for its similarity with the simulated particle spectrum. Figure V.44 suggests that the observed smaller mode is of secondary while the larger mode is of background continental and/or sea salt origin. Ultrafine particles do not appear within the data, so that no deductions regarding the occurrence of nucleation bursts in the sea salt laden marine boundary layer may be made. However, the comparison suggests that the box model of ion-induced secondary particle formation when combined to an accurate sea salt emission scheme may have the potential to plausibly reproduce the marine aerosol spectrum. Yet it may not be inferred that the assumed ion-induced aerosol formation scheme is accurate as a fortuitous analogy may not be excluded. In particular, it can not be ruled out that the ion-induced formation scheme yields an accurate secondary particle quantity although it is completely differs from the actual formation process. Especially the convergence property of aerosol dynamics, which precisely involves a similar yield of secondary accumulation mode particles for a large range of nucleation rates, has the strong potential to induce futile numeric analogies.

222
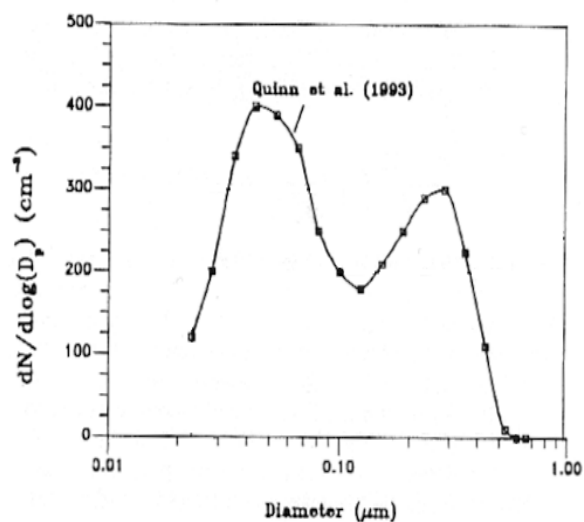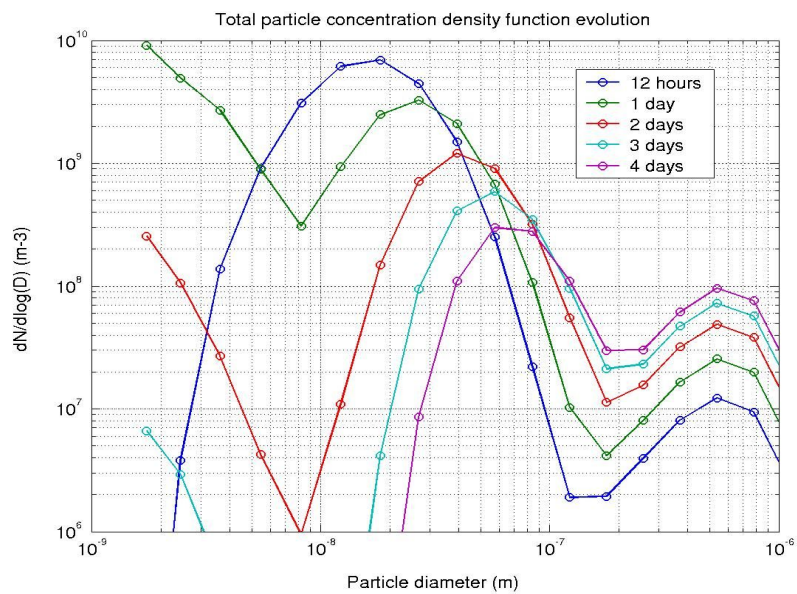
Figure V.44: Comparison of the aerosol distribution simulated with the zero-dimensional box model and a typical bimodal marine particle distribution under (adopted from Pandis et al., 1994; data according to Quinn et al, 1993).

2.4.2 Total atmospheric ion variability

Hõrrak et al. (1998) produce data related to the charged particle spectrum consecutive to assumed nucleation events. They subdivided the charged particle spectrum according to their mobility into estimated size classes ranging from small ions (d<1.8 nm), over intermediate

(1.6<d<7.4 nm) and large ion *1* (7.4<d<23 nm) through large ion *2* (23<d<79 nm). The small ions correspond to elementary ions, subcritical stable, as well as freshly nucleated clusters. The intermediate ions essentially represent the smaller ultrafine particles of the nucleation mode, while the large ions *1* stand for the larger particle fraction of the nucleation mode, that is the condensation mode particles. Large ions *2* represent to the least a major fraction of the accumulation mode.

A remarkable property of the findings of Hõrrak et al. (1998) is that the supposed nucleation occurrences induce a pronounced decrease of the number of charged particles in the accumulation mode. According to the growth dynamical findings presented in this study this may be interpreted as follows. Nucleation bursts produce a high number of charged small particles. These grow rapidly, that is within a few hours, to intermediate size, so that the number of charged particles in these size classes should also increase. The number of particles in the accumulation mode will remain relatively unchanged, as growth to this size takes notably more time. However, ion attachment onto these particles will become less frequent, due to concurrent ion removal via nucleation and consequent ion attachment onto nucleation and condensation mode particles. Ion attachment tends to be relatively charge indifferent onto particles in the accumulation mode. For this reason it has a charge spectrum broadening effect, that adds to the one of particle coagulation (see Figure V.38), so that a reduction of ion attachment onto these particles through competing processes results in a lower number of charged particles in the accumulation mode.

Figure V.45 shows the measurements of Hõrrak et al. (1998) while the typical variability generated through the aerosol boxmodel is represented in Figure V.46. The model small and intermediate ion variability is much more pronounced, while the the diurnal variability of the large ions is of similar order of magnitude when compared to the empirical data. The model result corresponds to a purely secondary population without the interference of primary particles, under which circumstances daily consecutive nucleation bursts occur. The measurement data reflects a more or less continental conditions at a measurement site in Estonia with a consequent number of primary aerosols and more or less effective nucleation inhibition, for which the small and intermediate ion variability is much less pronounced. The analogous variability of the condensation mode particles indicates anew that the number of particles within this mode is very effectively damped by the convergence property of aerosol growth dynamics through the interaction of condensation and coagulation.
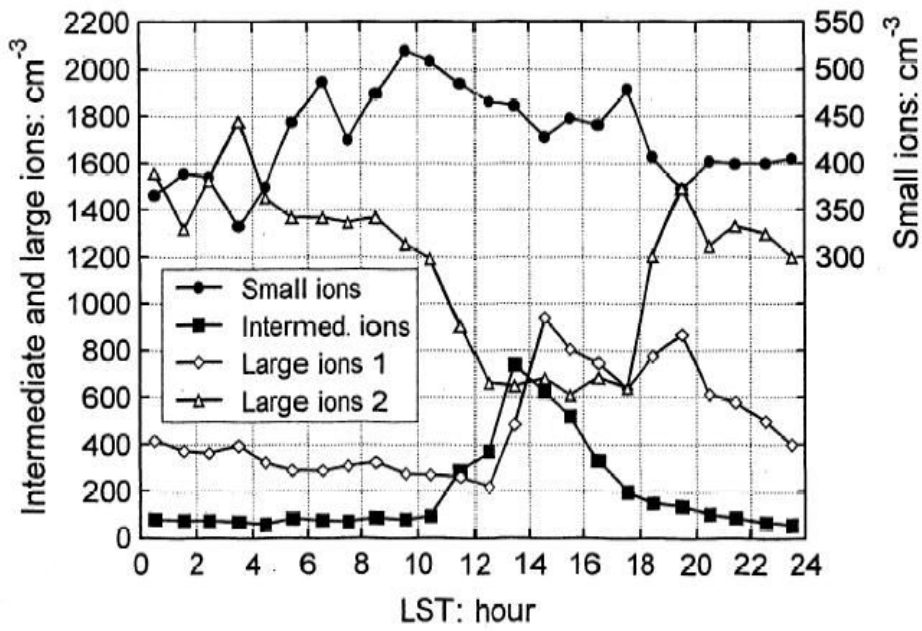
Figure V.45: 24 hour variation of small (<1.8 nm), intermediate (1.6-7.4 nm), large 1 (7.4-23 nm) and large 2 (23-79 nm) ions according to measurements of Hõrrak et al. (1998, adopted from this publication). Ion size is estimated from their mobility spectrum assuming they bear one elementary charge.
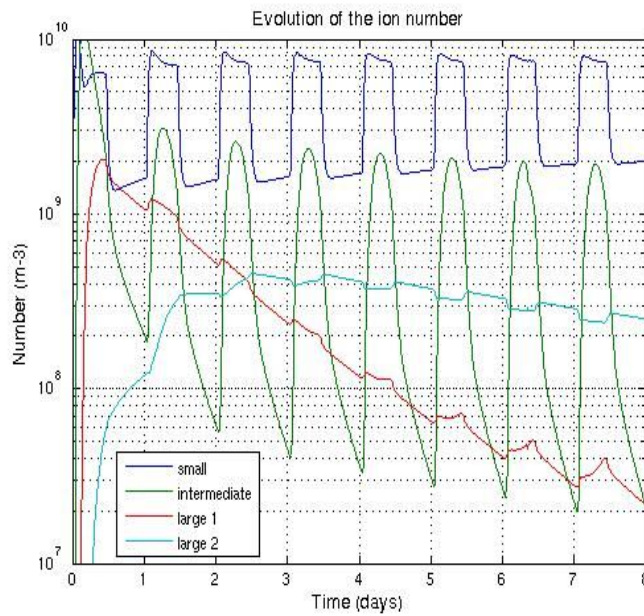
Figure V.46: Modelled charged particle number concentration as a time function. Particles are grouped according to the size intervals specified in the preceding figure caption.

225

The charged particle number decrease among accumulation mode sized particles compares qualitatively with the modelled particle number variability. The above dynamical ion attachment implications to aerosol population dynamics plausibly explain the observed variability. The box model of aerosol growth is thereby validated as to its formalism of ion attachment to reproduce observed charge dynamical effects.

V.2.5 Ionization rate and sulphuric acid sensitivity of the aerosol spectrum

In the present sub-section the sensitivity of the secondary aerosol with respect to the ion rate and sulphuric acid formation is explored. For the sensitivity to appear as clearly as possible the simulations are carried out in the absence of primary particles. Simulations under realistic conditions including aerosol cloud and rain drop interaction will be realised in the following section. The present section is limited to the exploration of aerosol growth dynamical characteristics. These may help understanding particle dynamics under more complex conditions. In order to assess the long time behaviour of the aerosol, simulation time is extended to eight calendar days. The foregoing subsections have revealed that a time interval of approximately two days is necessary to produce secondary accumulation mode particles large enough to be activated as cloud nuclei, assuming that sulphuric acid is the exclusive condensable under marine conditions, and that the critical activation radius as cloud condensation nuclei is 30 nanometres (this figure will prove to be accurate in the following section; size at 80% relative humidity). Eight days is the mean survival lapse of the atmospheric aerosol according to Hobbs (1993). If this figure is relevant in relationship with secondary particles in a cloud laden environment will be explored in the next section.

Typical conditions for aerosol growth at a height of 2000 m are assumed; temperature is lowered to 273.15 K, while the ambient pressure is set to 700 hPa, and the ionisation rate is set to $5 \cdot 10^6$ and $2.5 \cdot 10^6$ $s^{-1}m^{-3}$, respectively. These figures are realistic to the geographic variability of the ionisation rate but are well above the local solar cycle variability, which is of the order of 10% only (Usoskin et al., 2004, see above). The typical sulphuric acid formation rate is estimated at 10^{10} $m^{-3}s^{-1}$ (Clarke et al., 1998; Yu and Turco, 2001), and the solar cycle variability is assumed to allow for a doubling of this value, presupposing a linear relationship between the atmospheric concentration of dimethylsulphide and the sulphuric acid formation rate (Kniveton et al., 2003; see above). Although there is both modelling and observational

evidence for a correlation between the dimethylsulphide flux and the cloud nuclei yield (e.g. Yoon and Brimblecombe, 2002), the surface emission and chemical dynamics leading to the formation of sulphuric acid are still an open an entirely open question (e.g. de Bruyn et al., 2002).

Figure V.47 shows the discrete evolution of the aerosol particle spectrum, whereas the high to the low ionisation rate relative spectrum is depicted in Figure V.48. Note that simulations start at sunrise at 6 am. local time; the respective spectra show no nucleation mode thus differing from Figure V.25, which depicts the characteristic distribution within the nucleation burst. The ionisation rate variability of the cloud condensation number is both a function of the critical activation radius and a time function. When based on the number of particles above a certain size fixed in time, the cloud condensation number is conferred a potential connotation. Figure V.48 indicates that when the critical radius is high, the number of secondary particles that are activated may be anticorrelated with the ionisation rate. With decreasing critical radius this effect tends to be rapidly counterbalanced, and the correlation may become positive. From the ambiguity of the present observations, it is obvious that they may only serve as an indication to the actual correlation of the cloud droplet number and the ionisation rate, as particle activation, primary and secondary particle interaction, and cloud processing may tilt the nature of the correlation either way.

Figure V.49 depicts the sensitivity of the secondary aerosol spectrum to the variation of the sulphuric acid formation rate. Aerosol growth velocity is positively correlated with the sulphuric acid source function, so that a higher dimethylsulphide emission rate should lead to a higher number of secondary accumulation mode particles. Following the non-linear spectral dependency of the potential cloud condensation nuclei number upon variation of the ionisation rate, the cloud nuclei number as a function of the sulphuric acid formation rate depends on the actual activation dynamics. In conjunction with the preceding, the non-linearity of particle growth with respect to sulphuric acid is demonstrated by Figure V.50. A doubled sulphuric acid formation rate will tendentiously increase the nucleation rate, unless it is limited by the ionisation rate, as during the nucleation burst on the first simulated day. The resulting larger aerosol population will in turn tend to consume more sulphuric acid, with a consequent negative feedback on its concentration, while the particle number is more effectively reduced by coagulation, thus inducing a positive feedback on the sulphuric acid concentration rate.
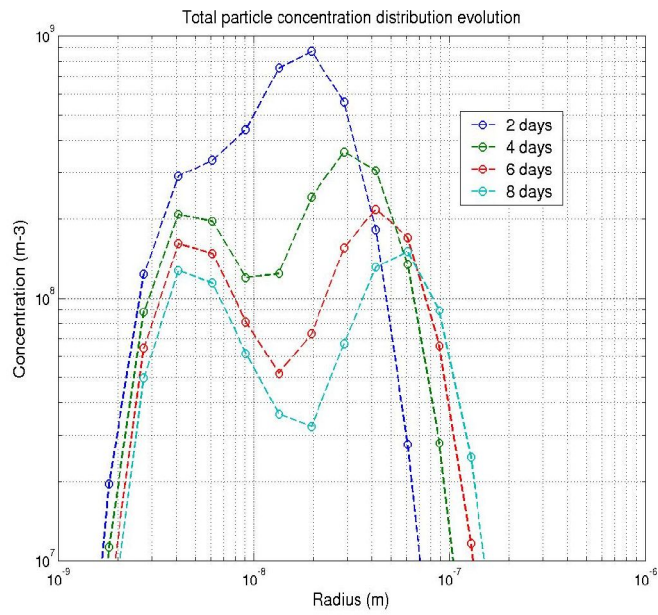
Figure V.47: Aerosol spectrum assuming the ion pair formation rate to be 5·10⁶ m⁻³ s⁻¹ and the ground pressure equivalent sulphuric acid formation rate to be 10¹⁰ m⁻³ s⁻¹. Temperature is 273.15 K, relative humidity is 0.8 and atmospheric pressure is 700 hPa. No background aerosols and no sea salt particle injection.
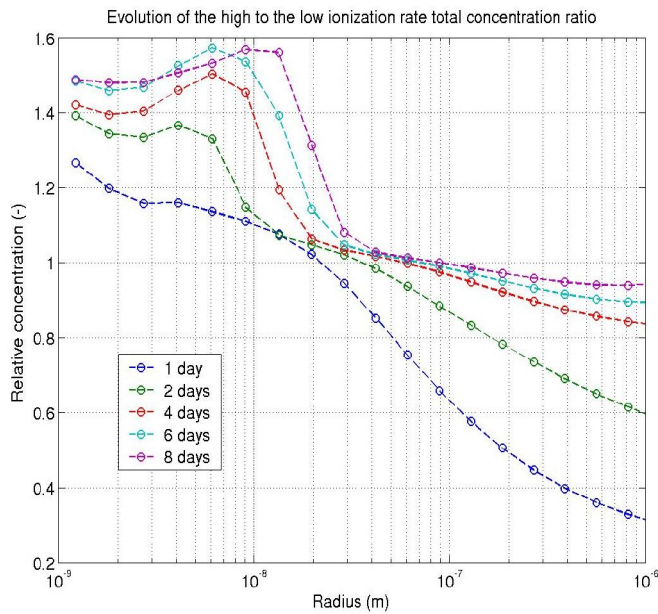
Figure V.48: 5·10⁶ to the 2.5·10⁶ ionisation rate relative aerosol spectrum. Conditions are equal to those of the preceding figure.
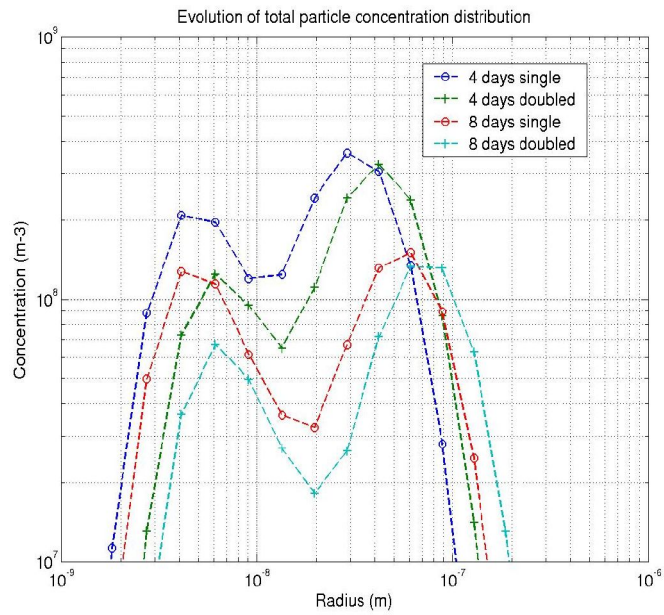
Figure V.49: Differentiation of the aerosol spectrum when the sulphuric acid formation rate is modified from 10^{10} to $2 \cdot 10^{10}$ m^{-3} s^{-1}. Same conditions than Figure V.47
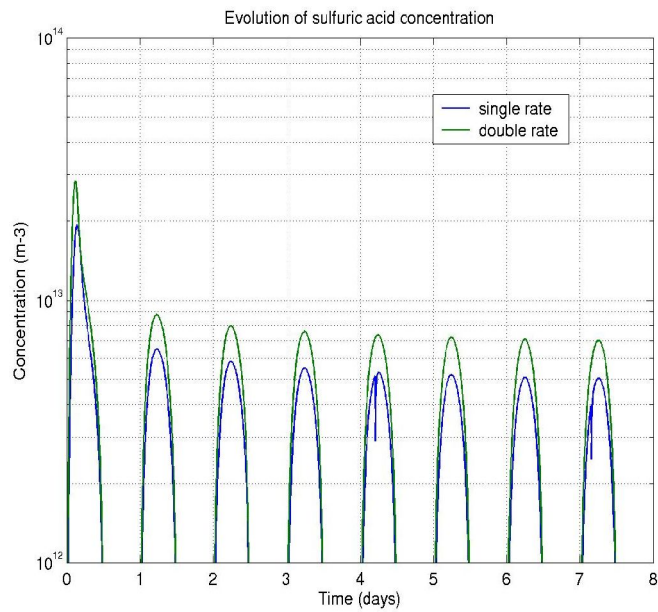
Figure V.50: Ambient sulphuric acid concentration as a time function for a formation rate of 10^{10} and $2 \cdot 10^{10}$ molecules per unit volume and time, respectively. Same conditions than in Figure V.47.

Growing particles consume more sulphuric acid due to their increased surface, further complicating the interaction of particle number, size, condensation and coagulation frequency. In this instance the overall effect is that the negative feedbacks of the increased original particle number, the enhanced per particle consumption may not compensate the higher formation rate and the more effective particle number reduction, so that the resulting sulphuric acid concentration is positively correlated with its formation rate. Note that the daytime maximum sulphuric acid concentration converges asymptotically, as suggested by the above stability analysis of aerosol growth dynamics under simplified conditions combined to the condensable mass balance equation.

The sulphuric acid formation rate may be massively enhanced in the atmosphere, especially in areas of massive sulphur dioxide emission such as polluted continental and coastal areas. It is referred to Kyzil et al. (2006) for an estimation of the variation of secondary particle formation due to pollution. Additional hygroscopic species, especially organics, may have a decisive impact to the yield of secondary particles (e.g. Spracklen et al., 2006). Additional condensing species may be represented by a higher sulphuric acid formation rate. Moreover, the spectral implications of a substantial increase of the source function of the total condensable is likely to provide further insight into aerosol growth dynamics. Figure V.51 depicts the ionisation rate sensitivity of the particle spectrum under conditions of enhanced sulphuric acid formation. It is apparent that the dynamical convergence property of the system is considerably enhanced along with particle growth velocity. Particles in the secondary accumulation mode reach a size that is typical to sea salt within the simulated time interval, while the relative particle number concentration in the same mode is sensibly equal to unity (Figure V.52). The condensation mode is also displaced to the larger particle side. Nevertheless, the relative particle number shows a similar sensitivity to the ionisation rate within this mode, as for temperature enhanced growth (Figure V.40), or under relatively pristine marine conditions (Figure V.48). Figure V.53 further demonstrates the enhanced damping properties of condensation and coagulation interaction in case of enhanced sulphuric acid production. The ambient sulphuric acid concentration is indifferent to the ionization rate and shows quick asymptotic behaviour for its daytime maximum. The sensitivity of the aerosol spectrum to a variation of the sulphuric acid formation rate at high yield is depicted in Figure V.54.
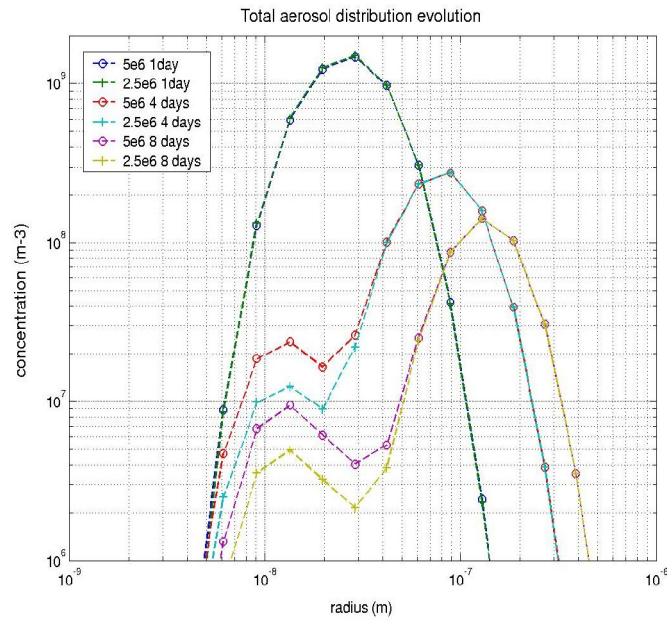
Figure V.51: Evolution of the aerosol distribution for two ionization rates at a higher sulphuric acid formation rate of 10^{11} molecules per cubic metre and second. The other conditions remain similar to those of Figure V.47.
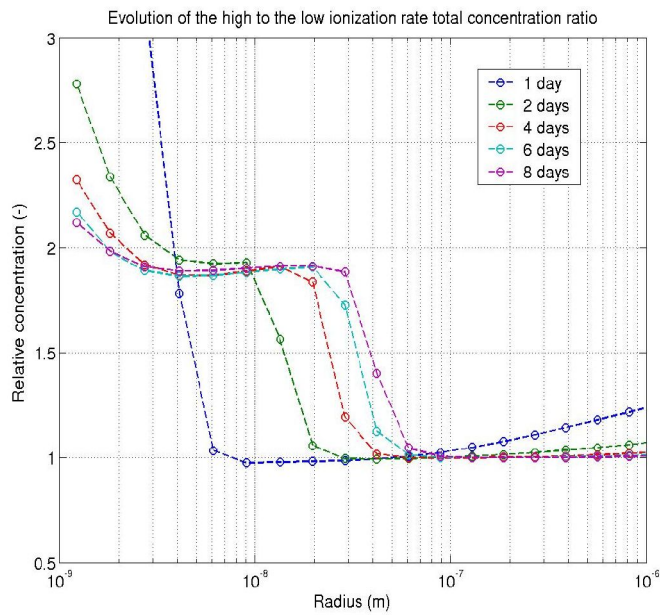
Figure V.52: Aerosol number concentration obtained with an ionisation rate of $5 \cdot 10^6$ relative to the spectrum obtained with $2.5 \cdot 10^6$ ion pairs per cubic meter and second as a function of particle radius at five moments in time. Other simulation conditions similar to those of Figure V.47.

231
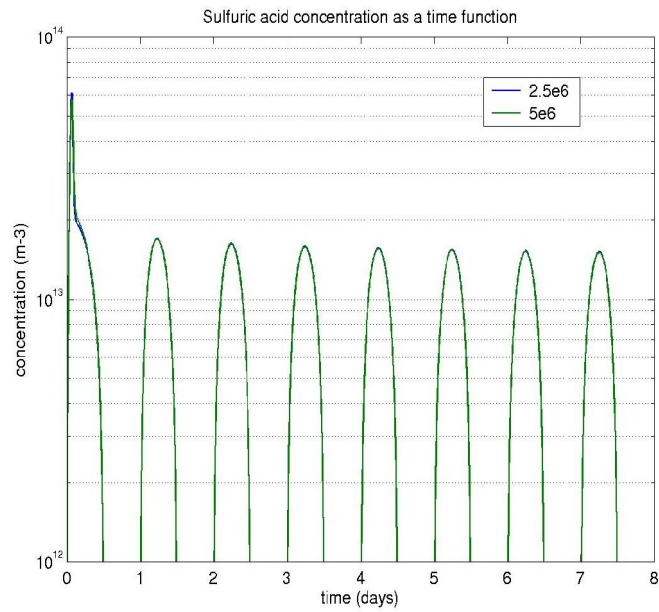
Figure V.53: Variability of the sulphuric acid number concentration for two ionization rates at high ambient sulphuric acid formation yield. Other simulation conditions specified witin the caption of Figure V.47.
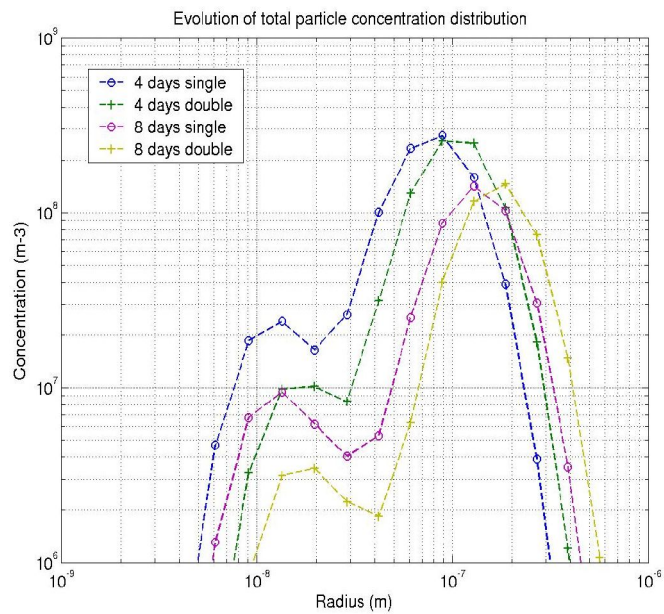
Figure V.54: Differential particle growth spectra for sulphuric acid formation rates of 10^{11} and $2·10^{11}$ m^{-3} s^{-1}, respectively, at an ionization rate of $5·10^6$ m^{-3} s^{-1}. Other conditions remain equal to those of Figure V.47.

232

Due to the enhanced convergence, the sensitivity of the accumulation mode to the condensable source function is less pronounced than under relatively pristine conditions (see Figure V.49). However, the residual sensitivity still involves a relevant potential as to the number of cloud condensation nuclei. Note that the elevated condensable concentration causes the ion-induced nucleation rate to be limited by the ionisation rate under polluted model conditions. The differential particle spectrum is thus the result of differential particle growth dynamics, and not, as might be erroneously assumed, of the number of ultrafine particles.

Figures V.55 and V.56 display contour plots of the particle number as a function of time and particle size via their condensable content at fixed ambient humidity. Note that the particle number concentration is shown on the size density scale to account for the size-time bi-dimensionality of the represented particle number function. On the first simulated day the particle size density shows a continuous decrease from the nucleation to the accumulation mode equivalent size. From day two, separated nucleation and accumulation modes appear, marking the turning point after which a large fraction of the newly nucleated particles is scavenged through coagulation to the benefit of the latter mode. Comparing the polluted to the pristine sulphuric acid formation spectra the enhanced growth velocity as well as the high initial particle number are apparent. Consequently the high pollution separation gap between the nucleation and the accumulation mode is deeper and the nucleation bursts are less intensive and shorter from day two on. The nucleation mode width increases with the sulphuric acid formation rate. Except for the nucleation mode, the aerosol spectra show no apparent sensitivity to the variation of the ionisation rate under either condition of sulphur dioxide pollution.
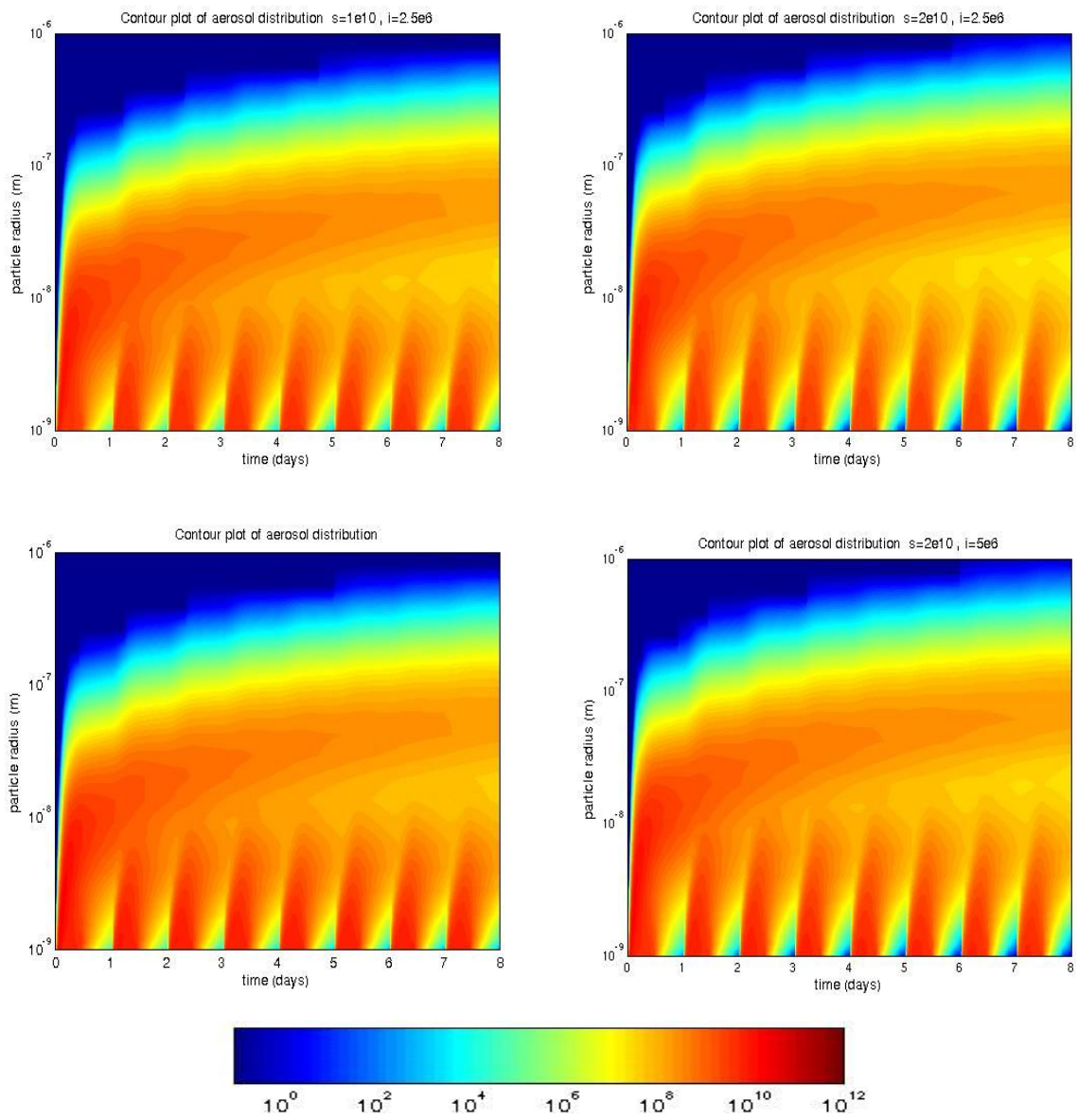
Figure V.55: Contour plots of the aerosol spectrum (dN/dlog r)as a function of time for the specified sulphuric acid and ion pair formation rates. The label indicates the aerosol number density per unit volume.
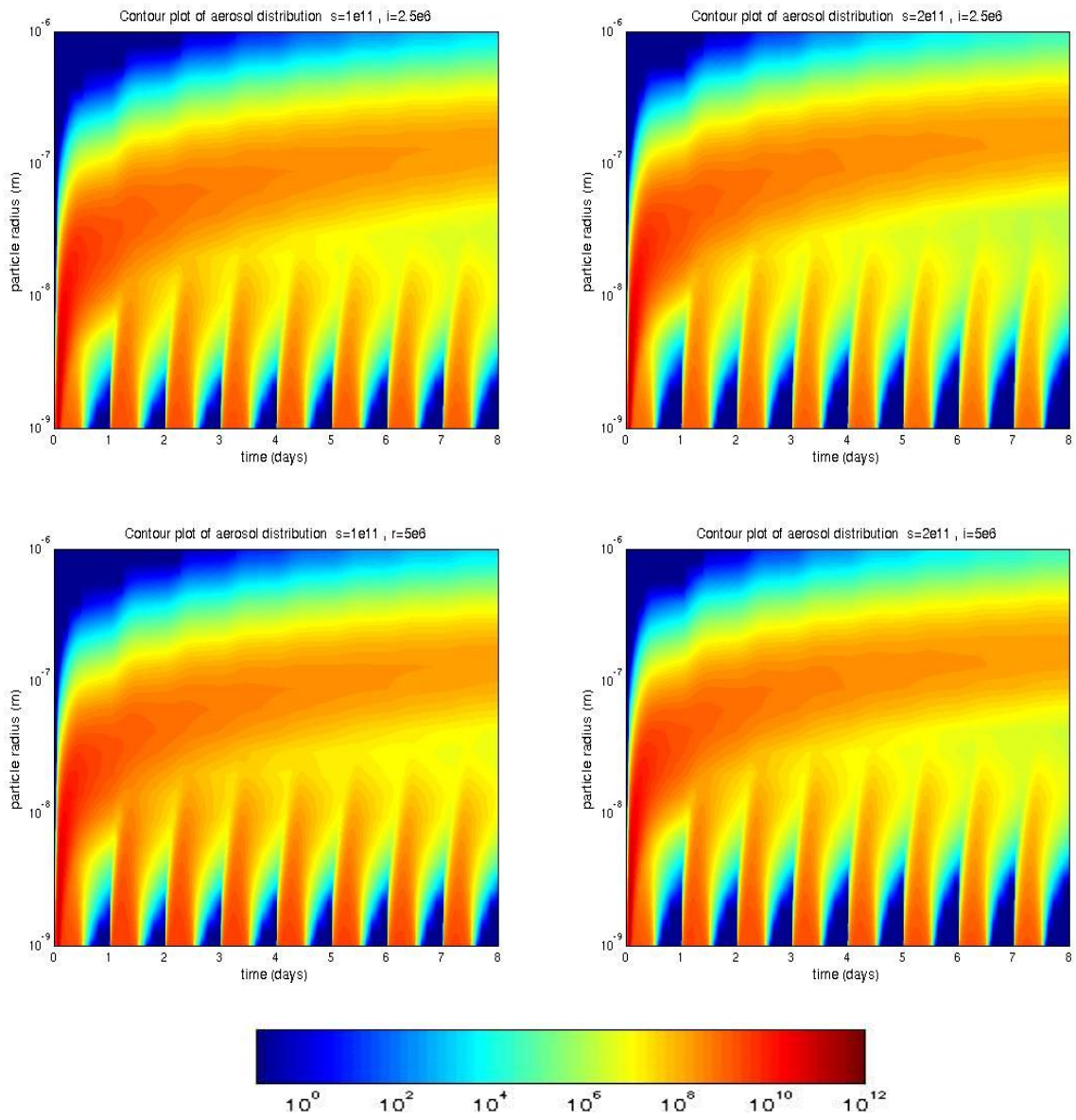
Figure V.56: Contour plots of the aerosol spectrum (dN/dlog r) as a function of time for the specified sulphuric acid and ion pair formation rates. The label indicates the aerosol number density per unit volume.

235

V.2.6 Further dynamic properties of the aerosol growth system

The specific growth dynamical properties of the secondary accumulation mode in the absence of primary particles are investigated in this sub-section. The accumulation mode is little affected by the diurnal variability of the nucleation mode, meaning that the internal dynamical properties of the secondary particle population are more apparent. Moreover, this mode is of particular interest to cloud microphysics since it is partially activated under typical marine conditions and thereby determines the cloud droplet number.

Figure V.57 depicts the ionisation rate sensitivity of the particle size of the secondary accumulation mode maximum as a time function. Note that the continuous variation in the framework of discrete particle size classes is obtained through a second degree polynomial interpolation of the original variation of the radius of the mode maximum. The particle size of the maximum is almost independent of the ion source function under both relatively pristine and polluted conditions. It is thus once again stressed that the initial variation of the nucleation rate is effectively levelled by the dissipative properties of the system. Figure V.58 displays the corresponding evolution of the maximum particle number concentration. In analogy to particle size, the number concentration tends to be independent of the original ionisation rate, while polluted sulphuric acid values converge much faster. The slight undulations of the results arise through the discrete nature of the particle size classes, the discontinuities standing for the limit between two contiguous classes. Figures V.59 and V.60 show the sensitivity of the size and particle number concentration of the accumulation mode maximum, respectively, to a variation of the sulphuric acid formation rate. The sensitivity of the particle size of mode maximum to the sulphuric acid yield contrasts with the preceding ionisation rate sensitivity. The dissimilar shape of the lowest sulphuric acid formation rate curve demonstrates the relevance of the choice of the upper boundary of the particle size range to particle growth dynamics. While the convex curves are obtained with a maximum particle size of the order of 1 micrometre, the lower linear curve considers particles up to a size of 10 micrometres approximately. Interestingly the 1 micrometre curves show a trend to become linear with increasing sulphuric acid yield. Particle number reduction is primarily the resultant of coagulation, which interacts with condensation influencing in turn the nucleation rate. The coagulation and condensation properties of the largest particles appear to have a significant

236
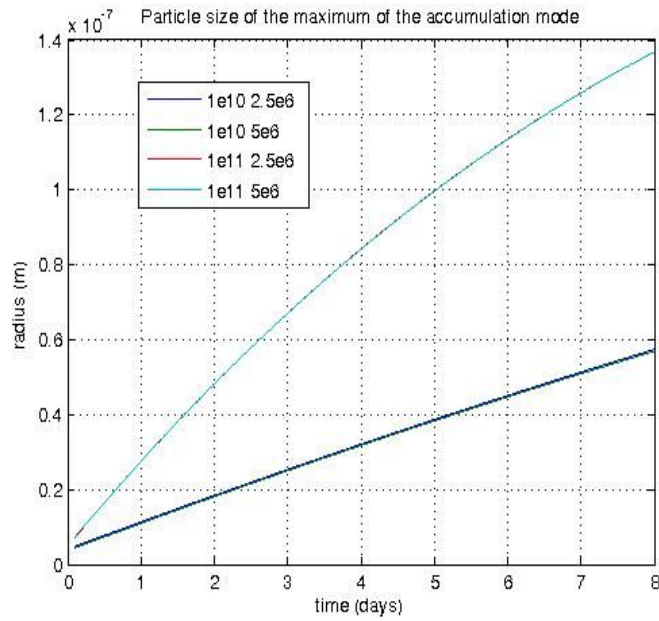
Figure V.57: Radius of the peak concentration of the accumulation mode as a time function. The original discrete data has been interpolated to a quadratic time function of the radius logarithm. The size discretisation of the aerosol and non-linear diurnal variations have thus been filtered.
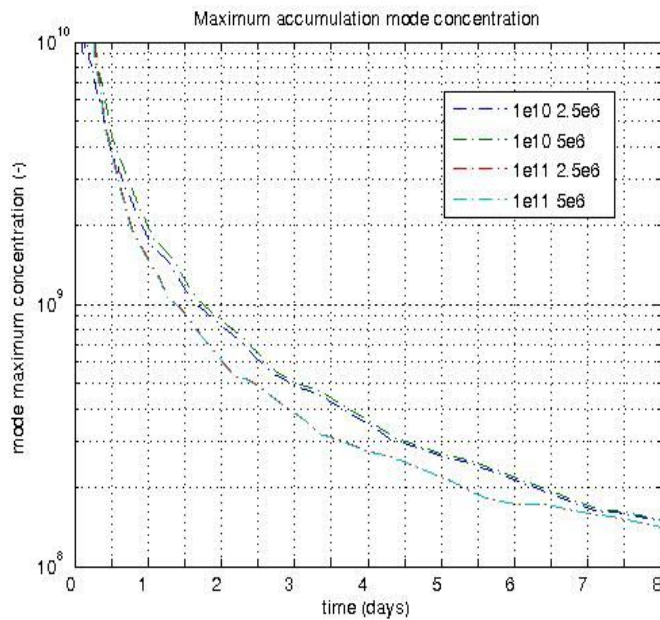
Figure V.58: The maximum number concentration of the accumulation mode as a time function. The irregularities in the concentration arise through the discrete nature of the particle size classes.

237
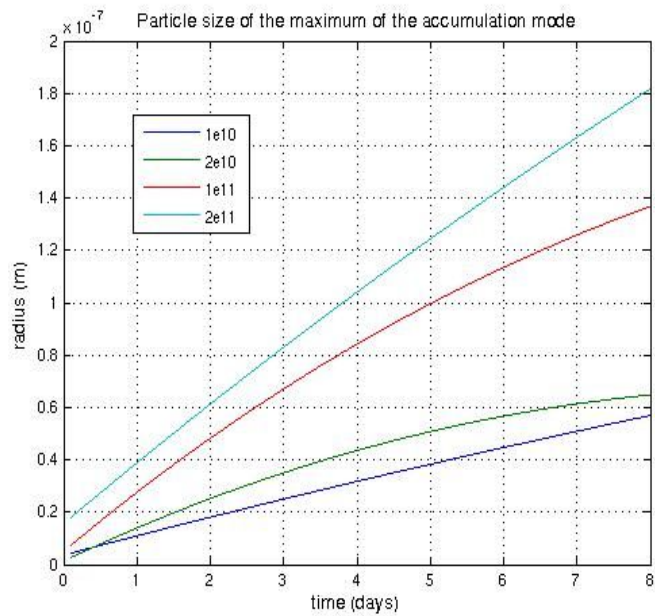
Figure V.59: Evolution of the particle size of the accumulation mode maximum for four rates of sulphuric acid formation. The logarithm of the radius has been fitted to a quadratic time function.
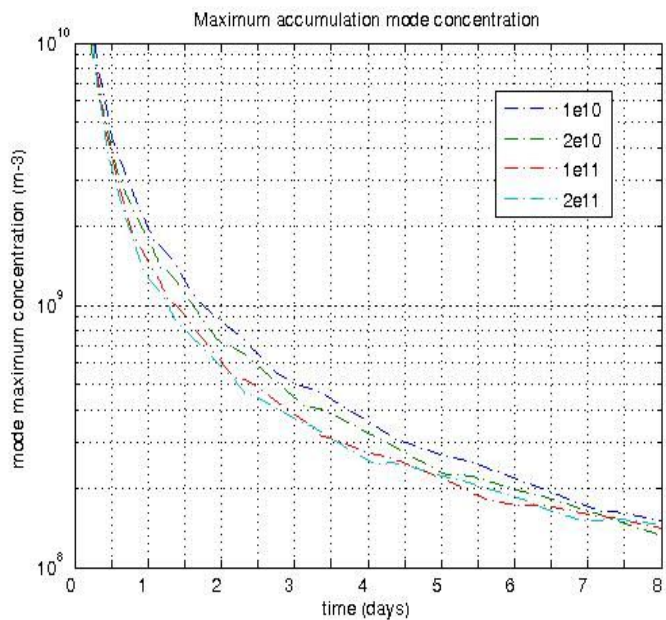
Figure V.60: Evolution of the accumulation mode maximum number concentration for four yield functions of sulphuric acid, in analogy to Figure V.58. A trend is visible to equal concentrations indifferently of the momentary respective radius.

238

incidence on the accumulation mode maximum radius. A remarkable property of the particle mode maximum concentration is that it shows convergence as to the sulphuric acid formation rate. The convergence property appears to be robust to the choice of the particle size boundary condition.

A simplified aerosol growth formalism was introduced through Equations V.6. When applied to the secondary accumulation mode along with their stable node solution V.7 under purely secondary conditions, these may yield further insight to secondary growth dynamics. Omitting the first two terms of the stable node aerosol concentration and assuming that the ion-induced nucleation rate is limited by the ionisation rate under model conditions one finds for the simplified particle equilibrium concentration:

$$N_{i,eq} = \sqrt{\frac{2(R_f)_\pm (R_f)_a}{\phi_{cond,i}\,\phi_{coag,i}}} \quad,$$

f V.12

where $\phi_{cond,i}$ is the condensation loss rate experienced by a particle of size class i, and $\phi_{coag,i}$ is the corresponding coagulation loss rate.

The relative equilibrium concentration in case of a doubled ionisation rate is:

$$\frac{N_{i,eq}^{2x}}{N_{i,eq}^{x}} = \sqrt{\frac{(R_f)_\pm^{2x}\,\phi_{coag,i}^{x}\,N_a^{x}}{(R_f)_\pm^{x}\,\phi_{coag,i}^{2x}\,N_a^{2x}}} \quad.$$

f V.13

This expression differs from the ionisation rate weighed coagulation loss flux ratio:

$$r_{coag} = \frac{(R_f)_\pm^{x}\,\Phi_{coag,i}^{2x}}{(R_f)_\pm^{2x}\,\Phi_{coag,i}^{x}} \quad.$$

f V.14

The ratio of the gain to the loss flux onto a certain particle size class i is:

$$r_{net} = \frac{\Phi_{cond,i-1}\,\Phi_{coag,i-1}}{\Phi_{cond,i}\,\Phi_{coag,i}} \quad.$$

f V.15

Note that in the preceding Equations V.14 and V.15 the particle relevant process rates have been replaced by their size class integrated flux counterpart.
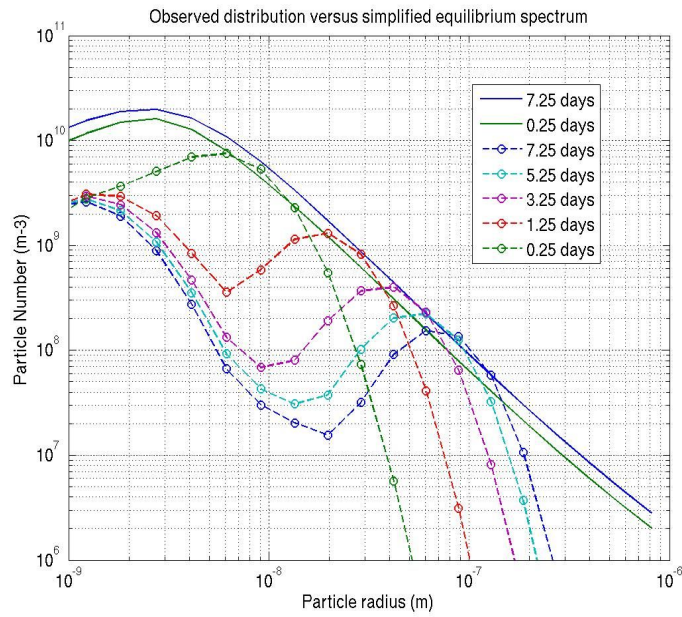
Figure V.61: Simplified particle equilibrium spectrum (see text) compared to the observed particle spectrum. It is apparent that the secondary accumulation mode maximum is related via Equation V.12 to the momentary ion-induced nucleation rate, which is equivalent to twice the ionisation rate.
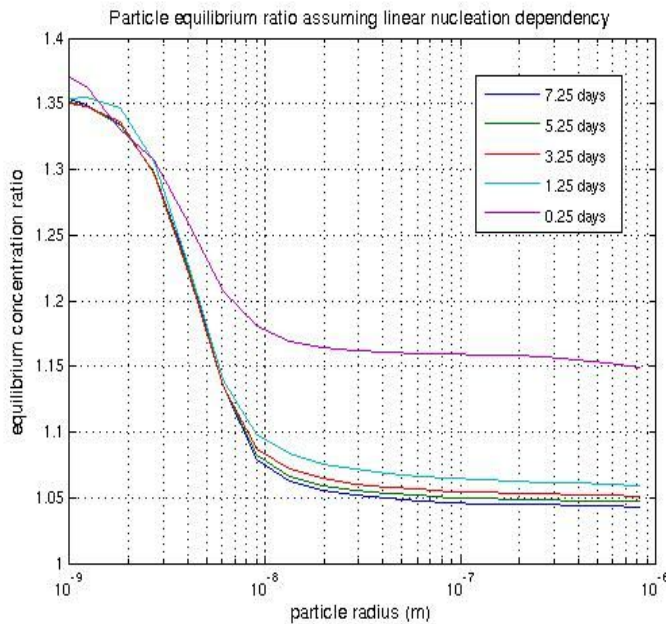
Figure V.62: Ratio of the doubled ionisation rate simplified equilibrium distribution to its simple counterpart. The combined coagulation and condensation loss ratio can not explain the simulated pattern of the ionisation rate sensitivity. The loss function alone can not reproduce relative figures lower than unity.

240
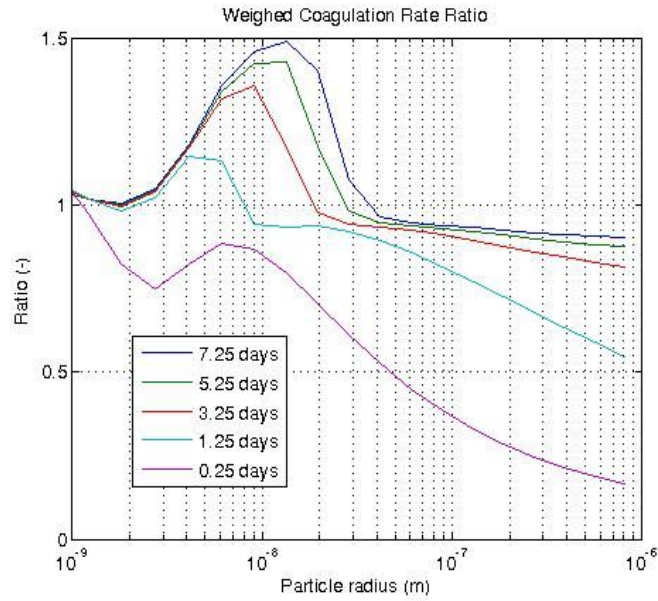
Figure V.63: Ionisation rate weighed coagulation losses. Accumulation mode part of the curves is reminiscent of the ionisation rate sensitivity depicted by the relative particle spectrum.
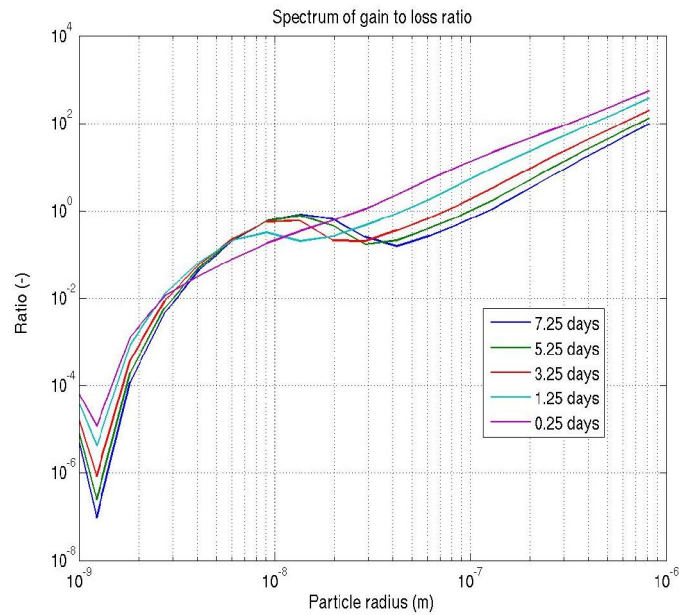
Figure V.64: Ratio of condensation and coagulation gain flux to the equivalent loss flux. It appears that the condensation mode is in pseudo-equilibrium condition, thus determining its temporal stability. Accumulation mode particles experience high gains, while particles in the separating gap suffer moderate losses resulting in a further deepening and displacement to the right of the gap.

241

Figure V.61 compares the equilibrium particle number concentration according to Equation V.12 as a particle size function to the simulated aerosol spectrum. The equilibrium number concentration is reduced proportionally to the fraction of the accumulation mode particles contained within the size class of the accumulation mode maximum. The equilibrium particle spectrum thus obtained is representative to the respective number of particles within a particle size class would the mode maximum be of that size. It is reminiscent of the actual aerosol distribution when the particle population is still relatively young. With increasing size of the accumulation mode maximum, the equilibrium spectrum rapidly diverges from the modelled spectrum, except for its maximum. The mode maximum appears to keep its relationship via Equation V.12 to the momentary ion-induced nucleation rate all along the simulated time interval. Knowing the momentary accumulation mode maximum concentration as well as the corresponding coagulation and condensation individual loss rates, it would thus be possible to determine the momentary nucleation rate. The aerosol equilibrium spectrum stays relatively constant in time. It thereby allows giving an approximation of the future evolution of the accumulation mode maximum. When combined to its particle number convergence property, a set of accumulation mode maximum trajectories may be given as a function of the condensable yield.

Figure V.62 shows the normalised simplified aerosol equilibrium spectrum according to Equation V.13. The results reflect the strong convergence property of the aerosol growth system relative to particle number. The prominence of this property is progressive with particle size as the coagulation loss rate tends to similar values to the point that the ratio tends to unity. However, the punctual coagulation and condensation loss rate ratio may not explain the observed tendency to a negative correlation of the particle number to the ionisation rate (see above), which is due to a growth dynamical mechanism acting continuously along the particle spectrum.

The area of dominance of coagulation growth is sketched in Figure V.63, showing the ionisation rate balanced coagulation loss rate ratio according to Equation V.14. The coagulation loss ratio of freshly nucleated particles should tend to be close to the ionisation rate ratio provided that the nucleation rate is limited by this number. If balanced by the ionisation rate the initial ratio should thus be close to unity. If coagulation and condensation effectively trigger a trend to a negative correlation between the ionisation rate and the particle number concentration its value should become inferior to unity, which happens for particles of

accumulation mode size. The pattern of the coagulation rate ratio within this size interval is reminiscent of the corresponding aerosol size spectrum ratio (see Figure V.25) stressing that the coagulation particle loss rate is a linear function of the local particle number distribution. Figure V.64 depicts the spectrally resolved aerosol loss to gain flux ratio. Particle size classes close to equilibrium present a ratio close to unity. The condensation mode particles fulfil this condition, which explains their overnight persistence. Nucleation mode particles experience extremely strong losses reflecting the ephemeral character of these particles. Particles of the lower size end of the secondary accumulation mode show moderate losses. These stand for the tendency of the separating gap between this mode and the condensation mode to move to and to deepen with increasing particle size.

V.3 Aerosol-Cloud Interaction in the Boundary Layer

V.3.1 Preliminarily considerations

The purpose of the single column boundary layer model (Chlond et al., 2004) initially was to test the consistency of the turbulent diffusion formalism of the European Centre Hamburg Model in representing cloud processes in the atmospheric boundary layer at the instance of marine stratocumuli. The original version was improved so to fairly represent the liquid water content and the turbulent kinetic energy, which may be related to the typical vertical updraft velocity. The dependence of the single column model on ad hoc forcing parameters of supposedly constant synoptic temperature and moisture advection may not ensure durably realistic figures. Daytime solar radiation tends to heat the model temperature up, so that a deficit of cool air advection leads to a negative entrainment velocity as well as a thinning of the liquid water path, which enhances further the heating of the model atmosphere. Too strong advective cooling leads to a weakening of the model inversion inducing a high entrainment velocity and the eventual disappearance of the stratocumulus cloud. The displacement of the boundary layer front is thus ideally a dynamical equilibrium between the daytime solar radiation induced heating and the constant forcing through synoptic cooling. However, shortwave radiative heating is not a constant but a strong function of the vertical liquid water distribution, so that an initially stable model situation bears a strong tendency to become eventually unstable through the time dependence of the radiative properties of the boundary layer. The large scale forcing parameters used by Chlond et al. (2004) bear a typical lapse of time during which figures are realistic is of 36 hours only, after which undesirable undulations or instability of the boundary layer front occur. The findings of the preceding section have shown that the time required for secondary particle to grow to cloud condensation nuclei size is typically not less than 24 hours. Also the typical time interval necessary for the aerosol population to reach pseudo-equilibrium conditions is minimum 2 days. Model initialisation at 0 am ensures numerical stability to the model domain before it is subject to transient shortwave radiative heating. The original large scale forcing parameters would thus restrict the effective aerosol growth interval to 24 hours only, which is insufficient to represent the typical

diurnal variability of the aerosol population as well as their interaction with cloud processes. The model of aerosol cloud interaction requires a substantial amount of computation time. To ensure a simulation interval of 36 hours while computation time is constrained to a reasonable amount of time, the aerosol formation local time is shifted for some of the below simulations, for which the influence of the aerosol on cloud dynamics and the typical diurnal variability at pseudo-equilibrium conditions are of less interest, so that photolytic sulphuric acid formation and thus nucleation may take place rapidly. These simulations render the cloud droplet and aerosol growth microphysical processes, their formal interaction, as well as the differential sensitivity of the aerosol population to sulphuric acid formation, ionisation and sea salt injection. The below long-time simulations of some 62 hours that are intended to assess the pseudo-equilibrium behaviour of the aerosol population. Here the synoptic cooling rate is approximately halved to $4 \cdot 10^{-8}$ max(z,500) K s^{-1} relative to its original value of $7.5 \cdot 10^{-8}$ max (z,500) K s^{-1} (Chlond et al., 2004) to ensure extended stability of the stratocumulus cloud.
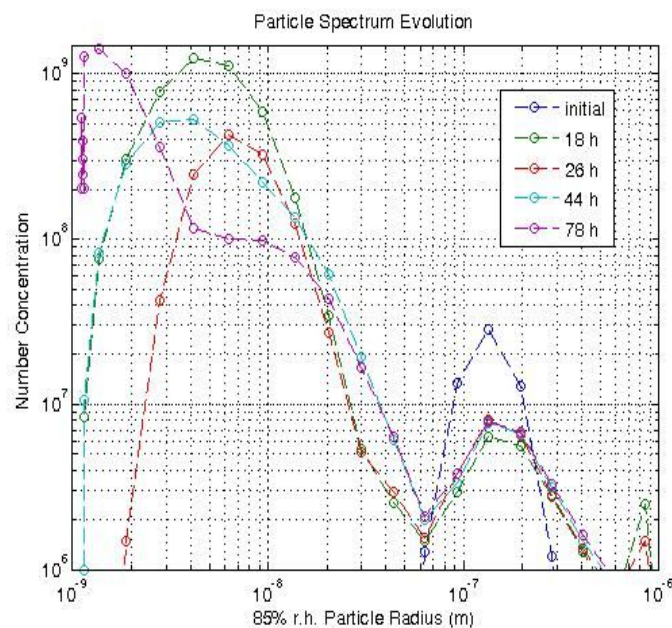
Figure V.65: Typical below cloud aerosol spectrum at different moments of their diurnal cycle. The aerosol size is given as an 85% relative humidity equivalent, assuming aqueous sulphuric acid composition. The sulphuric acid formation rate is 10^{10} mol. m^{-3} s^{-1}, the ionisation rate is $2.5 \cdot 10^6$ ion pairs per second and cubic metre.

245

V.3.2 Patterns of the main components of the aerosol cloud system

In this section an overview on the interconnection and variability of the most relevant variables of the aerosol cloud system is given. Figure V.65 sketches the typical evolution of the below cloud aerosol spectrum at the instance of the 250 metre distribution, assuming a ground ionisation rate of $2.5 \cdot 10^6$ ion pairs and a sulphuric acid formation rate of 10^{10} per unit time and volume, respectively. Comparing with Figure V.41 it is appears that there is no apparent secondary accumulation mode.
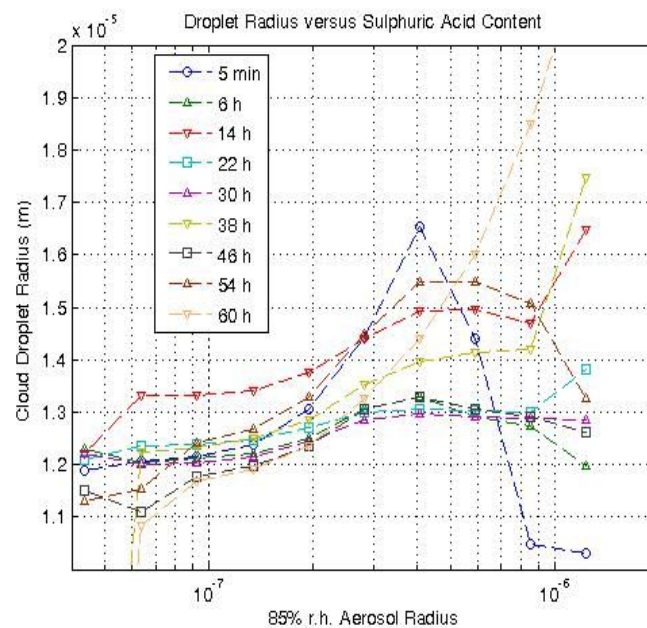
Figure V.66: Droplet size spectrum as a function of their solute content via their 85% relative humidity aqueous sulphuric acid radius. Specific symbols are used as a function of local time, starting at 0 am.. Model parameters are those of the preceding figure.

There is a persistent secondary particle mode, which is typical to the accumulation mode, but of much smaller size well below the limit of domination of coagulation as a growth process. The formation of a separation gap between the condensation and the coagulation mode is thus prevented. Hence, the secondary particle mode bears hybrid characteristics of both the accumulation and the nucleation-condensation mode. Secondary particles appear to grow until a size of typically 20 nanometres, above which they tend to be scavenged by the activated sea salt particle mode. The interaction with the much larger, and thereby much more coagulation effective cloud droplets impedes the formation of a distinct secondary accumulation mode

246

both inside (see Figure V.71 below) and under the cloud layer. This stresses that turbulent scavenging by cloud droplets and convection take place on a shorter typical time-scale than aerosol particle growth. The size of the cloud droplets is predominantly given by the excess amount of water vapour as well as the number of activated particles, both of which are relatively constant, so that the hybrid secondary mode maximum is stable. The pseudo-unitary 44h mode is in fact bimodal and is representative to the situation when the nucleation mode is about to superpose the hybrid mode. The number of particles in the sea salt mode decreases quickly through auto-scavenging at simulation onset and then tends to stabilize more or less. The underlying dynamics will be analysed in detail below.

Figure V.66 depicts typical cloud droplet size spectra as a function of the sulphuric acid solute content via their 85% relative humidity particle radius. Obviously, the solute content does not necessarily increase with droplet size, but may decrease after attaining an absolute maximum. The sketched cloud droplet size spectrum is thus qualitatively reminiscent of the activated aerosol number spectrum as shown in Figure V.65. Upon activation the model droplets are assumed to be of equal size, so that their individual probability to double their size through coalescence is identical. The general displacement upon coalescence of cloud droplets to the right hand side of the corresponding solute content spectrum produces the initial solute content cloud droplet size correlation. As their number density distribution is not constant, the resulting unequal coalescence flux distribution induces droplet size spectral divergence, so that particle classes close to the mode maximum tend to contain relatively more coalesced particles than larger aerosol particle classes. The mean cloud droplet size as a function of the aerosol size class thus expresses the mean coalescence history of the particles it contains. It is both an implicit function of the solute content, as coalescence also leads to an increase of this quantity, and a function of the initial spectrum of the activated aerosol particles, which determines the class specific net coalescence flux. As the average cloud droplet gets older the cloud droplet population tends to present a strict size increase with solute content as particles tend to accumulate in the largest aerosol class. Interestingly this trend is not sustained but subject to cycling. In the evening particles typically present equal size distribution, indicating a large fraction of freshly nucleated particles, while in the morning particles show intermediate age and midday particles are mostly mature. This phenomenon may not be explained in the present context and will be looked at again in the below sub-section on aerosol cloud dynamical effects. Note that the cloud droplet size also varies subsequently to
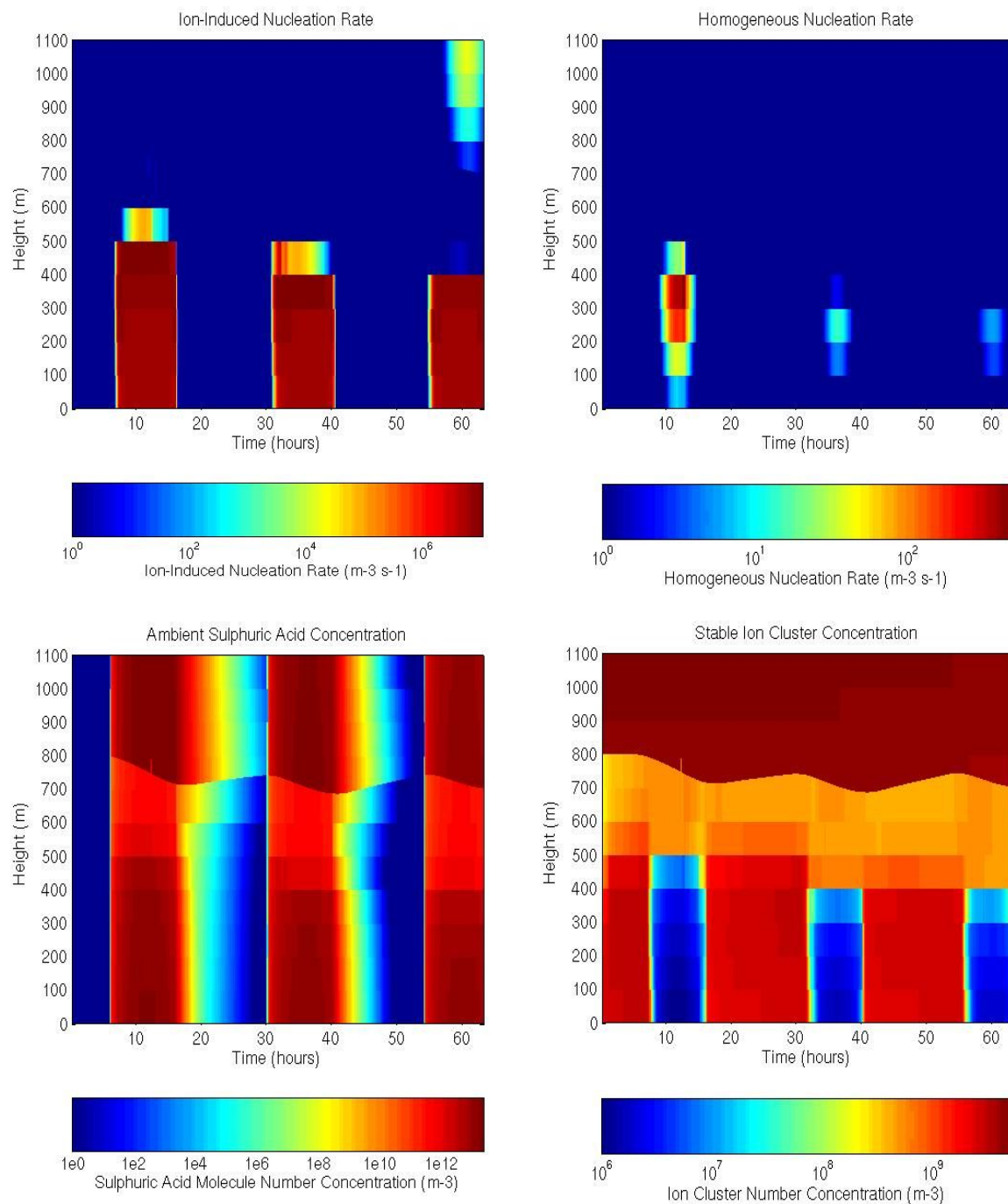
Figure V.67: Time-height contour plots of the ion-induced nucleation rate, the homogeneous nucleation rate, the sulphuric acid number concentration, and the small ion number concentration. Same parameters as for Figure V.65.

cloud liquid water content modification.

On the upper left and right panels of Figure V.67 depict the ion-induced and homogeneous nucleation rate as a function of time and height, respectively. The related ambient sulphuric

acid and stable ion cluster concentration are shown on the lower panels. The upper limit of the boundary layer appears on the lower panels as an undulating net disparity, starting at a height of 800 m above sea level, and declining ulteriorly to as low as 700 m approximately. It is conditioned by the temperature inversion marking the upper limit of the synoptic sub-tropical marine stratocumulus cloud layer.Consistently with the above zero-dimensional findings, and as expected for the chosen nucleation scheme, ion-induced nucleation clearly is the dominant process of secondary particle formation. Homogeneous nucleation merely plays a relevant secondary role when the ambient sulphuric acid concentration is above the approximate threshold of 10^{13} m^{-3}. Nucleation is effectively constrained to the area below the cloud through the related elevated sulphuric acid concentration as cloud droplets are effective sulphuric acid absorbers in combination with the assumed height constant sulphuric acid formation rate. In turn the sub-cloud stable cluster ion concentration is limited by the ion-induced nucleation rate, driving the corresponding concentrations to significantly lower values during the nucleation bursts. The sulphuric acid and especially the ion concentration demonstrate numerically stiff behaviour through their pronounced vertical concentration gradient. The sulphuric acid concentration is minimal at the top of the cloud, which is the spot of maximum scavenging and distance to the cloud free boundary layer. In analogy, the small ion concentration is minimal right above the ground. Interestingly the nucleation rate is maximal and superior to the local ion pair formation rate just below the lower cloud limit. The combined effect of the turbulent downward ion flux, the high relative humidity and the negative temperature gradient outnumbers the simulated below cloud sulphuric acid scarcity. Thus, enhanced below-cloud nucleation may be reproduced without taking into account higher in-cloud sulphuric acid productivity. The modelled effect, however, is not as pronounced as the observed one attributed to higher in-cloud photolysis (e.g. Radke and Hobbs, 1991).

Figure V.68 shows the integrated aerosol and cloud droplet number concentration as a function of time and height. The total aerosol number essentially expresses the secondary particle yield, which is several orders of magnitude more important than sea salt particle number formation. At simulation initialisation secondary particles are not yet present, so that at the onset of nucleation, as depicted on the left panel, the total aerosol concentration increases rapidly. The total aerosol number shows diurnal cycling, which is slightly delayed relative to the below cloud nucleation rate. In opposition to the sulphuric acid and ion concentration the total aerosol concentration shows much more transient behaviour, which
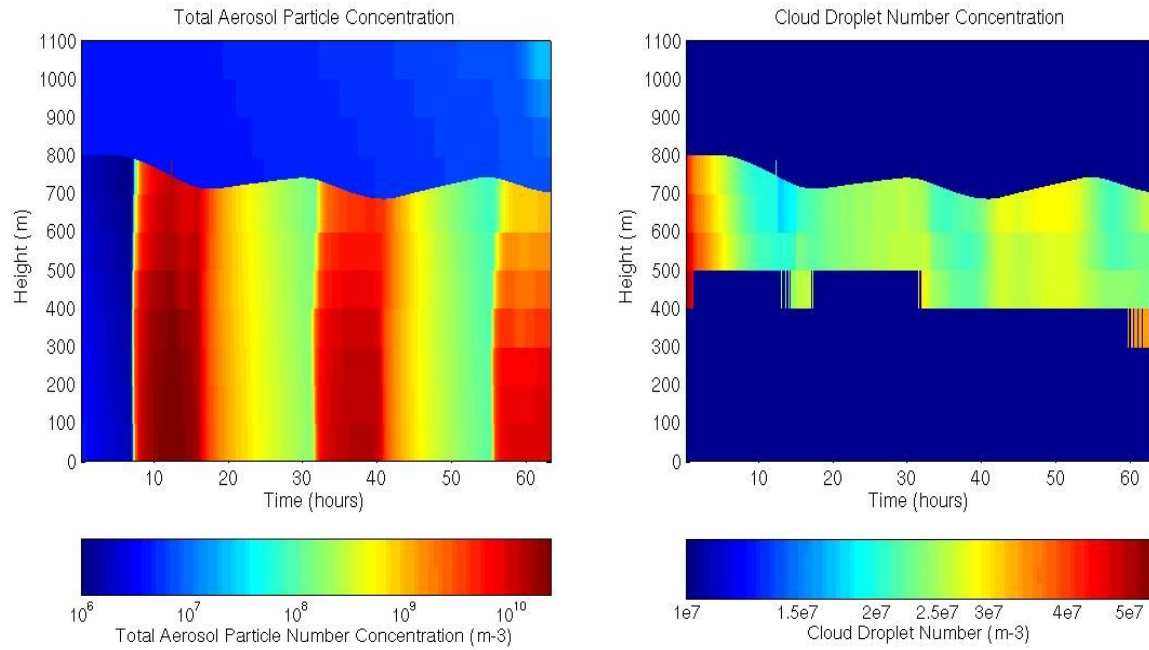
Figure V.68: Time-height contour plots of the total aerosol particle number and the cloud droplet number. Same parameters as for Figure V.65.

induces a relatively low vertical gradient, as the characteristic vertical mixing time is low relative to particle growth dynamics. At the beginning of simulation, the sea salt mode aerosol concentration is associated with typical pristine marine background values according to Kondratyev (1999, see Appendix B). By virtue of cloud processing the cloud droplet number decreases rapidly upon activation, testifying for enhanced number reduction efficiency through coalesence as suggested by Feingold et al. (1996). The droplet number decreases from about 55 to around 30 cm^{-3} during the first three simulation hours, which is a number reduction of 45%. Feingold et al. (1998) assessed the water vapour exchange between the droplet liquid phase and the gas phase explicitly. Discarding activation of newly grown secondary particles and the continuous sea salt emission flux, they found a reduction of around 60% in the same time interval, starting at around 40 particles per cubic centimetre. The particle number reduction via auto-scavenging and the activation feedback system thus seem to be comparable, although within the single column model coalescence appears to be slightly less intensive and/or more effectively damped by aerosol activation. On day one the minimal simulated droplet number is around 15 cm^{-3}, which is attained just before the first secondary particles become activated. Ulteriorly the droplet number unsteadily increases until reaching a maximum of about 25 particles per cubic centimetre around midnight. According to

250

observations compiled by Miles et al. (2000) on stratocumulus clouds this figure is close to the lower edge under marine conditions, for which the typical interval spans from approximately 20 to 150 cm^{-3}. On day two the variability is similar with a slightly higher maximum of around 30 particles cm^{-3}. According to the model results, the diurnal variability of the cloud droplet number thus presents a shift of typically 12 hours. This shift is considerably lower than the characteristic time interval of 24 hours for a particle to reach activation size. It corresponds, however, to the time necessary for the nucleation mode to overlie the hybrid condensation/accumulation mode. Conjointly with cloud dynamical processes that will be described below, the arrival of the freshly nucleated particles boosts the formation of new cloud nuclei size particles.

Typical patterns of the cloud droplet liquid water and the rainwater content, and the related effectiveness of autoconversion and accretion are shown in Figure V.69. The cloud liquid water content increases with height and the ensuing temperature decrease. While the upper cloud limit is clear-cut following the transient assessment of the height of the boundary layer front, the position of the lower cloud limit, which is of particular relevance to the cloud droplet spectrum, is affected by the model spatial resolution. Coarse resolution may lead to undesirable numerical undulation critical activation radius (which is in principle determined in the lowest activated cell), as upon its activation the cell tends to lose liquid water through precipitation formation and to become deactivated again. For this reason the following formalism was adopted: The relevant layer to the cloud droplet spectrum is the lowest layer presenting a total water content equivalent to more than 1% supersaturation. Under simulation conditions the approximate cloud liquid water mixing ratio equivalent to 1% supersaturation is 10^{-4} kg water per kg air. Layers of less than 1% percent supersaturation are considered to be in a transitional state of aerosol particle activation and growth through condensation. Consequently their size spectrum is considered to be monodisperse, at instant equilibrium with saturation pressure and the mass balance equation is not solved. Interestingly the rainwater content is not maximal in the upper portions of the cloud, where the formation rate is highest. The gravitational accumulation effect makes the rainwater content reach its maximum at the lower cloud limit. Underneath evaporative loss lets the rainwater content decrease until sea surface. Temporally, the rainwater content shows two major long-term precipitation occurrences as well as two shower events. Only the initial long-term event leads to substantial precipitation at sea level. Autoconversion is a strong function of the liquid water
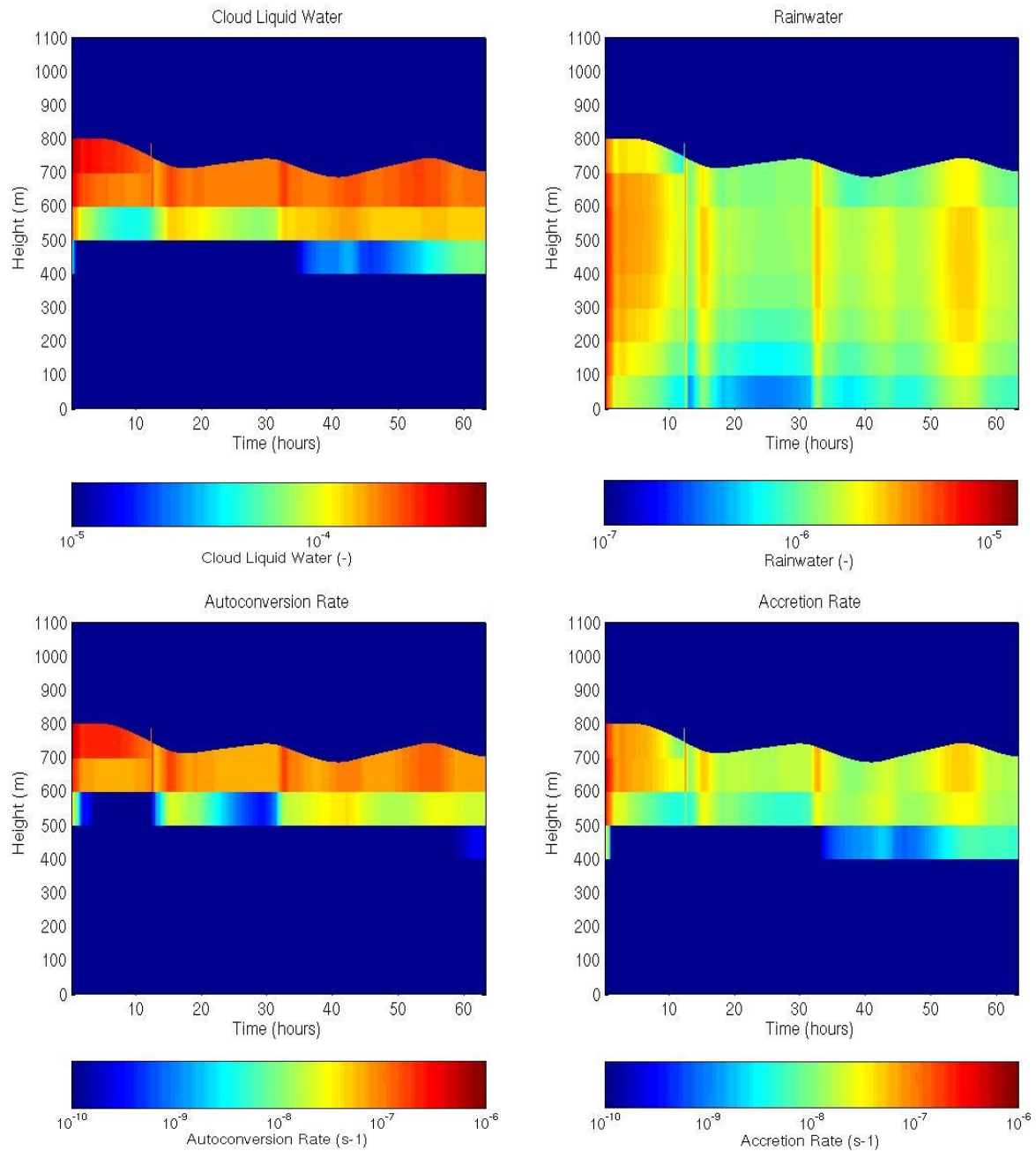
Figure V.69: Time-height contour plots of the cloud liquid water content, the rainwater, as well as the modelled autoconversion and accretion rate. Same parameters as for Figure V.65.

content, so that it is most effective in the uppermost cloud layer. Autoconversion triggers rainwater formation, which is enhanced by accretion. Since rainwater tends to accumulate in the lower cloud portion, the effectiveness of accretion primarily increases with decreasing height, leading to a positive feedback on the rainwater content. Within the lowest part of the

cloud, however, the effect of a higher rainwater content is outbalanced by less cloud water, so that the overall accretion rate is lower than in the central cloud portion. The dominance of autoconversion relative to accretion is conform to other model studies, such as Beheng and Doms (1986) who consistently find the autoconversion yield to be up to two orders of magnitude more important. The detailed mechanisms leading to precipitation as well as their sensitivity to the droplet number and size are studied in detail in a specific section.

V.3.3 Sensitivity of the aerosol spectrum

3.3.1 Sulphuric acid formation and ionisation rate sensitivity

Figure V.70 compares the sensitivities of the ion-induced secondary nucleation rate and of the total aerosol number, which is essentially equivalent to the total secondary particle number, to a variation of the sulphuric acid formation and the ionisation rate. Underneath the cloud new particle formation conditions are favourable, and the nucleation rate is limited by the ionisation rate. The nucleation rate is slightly superior to the ion formation rate through turbulent transport form inside the cloud. Within the stratocumulus, nucleation conditions are less favourable as stable particle formation is limited by cloud droplet scavenging of sulphuric acid. A doubling of the sulphuric acid formation rate therefore results in a considerable increase of the nucleation rate within the cloud, whereas the below cloud nucleation rate is not affected. Conversely, the ion-induced nucleation rate shows little sensitivity to the ionisation rate within the cloud, while the simulated below-cloud nucleation rate is more or less proportional to the ionisation rate at its chosen order of magnitude.

The lower panels of Figure V.70 stress the efficiency of vertical mixing of the boundary layer to the vertical profile of the total particle number concentration, as it shows an analogous pattern both inside and within the cloud in parallel to the below-cloud nucleation rate. Consistently with the above zero-dimensional findings, the total particle number is correlated with the condensable yield. Thus, despite its hybrid properties, the secondary mode shows behaviour typical to the nucleation mode as to its sensitivity to the nucleation rate, contrasting with the converging property of the accumulation mode relative to the total particle number within this mode. Rapid particle scavenging through the activated primary particle mode interferes with the homogenizing tendency of boundary layer convective transport, so that the
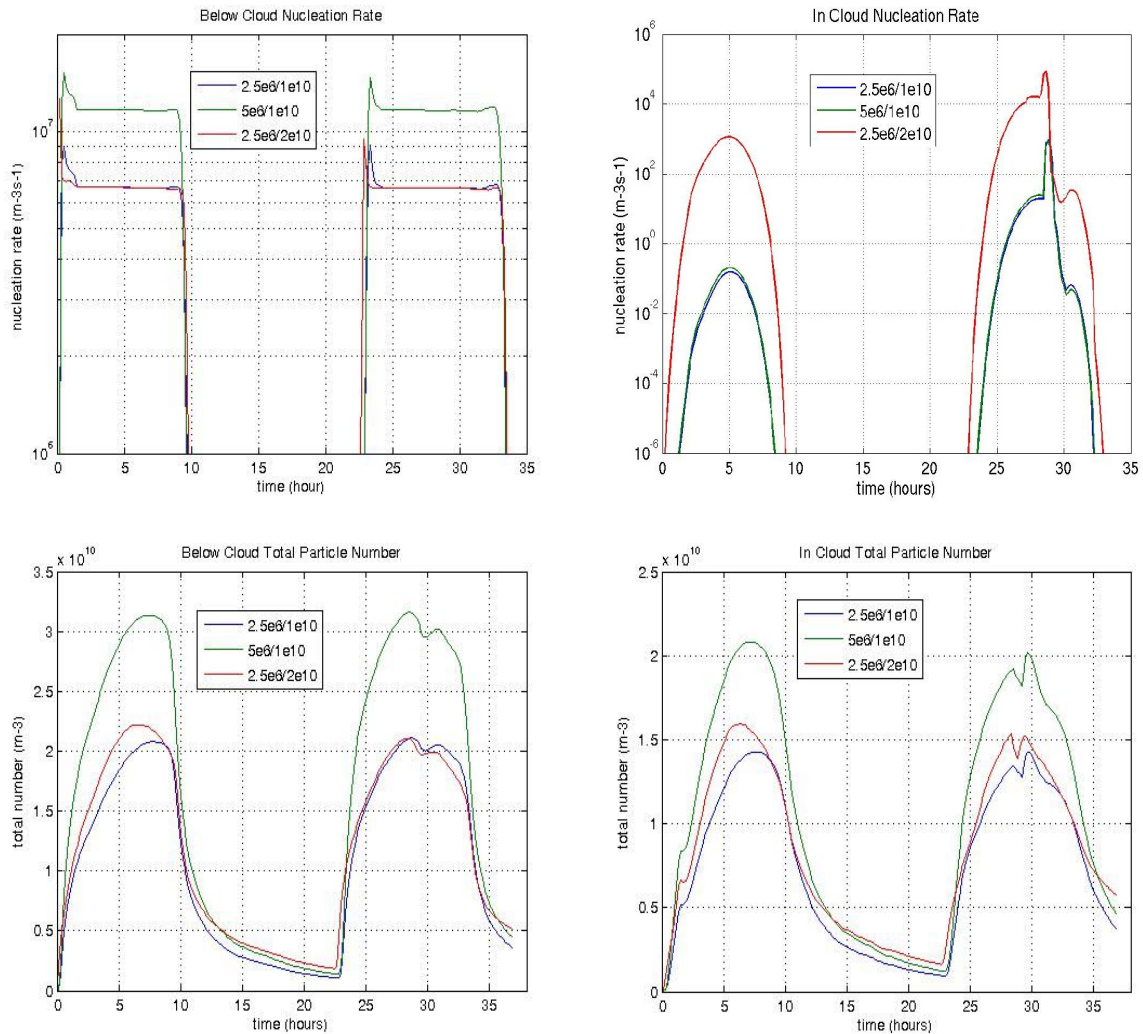
Figure V.70: Sulphuric acid and ionisation rate sensitivity of the modelled below cloud (left hand side) and in-cloud (right hand side) ion-induced nucleation rate (top) and the resulting total particle number (bottom). Sulphuric acid formation is supposed to start immediately during these short-time sensitivity tests. The below cloud height is 250 m, the in-cloud height corresponds to 650 m.

in-cloud total aerosol number is reduced to approximately 2/3 of its below-cloud number. The total particle number shows irregularities in its course during the second nucleation event. These are due to cloud dynamical processes that will be described below.

Figure V.71 depicts the spectrally resolved sensitivity of the below and in-cloud aerosol with respect to the sulphuric acid and the ion formation rate. The ionisation rate variability typical to the below-cloud area is shown in the upper left panel. It is reminiscent of the combined secondary and primary aerosol spectrum sensitivity under zero-dimensional conditions as shown in Figure V.42. The pseudo-unitary secondary particle mode shows decreasing
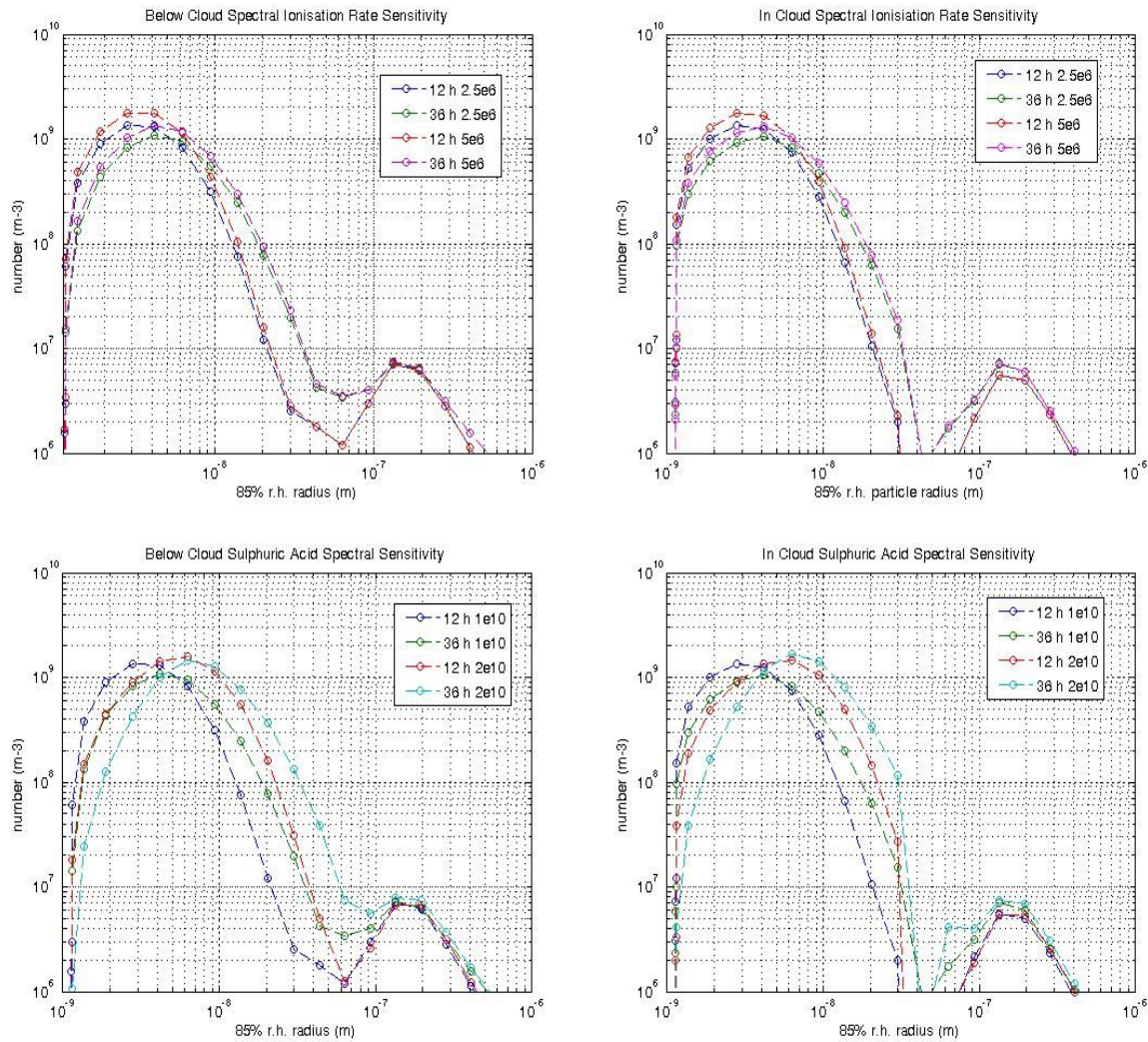
Figure V.71: Below cloud (left) and in-cloud (right) sensitivity of the aerosol spectrum with respect to the ionisation rate (top) and the sulphuric acid formation rate (bottom). The distributions shown are those of 250 and 650 metres, respectively.

sensitivity to the nucleation rate with particle size while the sea salt mode is unaffected by the limited variation of the ionisation rate. The in-cloud ionisation rate sensitivity of the aerosol distribution is in complete analogy, despite the deepened gap between the secondary particles and the activated primary particle mode. The lower panels depict the below and in-cloud aerosol spectral sensitivity to the sulphuric acid formation rate. As pointed out above, the secondary mode does not show the pronounced particle number convergence property observed for the secondary accumulation mode in the absence of cloud droplets. Consistently, the convergence tendency is particularly weak inside the cloud. The activated particle mode takes on the role of the secondary accumulation mode, as it shows little variability of its

255
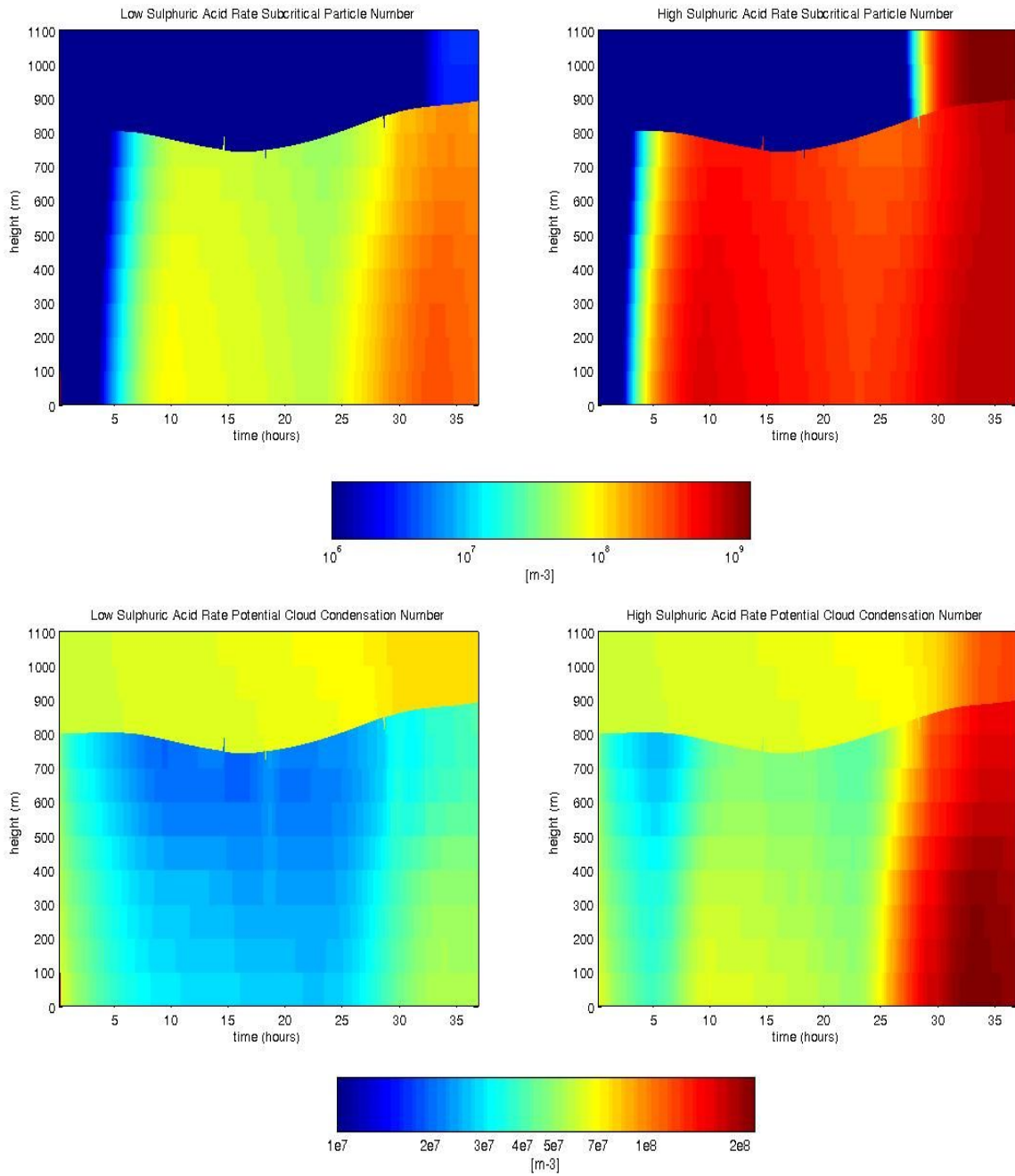
Figure V.72: Sensitivity of the subcritical particle number (top) and the total potential cloud condensation nuclei number (bottom) inside the stratocumulus cloud (650 m height) at a sulphuric acid formation rate of 10^{10} $m^{-3}s^{-1}$ (left) and $2 \cdot 10^{10}$ $m^{-3}s^{-1}$ (right). The subcritical particle number corresponds to the number of particles in the largest durably unactivated particle size class. Note that the depicted level of sensitivity will be damped by cloud droplet coalescence upon aerosol activation (see Figure V.77).

integrated particle number to the condensable yield. The marked variability of the pseudo-unitary secondary mode is further illustrated by Figure V.72. The upper panels show the

vertical profile as a time function of the in-cloud particle number within the largest durably and entirely inactivated particle size class of approximately 15 nanometre radius. Although the temporal variability pattern is similar, the particle concentration is half to one order of magnitude more important in case of a doubled sulphuric acid formation rate. The lower panels depict the sulphuric acid variability of the potential cloud condensation number. Here the term potential refers to the eventuality that an aerosol particle may be activated depending on ambient conditions. The critical activation limit has thus been fixed to the smallest size class observed to be partially activated under model conditions, which is equivalent to the 20 nanometre class. The potential cloud condensation number therefore is not a measure of the convergence property of the primary particle mode, as it comprises a considerable number of unprocessed secondary particles. Nevertheless, the simulated number of potential cloud condensation nuclei varies by a factor two to four only, which is notably lower when compared to the factor 10 variability of the subcritical particle number. A non-negligible part of the potential cloud condensation nuclei are of sea salt origin and a substantial part of the subcritical particles is scavenged by activated particles. These phenomena, along with cloud processing of the activated particles drives the potential cloud condensation nuclei number to much more similar numbers upon condensible yield variation. It follows from the above observations that it is inappropriate to define a critical size that determines without further considerations the cloud droplet number, as the most critical processes of cloud processing and aerosol scavenging are thereby left out. It is these processes, as well as the feedback of the particle spectrum on the critical activation size, that determine the actual number of activated particles.

3.3.2 Relative part of the primary and secondary particles to the cloud droplet number

In this sub-section the relative part of sea salt emission and ion-induced secondary particles to the cloud droplet number will be explored. The upper left panel of Figure V.73 compares the sea salt aerosol generated according to the parametrization of Clarke et al. (2006) to the aerosol spectrum obtained when ion-induced secondary particle formation is added. Following the chosen parametrization, sea salt particles show a bimodal pattern with emission taking place down to an 85% relative humidity equivalent particle radius of 10 nanometres approximately. Note that the sea salt particle radius is assessed under the assumption that their

hygroscopic property is similar to the one of sulphuric acid (see above). The sea salt particles within the smaller mode are of comparable size to the larger secondary particles. Their number density, however, is considerably lower, so that the majority of the pseudo-unitary secondary mode particles is effectively of secondary origin. The sea salt mode remains in turn largely unaffected by secondary particle formation. The upper right panel depicts the influence of sea salt emission as a function of the chosen parametrization on the aerosol spectrum. With the parametrization of Monahan et al. (1986), the total particle flux is reduced, while the smaller sea salt mode is non-existent. Consequently the sulphuric acid condensation losses onto aerosol particles tend to be lower, and secondary particle formation is enhanced. Also the secondary particles tend to grow faster, their incidence on the cloud droplet number is higher, and the tendency following the lower sea salt emission is counterbalanced to a certain extend.

The lower left panel of Figure V.73 depicts the potential cloud condensation nuclei number taking the smallest partially activated size class as critical limit of activation, and compares different different yields of sulphuric acid to a situation with no sulphuric acid at all. Both below and in-cloud values are displayed. It appears that sea salt may ensure a potential cloud condensation nuclei concentration of around 25 particles per cubic centimetre. Note that the below cloud value is higher because of the lesser incidence of cloud processing. A noon local time formation rate of 10^{10} molecules of sulphuric acid per cubic metre and second induces a divergence from pure sea salt values after about 24 hours, meaning that under model conditions it takes approximately one day for a notable amount of secondary particles to grow to potential activation size. Particle growth is boosted by condensation during the second nucleation event. This finding is supported by Figures V.33 and V.34 obtained under zero-dimensional conditions, showing that daytime net number concentration increase of Aitken particles is determined by condensation. When the sulphuric acid formation rate is set to $2 \cdot 10^{10}$ $m^{-3}s^{-1}$ the simulated potential cloud nuclei number diverges already during the first particle burst stressing once again the sensitivity with respect to the formation rate. At night-time the sea salt flux is not sufficient to sustain the relatively high levels of potential particles of approximately 50 per cubic centimetre against the losses through coagulation, coalescence and precipitation scavenging.

The lower right panel compares the time function of the actual cloud droplet number concentration under different aerosol formation and growth scenarios. The curves may be temporally subdivided into an initial phase of rapid cloud droplet number decrease through
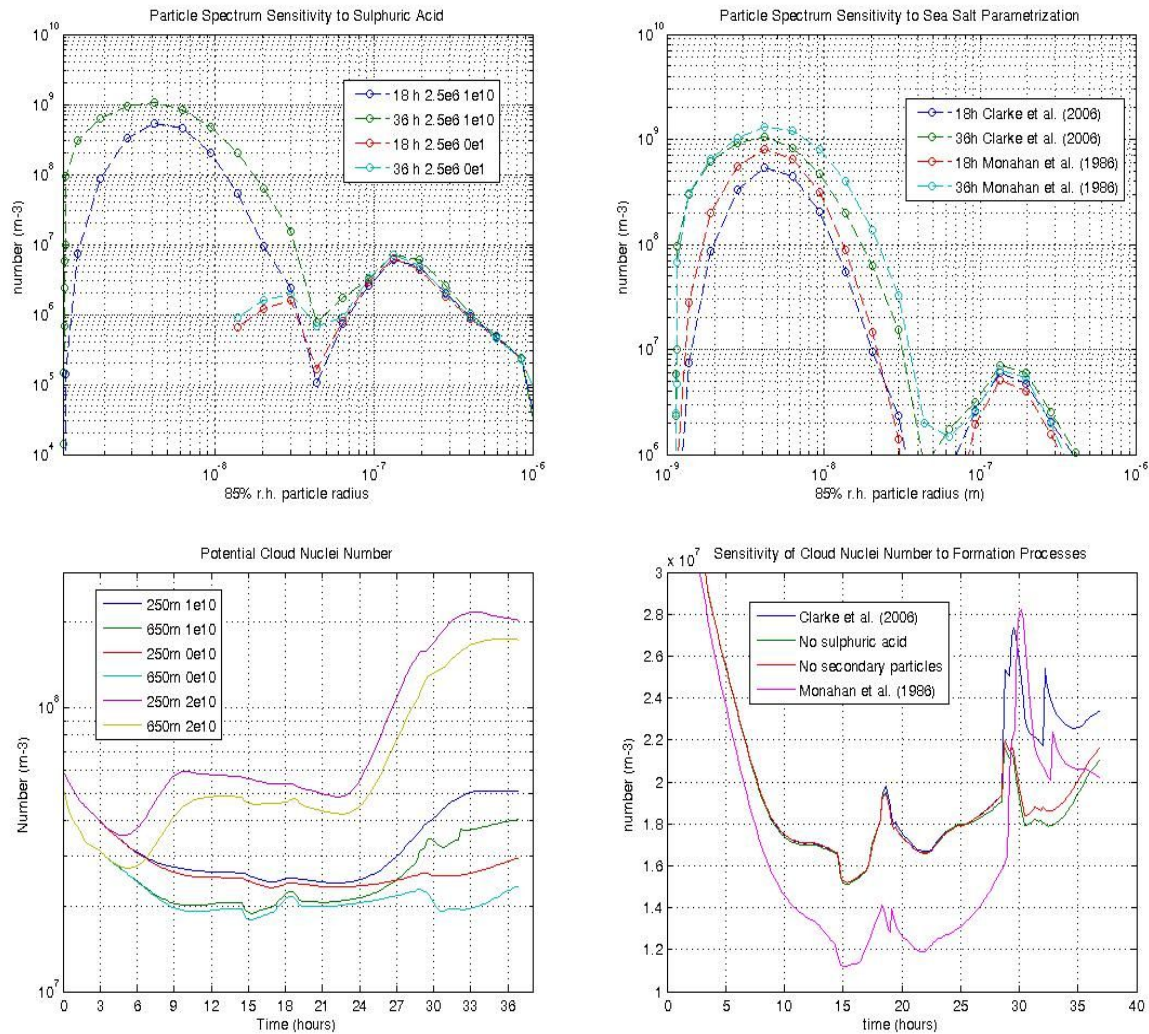
Figure V.73: In-cloud particle spectrum with and in the absence of sulphuric acid formation (top left), sensitivity of the in-cloud aerosol spectrum to the sea salt emission parametrization (top right), response of the potential cloud nucleation number to different levels of sulphuric acid yield (bottom left), and cloud droplet number concentration sensitivity to the sea salt emission parametrization, the absence of sulphuric acid and secondary particle formation, respectively (bottom right).

coalescence in the absence of a notable influence of sea salt vertical flux within the stratocumulus cloud. It is followed by a period of sustained cloud droplet number concentration through sea salt. The parametrization of Monahan et al. (1986) yields a pseudo-equilibrium droplet number that is approximately 30% less than the one of Clarke et al. (2006). Finally, synchronously with intensive updraft (see below) the curves related to secondary particle formation separate from the exclusive sea salt origin case. Consecutive to particle mechanical and critical activation radius interaction the initial variation of the droplet number, which may be associated to the condensation nuclei number, is reduced to around

20%. Thus, the contribution of the secondary particles to the droplet number is substantial only when a brusque variation of the critical radius takes place. The effect of condensation on sea salt particle activation is revealed by the comparison of the cloud droplet number in the absence of ion-induced nucleation and in the exclusion of sulphuric acid formation itself. Condensation growth of sea salt particles is thus shown to have a negligible influence on the cloud droplet number, which is consistent with their low contribution to the secondary accumulation mode. As a corollary sea salt aerosol integration into the cloud droplet spectrum via activation essentially essentially occurs as a consequence of their convective transport into the cloud.

3.3.3 In cloud interstitial sulphuric acid formation rate sensitivity

Clouds enhance atmospheric sulphur production both interstitially via enhanced photolysis and within the wet phase of the cloud droplet via enhanced heterogeneous chemistry. Under intermediately polluted continental conditions Hegg and Hobbs (1981) found the hourly sulphate productivity of atmospheric wave clouds to be equivalent to about 100% of their initial sulphur dioxide content. The ambient sulphur dioxide concentration was approximately 2 orders of magnitude superior to the typical marine concentration related by Clarke et al. (1998), which serves as a basis of the present investigation. When reduced proportionally the in-cloud productivity of the cloud would be approximately 10^{11} molecules sulphuric acid per cubic metre and second, that is 10 times the assessed production rate of Clarke et al. (1998). To investigate the incidence of cloud enhanced productivity on aerosol and cloud droplet dynamics, a tenfold increase of the gas-phase sulphuric acid yield is taken as a working hypothesis. Heterogeneous chemistry is not considered as a first approximation.

Figure V.74 depicts the reaction of the aerosol spectrum as well as the related nucleation parameters to enhanced in-cloud sulphuric acid formation. Although the in-cloud ambient production rate is increased tenfold, the sensitivity of the aerosol spectrum (upper left panel) is less pronounced as it would be if the formation rate was enhanced twofold within the entire boundary layer (see Figure V.71). As shown in the upper right panel, the area of effective nucleation is extended to the entire boundary layer, and the related particle formation rate is of the order of the ionisation rate during the daytime bursts. The ambient sulphuric acid concentration (lower right panel) is now high enough to yield ion-induced nucleation bursts
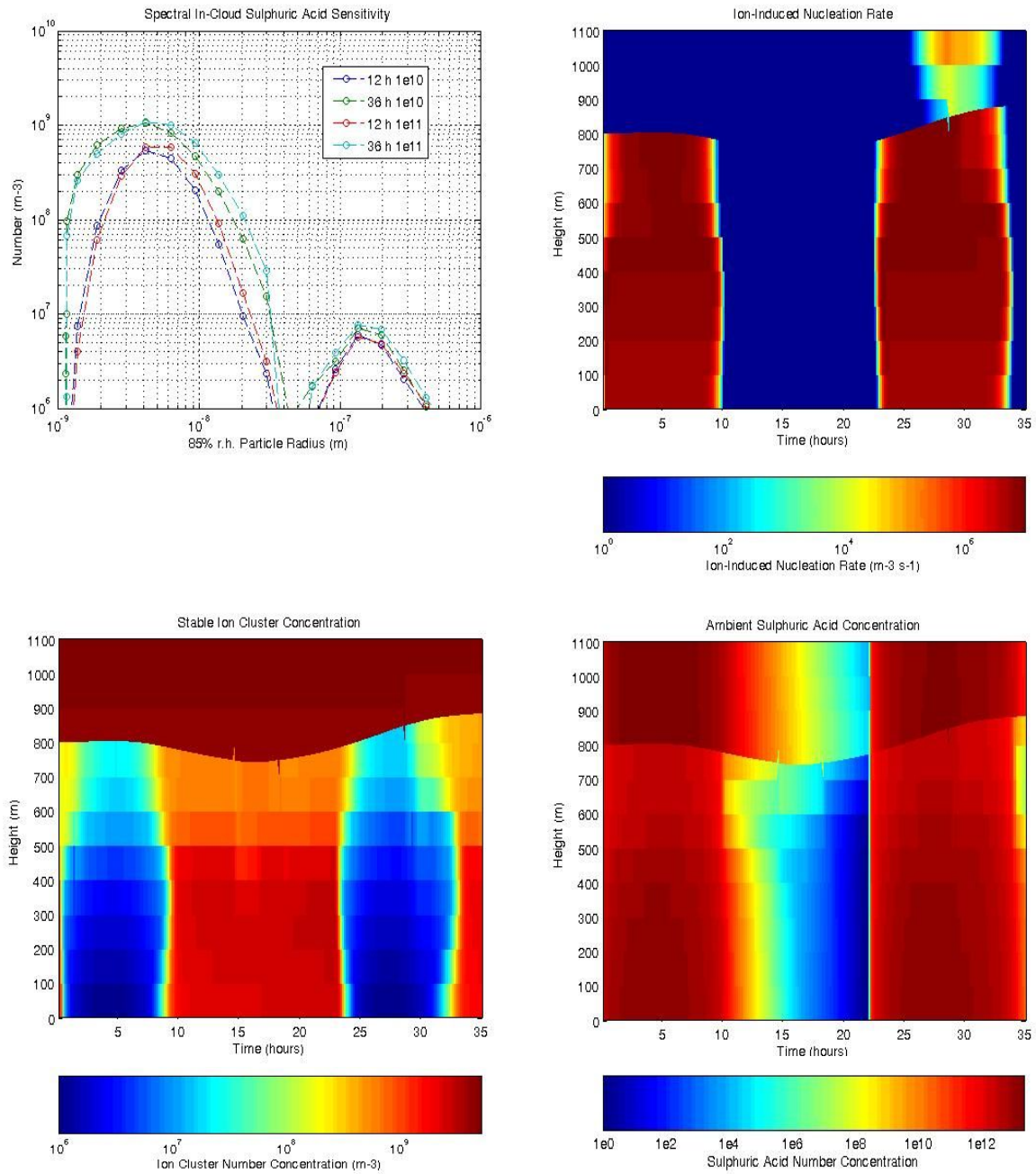
Figure V.74: Sensitivity of the in-cloud aerosol spectrum when in-cloud sulphuric acid yield is increased tenfold (top left), and corresponding vertical ion-induced nucleation rate (top right), cluster ion (bottom left) and sulphuric acid distribution (bottom right).

both below and within the cloud; however in-cloud sulphuric acid losses onto cloud droplets keep the vertical sulphuric acid gradient negative. Aerosol condensation growth is therefore moderately enhanced only, and is counterbalanced in its effect by enhanced scavenging, so that eventually, in the absence of a pronounced number sensitivity, particles are enlarged via

261

their higher content of sulphuric acid. During nucleation bursts the in-cloud cluster ion concentration is less reduced than its below-cloud counterpart, as shown in the lower left panel. Higher in-cloud nucleation and attachment losses onto cloud droplets negatively are effectively outbalanced by lower attachment losses onto a sensibly reduced aerosol, and additionally by a higher ion source function.

V.3.4 Model validation

In this section modelled aerosol spectra are compared to observations under clear marine conditions (Hoppel et al., 1994). The typical cloud droplet concentration encountered in this empirical study is 25 to 30 particles per cubic centimetre. Measurements were made within marine stratocumuli off the coast of Oregon. Due to their similar cloud droplet number concentration and ambient conditions, the dynamics of aerosol cloud interaction should be close to those encountered in the present study. However, it should be pointed out that measurements produced no evidence for ongoing aerosol nucleation under overcast conditions.

Figure V.75 compares typical modelled night-time aerosol spectra to in-cloud measurements of both the interstitial aerosol and the cloud droplet spectra. Note that the model spectrum of droplet size is not explicitly assessed, and therefore not represented. Cloud droplets are supposed to follow the Khrigian-Mazin distribution (see above), whereas the mean size is assessed specifically to their solute content assuming size invariant equilibrium vapour pressure. The modelled interstitial spectrum is made of both the secondary accumulation and the condensation mode, which do not show a net separation. The simulated cloud liquid water concentration is approximately twice the observed one, resulting in a higher mean drop radius, and supposedly in a stronger cloud droplet aerosol particle interaction. Nevertheless, the modelled secondary accumulation mode maximum is equal to approximately 20 nanometres when the condensable yield $\{R_f\}_a=2\cdot10^{10}$ $m^{-3}s^{-1}$, and thereby comparable to the observed one. The simulated accumulation mode shows a similar steep descent and pronounced gap towards the cloud droplet side, marking the dynamical interaction properties with these. The observed accumulation mode particle number density is slightly more important. Apart from growth dynamical considerations the discrepancy may be caused by the unequal relative humidity chosen to represent the particle equilibrium size spectrum. While Hoppel et al. (1994) show

the particle spectrum under dry conditions equivalent to *r=0.37*, the modelled results are shown for the more typical marine boundary layer humidity of *r=0.8*. As shown on the graph, an adaptation of the measured spectrum to 96% humidity results both in a broadening and a shift of the spectrum, so that the observed accumulation mode maximum should be closer to the modelled one. As indicated above, a major discrepancy between the modelled and the measured interstitial aerosol spectrum is the absence of a nucleation mode. Since simulation conditions are similar, this is a clear indication that ion nucleation, if it were to take place in the marine boundary layer, is not as efficient as suggested by ion-induced binary particle formation theory of aqueous sulphuric acid solutions.

Figure V.76 compares the below cloud aerosol spectra related to the previous figure. The observed spectrum confirms that turbulent exchange between the stratocumulus cloud and the underlying boundary layer is important enough to conserve the main characteristics of the cloud processed aerosol spectrum outside the saturated area. The separation gap between the formerly activated particles and the secondary accumulation mode is less pronounced when compared to its in-cloud counterpart, whereas the simulated and the observed gaps show similar depth. The simulated sea salt mode is less pronounced and broader, especially on its large particle end. The steeper descent of the large end of the observed primary mode, which is reminiscent of its accumulation mode counterpart, may be interpreted to result from relatively intensive precipitation scavenging.
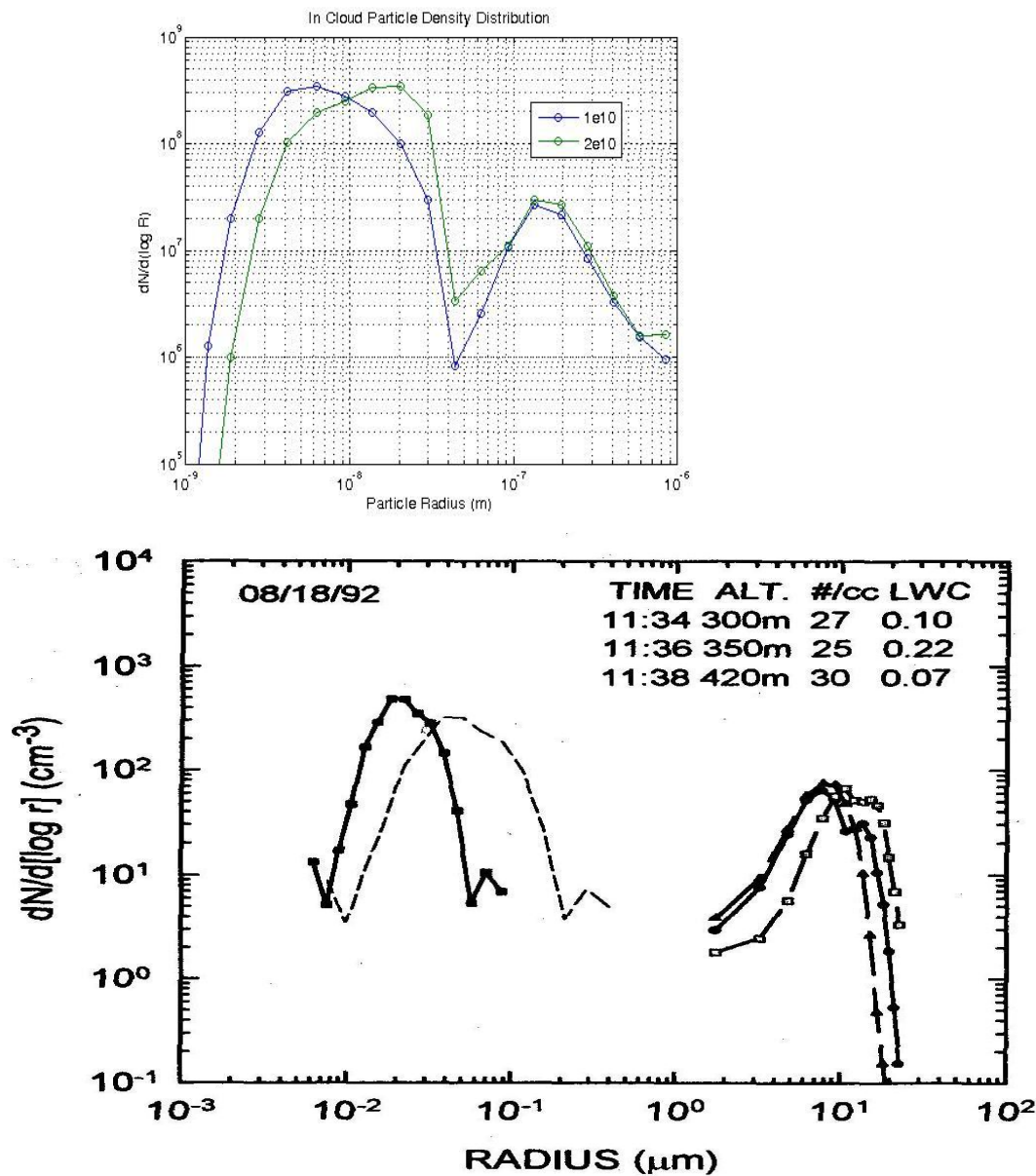
Figure V.75: Modelled in-cloud aerosol particle distribution versus empirical data of Hoppel et al. (1994) from stratocumulus measurements off the Oregon Pacific coast. The total measured cloud droplet concentration is 25-30 cm⁻³, while the simulated concentration is about 24 and 31 particles per cm³, respectively. The modelled cloud droplet spectrum is shown for a 85% relative humidity equivalent, as this study´s model formalism gives no information about the actual cloud droplet size spectrum. Note that the quasi-unimodal aerosol distribution consists of the secondary condensation and accumulation mode, while the observed distribution shows an accumulation mode only in the absence of recent nucleation. The model results show the 650 m aerosol distribution at 6 am, after 54 hours of simulation. The effective relative humidity is 37% during the interstitial aerosol measures, the adapted spectrum to 97% relative humidity is also shown (dotted line), assuming that particles consist of aqueous sulphuric acid.

264
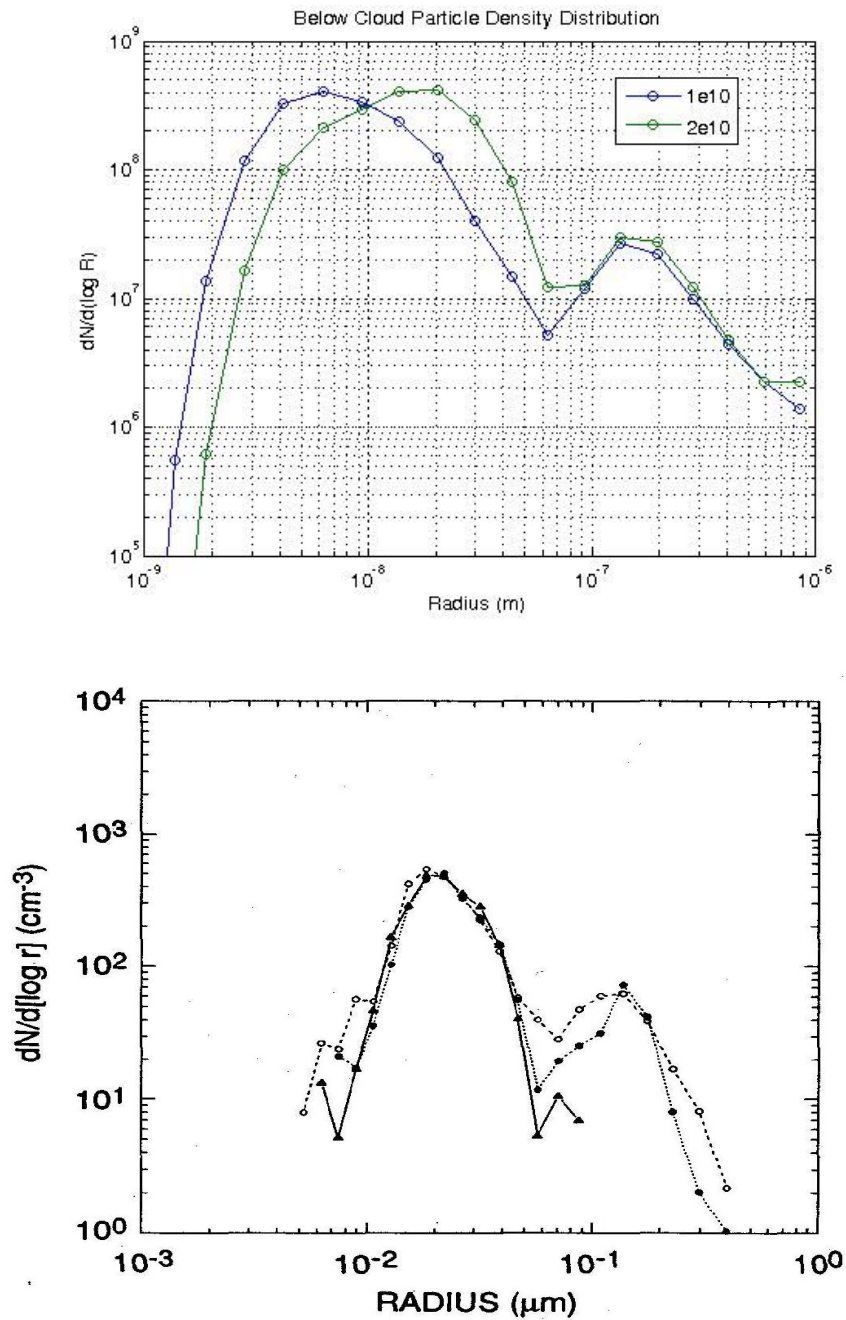
Figure V.76: Modelled below cloud aerosol spectrum versus measured distributions in the cloud topped marine boundary layer off the Oregon Pacific coast (Hoppel et al., 1994). The in-cloud interstitial distribution is also shown (solid line), demonstrating that the below cloud separation gap between the sea salt and the secondary mode is less pronounced. Note that the modelled secondary aerosol distribution is bi-modal, consisting of a condensation and an accumulation mode. The measured aerosol distribution is unimodal through the absence of recent nucleation. The modelled aerosol spectrum is adapted to 85% relative humidity and taken at a height of 250 m at 6 am. after 54 hours of simulation.

V.3.5 Aerosol cloud dynamical interaction

3.5.1 Aerosol activation

Figure V.77 compares the cloud droplet number and the main related activation parameters. The results are shown for two different sulphuric acid formation and ionisation rates, respectively, at a model height of 650 metres. It is apparent that more or less the first 32 simulated hours constitute the transition period. The first 12 hours show a quick decrease of the cloud droplet number (upper left panel), due to fast coalescence reduction in the absence of a relevant particle source. These are followed by an unstable range of abrupt cloud droplet number variation. Beyond the 32 hour limit a smooth diurnal variation regime becomes apparent that is definitely conditioned by the condensable yield. As pointed out above, the daytime nucleation of secondary particles is passed on to the cloud droplet number with a certain temporal shift due to the time necessary for the particles to reach activation size. The role of secondary particle growth is apparent as the maximum supersaturation (lower left panel) is still decreasing after about 35 hours, while the cloud droplet number is now increasing. The maximum supersaturation is limited by the increase of the potential cloud condensation number following secondary particle growth to this size. Considering that the maximum supersaturation is a function of both the uplift velocity and the potential cloud nuclei number, it is nevertheless the relationship between the supersaturation and the updraft that tends to be dominant during most of the day, as it is apparent from a comparison of the lower panels. For the cloud droplet number to increase at night-time a continuous increase of the updraft velocity is necessary, as it is demonstrated by the 44 hour decrease of the droplet number as the rhythm of the uplift velocity increase is somewhat interrupted. Subsequently the cloud droplet number further increases just until secondary particle growth limitation becomes effective at around midnight, thus leading to an apparent 12 hour shift between the maximum nucleation rate and droplet number.

The sensitivity of the cloud droplet number to the ion and sulphuric acid formation rate is consistent with the findings of the previous section in the absence of activated particles. The ionisation rate correlation is very weak on the first simulated day, while it is even slightly negative on the second day. The sulphuric acid sensitivity is much more pronounced from day
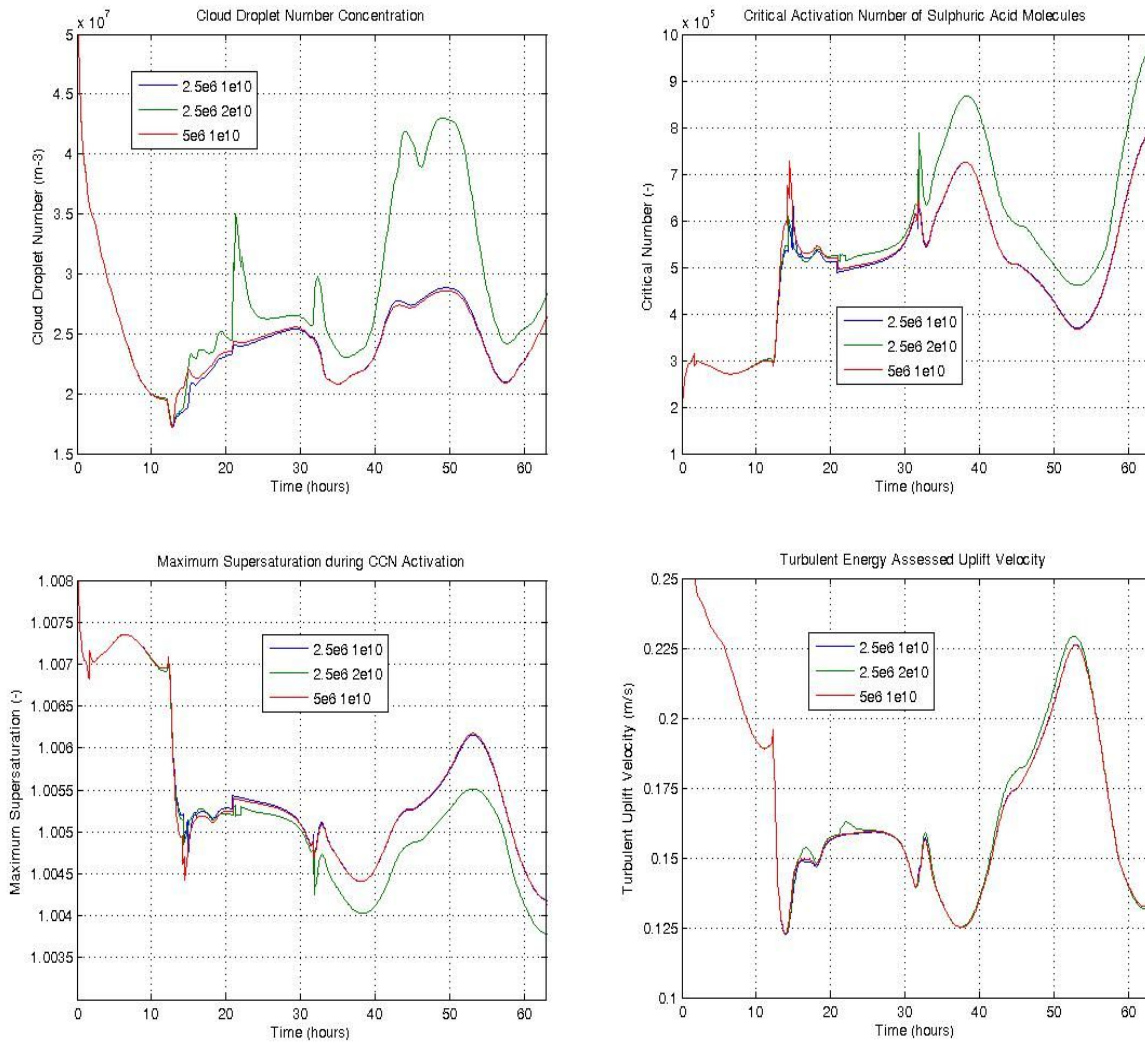
Figure V.77: Variability of the cloud droplet number for selected ionisation and sulphuric acid formation rates (top left). The correlation with the critical sulphuric acid molecule number per activated cloud condensation number (top right), the maximum supersaturation (bottom right) and the boundary layer model derived characteristic turbulent uplift velocity (bottom right) is also shown. Results are taken at a height of 650 m.

two on and is a function of the uplift velocity variation. When the uplift velocity is weakening or only moderately increasing, the doubling of the condensable formation rate leads to an increase of approximately four activated particles per cubic centimetre. During continuously intensive increase of the updraft, the combination of the shift of the critical activation radius and turbulent transport of cloud nuclei from below the cloud causes the cloud droplet number to be much more sensitive to the condensable yield. Following a doubling of the formation rate the droplet number increases as much as around 20 nuclei per cubic centimetre. For the drop number to remain at such a high level it has to be sustained by a strong source function.

267

Secondary particle growth can not act as such a source, as in the absence of continuous uplift velocity increase the droplet number tends to drop again. The pronounced link between the time dependence of the critical activation radius and the droplet number confers to the quantitative relationship between the condensable yield, the nucleation rate, and the cloud droplet number a pronounced relativity to cloud dynamical processes.

3.5.2 Precipitation formation

The upper left panel of Figure V.78 depicts the 50 metre drizzle rate as a time function for different rates of ionisation and sulphuric acid formation. Again the curves at equal condensable formation rate follow a remarkably similar evolution, while the higher sulphuric acid curve shows substantially lower drizzle rates following effective formation suppression. The general evolution of the drizzle rate is dominated by the variation of boundary layer turbulence (see Figure V.77), which determines the uplift velocity and thus the vertical transport of atmospheric moisture. Boundary layer turbulence in association with precipitation formation conditions the diurnal pattern of the cloud droplet solute spectrum as shown in Figure V.66. In case of relatively low turbulence the exchange between the in-cloud and the below cloud area is restricted, and the mean in-cloud residence time increases. Consistently droplet containing a high amount of solute tend to have experienced a high number of coalescence events so that their mean radius is maximal. This situation corresponds to the typical daytime situation. In the evening convection sets in and particle transport from below the cloud along with accretion removal diminishes the mean droplet age to the point that their mean size becomes indifferent to the solute content. Their mean size solute relationship resembles the assumed initial spectrum just upon cloud formation. In the early morning before sunrise particle mean age tends to increase again along with turbulent energy decrease. Nevertheless, the cloud liquid water content is still high and precipitation formation is still effective. Increasing mean age and high liquid water content induce a high mean radius of intermediate solute content droplets. High solute amount particles tend to have a smaller mean radius as their mean age is lower following pronounced precipitation scavenging. The 54 hour curve of Figure V.66 represents a typical early morning intermediate distribution.

Autoconversion is the dominating process of precipitation formation (not shown). For this reason a negative correlation of the drizzle rate with the sulphuric acid formation rate is
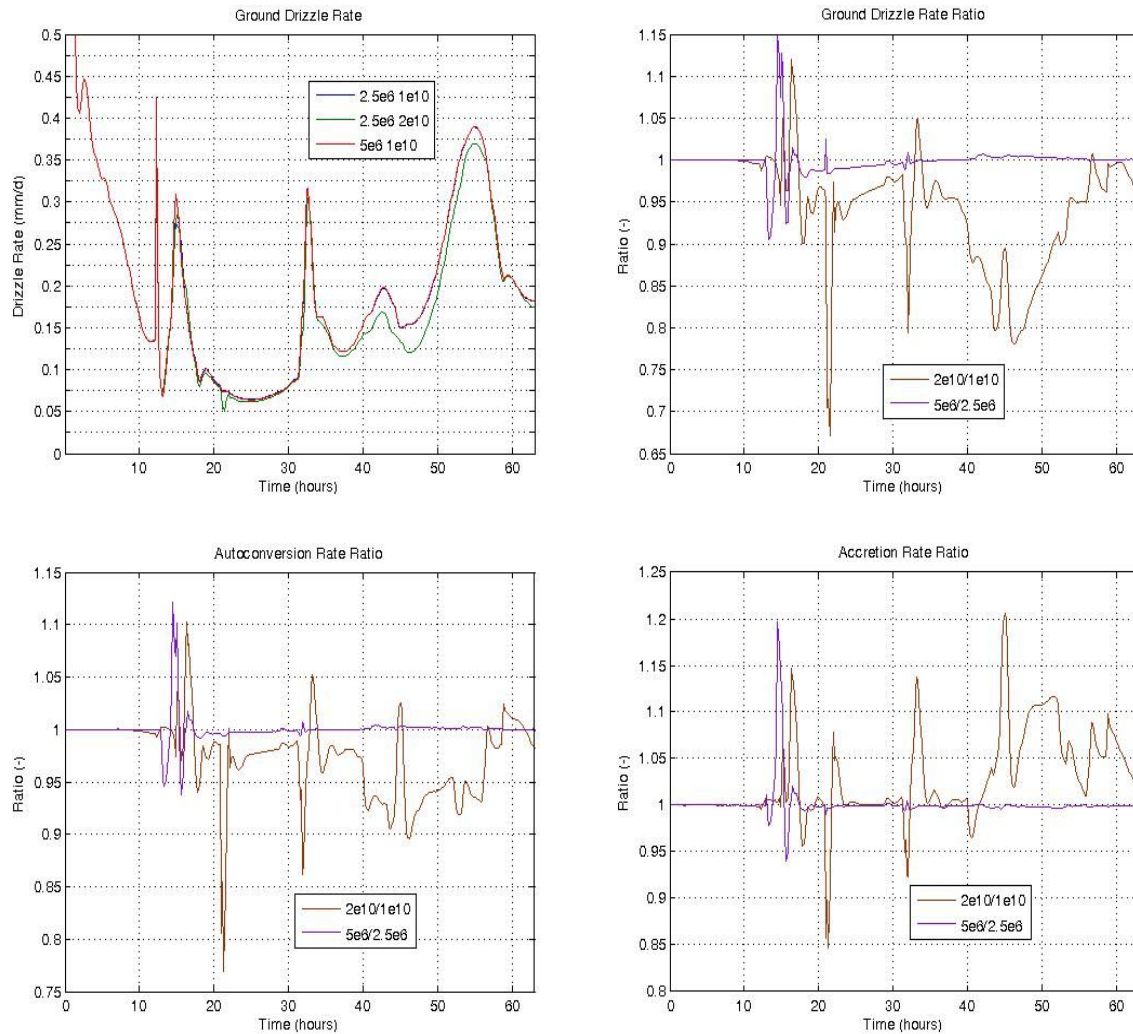
Figure V.78: Simulated surface (50 m) drizzle rate variability (top). Absolute values for selected ionisation and sulphuric acid formation rates are shown on the left hand side, the right hand side depicts the corresponding relative variability. The bottom panels display the variability of the autoconversion (left) and the accretion rate (right), both at a height of 650 m above ground. Note the apparent anticorrelation of the variables during relatively high precipitation events.

dominated by the negative correlation of the autoconversion rate over the positive correlation of the accretion rate. Autoconversion increases during intensive updraft along with the cloud liquid water content (see also Figure V.79). On the other hand, autoconversion is efficiently slowed down when the cloud droplet number increases, such as upon a positive variation of the condensable yield (lower left panel). A higher droplet number generally implies smaller cloud droplets, which require more coalescence events prior to reaching raindrop size. The ensuing positive feedback on the autoconversion rate via enhanced cloud liquid water

retention may not counterbalance this effect, although both the coagulation flux (see Equation IV.143) and the threshold function (Equation IV.152) depend more on the liquid water content than on the droplet size. Accretion shows invert behaviour following a variation of the condensable yield. Smaller droplets present a smaller cross-section, and the raindrop scavenging efficiency diminishes in consequence. However, the higher cloud liquid water content following precipitation suppression and the higher particle number outnumber the effect of the smaller droplets, so that the overall accretion rate is higher.

3.5.3 Cloud optical properties

Cloud optical properties are a function of the thickness of the cloud layer and the cloud droplet number and size distribution. The present one-dimensional model of aerosol cloud interaction gives little information on the cloud droplet number distribution. For this reason the following formula is adopted to assess the cloud optical depth (Hobbs, 1993):

$$\tau_C \simeq 2.4 \left(\frac{Q_C}{\rho_w} \right)^{2/3} N_C^{1/3} h$$

f V.16

where τ_C is the cloud optical depth, N_C is the cloud droplet number, h is the cloud layer thickness and Q_C is the specific cloud liquid water content. This formula assumes that $r_{C2} \approx r_{C3}$. The cloud optical depth is thus exclusively expressed as a function of the cloud thickness, droplet number and liquid water content, while the size spectral variability of the droplets is omitted.

The cloud albedo may be directly derived (Hobbs, 1993):

$$a_C = \frac{(1-\gamma)\tau_C}{2+(1-\gamma)\tau_C}$$

f V.17

where a_C is the cloud albedo, and $\gamma \approx 0.85$ is the cloud scattering asymmetry.

The upper left panel of Figure V.79 shows that the cloud liquid water content is correlated both with the turbulent uplift velocity (see Figure V.77) and the sulphuric acid formation rate via the cloud droplet number and the consequent precipitation suppression. The cloud optical depth (see the upper right panel) follows the same evolution as the liquid water content and the cloud droplet number, with secondary particle formation and atmospheric turbulence as
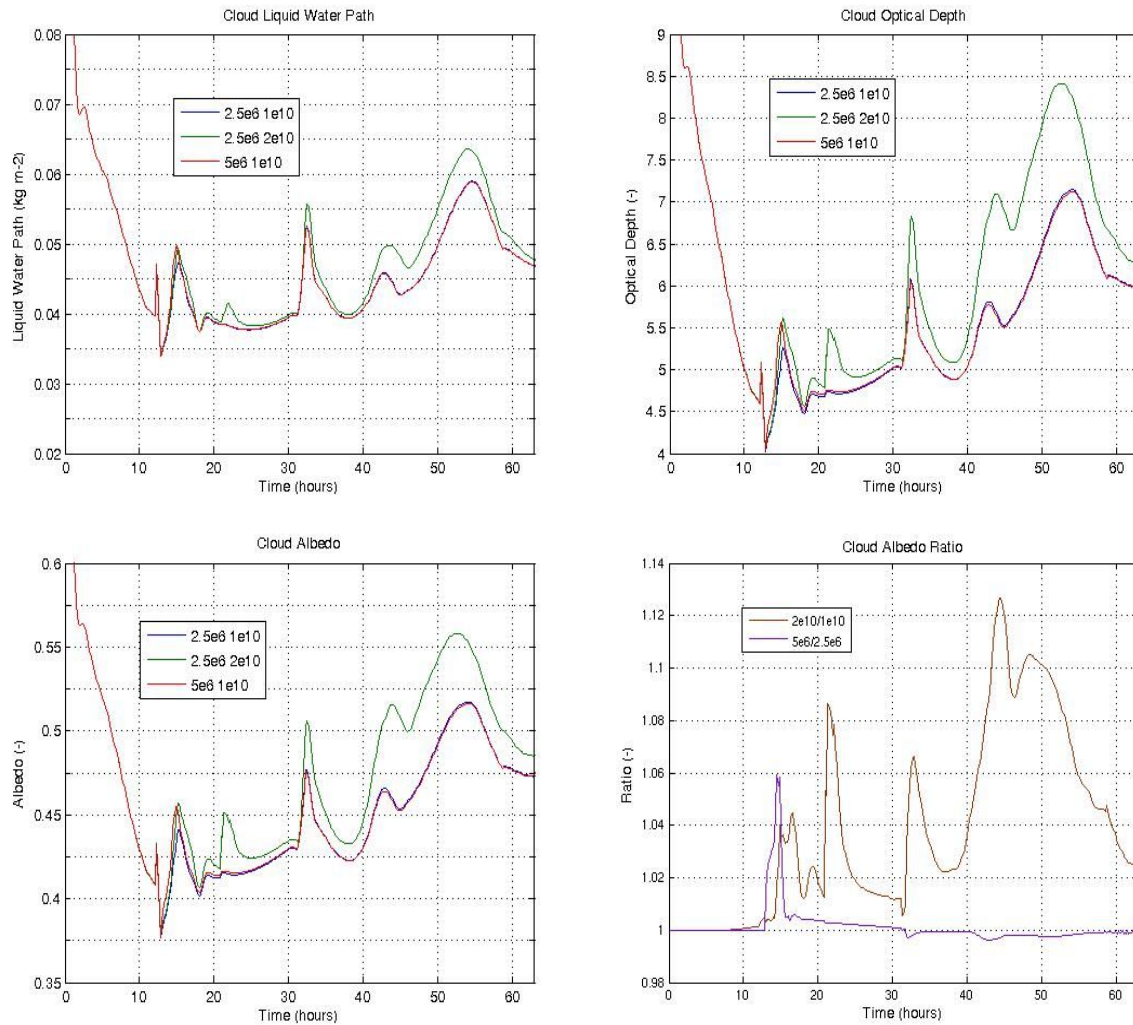
Figure V.79: Variability of the cloud optical properties as given by the evolution of the cloud liquid water path (top left) and the cloud droplet number concentration (see Figure V.77). The estimated cloud optical depth (see text for details) is shown in the upper right panel. The corresponding cloud albedo (left) as well as the relative albedo (right) variation are shown in the lower panels.

triggering elements. The response of cloud albedo to a variation of the cloud droplet number tends to be maximal when the latter one is low (Twomey, 1991). The simulated diurnal variability of the cloud albedo is thus as much as 20% for a cloud droplet number variation from 20 to 30 per cubic centimetre. In case of a doubled sulphuric acid formation rate the diurnal doubling of the cloud droplet number entails a modelled increase of the cloud albedo of as much as 30%. As the modelled albedo increase is maximal during night-time, its optically effective variability due to diurnal cloud microphysical processes would be correspondingly diminished to about 10 and 15%, respectively.

VI. Discussion and Conclusion

VI.1 General context recapitulation

Although observational evidence would rather point to an indirect mechanism of solar modulation of the troposphere via the upper atmosphere, there has been controversy recently on a possible direct mechanism following the empirical findings of Svensmark and Friis-Christensen (1997). Larsen (2005) as well as Marsh and Svensmark (2000) have formulated two antagonistic theories of a solar link to global climate via cloud formation. The basic assumptions these theories rely upon are affected by a substantial amount of unknowns. Marsh and Svensmark (2000) assume that ion nucleation is an essential process of secondary particle formation in the lower troposphere. Conferring bulk thermodynamic properties to cluster size particles Laakso et al. (2002) as well as Yu (2006b) have obtained major ion nucleation bursts under low troposphere conditions, while the thermodynamic data on cluster ion stability produced by Lovejoy et al. (2004) relegate relevant ion mediated secondary particle formation to the vicinity of the tropopause (Kazil et al., 2006). Recent laboratory measurements of Svensmark et al. (2007) back the model results obtained with the bulk property formalisms. Larsen's theory (2005) implies that marine biogeochemical production of dimethylsulphide and its consecutive release to the atmosphere are effectively modulated by the UVA and UVB radiation flux penetrating the ocean water. Microbiological studies, however, are equivocal as to the sensitivity of dimethylsulphide synthesising and removing plankton and bacteria to UV radiation. Only three out of five studies confirm that marine plankton is effectively inhibited by ultraviolet radiation at realistic flux levels.

Rather than focusing on the phenomenology of the conjectured mechanisms, this study explores their numerical implications in the context of aerosol and cloud microphysics. A special focus is put on the dynamics of aerosol growth and aerosol-cloud interaction, in particular on secondary particle nucleation, aerosol growth processes, cloud condensation nuclei activation, cloud droplet coalescence and scavenging, and on the relative contribution and interaction of primary and secondary particles.

VI.2 Discussion

VI.2.1 Ion-induced nucleation

Under the lights of the aforementioned uncertainties and unknowns regarding ion nucleation as a factual process of ultrafine particle formation, and the substantial deficiencies of both the thermodynamic and the mechanical formalism, this study makes the assumption that ion-induced nucleation is an efficient mechanism of secondary aerosol formation in the clean marine boundary layer. The underlying idea of this approach is to guarantee most favourable model conditions to investigate the aerosol sensitivity to the solar variability of the ionisation rate. In consequence ion nucleation rate merely serves as an effective and potentially realistic source function here.

Castleman and Holland (1982) show that it is especially the use of bulk properties in the context of ordered cluster ions that potentially jeopardizes the accuracy of the Thomson equation, although for certain configurations involving aqueous solutions theoretical results were found to compare reasonably with experimental data. Yu (2005) suggests a modified Thomson equation that takes into account the effects of ion-dipole interaction to cluster stability. The incidence of ion-dipole interaction on the Gibbs free formation energy of the cluster is not considered here. Instead, the enhancement of the dipole flux onto charged particles through electrostatic charge interaction is integrated consistently with the binary nucleation theory (Stauffer, 1976).

Except for the ion-dipole condensation enhancement factor, the formalism of ion-induced nucleation produced here largely follows the analytical method presented in Laakso et al. (2002). Results show the very pronounced sensitivity of nucleation to the ambient sulphuric acid concentration, atmospheric moisture and temperature. It is especially the existence of an intermediate stable ion cluster that considerably lowers the energy barrier of ultrafine particle formation, and thus induces the considerably higher efficiency of ion-induced over homogeneous nucleation. The resulting estimates of the ion nucleation rate are consistent within one order of magnitude with the mechanical formula of the ion dipole encounter frequency at the appearance limit of the formation energy barrier. The reasonable agreement of these fundamentally different methods at the limit of their respective range of application

upholds the assumption that the nucleation theory appropriately represents stable particle formation dynamics.

Ion-induced nucleation theory suggests a linear relationship between the ambient ion concentration and the nucleation rate. Non-linear properties of cluster ion dynamics as suggested by Yu (2002) may thus not be represented. These features are caused by the coagulative interaction of subcritical particles among themselves, as well as of subcritical and supercritical particles between each other. Nevertheless, the mechanical model of Yu (2002) suggests an almost linear dependence of the ultrafine particle yield on the ionisation rate when lower than about $5 \cdot 10^6$ $m^{-3}s^{-1}$.

Another jeopardy to the accuracy of the formalism of stable secondary particle formation arises paradoxically through the strong hygroscopic property of sulphuric acid. There is very little data available on the respective vapour pressures over aqueous sulphuric acid mixtures as a function of their mixing ratio (Masucci et al., 1996; Marti et al., 1997). For this reason, the sulphuric acid and water vapour pressures are assessed here via their activity as ions in solution following their dissociation. The activity data of Clegg et al. (1994) is extended to non-dissociated sulphuric acid via the evaluation of its first dissociation constant with the thermodynamic data of Ayers et al. (1980) and Giauque et al. (1960). The uncertainty linked to sulphuric acid vapour pressure measurements appears as the data of Marti et al. (1997) performs much less well in determining the dissociation constant than the thermodynamic data of Giauque et al. (1960). The sensitivity of the ion-induced nucleation rate to the first dissociation constant of sulphuric acid is comparable to the one to ambient sulphuric acid and relative humidity.

VI.2.2 Aerosol growth dynamics

Comparison with empirical data of Quinn et al. (1993) shows that the box model of aerosol growth allows reproducing the typical bimodal feature of the marine aerosol, showing an accumulation mode of secondary particles within the Aitken size range and a sea salt mode of sub-micron size. Quantitatively, however, the model secondary accumulation mode is somewhat higher and wider. Precisely, Pirjola et al. (1998) predict that numerical error diffusion within the formalism of discrete aerosol particle size class leads to an artificial widening of the aerosol spectrum. The widening is the more pronounced the more the number

of particle size classes is reduced. Pirjola et al. (1998) conclude that a minimum of about 8 size classes per particle size order of magnitude should lead to a reasonable representation of aerosol growth dynamics. In this study the number of aerosol size bins is fixed to 29 from sub-nanometre to micrometre size, and should therefore meet the above discretisation criterion. The aerosol growth dynamical analysis demonstrates that the accumulation mode particle number may be linked to the coagulation loss flux involving the nucleation mode. As a corollary, a widening of the accumulation mode spectrum has a particle number reducing effect on the nucleation mode, and the separation gap between these modes is somewhat levelled through numerical diffusion.

Zero-dimensional sensitivity tests point out that the secondary accumulation mode growth is relatively indifferent to the ionisation rate, in contrast with the total number of secondary particles, which is a strong function of the ambient ion number via the relatively elevated number of ultrafine particles. Moreover, there is a tendency to a slight anticorrelation of the accumulation mode and the nucleation rate. This effect is triggered by the strong interaction between the integrated sulphuric acid consumption and coagulative particle number reduction of the aerosol, and the individual condensation growth rate and coagulative scavenging probability. A simplified model of aerosol growth allows making the convergence property of the aerosol growth dynamics plausible. The appropriateness of the simple model is demonstrated as it reproduces the momentary accumulation mode particle number via the equilibrium assumption of the condensation and coagulation particle loss and the nucleation gain flux. While the effectiveness of coagulation to reduce the total particle number is a known phenomenon (see Kerminen et al., 2001), the tendency to an anti-correlation of the accumulation mode and the ionisation rate has not yet been evoked, although Yu and Turco (2001, their Figure 7) find a slight inverse correlation of the 30 nanometre particles without commenting on it. Simple mass balance considerations point to the convergence property of the accumulation mode secondary aerosol with respect to the ionisation rate. As the relative number size density distribution of the secondary aerosol is only marginally affected by the ionisation rate, and the gas phase fraction of the atmospheric sulphuric acid tends to be negligible, a surplus of ultrafine particle particles has to be counterbalanced by a deficit of larger particles at constant condensable yield. The larger accumulation mode particles rapidly become the dominant element of the aerosol mass balance, so that a relatively large number variation of small particles has a negligible influence on the accumulation mode in terms of

276

the mass balance. As a corollary the aerosol number spectrum shows no convergence with respect to the sulphuric acid formation rate. The convergence property shows to be apparent, however, in the integrated accumulation mode particle number, which tends to be indifferent to the condensable yield. The variation of the sulphuric acid formation rate produces a shift of the accumulation mode due to differential aerosol growth velocity, leading to a considerable variation of the potential cloud condensation nuclei number.

The zero-dimensional box model of charged aerosol growth dynamics allows reproducing an effect that shows in observations of Hõrrak et al. (1998) in relationship with ultrafine particle number variation. Their aerosol mobility measurements suggest that the number of larger charged particles tends to be reduced during presumed nucleation events. This effect is found to be the resultant of ion attachment, which tends to take place preferentially onto smaller oppositely charged particles due to effective enhancement, thus leading to their neutralisation. A higher flux of ions onto nucleation mode particles is compensated by a lower flux onto the accumulation mode, and hence results in a lower fraction of charged particles within this mode. The effect is found exactly within the particle size range found by Hõrrak et al. (1998). The ion attachment formalism of the aerosol growth model is thereby validated.

The aerosol growth model assumes that sulphuric acid is the exclusive atmospheric non-volatile species. Sea salt particles are chemically assimilated with secondary particles. The negligence of other condensable species, such as organics, may seem appropriate under mid-latitude pristine marine conditions. In particular, the relevance of methanesulfonate seems to be constrained to polar regions (Quinn et al., 2000). The parametrization of sulphuric acid formation relies on empirical data of Clarke et al. (1998) off the South and Central American Pacific coast. However, the atmospheric sulphate yield is highly variable and depends on anthropogenic sulphur dioxide pollution, which pertains quite a large fraction of the open ocean along the coastal areas (e.g. Kazil et al., 2006). Sensitivity studies with a sulphuric acid yield increased tenfold may reproduce the effect of both moderately high pollution and the presence of additional condensable species such as organics. Except for their acceleration, these tests reveal no relevant modification of the aerosol growth dynamical features, in particular of the ionisation and sulphuric acid formation rate sensitivities.

VI.2.3 Aerosol cloud interaction

The one-dimensional simulation results of secondary aerosol formation and cloud aerosol interaction support the zero-dimensional findings on aerosol growth dynamics. The potential cloud nuclei number shows little sensitivity to the ionisation rate, while a variation of the sulphuric acid formation rate induces a shift of the aerosol size distribution. However, growth of the secondary accumulation mode both in size and in number is limited by pronounced coagulational interaction with the activated sea salt mode. As a feedback the accumulation mode is only imperfectly separated from the nucleation and condensation modes. The exchange between the in-cloud and the below cloud area is intensive enough for the aerosol to present similar characteristics in the entire boundary layer, except that underneath the cloud the absence of an immediate repulsing cloud droplet mode involves a less profound separation gap to the accumulation mode. Hoppel et al. (1994) find both qualitatively and quantitatively similar aerosol distributions under clear marine conditions. They put forward that the in-cloud critical activation radius, the droplet number, as well as the cloud interstitial aerosol population might be inferred from ground observations, which is confirmed by the findings of this study.

Feingold et al. (1996) report that the typical stratocumulus in-cloud residence time of an aerosol particle is about 12 minutes. Within the present turbulent diffusion model the typical residence time may be deduced from the gross uni-directional particle flux. For a turbulent diffusion constant of approximately 60 m^2s^{-1} and a vertical cloud height of typically 250 m the typical residence time is thus $\tau \approx 250^2/60 \approx 1000~s$, or approximately 18 minutes, which because of the typical cloud height variability is quite comparable. Feingold et al. (1996) investigate the coalescence effectiveness of the cloud droplet population and find that the total cloud droplet number under typical stratocumulus conditions is reduced by around 60% percent within three hours in the absence of a cloud nuclei source. The present modelling results are consistent with these findings as the reduction effectiveness is estimated to be approximately 40% in three hours. The coalescence effectiveness reduces the tenfold increase of the potential cloud nuclei number as a result of a doubling of the sulphuric acid formation rate to 20 to 100%, depending on the turbulent state of the atmosphere.

Turbulent uplift determines both the number of activated particles and the precipitation effectiveness of the stratocumulus cloud. In the absence of advected background aerosol, the

typical cloud droplet number is found to vary typically between around 20 particles per cubic centimetre when the secondary particle reservoir is empty and around 40 particles, depending on the sulphate yield. When updraft is intensive the critical activation radius is lowered and a large number of non-activated particles is transported from below the cloud inside the saturated area. The enhanced exchange flux reduces the effective cloud residence time of the aerosol particles, so that cloud processing of these becomes less pronounced. Consequently, the cloud droplet number is increased while their size solute content spectrum resembles the one of freshly activated particles, for which the model assumption is that their mean size is independent of their solute content.

Precipitation effectiveness is both a function of boundary layer dynamics and the potential cloud condensation nuclei number (Albrecht, 1989). As updraft in relationship with a stratocumulus topped boundary layer typically increases at night-time when longwave cooling at cloud top is more effective, nocturnal stratocumuli present an enhanced tendency to produce precipitation. The modelled ground drizzle rate varies from 0.1 to 0.4 millimetres per day. These rates are in agreement with observations of vanZanten et al. (2005) who find the nocturnal drizzle rates to vary between zero and 0.6 millimetres per day. Consistently with the usual hypotheses pertaining the second aerosol indirect effect (Twomey, 1991), the precipitation formation is modelled to be inversely correlated with the cloud droplet number. The modelled relative variation of the precipitation flux just above sea surface reaches 20% following a doubling of the condensable yield. A comparison of the autoconversion and the accretion rate sensitivity shows that autoconversion is the triggering element while the accretion rate tends to have a compensating effect. The autoconversion effectiveness is inversely correlated with the particle number as particles need more time to reach raindrop size through coalescence. On the other hand the accretion rate increases with increasing droplet number as the cloud liquid water increases through effective precipitation suppression.

As the present model does not consider the interaction of the cloud droplet number and cloud radiative properties, the cloud dynamical incidence of secondary particles is found to be moderate. This result is in accordance with the model study of Jiang and Feingold (2006), showing that the correlation between the droplet number and cloud dynamics as given by the liquid water path and the cloud layer depth is limited and equivocal when the radiative properties are not included. In default of cloud optical properties the incidence of the droplet number on cloud dynamics takes place via their incidence on precipitation formation, the

cloud water content, latent heat release, and the subsequent variation of atmospheric dynamics.

The evaluated cloud albedo of 0.45 to 0.55, as well as the cloud liquid water content, are consistent with typical stratocumulus observations and model results (e.g. Ackerman et al., 1995, their Figures 5 and 3, respectively). The sensitivity of cloud optical properties to the droplet number is stressed by the up to 10% difference of the cloud albedo upon a doubling of the sulphuric acid formation rate. The modelled diurnal variability, however, is conditioned by the pertinence of the simulated droplet number and variability. The diurnal variability of the albedo is only partially relevant, as a substantial part of it takes place during night-time.

Sea salt particle emission was assessed with the parametrizations of Monahan et al.(1986) and Clarke et al. (2006). The latter study implies that particle emission in the sea salt specific size range (>0.1 µm) is approximately half an order of magnitude more effective, and that Aitken particles are emitted down to a dry size of 10 nanometres. While the parametrization of Clarke et al. (2006) produces a higher number of potential cloud condensation nuclei, the amount of secondary particles is reduced as the condensation sink of the primary mode is higher. Sea salt particles are shown to ensure a basic amount of cloud condensation nuclei, involving a minimum cloud droplet number specific to the cloud dynamical state of the atmosphere. For surface wind conditions of around 9 m s^{-1} the Monahan et al. (1986) basic cloud droplet number is 12 to 14 particles per cubic centimetre, while Clarke et al. (2006) yields 16 to 18 droplets. These amounts are consistent with the findings reported by Yoon and Brimblecombe (2002).

The parametrisation of sulphuric acid formation used in this study relies on model results of Clarke et al. (1998). They assume the tropical daily release of dimethylsulphide off the South American Pacific to be approximately 5.7 µmol m^{-2}. This figure is consistent with Bates et al. (1987a) who estimated the typical tropical North Pacific dimethylsulphide flux to be 4.5 µmol m^{-2} d^{-1}. Clarke et al. (1998) assumed that the conversion efficiency factor of dimethylsulphide to sulphur dioxide is 0.7, which is within the usual range but superior to recent estimates of de Bruyn et al. (2002) who found figures of 20 to 40%. A lower conversion efficiency would decrease the atmospheric sulphate yield. The parametrization used in this study implies a daily sulphate formation of approximately 0.45 nmol m^{-3}. Assuming a boundary layer thickness of 1300 m (Clarke et al., 1998) the combined oceanic and anthropogenic sulphur sources would thus yield a non sea salt sulphate production of approximately 0.6 µmol m^{-2} d^{-1}, implying that

the local apparent dimethylsulphide to non sea salt sulphate conversion efficiency is 10.5%. Under relatively pristine conditions the fraction of non sea salt sulphate having a marine origin is about 50% (Gondwe et al., 2003), so that a doubling of the sulphuric acid yield corresponds to a quadrupling of dimethylsulphide flux. The diagnosed variability of 2 to 15 cloud droplets per cubic centimetre, depending on the atmospheric boundary layer turbulent properties and the state of the secondary particle reservoir, would thus entail a relative slope of the cloud droplet number with dimethylsulphide emission of 0.0015 to 0.01, approximately, using 1 μmol DMS m^{-2} d^{-1} and 100 particles cm^{-3} as scaling values. The equivalent potential cloud condensation number slope is approximately 0.11 assuming that the cloud nuclei increases from 50 to 200 nuclei per cubic centimetre. This figure is close to the one of Yoon and Brimblecombe (2002) who find a relative slope of 0.07. Their study considers particle entrainment from the free troposphere, sea salt emission, and integrates a moment based secondary aerosol growth scheme as well as semi-explicit atmospheric chemistry concerning sulphuric acid. Marine boundary layer free troposphere exchange is not considered in this model study, as the secondary particle yield in the modelled part of the free troposphere is relatively low, and turbulent transport through the temperature inversion front is switched of to elude inappropriate losses. Aerosol transport from the free troposphere is qualitatively equivalent to the emission of sea salt particles at the ocean surface. It should therefore have no supplementary incidence on secondary aerosol growth dynamics as far as it is likely to enforce the effect of sea salt particles. Sea salt tends to reduce the sensitivity of the cloud droplet number to marine dimethylsulphide emission via its positive correlation with the critical activation radius and the scavenging effect of secondary particles. The assessment of the sensitivity slope is substantially biased in this study by the estimation of the fraction of marine non sea salt sulphate.

In this study aerosol dynamics are decoupled from atmospheric chemistry. The sulphuric acid source function is parametrized as an explicit time function, which supposedly renders the photolytic variability. This assumption is appropriate as far as the sulphate yield is not a function of its own momentary concentration. As sulphuric acid is a chemically stable terminal product this condition is fulfilled. However, as sulphate aerosols modify the radiative properties of the atmosphere, there is a potential photolytic interaction between the sulphuric acid yield, secondary aerosol formation and activation, and cloud dynamics (Feingold and Kreidenweis, 2002). Koch et al. (2003) find that the global atmospheric sulphate burden

should be anticorrelated with the cloud amount because photolytic sulphate formation is reduced blow the cloud cover. This negative effect, as well as the wet phase and photolytic sulphuric acid production enhancement inside the cloud layer are not respected in the present aerosol-cloud interaction model. As the absence of a notable sensitivity of the aerosol potential cloud nuclei number with the ambient ionisation rate is inherent to aerosol growth dynamics, the decoupling of the sulphur yield from aerosol and cloud dynamics has no influence on this feature. The decoupling of atmospheric chemistry and radiation, and especially the underscoring of in-cloud sulphate production might have a notable incidence on the sensitivity of the cloud droplet number to the sulphuric acid yield. Yet, sensitivity tests with a differential in-cloud and below cloud sulphuric acid source function show no change of aerosol growth dynamical characteristics, although the area of relevant secondary particle nucleation is extended from underneath to predominantly within the cloud.

VI.3 Conclusion

The present model study aims at investigating the secondary aerosol growth and aerosol-cloud interaction dynamics in relationship with the indirect sun-cloud-climate hypotheses of Marsh and Svensmark (2000), and Larsen (2005). It is subject to a certain number of key assumptions and simplifications:

1) Ion-induced nucleation is the dominating process of secondary aerosol formation in the marine boundary layer.

2) All secondary species within the aerosol liquid phase may be chemically associated with sulphuric acid.

3) Atmospheric chemistry is decoupled from the aerosol.

4) Cloud specific formation of sulphuric acid may be neglected.

5) The contribution of free troposphere aerosols to the cloud droplet number is not taken into account.

6) The interaction of cloud microphysics, atmospheric radiation and cloud dynamics is not allowed for.

In the absence of uncontroversial empirical evidence, the first assumption is intended to maximize the solar sensitivity of marine stratocumulus properties. Assumptions 2) to 6) are useful simplifications to restrict the complexity of the phenomena to a virtual level that may be tackled computationally. Within the limits of these simplifications the modelling results suggest the following main observations:

1) The total number of secondary particles is a function of the atmospheric ionisation rate.

2) The potential cloud condensation number tends to be indifferent to a variation of the ionisation rate due to the pronounced aerosol growth dynamical convergence property.

3) There is a substantial sensitivity of the potential cloud condensation number to the sulphuric acid yield.

4) The correlation of the cloud droplet number and the sulphuric acid yield is a complex function of aerosol spectral properties and the updraft within the cloud.

5) The characteristic time interval for the secondary aerosol to reach pseudo-stable conditions is about two days. As aerosol-cloud interaction is relatively fast the cloud dynamical

characteristic interval is similar.

6) Sea salt particles contribute considerably to the cloud droplet number under pristine conditions.

7) The thermodynamic effect of the cloud droplet number on cloud dynamics via modification of the amount of condensed water is secondary.

8) The efficiency of precipitation formation may be considerably influenced by the secondary aerosol.

9) The total secondary aerosol condensable yield may considerably affect cloud optical properties.

As a consequence the present study found no support for a link between the solar cycle and tropospheric cloudiness via ion nucleation as an effective process of secondary particle formation according to the hypothesis of Marsh and Svensmark (2000). However, a considerable potential of atmospheric sulphuric acid to influence marine cloud properties is revealed. The alternative formulation that atmospheric ionisation may directly interfere with aerosol activation (Kirkby, 2000) that by-passes aerosol formation and growth dynamics, remains untouched. The results were shown to be robust with regard to the simplifications 2) to 4). Aerosols originating from the free troposphere should have no qualitative incidence on the dynamics of aerosol cloud interaction, as their path of influence is formally similar to the one of sea salt particles. Yet, they should have quantitative repercussions on the relationship between the cloud droplet number and the sulphuric acid yield. The negligence of cloud radiative properties should not affect the ionisation rate sensitivity as it predominantly relies on aerosol mechanical properties. However, the interaction of cloud microphysics and dynamics should have an influence on the relationship between the sulphuric acid yield and the cloud droplet number. Further investigations are required to allow for a realistic representation of the cloud radiative properties.

VII. Appendices

VII.1 Appendix 1: assessment of the species' activities

VII.1.1 The Gibbs-Duhem Equation

Let $\overline{G_i}$ be the variation of the Gibbs free energy of a system with the number of molecules n of species i, it is (Robinson and Stokes, 1959):

$$\overline{G_i} \equiv \frac{\partial G}{\partial n_i} \equiv \mu_i,$$

f VII.1

where μ_i is the chemical potential of species i, and G is the Gibbs Free Energy of the system. The total derivative of the Gibbs free energy is:

$$dG = \sum_i \mu_i \, dn_i.$$

f VII.2

The integration of the previous expression yields:

$$G = \sum_i \mu_i n_i.$$

f VII.3

The differentiation of the preceding equation leads to:

$$dG = \sum_i (\mu_i \, dn_i + n_i \, d\mu_i).$$

f VII.4

After comparison of Equations VII.2 and VII.4 , one obtains the generalized Gibbs-Duhem equation:

$$\sum_i n_i \, d\mu_i = 0.$$

f VII.5

The chemical potential of a species i in solution is defined by:

$$\mu_i = \mu_i^{\circ}\{Ac_i\} + kT \ln(Ac_i)$$

f VII.6 ,

where μ° is the reference chemical potential, k is the Boltzmann constant, T is the temperature and Ac_i is the activity of the species i in the solution. It should be noted that the unit of the activity depends on its base (i.e. either fractional or molal in this study), so that the numerical value of the reference chemical potential is also relative to the considered base. The activity is equal to unity, when the system is in the reference state.

The previous and Equation VII.5 yield the specific form of the Gibbs-Duhem equation to solutions (Robinson and Stokes, 1959):

$$\sum_i n_i \; d \ln Ac_i = 0$$

f VII.7

VII.1.2 Relationship between the molal and fractional activity

The activity of species in solution is often expressed on the molal scale, whilst phase transition involves mostly a consideration on the fractional scale in order to relate gas phase partial pressure to solute activity.

Let there be the stoichiometric equation of dissociation:

$$A_n C_m \Leftrightarrow n\,A + m\,C$$

f VII.8 ,
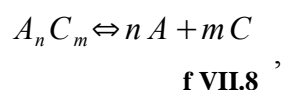
where A is the anion, C is the cation, and n and m are the number of anions and cations contained in one molecule prior to dissociation, respectively.

The activities on the molal and the fractional scales are introduced by:

$$a_C \equiv \gamma_C [C]$$
$$\alpha_C \equiv f_C\, \xi_C \; ,$$

f VII.9

where a_C is the molal activity of the cation, γ_C is the corresponding molal activity coefficient, $[C]$ is the molal concentration of the cation, α_C is its fractional activity, f_C is the fractional activity coefficient, and ξ_C is the fractional concentration of the cation given by:

$$\xi_C \equiv \frac{n_C}{n_{H_2O} + \sum n_i} \quad ,$$

f VII.10

where $\sum n_i$ stands for the mole number of the sum of the dissociated and the undissociated species in solution, and n_{H2O} is the mole number of the solvent (i.e. water).

The reference state specific chemical potential of the cation in solution is:

$$\mu_C = \mu_C^\circ\{a\} + kT \ln a_C$$
$$= \mu_C^\circ\{\alpha\} + kT \ln \alpha_C \quad .$$

f VII.11

The related equations of the anion are in analogy. It is important to note that the standard chemical potential of an isolated charged particle is different from its counterpart in a neutral solution. Here charge equilibrium is inferred. Thus, considering Equation VII.8 the chemical potential of the charged species in solution is defined by:

$$\mu_l = n \mu_A + m \mu_C$$

f VII.12

where μ_l is the chemical potential of the dissolved species.

Note that the following link between chemical potential of the solute and the gaseous species exists:

$$\mu_l^\circ = \mu_g^\circ + kT \ln p^\circ$$
$$\mu_g = \mu_g^\circ + kT \ln p \quad .$$

f VII.13

Comparing to Equation VII.11 under equilibrium $\mu_l = \mu_g$, one obtains:

$$\alpha = \frac{p}{p^\circ}$$
$$\mu_l^\circ = \mu^\circ\{\alpha\} \quad ,$$

f VII.14

where p^o is the partial pressure of the species over the pure liquid, and p is the partial pressure of the species over the liquid mixture.

Considering Equations VII.11 and VII.12 the relationship between the activities of the dissociated cation and anion and the activity of the species AC in solution is:

287

$$a = a_A^n a_C^m$$
$$\alpha = \alpha_A^n \alpha_C^m \quad .$$

f VII.15

After insertion of Equations VII.9 and VII.10 into the preceding set of equations one obtains (Robinson and Stokes, 1959):

$$a = \gamma_{AC}^{n+m} [A]^n [C]^m$$
$$\alpha = f_{AC}^{n+m} \frac{n_A^n n_C^m}{\left(n_{H_2O} + \sum n_i\right)^{n+m}} \quad .$$

f VII.16

Here the concept of the mean activity coefficient has been introduced. It is given by the following set of equations on both the molal and fractional scale:

$$\gamma_{AC} = \left(\gamma_A^n \gamma_C^m\right)^{1/(n+m)}$$
$$f_{AC} = \left(f_A^n f_C^m\right)^{1/(n+m)} \quad .$$

f VII.17

Using the preceding relationships, one may proceed to the determination of the link between the molal and the fractional scale based on the generalized formulation of the chemical potential given by Equation VII.11. First the case of a non-dissociating species, for which water as a solvent may serve as an example, will be analysed. When the ratio of the activity coefficients is analysed, Equation VII.11 yields:

$$\ln \frac{\gamma_{H_2O}}{f_{H_2O}} = \frac{\mu^\circ(\alpha) - \mu^\circ(a)}{kT} - \ln \frac{[H_2O]}{\dfrac{n_{H_2O}}{n_{H_2O} + \sum n_i}} \quad .$$

f VII.18

The first term on the right hand side may be determined considering that:
$$\sum n_i \rightarrow 0 \quad \Rightarrow \quad (\gamma \rightarrow 1) \wedge (f \rightarrow 1)$$

f VII.19 $\quad .$

When there is no interaction of the solvent and the solute, both the fractional and the molal activity coefficient of the solvent tend to unity. Thus one finds:

288

$$\frac{\mu^{\circ}\{\alpha\}-\mu^{\circ}\{a\}}{kT}=ln[H_2O]$$

<div align="center">

f VII.20

</div>

and (Robinson and Stokes, 1959):

$$\frac{\gamma_{H_2O}}{f_{H_2O}}=\frac{n_{H_2O}}{n_{H_2O}+\sum n_i}.$$

<div align="center">

f VII.21

</div>

Using Equations VII.9and VII.11 one finds for the dissociating species:

$$(n+m)ln\frac{\gamma_{AC}}{f_{AC}}=\frac{\mu^{\circ}\{\alpha\}-\mu^{\circ}\{a\}}{kT}-ln\left(\frac{[A]^n[C]^m}{\frac{n_A^n n_C^m}{(n_{H_2O}+\sum n_i)^{n+m}}}\right),$$

<div align="center">

f VII.22

</div>

using the relationship VII.19 for the dissociating species:

$$\frac{\mu^{\circ}\{\alpha\}-\mu^{\circ}\{a\}}{kT}=\lim_{n_{AC}\to 0}\left(ln\frac{n_A^n n_C^m}{n_A^n n_C^m}-ln\frac{n_{H_2O}^{(n+m)}}{M_{H_2O}^{(n+m)}}\right)$$
$$=-(n+m)ln[H_2O]$$

<div align="center">

f VII.23

</div>

And thus (Robinson and Stokes, 1959):

$$\frac{\gamma_{AC}}{f_{AC}}=\frac{n_{H_2O}}{n_{H_2O}+\sum n_i}.$$

<div align="center">

f VII.24

</div>

Comparing VII.21 and VII.24, one finds that the equations of the dissociating and the non-dissociating case are identical.

VII.1.3 Evaluation of the bulk activity coefficients

The classical nucleation theory assumes that ultrafine particles and clusters have bulk thermodynamic properties. Further it is assumed here that secondary aerosol particle solution is a mixture of sulphuric acid as hygroscopic solute and water as solvent. As a consequence,

the activity of water in solution is a function of the activities of sulphuric acid and its dissociation products. The particle charge bearing ion is chemically associated to sulphuric acid.

Nucleation theory involves the fractional mass (see above), while the activity of a species in solution is usually expressed on the molal base in relationship with electrolyte solutions. These two expressions are linked by:

$$[B] = (X_B^{-1} - 1)^{-1} \, m_B^{-1}$$

f VII.25 ,

where *[B]* is the molal concentration of the species *B*, X_B is the corresponding mass fraction, and m_B is the molecular mass.

The relationship between the mass fraction X_B and the mole fraction ξ_B is as follows:

$$X_B = \left((\xi_B^{-1} - 1) \frac{m_A}{m_B} + 1 \right)^{-1}.$$

f VII.26

Consistently the link between the molal concentration and the mole fraction is:

$$[H_2SO_4] = (\xi_B^{-1} - 1)^{-1} m_A^{-1}.$$

f VII.27

The binary system of sulphuric acid in aqueous solution is governed by the following equations (e.g. Clegg et al., 1994):

$$(1) \quad K_1 = \frac{\gamma_H \gamma_{HSO_4} \, [H^+] \, [HSO_4^-]}{\gamma_{H_2SO_4} \, [H_2SO_4]}$$

$$(2) \quad K_2 = \frac{\gamma_H \gamma_{SO_4} \, [H^+] \, [SO_4^{2-}]}{\gamma_{HSO_4} \, [HSO_4^-]}$$

$$(3) \quad [H_2SO_4]_t = [H_2SO_4] + [HSO_4^-] + [SO_4^{2-}]$$

$$(4) \quad [H^+] = [HSO_4^-] + 2[SO_4^{2-}] + [OH^-] \quad ,$$

$$(5) \quad \gamma_{AC}^3 \equiv \frac{\gamma_H^2 \gamma_{SO_4} \, [H^+]^2 \, [SO_4^{2-}]}{4 \, [H_2SO_4]_t^3}$$

$$(6) \quad \beta \equiv \frac{[SO_4^{2-}]}{[H_2SO_4]_t}$$

f VII.28

where K_1 and K_2 are the first and the second dissociation constants of sulphuric acid, respectively, γ_i is the respective molal activity coefficient, γ_{AC} is the mean molal activity coefficient of sulphuric acid given by definition, $[H_2SO_4]_t$ is the total molal concentration of sulphuric acid in solution, and β is the degree of secondary *dissociation* of sulphuric acid.

In addition the following approximations are appropriate:

$$(7)\ \ [OH^-] \simeq 0$$
$$(8)\ \ [H_2SO_4] \simeq 0\ .$$

f VII.29

The assumptions (7) and (8) are to be used in relationship with the mass balance Equation (3) and the ionic equilibrium Equation (4). Equations (7) and (8) are related to the strong acid property of sulphuric acid.

By multiplication of Equations (1) and (2), one finds:

$$K_1 K_2 = \frac{\gamma_H^2 \gamma_{SO_4} [H^+]^2 [SO_4^{2-}]}{\gamma_{H_2SO_4} [H_2SO_4]}\ .$$

f VII.30

Inserting Equation (5) into the preceding:

$$\gamma_{H_2SO_4} [H_2SO_4] = \frac{4 \gamma_{AC}^3 [H_2SO_4]_t^3}{K_1 K_2}\ .$$

f VII.31

Equation (6) and the combination of Equations (6), (3) and (4) yield, respectively:

$$[SO_4^{2-}] = \beta\ [H_2SO_4]_t$$
$$[HSO_4^-] = (1-\beta)\ [H_2SO_4]_t$$
$$[H^+] = (1+\beta)\ [H_2SO_4]_t\ .$$

f VII.32

Equation (5) leads to:

$$\gamma_H^2 \gamma_{SO_4} = \frac{4 \gamma_{AC}^3 [H_2SO_4]_t^3}{[H^+]^2 [SO_4^{2-}]}\ .$$

f VII.33

Equation (2) gives:

$$\frac{\gamma_H \gamma_{SO_4}}{\gamma_{HSO_4}} = \frac{K_2}{K_2^*} \quad ,$$

f VII.34

where K_2^* is the dissociation product:

$$K_2^* = \frac{[H^+][SO_4^{2-}]}{[HSO_4^-]} \quad .$$

f VII.35

Finally the combination of Equations VII.33 and VII.34 yields:

$$\gamma_H \gamma_{HSO_4} = \frac{4\gamma_{AC}^3 [H_2SO_4]_t^3}{K_2 \ [HSO_4^-] \ [H^+]} \quad .$$

f VII.36

With Equations VII.31 to VII.36 the unknowns of the aqueous sulphuric acid system may be expressed as a function of the second and the first dissociation constants, the degree of dissociation, the mean activity coefficient and the total molal concentration of sulphuric acid.

As to Equation VII.31, both the molar concentration of non-dissociated sulphuric acid and its activity coefficient are unknowns. However, provided that appropriate formulations of the second, and especially the first dissociation constant are at hand, the activity may be directly determined. Multiplying by the inverse molar mass of water, Equation VII.24 becomes:

$$f_{H_2SO_4} = \gamma_{H_2SO_4} \frac{[H_2O] + \sum [B_i]}{[H_2O]} \quad .$$

f VII.37

This equation is integrated into Equation VII.16 along with Equation VII.31. One finds for the fractional activity of sulphuric acid:

$$\alpha_{H_2SO_4} = \gamma_{H_2SO_4} \frac{[H_2SO_4]}{[H_2O]}$$
$$= \frac{4\gamma_{AC}^3 \ [H_2SO_4]_t^3 \ m_{H_2O}}{K_1 K_2} \quad .$$

f VII.38

The Henry constant H of sulphuric acid on the molal base is defined as follows:

$$H_{H_2SO_4} = \frac{a_{H_2SO_4}}{p_{H_2SO_4}} \quad .$$

<div align="center">

f VII.39

</div>

Note that in the preceding expression $p_{H_2SO_4}$ is usually expressed in terms of the absolute vapour pressure [Pa] at standard ambient pressure.

The preceding equation along with Equation VII.38 leads to the following relationship:

$$K_1 = \frac{4\gamma_{AC}^3 \, [H_2SO_4]_t^3}{H_{H_2SO_4} \, p_{H_2SO_4} \, K_2} \quad .$$

<div align="center">

f VII.40

</div>

As the Henry constant itself is an unknown, it would be helpful to reduce this expression to the limiting case of a pure substance. Equations VII.38 and VII.9 allow replacing the molal through the fractional activity, which along with Equation VII.14 leads to:

$$H_{H_2SO_4} = \frac{[H_2O]}{p_{H_2SO_4}^{\circ}} \quad .$$

<div align="center">

f VII.41

</div>

According to Ayers (1980) the saturation pressure of sulphuric acid in aqueous solution was experimentally found to be:

$$\begin{aligned} p_{H_2SO_4} &= p_{atm} \exp\left(-\frac{\Delta_r^{\circ} G}{RT}\right) \cdot \alpha_{H_2SO_4} \\ &= p_{atm} \exp\left(-\frac{(1.0156 \cdot 10^4 \pm 1.75 \cdot 10^2)}{T} + (16.259 \pm 0.437) + \frac{\Delta\mu}{RT}\right) \quad . \end{aligned}$$

<div align="center">

f VII.42

</div>

The relation between the variation of the chemical potential upon dissolution into the binary liquid phase and the activity of sulphuric acid in solution follows from Equations VII.13. $\Delta_r^{\circ} G$ is the Gibbs free energy of vaporization at standard temperature and pressure conditions. Gmitro and Vermeulen (1964) have estimated the Henry constant of sulphuric acid to be equal to $1.16 \cdot 10^3$ mol kg^{-1} Pa^{-1} from thermodynamic data of diverse origin. However, the use of the preceding equation leads to a Henry constant that is in between $2.55 \cdot 10^4$ and $3.44 \cdot 10^4$. These figures are well below the value of Gmitro and Vermeulen (1964). As they are derived from direct measurements of the saturation pressure on the one hand, and as Marti et al. (1997) found his experimental data to be much more conform with the data of Ayers (1980) on the other hand, the mean value of the preceding interval is retained here.

As the enthalpy of dissociation of sulphuric acid is not known, an appropriate method to

estimate the variation of the dissociation constant with temperature may be:

$$K_{1,\alpha}(T) = K_{1,\alpha}(T^\circ) - \frac{\ln(K^\circ_{1,\alpha})}{T^\circ} K^\circ_{1,\alpha}(T - T^\circ)$$

f VII.43

The preceding relationship corresponds to the first term of the Taylor expansion of the Gibbs free energy equation at equilibrium.

Note that:

$$K_{1,\alpha} = \frac{K_1}{[H_2O]}$$

f VII.44

is the dissociation constant on the fractional base.

The second dissociation constant is given as a temperature function by Clegg et al. (1994):

$$\log_{10}(K_2) = 562.69486 - 102.5154\,log_e(T) - 1.117033 \cdot 10^{-4}\,T^2 \\ + 0.2477538\,T - 13273.75\,T^{-1}$$

f VII.45

Note that T is the absolute temperature.

The activity of water is assessed according to the Gibbs-Duhem Equation along with Equations VII.32, VII.34 and VII.36:

$$\begin{aligned} dln\,a_{H_2O} &= -\frac{[H_2SO_4]_t}{[H_2O]}\,\left[(1+\beta)\,dln\,a_H + (1+\beta)\,dln\,a_{HSO_4} + \beta\,dln\,a_{SO_4}\right] \\ &= -\frac{[H_2SO_4]_t}{[H_2O]}\,\left[dln\,a_H\,a_{HSO_4} + \beta\,dln\,\frac{a_H\,a_{SO_4}}{a_{HSO_4}}\right] \\ &= -\frac{[H_2SO_4]_t}{[H_2O]}\,\left[dln\,\frac{4\,\gamma^3_{AC}[H_2SO_4]^3_t}{K_2} + \beta\,dln\,K_2\right] \\ &= -\frac{3}{[H_2O]}\,\left([H_2SO_4]_t\,d\ln\gamma_{AC} + d[H_2SO_4]_t\right) \end{aligned}$$

f VII.46

The lower integration limit is given by:

$$[H_2SO_4]_t \to 0 \quad \Rightarrow \quad a_H \to m^{-1}_{H_2O}$$

f VII.47

Equation VII.46 may be integrated numerically knowing the dependency of the mean activity coefficient and of the degree of dissociation on the total molal concentration of sulphuric acid. The fractional activity coefficient of water is according to Equation VII.21:

294

$$f_{H_2O} = \gamma_{H_2O} \left(1 + m_{H_2O} \sum [B_i]\right)$$

f VII.48 ,

which implies that the fractional activity of the solute, or water in particular is:

$$\alpha_{H_2O} = \gamma_{H_2O}$$

f VII.49 .

VII.2 Appendix 2: Empirical interpolation formulas

VII.2.1 The density of aqueous sulphuric acid as a function of composition and temperature

A polynomial relationship of the density of the sulphuric acid solution as a function of temperature and solution strength is built for the data provided by UIO (1998, see Figure VII.1).

At first linear fits were made of the density as a function temperature at fixed composition. The obtained coefficients were then interpolated to obtain a polynomial fitting function as a function of composition. Thus the following formula is reached:

$$
\begin{aligned}
\rho = & (1.4932708930115796\mathrm{e}{+}01\, X^5 - 2.7874520003993560\mathrm{e}{+}01\, X^4 + 1.5048589724162971\mathrm{e}{+}01\, X^3)\, T \\
& + (1.3144863826183728\mathrm{e}{-}01\, X^2 - 2.7454710519533134\mathrm{e}{+}00\, X - 1.0818442472672002\mathrm{e}{-}01)\, T \\
& - 5.8591758476482109\mathrm{e}{+}03\, X^5 + 1.1078087922652052\mathrm{e}{+}04\, X^4 - 6.2373548145382965\mathrm{e}{+}03\, X^3 \\
& + 6.9518810733530461\mathrm{e}{+}02\, X^2 + 1.4184247153159934\mathrm{e}{+}03\, X + 1.0299754819387153\mathrm{e}{+}03
\end{aligned}
$$

.

f VII.50

The formula is valid for the following temperature and mass fraction range:

$$
\begin{aligned}
& 0 \le X \le 0.765 \\
& 273 \le T\,(0 \le X < 0.123) \le 300 \\
& 262 \le T\,(0.123 \le X < 0.291) \le 300 \\
& 241 \le T\,(0.291 \le X < 0.585) \le 300 \\
& 235 \le T\,(0.585 \le X \le 0.765) \le 300
\end{aligned}
$$

.

f VII.51

The parametrization entails a linear function of the solution density as a function of temperature, while the observed values show a slight undulation (see Figure VII.2). This effect should result from the uncertainty of the measurements and therefore be an artefact.
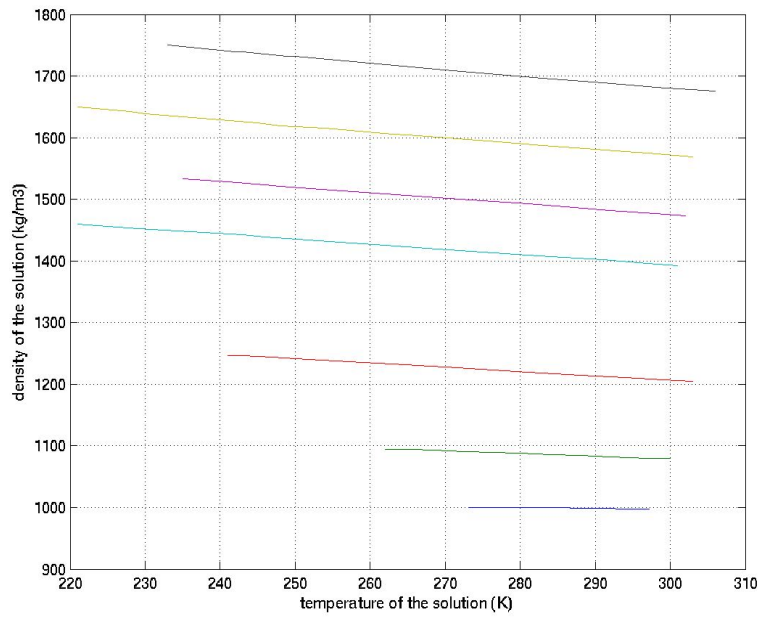
Figure VII.1: Density of the aqueous sulphuric acid solution as a function of temperature, for certain sulphuric acid mass fractions (UIO, 1998).
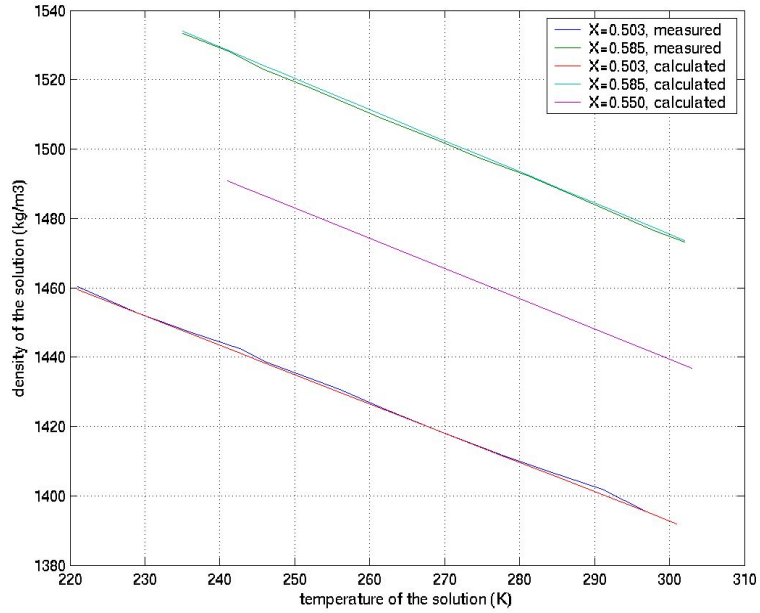
Figure VII.2: Comparison of parametrized to observed values at certain mass fractions of sulphuric acid. Note the undulating shape of the observed values

297

VII.2.2 The dissociation properties of aqueous sulphuric acid

2.2.1 The mean activity coefficient

The mean activity coefficient of sulphuric acid is defined by Equation VII.28(5). Rather than determining this value explicitly according to the formalism of Pitzer (1981), it seems preferential to find a polynomial interpolation formula using the evaluation data given by Clegg and Brimblecombe (1995), which is based on the Pitzer (1981) formalism.
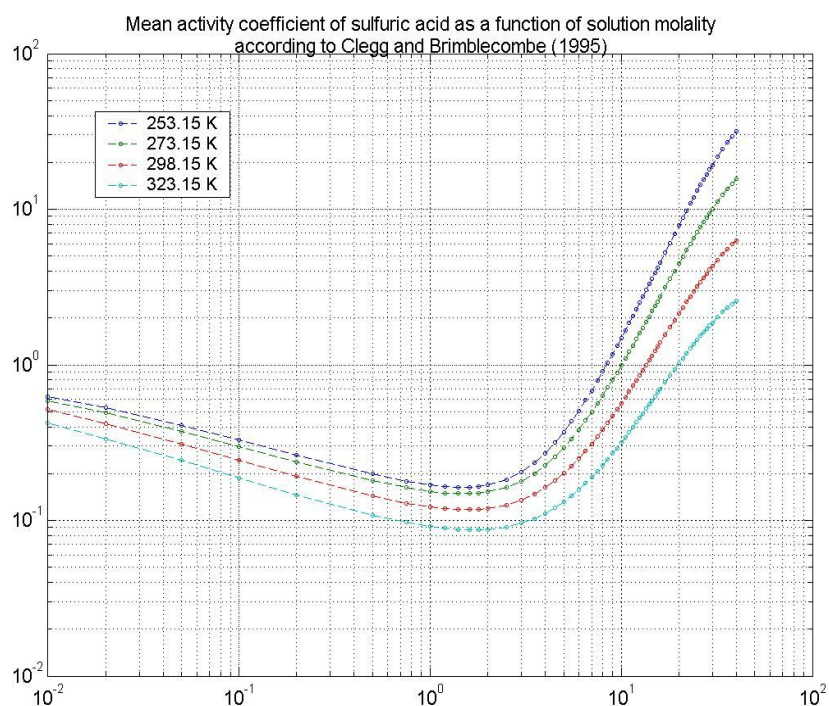
Figure VII.3: Molal mean activity coefficient of sulphuric acid (-) as a function of the solution molal concentration (mol/kg) for certain temperatures typical to atmospheric conditions (Clegg and Brimblecombe,1995).

In order to obtain both a reasonable number of equations and accurate results, the concentration range has been split into three parts.

The equation for $10^{-2} \leq [H_2SO_4]_t \leq 1.2$ is:

$$\ln(\gamma_{AC}) = T^{-2} \sum_{i=1}^{n=9} A_i \cdot Y^{n-i} + T^{-1} \sum_{i=1}^{n=9} B_i \cdot Y^{n-i} + \sum_{i=1}^{n=9} C_i \cdot Y^{n-i}$$

$$A = \begin{vmatrix} 5.6288019961495331e+004 \\ 3.9052014899159555e+005 \\ 1.0873660620228876e+006 \\ 1.5743283416150671e+006 \\ 1.3120346599944588e+006 \\ 6.6101396822438471e+005 \\ 1.3993006557187947e+005 \\ -1.5563586244333425e+005 \\ -6.8468393126269279e+005 \end{vmatrix}, B = \begin{vmatrix} -3.3571117154696367e+002 \\ -2.3055604696492569e+003 \\ -6.3345584460968394e+003 \\ -9.0192014797978863e+003 \\ -7.4044031476406381e+003 \\ -3.7160964181383961e+003 \\ -7.7745004223432863e+002 \\ 1.1388787840797538e+003 \\ 5.5424935518060283e+003 \end{vmatrix}, C = \begin{vmatrix} 4.4363376089820072e-001 \\ 3.0063529636101753e+000 \\ 8.1453417463986852e+000 \\ 1.1502079237912083e+001 \\ 9.6663680499492290e+000 \\ 5.4236755379381139e+000 \\ 1.7000485349764918e+000 \\ -2.4398652703191548e+000 \\ -1.2988230017240971e+001 \end{vmatrix}$$

f VII.52

For the interval $1.2 \leq [H_2SO_4]_t \leq 6$ the interpolation polynomial is the following:

$$\ln(\gamma_{AC}) = T^{-2} \sum_{i=1}^{n=11} A_i \cdot Y^{n-i} + T^{-1} \sum_{i=1}^{n=11} B_i \cdot Y^{n-i} + \sum_{i=1}^{n=11} C_i \cdot Y^{n-i}$$

$$A = \begin{vmatrix} -8.0725892694281111e+009 \\ 3.5960953564391151e+010 \\ -6.9769086852012833e+010 \\ 7.7357891167914658e+010 \\ -5.4057965794118996e+010 \\ 2.4752463033652279e+010 \\ -7.4735828606967907e+009 \\ 1.4571970673054152e+009 \\ -1.7346556296884415e+008 \\ 1.1064505663851449e+007 \\ -9.7903513087576185e+005 \end{vmatrix}, B = \begin{vmatrix} 5.5520317701469585e+007 \\ -2.4745835939745799e+008 \\ 4.8032229046058452e+008 \\ -5.3275581368196666e+008 \\ 3.7237122632648188e+008 \\ -1.7051195036708811e+008 \\ 5.1476345968852833e+007 \\ -1.0032119708734617e+007 \\ 1.1935482729269448e+006 \\ -7.5943824460918404e+004 \\ 7.5613169709306530e+003 \end{vmatrix}, C = \begin{vmatrix} -9.2908102226731629e+004 \\ 4.1451129116829642e+005 \\ -8.0529714965703501e+005 \\ 8.9389336623078201e+005 \\ -6.2517009086803405e+005 \\ 2.8639143237351230e+005 \\ -8.6477380800203988e+004 \\ 1.6851404167475732e+004 \\ -2.0033069841199717e+003 \\ 1.2678453137350425e+002 \\ -1.6366506271633163e+001 \end{vmatrix}$$

f VII.53

The third polynomial is valid for $6 \leq [H_2SO_4]_t \leq 40$:

$$\ln(\gamma_{AC}) = T^{-2} \sum_{i=1}^{n=9} A_i \cdot Y^{n-i} + T^{-1} \sum_{i=1}^{n=9} B_i \cdot Y^{n-i} + \sum_{i=1}^{n=9} C_i \cdot Y^{n-i}$$

$$A = \begin{vmatrix} -1.2146492453362845e+007 \\ 1.0537197831666107e+008 \\ -3.8842492773664516e+008 \\ 7.8880531329091012e+008 \\ -9.5465665309856772e+008 \\ 6.9294039719027436e+008 \\ -2.8580715040677375e+008 \\ 5.7290271930878215e+007 \\ -4.0835086455057841e+006 \end{vmatrix}, B = \begin{vmatrix} 9.1421230286990991e+004 \\ -8.0176851231196593e+005 \\ 3.0048333486820138e+006 \\ -6.2587282352723889e+006 \\ 7.8793673949993895e+006 \\ -6.0947930529288454e+006 \\ 2.8037846251125927e+006 \\ -6.9156341858340241e+005 \\ 7.4261624967097348e+004 \end{vmatrix}, C = \begin{vmatrix} -1.6950581205126008e+002 \\ 1.5004022482361534e+003 \\ -5.6983703361517973e+003 \\ 1.2100136111433607e+004 \\ -1.5669560815485111e+004 \\ 1.2635147608803540e+004 \\ -6.1800592620531479e+003 \\ 1.6707947764734586e+003 \\ -2.0441793140765128e+002 \end{vmatrix}$$

f VII.54

For the three preceding equations Y is defined as:

$$Y = \log_{10}([H_2SO_4]_t)$$

f VII.55

The interval of validity of the equations is:

$$10^{-2} \leq [H_2SO_4]_t \leq 40$$
$$253.15 \leq T \leq 323.15 \quad,$$

f VII.56

which is equivalent to the mass fraction range:

$$9.80 \cdot 10^{-4} \leq X \leq 0.796$$

f VII.57

The regression correlation coefficient is defined by:

$$c = \frac{\sum\limits_i^n (x_i - \bar{x})^2}{\sum\limits_i^n (\hat{x} - \bar{x})^2}$$

f VII.58

The mean relative error is given by:

$$\bar{r} = 1/n \sum\limits_i^n \frac{|\hat{x}_i - x_i|}{x_i}$$

f VII.59

Figure VII.3 shows the calculated data of Clegg and Brimblecombe (1995) according to the formalism of Pitzer (1992). The interpolated values are not shown because they are too close to the data to be distinguishable. It appears that the variability of the mean activity coefficient is high and increases with temperature. The correlation coefficients of Equations VII.52 to VII.54 are 0.9998, 1.0000 and 0.9999 respectively. As an example, the relative error of the extrapolated values at 273 K is shown in Figure VII.4. It appears that for small molal concentrations the relative error is one order of magnitude larger. The mean relative errors are 1.277e-3, 3.601e-4 and 4.926e-4 respectively. These figures indicate that the interpolations are accurate to the point that the mean relative error is close to the precision of the original data, which is 1e-4.
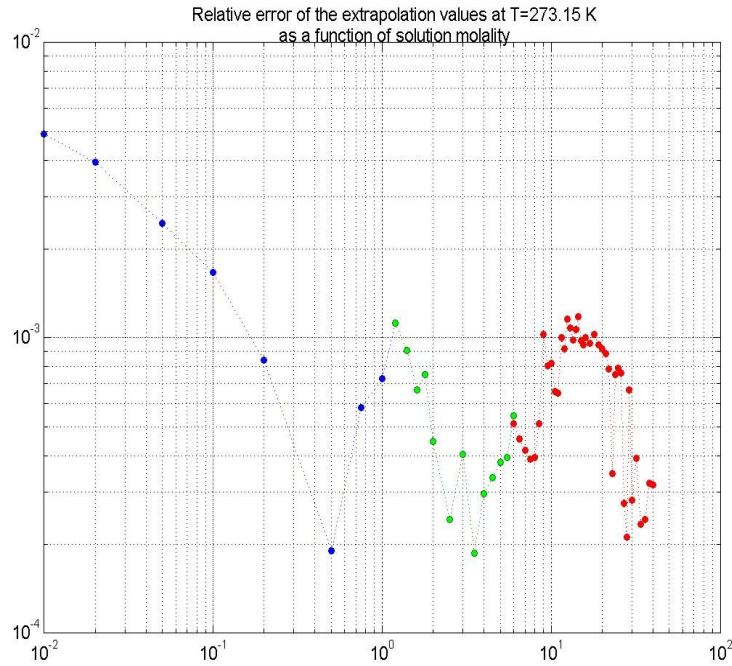
Figure VII.4: Relative error of the sulphuric acid mean molal activity coefficient parametrization when compared to the activity coefficient data of Clegg and Brimblecombe (1995) at 273.15 K.

2.2.2 The first dissociation constant of sulphuric acid K_1

The estimation of the first dissociation constant of sulphuric acid is is afflicted by a high degree of uncertainty due to its pronounced hygroscopic property. Unless the solution is very concentrated, sulphuric acid dissociation is almost complete. Nevertheless, it is attempted here to evaluate the first dissociation constant indirectly. Two estimations are obtained when Equation VII.40 is either combined to measurements of the sulphuric acid equilibrium partial pressure given by Marti (1997), or used in conjunction with Equation VII.42 and thermodynamic data on the variation of the chemical potential given by Giauque et al. (1960). The Henry constant is determined when Ayers' (1980) formula is applied to pure sulphuric acid. Figure VII.5 shows the results for both the data of Marti (1997), and of Giauque et al. (1960) and Ayers (1980). The dissociation constant appears to be a function of the solution concentration, which is obviously inaccurate and linked to the bias of the data.

Sulphuric acid partial pressure over diluted solutions is barely measurable, which should

explain the higher imprecision of Marti´s data (1997). The higher accuracy reached with the data of Giauque et al. (1960) and Ayers (1980) stresses the appropriateness of the approach to assess the activity of aqueous sulphuric acid rather from activity data than from direct measurements of the sulphuric acid partial pressure. The similar order of magnitude of the estimates of the first dissociation constant sustains the formal accuracy of both assessment methods. The mean estimation value resulting from the data of Giauque et al. (1960) will therefore serve as an approximation of the first dissociation constant at T=298 K within a certain confidence interval. The corresponding values are:

$$\widehat{K}_1(T=298.15\,K)=7.94\cdot10^9\,mol/kg$$
$$6\cdot10^9<K_1(T=298.15)<10^{10}\,mol/kg \quad .$$

f VII.60
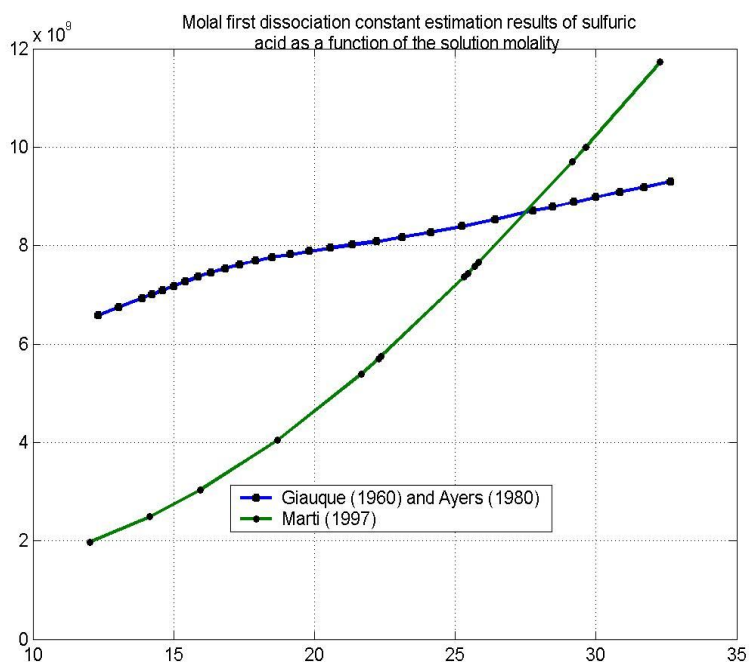
Figure VII.5: First molal dissociation constant of sulphuric acid (mol/kg) as assessed from the pressure data of Marti (1997) and from the thermodynamic and pure solution pressure data of Giauque et al. (1960) and Ayers (1980), respectively, as a function of the molal concentration of the solution (mol/kg).

VII.2.3 The saturation pressure of water

The saturation pressure of water vapour over a flat pure water body as a function of temperature may be interpolated using data given by Lide (2003). The following polynomial fitting function is obtained:

$$p_{sat}(H_2O) = 2.6026732015552300\text{e-}06 \; T^5 - 3.2622614877831973\text{e-}03 \; T^4 + 1.6487578187322884\text{e+}00 \; T^3$$
$$- 4.1966315066108518\text{e+}02 \; T^2 + 5.3756891891598621\text{e+}04 \; T - 2.7704893291280358\text{e+}06 \quad ,$$

f VII.61

which is valid for the following temperature range:

$$258.15 \leq T \leq 303.15$$

f VII.62 .

The correlation coefficient of the above fitting function with its underlying data is c=1.00000, the corresponding mean relative error is equal to 0.00000.

VII.2.4 Typical marine aerosol spectrum parametrization

Kondratyev (1999) provides the following lognormal parametrization scheme for aerosol spectra:

$$\frac{\partial N}{\partial \log r} = \sum_{i=1}^{3} \frac{N_i}{\sqrt{2\pi} \log \sigma_i} \exp\left(\frac{\left(\log(r/r_i)\right)^2}{2(\log \sigma_i)^2}\right) \quad ,$$

f VII.63

where N is the spectrally integrated aerosol particle number concentration, N_i is the total particle number within the respective spectral integration increment, r is particle radius, r_i is the integration increment mean particle radius and $\log \sigma_i$ is the increment specific standard deviation of the particle distribution.

Under typical marine conditions the parameters of the preceding expression take the following values (Kondratyev, 1999):

$$i = 1: N_i = 1.33 \cdot 10^8 \, m^{-3}, r_i = 39 \cdot 10^{-9} \, m, \log \sigma_i = 0.657$$
$$i = 2: N_i = 6.66 \cdot 10^7 \, m^{-3}, r_i = 133 \cdot 10^{-9} \, m, \log \sigma_i = 0.210$$
$$i = 3: N_i = 3.06 \cdot 10^6 \, m^{-3}, r_i = 290 \cdot 10^{-9} \, m, \log \sigma_i = 0.396$$

f VII.64

According to their respective size and total particle number concentration the integration increments 1 to 3 may be attributed to the secondary accumulation (=Aitken) mode, the sea salt (=accumulation) mode and the continental background aerosol (=dust) mode, respectively.

VIII. Conventions

VIII.1 Terminology

Nucleation

The terminology used in literature in relationship with ion nucleation appears to be somewhat equivocal. While most authors qualify *heterogeneous* nucleation as the secondary particle formation involving a passive, prerequisite element that lowers the saturation vapour pressure of the condensing species, in particular in relationship with aerosol particle activation as a cloud droplet, this concept is extended here to the context of ion nucleation that basically has the same effect. Consistently *homogeneous* nucleation refers to the absence of a third party that catalyses the formation process. These terms should not be confounded with the terms *heteromolecular* and *homomolecular* referring to the chemical nature of the condensing species, thus leading to unary, binary, etc. nucleation. Classical ion involving nucleation theory is addressed with the term *ion-induced* nucleation in opposition to the mechanical approach qualified by the term *ion-mediated* nucleation (Yu and Turco, 2001; Laakso et al., 2002). The generic term for the process of secondary particle formation involving ions is *ion nucleation*.

Ions

Charge bearing particles may be subdivided with increasing size into, *elementary* and single molecule ions, cluster ions (stable or unstable), and supracritical *intermediate* and *large* ions (c.f. Hõrrak et al., 1998; Arnold, 2006). For simplification reasons the term *(small) ion* refers indifferently to subcritical ions, either elementary or clusters, in this study. Intermediate ions are associated with *ultrafine particles* in the nucleation mode, while large ions refer to larger particles or *condensation nuclei*. Note that Arnold uses the term *intermediate* for unstable clusters in the size range between elementary ions and ultrafine particles.

Aerosol modes

For both growth dynamical and generic reasons, aerosol tend to gather in modes within the aerosol size spectrum. Consistently, these modes are qualified according to the interval of the aerosol size spectrum these modes are commonly situated in. Thus with ascending size one distinguishes (e.g. Seinfeld and Pandis, 1998) between the nucleation (1-10 nanometres), the Aitken (10-100 nanometres), the accumulation (100-1000 nanometres), and the coarse mode ($>10^3$ nanometres). Generically, the nucleation mode is related to freshly nucleated particles, and the Aitken mode may also contain a large fraction of secondary particles (Quinn et al., 2000). Sea salt is emitted predominantly to the accumulation mode when particle mass is considered, but may also be emitted to the Aitken mode (Clarke et al., 2006). Atmospheric dust is generally contained in both the coarse and the accumulation mode.

In the context of a study on marine aerosol growth dynamics, a distinction of the aerosol modes according to their growth dynamical properties seems more appropriate. Thus, the *nucleation mode* is related to recent nucleation exclusively. During night-time a residual, but relatively stable secondary particle mode may be observed, at about 10 nanometre size. This mode is designated as the *condensation mode*, as particles have mainly grown through this process. Larger secondary particles grow mainly through coagulation and tend to accumulate within a further separate mode of Aitken particle size, which is consistently designated as the *(secondary) accumulation mode*. Due to their predominantly larger size, sea salt particles form a distinct mode, which in accordance with its origin is called the *primary (particle) mode* in the framework of this study.

VIII.2 Constants and symbols

Units

In principle all formulas, graphs and particular values are related to SI-Units (kg, m, s, C, K), unless expressly specified differently.

Recurring pre-, sub- and superscripts

$\pm$	ion
$+$	positive ion
$-$	negative ion
$\circ$	at standard pressure and temperature, *p=1 atm*, *T=25°C*; pure substance in relationship with vapour pressure
*	critical
a	acid; air
a, b	chemical species indexes
acc	accretion
act	activated
att	attachment
auto	autoconversion
av	average
coag	coagulation
cond	condensation
e	relative to eddy in turbulent flow
eq	equilibrium
eva	evaporation
f	friction force; formation
g	gas phase, gravitation
i, j, k	aerosol solute bin indexes
l	liquid phase

l, m, q	aerosol charge bin indexes
m	molecule
max	maximum
min	minimum
nact	not activated
p	aerosol particle; particle interaction
r	reaction
s	sea salt
sat	saturation
sed	sedimentation
w	water
B	Brownian; molecular regime
C	cloud; cloud droplet
D	diffusion regime; diffusion
DP	diffusiophoresis
E	electrostatic collection; entrainment
G	turbulent gravitational
I	turbulent inertial
IP	impaction collection
IT	interception collection
K	Kolmogorov microscale
P	particle
R	rainwater; raindrop
T	transition regime; turbulent
TP	thermophoresis
V	water vapour
δ	small variation
Γ	turbulent shear
Δ	variation

Latin letter symbols

a	number of molecules of specie a [-]; acceleration [m s^{-2}]; albedo [-] activity on the molal base [mol kg^{-1}]
b	number of molecules of specie b [-]
c_p	bulk heat capacity at constant pressure [J kg^{-1}]
c_{rec}	ionic recombination coefficient [m^3 s^{-1}]
e	water vapour pressure [Pa]
f	activity coefficient on the fractional base [-]
g	acceleration through gravity [m s^{-2}]
h	height [m]
k	thermal conductivity [J K^{-1} m^{-1} s^{-1}]; Boltzmann constant, $k=1.3806503e\text{-}23\ J\ K^{-1}$
l	length [m]
m	molecular mass of the specie i [kg mol^{-1}]; number of dissociable cations per molecule [-]]
n	molecule number per particle; mole number of specie i [mol], number of dissociable anions per molecule [-]
n_{AV}	Avogadro constant, $n_{AV}=6.02214139e23\ mol^{-1}$
p	pressure [Pa], partial presuure [-]
p_{max}	collision impact parameter [m]
q	water content [kg m^{-3}]; elementary electric charge, $q=1.602189e\text{-}19\ C$
r	radius [m]; radial distance[m]
r_e	effective collection cross-section radius [m]
r_{max}	effective collision cross-section radius [m]
s	air water vapour supersaturation [-]
t	time [s]
v	velocity; mean velocity; drift velocity [m s^{-1}]
v_{ij}	relative velocity of particles i and j [m s^{-1}]
v_{St}	velocity of the Stokes flow field [m s^{-1}]
w	vertical velocity [m s^{-1}]
w_E	entrainment velocity [m s^{-1}]

A	anion, in stoichiometric equation [no unit]; attachment coefficient of ions onto aerosol particle [$m^3\ s^{-1}$]
B	chemical species, in stoichiometric equation [no unit]
Ac	activity on unspecified base [no unit]
C	cation, in stoichiometric equation [no unit], Cunningham slip flow correction factor [-]
D	diffusion coefficient [$m^2\ s^{-1}$]; second derivative of the relative Gibbs free formation energy divided by two [J]
E	evaporation rate [s^{-1}]; energy [J]; electrical field [$N\ C^{-1}$]; enhancement factor [-]
E_{cin}	cinetic energy [J]
E_{pot}	potential energy [J]
F	physical force [N]
G	Gibbs free formation energy [J]
H	enthalpy [$J\ kg^{-1}$]
J	source function [$m^{-3}\ s^{-1}$]
J_{ij}	binary nucleation flux through particle node ij [$m^{-3}\ s^{-1}$]
$J(i+1,j)\ /\ J(i-1,j)$	binary nucleation flux through particle node ij, directed onto node $i+1,j$ / from node $i-1,j$ [$m^{-3}\ s^{-1}$]
J_{tot}	binary nucleation rate [$m^{-3}\ s^{-1}$]
$(J_{tot})_\pm$	ion-induced binary nucleation rate [$m^{-3}\ s^{-1}$]
K	kernel [$m^3\ s^{-1}$]
K_i	i-th dissociation constant [$mol\ kg^{-1}$]
K^*_i	i-th dissociation product [$mol\ kg^{-1}$]
Kn	Knudsen number [-]
L	dipole moment [C m]; latent heat of evaporation [$J\ kg^{-1}$]
M	mass [kg]
N	total particle number concentration [m^{-3}]
N_i	number concentration of element i [m^{-3}]
P_{cc}	coalescence probability
P_{cs}	relative effective collision efficiency cross-section
P_{ct}	relative effective collection efficiency cross-section

P_{st}	sticking coefficient [no unit]
Q	water mixing ratio [-]
Pr	Prandtl number [-]
R	condensation rate [s^{-1}]; formation rate [$m^{-3}\ s^{-1}$]; ideal gas constant, $R=8.314472\ J\ kg^{-1}\ mol^{-1}$
Re_r	relative Reynolds number [-]
Re_{St}	Stokes number [-]
Re_{St}^{*}	critical Stokes number of particle impaction [-]
S	surface [m^2]
Sc	Schmidt number [-]
Sh	Sherwood number [-]
T	absolute temperature [K]
W	fraction of ocean surface covered by whitecap [-]
X_i	mass fraction of species i [-]
Z	Zeldovitch non-equilibrium factor [-]

Greek letter symbols

α	electric polarizability of a dipole [m^3]; fractional activity [-]
β	degree of chemical dissociation [-]
γ	molal activity coefficient
ε	dissipation rate of turbulent kinetic energy per unit mass of air [$m^2\ s^{-3}$]
ε_0	vacuum permittivity [$C^2\ N^{-1}\ m^{-2}$]
ε_r	relative permittivity or dielectric constant [-]
φ	growth angle of binary nucleation flux [-]
ϕ	flux directed onto element [s^{-1}]
η	dynamic viscosity [$kg\ m^{-1}\ s^{-1}$]
λ	mean free path [m]; characteristic length scale [m]
μ	reduced mass of two species [kg]; chemical potential [$J\ mol^{-1}$]
ν	cinematic viscosity of the air [$m^2\ s^{-1}$]
ξ_i	mole fraction of species i [-]

ρ	density [kg m^{-3}]
σ	surface tension [N m^{-1}]; mean effective molecular diffusion collision diameter [m]
τ	transition factor relative to the diffusion kernel [-]; characteristic lapse of time [s]; optical depth [-]
υ	special atomic molecular diffusion volume [m^3]
ψ	particle collision angle [-]
Δ	mean particle separation distance relative to the apsidal distance [m]
Δ′	mean particle separation distance relative to particle radii [m]
Γ	velocity gradient [s^{-1}]
Φ	flux related to unit volume [m^{-3} s^{-1}]
Θ_l	liquid water potential temperature [K]

IX. References

Ackerman, A.S., O.B. Toon, and P.V. Hobbs, 1995, *A Model for Particle Microphysics, Turbulent Mixing and Radiative Transfer in the Stratocumulus-Topped Marine Boundary Layer and Comparisons with Measurements,* Journal of the Atmospheric Sciences, Vol. 52, No. 8, pp. 1204-1236, 1995

Albrecht, B.A., 1989, *Aerosols, Cloud Microphysics and Fractional Cloudiness,* Science, New Series, Vol. 245, Issue 4923, pp. 1227-1230, 1989

Andronache, C., T. Grönholm, L. Laakso, V. Philips and A. Venäläinen, 2006, *Scavenging of ultrafine particles by rainfall at a boreal site: observations and model estimations,* Atmospheric Chemistry and Physics, Vol. 6, pp. 4739-4754, 2006

Arnold, F., 2006, *Atmospheric Aerosol and Cloud Condensation Nuclei Formation: A Possible Influence of Cosmic Rays?,* Space Science Reviews, Vol. 125, pp. 169-186, 2006

Ayers, G.P., R.W. Gillett, and J.L. Gras, 1980, *On the Vapor Pressure of Sulphuric Acid,* Geophysical Research Letters, Vol. 7, No. 6, pp. 433-436, 1980

Bates, T.S., R.J. Charlson, R.H. Gammon, 1987, *Evidence for the climatic role of marine biogenic sulphur,* Nature, Vol. 329, pp. 319-321, 1987

Bates, T.S., J.D. Cline, R.H. Gammon, and S.R. Kelly-Hansen, 1987a, *Regional and Seasonal Variations in the Flux of Oceanic Dimethylsulfide to the Atmosphere,* Journal of Geophysical Research, Vol. 92, No. C3, pp. 2930-2938, 1987

Beard, K.V., 1976, *Terminal Velocity and Shape of Cloud and Precipitation Drops Aloft,* Journal of the Atmospheric Sciences, Vol. 33, pp. 851-864, 1976

Beard, K.V., and H.T. Ochs III, 1993, *Warm-Rain Initiation: An Overview of Microphysical Mechanisms,* Journal of Applied Meteorology, Vol. 32, pp. 608-625, 1993

Beheng, K.D., and G. Doms, 1986, *A General Formulation of Collection Rates of Cloud and Raindrops Using the Kinetic Equation and Comparison with Parameterizations,* Beiträge zur Physik der Atmosphäre, Vol. 59, No. 1, 1986

Carslaw, K.S., R.G. Harrison, and J. Kirkby, 2002, *Cosmic Rays, Clouds, and Climate ,* Science, Vol. 298, pp. 1732-1736, 2002

Chapman, S., T.G. Cowling, 1939, *The Mathematical Theory of Non-Uniform Gases,* Cambridge Mathematical Library, Cambridge University Press, first published 1939, reprint 1990

Charlson, R.J., J.E. Lovelock, M.O. Andreae, S.G. Warren, 1987, *Oceanic phytoplankton, atmospheric sulphur, cloud albedo and climate,* Nature, Vol. 326, pp. 655-661, 1987

Chen, C.-C., C.-J. Tao, and H.-J. Shu, 2000, *Heterogeneous Nucleation of n-Butanol Vapor on Submicrometer Charged and Neutral Particles of Lactose and Monosodium Glutamate,* Journal of Colloid and Interface Science, Vol. 224, pp. 11-22, 2000

Chlond, A., F. Müller, and I. Sednev, 2004, *Numerical simulation of the diurnal cycle of marine stratocumulus during FIRE – An LES and SCM modeling study,* Quarterly Journal of the Royal Meteorological Society, Vol. 130, pp. 3297-3321, 2004

Clarke, A.D., 1987, *The Pacific Marine Aerosol: Evidence for Natural Acid Sulfates,* Journal of Geophysical Research, Vol. 92, No. D4, pp. 4179-4190, 1987

Clarke, A.D., D. Davis, V.N. Kapustin, F. Eisele, G. Chen, I. Paluch, D. Lenschow, A.R. Bandy, D.

Thorton, K. Moore, L. Mauldin, D. Tanner, M. Litchy, M.A. Carroll, J. Collins, and G. Albercook, 1998, *Particle Nucleation in the Tropical Boundary Layer and Its Coupling to Marine Sulfur Sources,* Science, Vol. 282, pp. 89-92, 1998

Clarke, A.D., S.R. Owens, and J. Zhou, 2006, *An ultrafine sea-salt flux from breaking waves: Implications for cloud condensation nuclei in the remote marine atmosphere,* Journal of Geophysical Research, Vol. 111, D06202, doi: 10.1029/2005JD006565, 2006

Clegg, S.L., and P. Brimblecombe, 1995, *Application of a Multicomponent Thermodynamic Model to Activities and Thermal Properties of 0-40 mol kg$_{-1}$ Aqueous Sulfuric acid from <200 to 328 K,* Journal of Chemical & Engineering Data, Vol. 40, pp. 43-64, 1995

Clegg, S.L., K.S. Carslaw, and P. Brimblecombe, 1998, *Comment on "Vapor pressures in the ternary system water-nitric acid-sulphuric acid at low temperature: A reexamination" by D.-E. Taleb, J.-L. Ponche and P. Mirabel: Part 2,* Journal of Geophysical Research, Vol. 103, No. D13, pp. 16291-16294, 1998

Clegg, S.L., J.A. Rard, and K.S. Pitzer, 1994, *Thermodynamic Properties of 0-6 mol kg^{-1} Aqueous Sulfuric Acid from 273.15 to 328.15 K,* Journal of the Chemical Society, Faraday Transactions, Vol. 90, No. 13, pp. 1875-1894, 1994

Currie, R.G., 1992, *Deterministic Signals in USA Precipitation Records: Part II,* International Journal of Climatology, Vol. 12, pp. 281-304, 1992

Currie, R.G., 1993, *Luni-Solar 18.6- and Solar Cycle 10-11- Year Signals in USA Air Temperature Records,* International Journal of Climatology, Vol. 13, pp. 31-50, 1993

Davenport, H.M., and L.K. Peters, 1978, *Field studies of atmospheric particulate concentration changes during precipitation,* Atmospheric Environment, Vol. 12, pp. 997-1008, 1978

de Bruyn, W.J., M. Harvey, J.M. Cainey, and E.S. Saltzman, 2002, *DMS and SO$_2$ at Baring Head, New Zealand: Implications for the Yield of SO$_2$ from DMS,* Journal of Atmospheric Chemistry, Vol. 41, pp. 189-209, 2002

de Leeuw, G., F.P. Neele, M. Hill, M.H. Smith, and E. Vignati, 2000, *Production of sea spray aerosol in the surf zone,* Journal of Geophysical Research, Vol. 105, No. D24, pp. 29397-29409, 2000

Diehl, R., R. Kallenbach, E. Parizot, and R. Von Steiger, 2001, *The Astrophysics of Galactic Cosmic Rays,* Space Science Reviews, Vol. 99, pp. 3-11, 2001

Duynkerke, P.G., S.R. de Roode, M.C. van Zanten, J. Calvo, J. Cuxart, S. Cheinet, A. Chlond, H. Grenier, P.J. Jonker, M. Köhler, G. Lenderink, D. Lewellen, C.-L. Lappen, A.P. Lock, C.-H. Moeng, F. Müller, D. Olmeda, J.-M. Piriou, E. Sanchez, and I. Sednev, 2004, *Observations and numerical simulations of the diurnal cycle of the EUROCS stratocumulus case,* Quarterly Journal of the Royal Meteorological Society, Vol. 130, pp. 3269-3296, 2004

Eichkorn, S., S. Wilhelm, H. Aufmhoff, K.H. Wohlfrom, and F. Arnold, 2002, *Cosmic ray-induced aerosol-formation: First observational evidence from aircraft-based ion mass spectrometer measurements in the upper troposphere,* Geophysical Research Letters, Vol. 29, No. 14, doi: 10.1029/2002GL015044, 2002

Feingold, G., and S.M. Keidenweis, 2002, *Cloud processing of aerosol as modeled by a large eddy simulation with coupled microphysics and aqueous chemistry,* Journal of Geophysical Research, Vol. 107, No. D23, doi:10.1029/2002JD002054, 2002

Feingold, G., S.M. Kreidenweis, B. Stevens, and C.R. Cotton, 1996, *Numerical simulations of stratocumulus processing of cloud condensation nuclei through collision coalescence,* Journal of Geophysical Research, Vol. 101, No. D16, pp. 21391-21402, 1996

Feynman, J., and A. Ruzmaikin, 1999, *Modulation of Cosmic Ray Precipitation Related to Climate,* Geophysical Research Letters, Vol. 26, No. 14, pp. 2057-2060, 1999

Feynman, R.P., R.B. Leighton, and M. Sands, 1963, *The Feynman Lectures on Physics,* Addison-Wesley Publishing Company, 1963

Fitzgerald, J.W., 1991, *Marine Aerosols: A Review,* Atmospheric Environment, Vol. 25A, No. 3, pp. 533-545, 1991

Fuchs, N.A., 1964, *The mechanics of aerosols,* Pergamon Press, 1964

Fuller, E.N., P.D. Schettler, J.C. Giddings, 1966, *A new method for prediction of binary gas-phase diffusion coefficients,* Industrial & Engineering Chemistry, Vol. 58, Is. 6, pp. 18-27, 1966

Giauque, W.F., E.W. Hornung, J.E. Kunzler, and T.R. Rubin, 1960, *The Thermodynamic Properties of Aqueous Sulfuric Acid Solutions and Hydrates from 15 to 300°K,* Journal of the American Chemical Society, Vol. 82, pp. 62-70, 1960

Gmitro, J.I., and T. Vermeulen, 1964, *Vapor-Liquid Equilibria for Aqueous Sulfuric Acid,* A.I.Ch.E. Journal, Vol. 10, No. 5, pp. 740-746, 1964

Gondwe, M., M. Krol, W. Gieskes, W. Klassen, and H. De Baar, 2003, *The contribution of ocean-leaving DMS to the global atmospheric burdens of DMS, MSA, SO$_2$ and NSS SO$_4$,* Global Biogeochemical Cycles, Vol. 17, No. 2, doi: 10.1029/2002GB001937, 2003

Haigh, J.D., 1994, *The role of stratospheric ozone in modulating the solaer radiative forcing of climate,* Nature, Vol. 370, pp. 544-546, 1994

Haigh, J.D., 1996, *The Impact of Solar Variability on Climate,* Science, Vol. 272, No. 5264, pp. 981-984, 1996

Hamielec, A.E., and A.I. Johnson, 1962, *Viscous flow around fluid spheres at intermediate Reynolds numbers*, Canadian Journal of Chemical Engineering, Vol. 40, pp. 41-45, 1962

Hamill, P., 1975, *The Time Dependent Growth of H$_2$O-H$_2$SO$_4$ Aerosols by Heteromolecular Condensation,* Journal of Aerosol Research, Vol. 6, pp. 475-482, 1975

Hänel, G., 1987, *The Role of Aerosol Properties During the Condensational Stage of Cloud: A Reinvestigation of Numerics and Microphysics,* Beiträge zur Physik der Atmosphäre, Vol. 60, No. 3, pp. 321-339, 1987

Hegg, D.A., and P.V. Hobbs, 1981, *Cloud Water Chemistry and the Production of Sulfates in Clouds,* Atmospheric Environment, Vol. 15, No. 9, pp. 1597-1604, 1981

Hervig, M., and D. Siskind, 2006, *Decadal and inter-hemispheric variability in polar mesospheric clouds, water vapor, and temperature,* Journal of Atmospheric and Solar-Terrestrial Physics, Vol. 68, pp. 30-41, 2006

Hobbs, P.V., 1993, *Aerosol-Cloud-Climate Interactions,* in: International Geophysics Series, Vol. 54, Academic Press, 1993

Holland, P.M., and A.W. Castleman, Jr., 1982, *Thomson Equation Revisited in Light of Ion-Clustering Experiments,* Journal of Physical Chemistry, Vol. 86, pp. 4181-4188, 1982

Hoppel, W.A., 1977, *Ion-Aerosol Attachment Coefficients and the Diffusional Charging of Aerosols,* in: Electrical processes in atmospheres, Proceedings of the Fifth International Conference on Atmospheric Electricity held at Garmisch-Partenkirchen (Germany), 1977, pp. 60-69, Dr. Dietrich Steinkopff Verlag, 1977

Hoppel, W.A., and G.M. Frick, 1986, *Ion-Aerosol Attachment Coefficients and the Steady-State Charge Distribution on Aerosols in a Bipolar Ion Environment,* Aerosol Science and Technology, Vol. 5, pp. 1-21, 1986

Hoppel, W.A., G.M. Frick, J.W. Fitzgerald, and R.E. Larson, 1994, *Marine boundary layer measurements of new particle formation and the effects nonprecipitating clouds have on aerosol size distribution,* Journal of Geophysical Research, Vol. 99, No. D7, pp. 14443-14459, 1994

Hoppel, W.A., G.M. Frick, and R.E. Larson, 1986, *Effect of Nonprecipitating Clouds on the Aerosol Size Distribution in the Marine Boundary Layer,* Geophysical Research Letters, Vol. 13, No. 1, pp. 125-128, 1986

Hõrrak, U., J. Salm, and H. Tammet, 1998, *Bursts of intermediate ions in atmospheric air,* Journal of Geophysical Research, Vol. 103, No. D12, pp. 13909-13915, 1998

Houze, R.A., 1993, *Cloud Dynamics,* International Geophysics Series, Vol. 53, Academic Press, Elsevier, 1993

Hoyt, D.V., and K.H. Schatten, 1997, *The Role of the Sun in Climate Change,* Oxford University Press, 1997

Jacobson, M.Z., 1999, *Fundamentals of atmospheric modeling,* Cambridge University Press, Cambridge, UK, 1999

Jiang, H., and G. Feingold, 2006, *Effect of aerosol on warm convective clouds: Aerosol-cloud -surface flux feedbacks in a new coupled large eddy model,* Journal of Geophysical Research, Vol. 111, D01202, doi:10.1029/2005JD006138, 2006

Kazil, J., E.R. Lovejoy, M.C. Barth, and K. O'Brien, 2006, *Aerosol nucleation over the oceans and the role of galactic cosmic rays,* Atmospheric Chemistry and Physics, Vol. 6, pp. 4905-4924, 2006

Keefe, D., P.J. Nolan, and J.A. Scott, 1968, *Influence of Coulomb and Image Forces on Combination in Aerosols,* Proceedings of the Royal Irish Academy, Vol. 66 A, pp. 17-29, 1968

Kerminen, V.-M., L. Pirjola, and M. Kulmala, 2001, *How significantly does coagulational scavenging limit atmospheric particle production?,* Journal of Geophysical Research, Vol. 106, No. D20, pp. 24119-24125, 2001

Kessler, E., 1969, *On the Distribution and Continuity of Water Substance in Atmospheric Circulations,* Meteorological Monographs, Vol. 10, No. 32, American Meteorological Society, 1969

Kirkby, J., 2000, *A Study of the Link between Cosmic Rays and Clouds with a Cloud Chamber at the CERN PS,* The Cloud Collaboration, http://arxiv.org/abs/physics/0104048

Klett, J.D., and M.H. Davis, 1973, *Theoretical Collision Efficiencies of Cloud Droplets at Small Reynolds Numbers,* Journal of the Atmospheric Sciences, Vol. 30, pp. 107-117, 1973

Kniveton, D.R., M.C. Todd, J. Sciare, and N. Mihalopoulos, 2003, *Variability of atmospheric dimethylsulphide over the southern Indian Ocean due to changes in ultraviolet radiation,* Global Geochemical Cycles, Vol. 17, No. 4, doi: 10.1029/2003GB002033, 2003

Kondratyev, K.Y., 1999, *Climatic effects of aerosols and clouds,* Springer-Praxis series in atmospheric physics and climatology, Springer, 1999

Kristjansson, J.E., and J. Kristiansen, 2000, *Is there a cosmic ray signal in recent variations in global cloudiness and cloud radiative forcing ?,* Journal of Geophysical Research, Vol. 105, No. D9, pp. 11851-11863, 2000

Kristjansson, J.E., J. Kristiansen, and E. Kaas, 2004, *Solar activity, cosmic rays, clouds and climate – an update,* Advances in Space Research, Vol. 34, pp. 407-415, 2004

Kulmala, M., 1990, *Simulating the Formation of Acid Aerosols,* in: Acidification in Finland, P. Kaupi ed., Springer-Verlag, 1990

Kulmala, M., I. Riipinen, M. Sipälä, H.E. Manninen, T. Petäjä, H. Junninen, M. Dal Maso, G. Mordas, A. Mirme, M. Vana, A. Hirsikko, L. Laakso, R.M. Harrison, I. Hanson, C. Leung, K.E.J. Lehtinen, V.-M. Kerminen, *Toward Direct Measurement of Atmospheric Nucleation,* Science, Vol. 318, pp. 89-92, 2007

Laakso, L., J.M. Mäkelä, L. Pirjola, and M. Kulmala, 2002, *Model studies on ion-induced nucleation in the atmosphere,* Journal of Geophysical Research, Vol. 107, No. D20, doi: 10.1029/2002JD002140, 2002

Labitzke, K., 2003, *The global signal of the 11-year sunspot cycle in the atmosphere: When do we need the QBO?,* Meteorologische Zeitschrift, Vol. 12, No. 4, pp. 209-216, 2003

Landau, L.D., and E.M. Lifshitz, 1976, *Mechanics, Course of Theoretical Physics,* Vol. 1, Pergamon, New York, 1976

Larsen, S.H., 2005, *Solar variability, dimethyl sulphide, clouds, and climate,* Global Geochemical Cycles, Vol. 19, GB1014, doi: 10.1029/2004GB002333, 2005

Lawrence, M.G., 1993, *An empirical analysis of the strength of the phytoplankton-dimethylsulphide-cloud-cimate feedback cycle,* Journal of Geophysical Research, Vol. 98, pp. 20663-20673, 1993

Lean, J., 1991, *Variations in the Sun's Radiative Output,* Reviews of Geophysics, Vol. 29, No. 4, pp. 505-535, 1991

Lean, J., G.J. Rottman, H.L. Kyle, T.N. Woods, J.R. Hickey, and L.C. Puga, 1997, *Detection and parameterization of variations in solar mid- and near-ultraviolet radiation (200-400 nm),* Journal of Geophysical Research, Vol. 102, No. D25, pp. 29939-29956, 1997

Lee, S.-H., J.M. Reeves, J.C. Wilson, D.E. Hunton, A.A. Viggiano, T.M. Miller, J.O. Ballentin, and L.R. Lait, 2003, *Particle Formation by Ion Nucleation in the Upper Troposphere and Lower Stratosphere,* Science, Vol. 301, pp. 1886-1889, 2003

Lewis, E.R., and S.E. Schwartz, 2004, *Sea Salt Aerosol Production: Mechanisms, Methods, Measurements and Models,* Geophysical Monography Series, Vol. 152, American Geophysical Union, Washington, 2004

Lide, D.R., 2003, *CRC Handbook of Chemistry and Physics,* CRC Press, 84th edition, 2003

Lin, C.L., and S.C. Lee, 1975, *Collision Efficiency of Water Drops in the Atmosphere,* Journal of the Atmospheric Sciences, Vol. 32, pp. 1412-1418, 1975

Liu, Y., and P.H. Daum, 2004, *Parameterization of the Autoconversion Process. Part I: Analytical Formulation of the Kessler-Type Parameterizations,* Journal of the Atmospheric Sciences, Vol. 61, pp. 1539-1548, 2004, Vol. 62, pp. 3007-3008, 2005

Liu, Y., P.H. Daum, and R. McGraw, 2004, *An analytical expression for predicting the critical radius in the autoconversion parameterization,* Geophysical Research Letters, Vol. 31, L06121, doi: 10.1029/2003GL019117, 2004

Liu, Y., P.H. Daum, R. McGraw, and M. Miller, 2006, *Generalized threshold function accounting for effect of relative dispersion on threshold behavior of autoconversion process,* Geophysical Research Letters, Vol. 33, L11804, doi: 10.1029/2005GL025500, 2006

Liu, Y., P.H. Daum, R. McGraw, and R. Wood, 2006a, *Parameterization of the Autoconversion Process. Part II: Generalization of Sundqvist-Type Parameterizations,* Journal of the Atmospheric Sciences, Vol. 63, No. 3, pp. 1103-1109, 2006

Loeb, L.B., 1955, *Basic Processes of Gaseous Electronics,* University of California Press, Berkeley and Los Angeles, 1955

Long, A.B., 1974, *Solutions to the Droplet Collection Equation for Polynomial Kernels,* Journal of the Atmospheric Sciences, Vol. 31, pp. 1040-1052, 1974

Loosmore, G.A., and R.T. Cederwall, 2004, *Precipitation scavenging of atmospheric aerosols for emergency response applications: testing an updated model with new real-time data,* Atmospheric Environment, Vol. 38, pp. 993-1003, 2004

Lovejoy, E.R., J. Curtius, and K.D. Froyd, 2004, *Atmospheric ion-induced nucleation of sulfuric acid and*

water, Journal of Geophysical Research, Vol. 109, D08204, doi: 10.1029/2003JD004460, 2004

Manley and Manson, 1952, *Particle motions in sheared suspensions. II. Collisions of uniform spheres,* Journal of Colloid Science, Vol. 7, p. 354 ff., 1952

Marsh, N., and H. Svensmark, 2000, *Cosmic Rays, Clouds, and Climate,* Space Science Reviews, Vol. 94, pp. 215-230, 2000

Marsh, N., and H. Svensmark, 2003a, *Solar Influence on Earth's Climate,* Space Science Reviews, Vol. 107, pp. 317-325, 2003

Martensson, E.M., E.D. Nilsson, G.D. Leeuw, L.H. Cohen, and H.C. Hansson, 2003, *Laboratory simulations and parameterization of the primary marine aerosol production,* Journal of Geophysical Research, Vol. 108, No. D9, 4297, doi:10.1029/2002JD002263, 2003

Marti, J.J., A. Jefferson, X.P. Cai, C. Richert, P.H. McMurry, and F. Eisele, 1997, *H_2SO_4 vapor pressure of sulfuric acid and ammonium sulfate solutions,* Journal of Geophysical Research, Vol. 102, No. D3, pp. 3725-3735, 1997

Masucci, M., S.L. Clegg, and P. Brimblecombe, 1996, *Equilibrium Vapor Pressure of H_2O above Aqeous H_2SO_4 at Low Temperature,* Journal of Chemical and Engineering Data, Vol. 41, No. 4, pp. 765-778, 1996

Miles, N.L., J. Verlinde, and E.E. Clothiaux, 2000, *Cloud Droplet Size Distribution in Low-Level Stratiform Clouds,* Journal of the Atmospheric Sciences, Vol. 57, No. 2, p. 295-311, 2000

McCracken, K.G., J. Beer, and F.B. McDonald, 2004, *Variations in the cosmic radiation, 1890-1986, and the solar and terrestrial implications,* Advances in Space Research, Vol. 34, pp. 397-406, 2004

McGraw, R., and Y. Liu, 2003, *Kinetic Potential and Barrier Crossing: A Model for Warm Cloud Drizzle Formation,* Physical Review Letters, Vol. 90, No. 1, doi: 10.1103/PhysRevLett.90.018501, 2003

Modgil, M.S., S. Kumar, S.N. Tripathi, and E.R. Lovejoy, 2005, *A parameterization of ion-induced nucleation of sulphuric acid and water for atmospheric conditions,* Journal of Geophysical Research, Vol. 110, D19205, doi: 10.1029/2004JD005475, 2005

Mohnen, V.A., 1977, *Ions, Basic Research,* in: Electrical Processes in Atmospheres, Proceedings of the Fifth International Conference on Atmospheric Electricity held at Garmisch-Partenkirchen (Germany), 1974, pp. 1-17, Dr. Dietrich Steinkopff Verlag, 1977

Monahan, E.C., K.L. Davidson, and D.E. Spiel, 1982, *Whitecap Aerosol Productivity Deduced From Simulation Tank Measurements,* Journal of Geophysical Research, Vol. 87, No C11, pp. 8898-8904, 1982

Monahan, E.C., D.E. Spiel, and K.L. Davidson, 1986, *A Model of Marine Aerosol Generation via Whitecaps and Wave Distribution,* in: Oceanic Whitecaps, E.C. Monahan and G. Mac Niocaill (eds.), D. Reidel Publishing Company, pp. 167-174, 1986

Nadykto, A.B., and F. Yu, 2003, *Uptake of neutral polar vapor molecules by charged clusters/particles: Enhancement due to dipole-charge interaction,* Journal of Geophysical Research, Vol. 108, No. D23, doi: 10.1029/2003JD003664, 2003

Nagato, K., C.S. Kim, M. Adachi, and K. Okuyama, 2005, *An experimental study of ion-induced nucleation using a drift tube ion mobility spectrometer/mass spectrometer and a cluster-differential mobility analyzer/Faraday cup electrometer,* Journal of Aerosol Science, Vol. 36, pp. 1036-1049, 2005

Neff, U., S.J. Burns, A. Mangini, M. Mudelsee, D. Fleitmann, and A. Matter, 2001, *Strong coherence between solar variability and the monsoon in Oman between 9 and 6 kyr ago,* Nature, Vol. 411, pp. 290-293, 2001

Nicolis, G., 1995, *Introduction to Nonlinear Science,* Cambridge University Press, 1995

Pandis, S.N., L.M. Russell, and J.H. Seinfeld, 1994, *The relationship between DMS flux and CCN concentration in remote marine regions,* Journal of Geophysical Research, Vol. 99, pp. 16945-16957, 1994

Pinsky, M.B., and A.P. Khain, 2004, *Collision of Small Drops in a turbulent Flow. Part II: Effects of Flow Accelerations,* Journal of the Atmospheric Sciences, Vol. 61, pp. 1926-1939, 2004

Pinsky, M.B., A.P. Khain, and M. Shapiro, 1999, *Collision of Small Drops in a Turbulent Flow. Part I.: Collision Efficiency. Problem Formulation and Preliminary Results,* Journal of the Atmospheric Sciences, Vol. 56, pp. 2585-2600, 1999

Pinsky, M.B., A.P. Khain, and M. Shapiro, 2001, *Collision Efficiency of Drops in a Wide Range of Reynolds Numbers: Effect of Pressure on Spectrum Evolution,* Journal of the Atmospheric Sciences, Vol. 58, pp. 742-764, 200

Pirjola, L., and M. Kulmala, 1998, *Modelling the formation of H_2SO_4-H_2O particles in rural, urban and marine conditions,* Atmospheric Research, Vol. 46, pp. 321-347, 1998

Pirjola, L., M. Kulmala, M. Wilck, A. Bischoff, F. Stratmann, and E. Otto, 1998, *Effects of Aerosol Dynamics on the Formation of Sulphuric Acid Aerosols and Cloud Condensation Nuclei,* Report Series in Aerosol Science , Finnish Association for Aerosol Research, No. 38, 1998

Pitzer, K.S., 1981, *The Treatment of Ionic Solutions over the Entire Miscibility Range,* Berichte der Bunsengesellschaft Physikalische Chemie, Vol. 85, pp. 952-959, 1981

Quinn, P.K., T.S. Bates, T.L. Miller, D.J. Coffman, J.E. Johnson, J.M. Harris, J.A. Ogren, G. Forbes, T.L. Andersen, D.S. Covert, and M.J. Rood, 2000, *Surface submicron aerosol chemical composition: What fraction is not sulfate?,* Journal of Geophysical Research, Vol. 105, No. D5, pp. 6785-6805, 2000

Quinn, P.K., D.S. Covert, T.S. Bates, V.N. Kapustin, D.C. Ramsey-Bell, and L.M. McInnes, 1993, *Dimethylsulfide/Cloud Condensation Nuclei/Climate System: Relevant Size-Resolved Measurements of the Chemical and Physical Properties of Atmospheric Aerosol Particles,* Journal of Geophysical Research, Vol. 98, No. D6, pp. 10411-10427, 1993

Radke, L.F., J.A. Coakley, and M.D. King, 1989, *Direct and Remote Sensing Observations of the Effects of Ships on Clouds,* Science, Vol. 246, pp. 1146-1149, 1989

Radke, L.F., and P.V. Hobbs, 1991, *Humidity and Particle Fields Around Some Small Cumulus Clouds,* Journal of the Atmospheric Sciences, Vol. 48, No. 9, pp. 1190-1193, 1991

Raes, F., and A. Janssens, 1985, *Ion-induced aerosol formation in a H_2O-H_2SO_4 System – I. Extension of the classical theory and search for experimental evidence,* Journal of the Aerosol Science, Vol. 16, No. 3, p. 217-227, 1985

Raes, F., and A. Janssens, 1986, *Ion-induced aerosol formation in a H_2O-H_2SO_4 System – II. Numerical calculations and conclusions,* Journal of the Aerosol Science, Vol. 17, No. 4, pp. 715-722, 1986

Ramanathan, V., R.D. Cess, E.F. Harrison, P. Minnis, B.R. Barkstrom, E. Ahmad, and D. Hartmann, 1989, *Cloud-Radiative Forcing and Climate: Results from the Earth Radiation Budget Experiment,* Science, Vol. 243, pp. 57-63, 1989

Reiss, H., 1950, *The Kinetics of Phase Transitions in Binary Systems,* Journal of Chemical Physics, Vol. 18, No. 6, pp. 840-848, 1950

Reiter, R., 1992, *Phenomena in atmospheric and environmental electricity,* Elsevier, 1992

Ringer, M.A., and K.P. Shine, 1997, *Sensitivity of the Earth's radiation budget to interannual variations in cloud amount,* Climate Dynamics, Vol. 13, pp. 213-222, 1997

Robinson, R.A., and R.H. Stokes, 1959, *Electrolyte Solutions, The measurement and Interpretation of Conductance, Chemical Potential and Diffusion in Solutions of Simple Electrolytes,* Second Edition, Butterworths Scientific Publications, London, 1959

Saffmann, P.G., and J.S. Turner, 1956, *On the collision of drops in turbulent clouds,* Journal of Fluid Mechanics, Vol. 1, pp. 16-30, 1956

Sahni, D.C., 1966, *The effect of a black sphere on the flux distribution in an infinite moderator,* Journal of Nuclear Energy, Parts A/B, Vol. 20, pp. 915-920, 1966

Saltzman, B., 2002, *Dynamical Paleoclimatology,* in: International Geophysics Series, Vol. 80, Academic Press, 2002

Schlamp, R.J., S.N. Grover, H.R. Pruppacher, and A.E. Hamielec, 1976, *A Numerical Investigation of the Effect of Electric Charges and Vertical External Electric Fields on the Collision Efficiency of Cloud Drops,* Journal of the Atmospheric Sciences, Vol. 33, pp. 1747-1755, 1976

Schlesinger, M.E., and N. Ramankutty, 1992, *Implications for global warming of intercycle solar irradiance variations,* Nature, Vol. 360, pp.330-333, 1992

Seinfeld, J.H., and S.N. Pandis, 1998, *Atmospheric chemistry and physics: From air pollution to climate change,* John Wiley & Sons, New York, 1998

Shea, M.A., and D.F. Smart, 2004, *Preliminary study of cosmic rays, geomagnetic field changes and possible climate changes,* Advances in Space Research, Vol. 34, pp. 420-425, 2004

Skelland, A.H.P., 1974, *Diffusional Mass Transfer,* John Wiley, 1974

Slinn, W.G.N., 1977, *Some Approximations for the Wet and Dry Removal of Particles and Gases from the Atmosphere,* Water, Air, and Soil Pollution, Vol. 7, pp. 513-543, 1977

Smirnov, V.I., 1971, *The Rate of Quasi-Steady Growth and Evaporation of Small Drops in a Gaseous Medium,* Pure and Applied Geophysics, Vol. 86, Is. III, pp. 184-194, 1971

Spracklen, D.V., K.S. Carslaw, M. Kulmala, V.-M. Kerminen, G.W. Mann, and S.-L. Sihto, 2006, *The contribution of boundary layer nucleation events to total particle concentrations on regional and global scales,* Journal of Atmospheric Chemistry and Physics, Vol. 6, pp. 5631-5648, 2006

Stauffer, D., 1976, *Kinetic Theory of Two-Component ("Heteromolecular") Nucleation and Condensation,* Journal of Aerosol Science, Vol. 7, pp. 319-333, 1976

Stöcker, H., 1995, *Taschenbuch Mathematischer Formeln und Moderner Verfahren,* Verlag Harri Deutsch, 3rd edition, Thun, 1995

Svensmark, H., and E. Friis-Christensen, 1997, *Variation of cosmic ray flux and global cloud coverage – a missing link in solar-climate relationships,* Journal of Atmospheric and Solar-Terrestrial Physics, Vol. 59, No. 11, pp. 1225-1232, 1997

Svensmark, H., J.O.P. Pedersen, N.D. Marsh, M.B. Enghoff, and U.I. Uggerhøj, 2007, *Experimental evidence for the role of ions in particle nucleation under atmospheric conditions,* Proceedings of the Royal Society A, Vol. 463, pp. 385-396, 2007

Tammet, H., U. Hõrrak, L. Laakso, and M. Kulmala, 2006, *Factors of air ion balance in a coniferous forest according to measurements in Hyytiälä, Finland,* Atmospheric Chemistry and Physics, Vol. 6, pp. 3377-3390, 2006

Tanaka, H.K.M., 2005, *Cosmogenic ion production rate in the high–middle–low altitude troposphere and its influence on the terrestrial cloud physics,* Journal of Atmospheric and Solar-Terrestrial Physics, Vol. 67, pp. 1544-1558, 2005

Thomson, J.J., 1906, *Conduction of Electricity through Gases*, Cambridge University Press, 1906

Tinsley, B.A., 2000, *Influence of solar wind on the global electric circuit, and inferred effects on cloud mirophysics, temperature and dynamics in the troposphere,* Space Science Reviews, Vol. 94, pp. 231-258, 2000

Tinsley, B.A., R.P. Rohrbaugh, and M. Hei, 2000, *Effects of Image Charges on the Scavenging of Aerosol Particles by Cloud Droplets and on Droplet Charging and Possible Ice Nucleation Processes,* Journal Of the Atmosphereric Sciences, Vol. 57, pp. 2118-2134, 2000

Twomey, S., 1991, *Aerosols, Clouds and Radiation,* Atmospheric Environment, Vol. 25A, No. 11, pp. 2435-2442, 1991

UIO, 1998, *Density measurements as a function of weight fraction and temperature,* Chemical Institute, University of Oslo, http://www.kjemi.uio.no/09_spekt/Atmosfaere/LAMOCS/density.doc

Usoskin, I.G., O.G. Gladysheva, and G.A. Kovaltsov, 2004, *Cosmic ray-induced ionization in the atmosphere: spatial and temporal changes,* Journal of Atmospheric and Solar-Terrestrial Physics, Vol. 66, pp. 1791-1796, 2004

Waldmann, L., 1959, *Über die Kraft eines inhomogenen Gases auf kleine suspendierte Kugeln,* Zeitschrift für Naturforschung, Vol. 14A, pp. 589-599, 1959

vanZanten, M.C., B. Stevens, G. Vali, and D.H. Lenschow, 2005, *Observations of Drizzle in Nocturnal Marine Stratocumulus,* Journal of the Atmospheric Sciences, Vol. 62, pp. 88-106, 2005

von Schilling, H., 1972, *Statistische Physik in Beispielen,* veb Fachbuchverlag, Leipzig, 1972

Wood, R., and P.N. Blossey, 2005, *Comments on "Parameterization of the Autoconversion Process. Part I: Analytical Formulation of the Kessler-Type Parameterizations",* Journal of the Atmospheric Sciences, Vol. 62, pp. 3003-3006, 2005

Yoon, Y.J., and P. Brimblecombe, 2002, *Modelling the contribution of sea salt and dimethyl sulfide derived aerosol to CCN,* Atmospheric Chemistry and Physics, Vol. 2, pp. 17-30, 2002

Yu, F., 2002, *Altitude variations of cosmic ray induced production of aerosols: Implications for global cloudiness and climate,* Journal of Geophysical Research, Vol. 107, No. A7, doi: 10.1029/2001JA000248, 2002

Yu, F., 2003, *Nucleation rate of particles in the lower atmosphere: Estimated time needed to reach pseudo-steady state and sensitivity to H_2SO_4 gas concentration,* Geophysical Research Letters, Vol. 30, No. 10, 1526, doi: 10.1029/2003GL017084, 2003

Yu, F., 2005, *Modified Kelvin-Thomson equation considering ion-dipole interaction: Comparison with observed ion-clustering enthalpies and entropies,* The Journal of Chemical Physics, Vol. 122, 084503, doi: 10.1063/1.1845395, 2005

Yu, F., 2006, *Effect of ammonia on new particle formation: A kinetic $H_2SO_4 – H_2O – NH_3$ nucleation model constrained by laboratory measurements,* Journal of Geophysical Research, Vol. 111, D01204, doi: 10.1029/2005JD005968, 2006

Yu, F., 2006a, *Binary $H_2SO_4 – H_2O$ homogeneous nucleation based on kinetic quasi-unary nucleation model: Look-up tables,* Journal of Geophysical Research, Vol. 111, D04201, doi: 10.1029/2005JD006358, 2006

Yu, F., 2006b, *From molecular clusters to nanoparticles: second-generation ion-mediated nucleation model,* Atmospheric Chemistry and Physics, Vol. 6, pp. 5193-5211, 2006

Yu, F., and R.P. Turco, 2001, *From molecular clusters to nanoparticles: Role of ambient ionization in tropospheric aerosol formation,* Journal of Geophysical Research, Vol. 106, No. D5, pp. 4797-4814, 2001

Danksagung

Diese Arbeit wurde an der Abteilung Klimaprozesse von Herrn Prof. Hartmut Grassl des Max-Planck-Instituts für Meteorologie ausgeführt. Für diese Gelegenheit möchte sich der Autor bei Herr Professor Grassl herzlichst bedanken. Die wissenschaftliche Atmosphäre des Max-Planck-Institut bot für dieses Vorhaben den idealen Rahmen, nicht zuletzt wegen der phantastischen Aussicht im Geomatikum, welche, das Studienobjekt im Blick, immer wieder einen inspirierenden Einfluss ausübte.

Ein besonderer Dank geht ebenfalls an das Ministerium für höhere Bildung, Kultur und Forschung des Grossherzogtums Luxemburg, welches einen Grossteil des finanziellen Aspektes aufbrachte, sowie an Herrn Prof. Martin Claussen für die Unterstützung während der letzten zusätzlichen Monaten dieser Arbeit. Ohne finanzielle Unterstützung lässt sich eine derartige Arbeit nicht realisieren, daher der Autor diese Hilfe aufrichtig zu würdigen weiss.

Im Speziellen möchte sich der Verfasser für die persönliche Betreuung bei Herrn Dr. Andreas Chlond und Herrn Dr. Frank Müller bedanken. Ihre kritischen Kommentare und Anregungen haben dieser Arbeit sehr entscheidende Impulse gegeben, ohne die diese Arbeit sicherlich nicht ihre endgültige Form erhalten hätte.

Ein sehr persönlicher Dank geht an Frau Laury Sarti, die sich als bestmögliche Beraterin in sehr vielseitigen Situationen des Lebens erwiesen hat, und daher mehr zu dieser Arbeit beigetragen hat als sich von ihrem Inhalt her vermuten liesse.